Title

Actin Mechanisms in Retinal Pigment Epithelium Trogocytosis and the Consequences of Retinal Detachment on Rod Synaptic Ultrastructure

Author

Torten, Gil

Publication Date

2024

UNIVERSITY OF CALIFORNIA

Los Angeles

Actin Mechanisms in Retinal Pigment Epithelium Trogocytosis and the Consequences of Retinal Detachment on Rod Synaptic Ultrastructure

A dissertation submitted in partial satisfaction of the requirements for the degree Doctor of Philosophy in Neuroscience

by

Gil Torten

2024

ABSTRACT OF THE DISSERTATION

Actin Mechanisms in Retinal Pigment Epithelium Trogocytosis and the Consequences of Retinal Detachment on Rod Synaptic Ultrastructure

by

Gil Torten

Doctor of Philosophy in Neuroscience

University of California, Los Angeles, 2024

Professor David S. Williams, Chair

Ingestion of photoreceptor outer segments (POS/OS) by the retinal pigment epithelium (RPE) is a fundamentally important process for vision. The RPE form an actin based phagocytic cup that extends along the OS and engages in trogocytosis to break off a piece of the OS for subsequent ingestion. This process is highly dynamic, and so we have used live cell imaging with high temporal resolution to understand the kinetics of ingestion and the localization of different relevant proteins throughout the ingestion process. We have found that the phagocytic cup is initiated by mDia1 formin

activity. The Arp2/3 complex creates branched actin around the rim of the cup and beneath phagosomes to hold them in their proper location for scission and ingestion. Once excised, Myosin 7a traffics the phagosome basally into the cell for subsequent degradation. When photoreceptor-RPE interaction stops, such as during a retinal detachment, there are consequences to the photoreceptor synapse. Utilizing the high resolution capabilities of electron microscope (EM) tomography, we then explored the ultrastructure of the rod photoreceptor synapse (or rod spherule, RS) after 7 days of retinal detachment. 7 days of retinal detachment results in significant degeneration to the synaptic ultrastructure at the outer plexiform layer, including a loss of rod bipolar dendrites, simplification of horizontal cell axon terminals, fragmentation of the synaptic ribbon, and a simplification of the rod spherule invagination membrane. Following up, we then explored the timescale of these degenerative changes, performing tomography on synapses in retinas detached for 30min., 1hr., 24hrs., 48hrs., and 72hrs., in order to understand how long of a detachment may be too late for full recovery. By 24hrs. of detachment, there is significant remodeling including elongated ribbons and simplified horizontal cell processes; at least one rod bipolar cell process per rod spherule retracts by 24hrs. of detachment in a majority of cases. 24hrs. is likely the latest time point for reattachment without incurring long term visual deficits due to synaptic degeneration. By better understanding the way that OS are phagocytosed, as well as the consequences to the rod synapse when they are not, we can learn significant additional information about the health and maintenance of the rod photoreceptor.

The dissertation of Gil Torten is approved.

Steven Fisher

Margot Elizabeth Quinlan

Yirong Peng

David S. Williams, Committee Chair

University of California, Los Angeles

2024

TABLE OF CONTENTS

LIST OF FIGURES AND TABLES

Chapter 1

Chapter 2

Chapter 3

ACKNOWLEDGEMENTS

Chapter 1, Figs. 1-3A-D, and 1-4 were adapted from Umapathy A., Torten G., Paniagua AE., Chung J., Tomlinson M., Lim C., Williams DS. (2023) Spatiotemporal Live-Cell Analysis of Photoreceptor Outer Segment Membrane Ingestion by the Retinal Pigment Epithelium Reveals Actin-Regulated Scission. J Neurosci 43:2653–2664.

Chapter 2 is a preface, along with the entirety of Torten G, Fisher SK, Linberg KA, Luna G, Perkins G, Ellisman MH, Williams DS (2023) Three-Dimensional Ultrastructure of the Normal Rod Photoreceptor Synapse and Degenerative Changes Induced by Retinal Detachment. J Neurosci 43:5468–5482.

Please see the Preface of each Chapter, for detailed contributions from each author.

This work was supported by the National Institute of Health Vision Science Training Grant 5T32EY007026-42 at UCLA.

VITA

EDUCATION

University of California Santa Barbara (UCSB) March 2019

B.A. in Biology, College of Creative Studies

PUBLICATIONS

- Umapathy, A., **Torten, G.**, Paniagua, A. E., Chung, J., Tomlinson, M., Lim, C., & Williams, D. S. (2023). Spatiotemporal Live-Cell Analysis of Photoreceptor Outer Segment Membrane Ingestion by the Retinal Pigment Epithelium Reveals Actin-Regulated Scission. *The Journal of neuroscience : the official journal of the Society for Neuroscience*, *43*(15), 2653–2664. https://doi.org/10.1523/JNEUROSCI.1726-22.2023
- **Torten, G.***, Fisher, S. K.*, Linberg, K. A., Luna, G., Perkins, G., Ellisman, M. H., & Williams, D. S. (2023). Three-Dimensional Ultrastructure of the Normal Rod Photoreceptor Synapse and Degenerative Changes Induced by Retinal Detachment. *The Journal of neuroscience : the official journal of the Society for Neuroscience*, *43*(30), 5468–5482. https://doi.org/10.1523/JNEUROSCI.2267-22.2023. *Contributed equally

PRESENTATIONS AND GRANTS

Conference Presentations –

- Poster Presentation. *ComSciCon 2023 Flagship Workshop*. Emerson College, Boston MA, 7/2023
- Oral Presentation and Discussion Lead. *RPE Symposium 2023.* Queenstown, New Zealand, 3/2023.
- Oral Presentation. *ISER (International Society of Eye Research) 2023 International Conference*. Gold Coast, Australia, 2/2023.
- Poster Presentation. *ARVO (Association for Research in Vision and Ophthalmology) 2021 International Conference.* Virtual, 5/2021
- Poster Presentation. *College of Creative Studies Research and Creative Activities Conference*. University of California Santa Barbara, 11/2018
- Oral and Poster Presentation. *College of Creative Studies Research and Creative Activities Conference.* University of California Santa Barbara, 11/2017

Academic and Outreach Presentations –

- *Neuroscience Behind Vision and Optical Illusions*. Independent class taught at Splash 2022 at UCLA, 4/2022
- *The Search for the Holy Grail: Finding the True Phagocytic Cup*. Presentation for the UCLA Library, 3/2022
- Jules Stein Eye Institute Journal Club, 2/2022
- UCLA Neuroscience Program; Neuroscience Associated Research Fellows Talk (NARF), 12/2019
- Sculpture Gallery and TED-Style Talk. *UCSB Art Walk 2019*. University of California Santa Barbara, 4/2019

Grants Acquired –

- NIH T32 Vision Science Training Grant, UCLA (7/2021-Present)
- Retina Research Foundation/Joseph M. and Eula C. Lawrence Travel Grant for ARVO 2021, (5/2021)
- Society for Neuroscience 2019 (Chicago, Illinois) Travel Grant, UCLA (10/2019)
- UC Santa Barbara URCA Grant, University of California Santa Barbara (8/2018)

Chapter 1: What is actin's role in ingesting photoreceptor outer segments (POS)?

PREFACE

Chapter 1 covers my work investigating the actin mechanisms of RPE phagocytosis. When I began my Ph.D. I worked alongside Dr. Ankita Umapathy, a postdoctoral researcher in the lab, and explored ARPE-19 as an actin model in support of Dr. Umapathy's work; Dr. Umapathy had spent much time developing primary mouse RPE as a live imaging model, while I worked on ARPE-19 in parallel. I worked collaboratively with Dr. Umapathy during my first couple years in the lab, before Ankita had finished her postdoctoral training. At this point, Dr. Umapathy had produced much of the data and hypotheses to complete a manuscript (Umapathy et al., 2023), and had performed a large number of experiments of which she derived important hypotheses and conclusions from. By the time that she left the lab, Dr. Umapathy had produced much of the data and hypotheses required to complete this manuscript, but the figures were incomplete, the manuscript was unfinished, and more data needed to be collected for publication. Dr. David Williams worked significantly to finalize this manuscript, and I contributed to this effort. For this manuscript, I performed additional phosphatidylserine experiments, quantified a range of data collected both by myself and Dr. Umapathy, and supported the manuscript writing effort with thorough review and intellectual suggestions. I also accomplished the further experiments required by the reviewers and helped rewrite the manuscript for the resubmission (particularly through editing figures and writing figure legends). Dr. Williams completed a majority of the manuscript writing and the reviewer response. Other relevant contributions to this manuscript include Dr. Antonio Paniagua, who provided an experimental image, as well as Julie Chung, Madeline Tomlinson, and Caleb Lim, undergraduates who contributed to early data analysis under Dr. Umapathy.

Umapathy et al., 2023 was a combined collaborative effort between a number of researchers, and so it was not appropriate to include this manuscript in full within the dissertation. However, I did significantly contribute to this manuscript, and the results carry much weight with regards to my follow-up work, and so data from this manuscript has been adapted and used in two figures within the dissertation (Figs. 1-3A-D, Fig. 1-4) and referenced appropriately throughout.

When listing contributions, those that contributed to my training for the work in this chapter should be noted. Dr. Umapathy provided me with live imaging training on the CSU-X1 Spinning Disk Field Scanning Confocal System, and Dr. Antonio Paniagua, Barry Burgess, and Dr. Roni Hazim provided me with all other relevant training including cell culture, primary RPE dissection, outer segment preparations, and more. In addition to training, two others contributed to the work presented in Chapter 1 of this dissertation: Dr. William Blake Gilmore created and provided a range of Myosin 7a imaging constructs, notably the lentiviral rescue construct used in Fig. 1-10E, and Olivia Mulry provided cell culture and live imaging assistance. Olivia Mulry also created tomogram segmentations for Chapter 3.

With this training, I followed up on Dr. Umapathy's work in three different ways. Chapter 1 of this dissertation will cover my work investigating the actin structures of ARPE-19, further optimizing the primary mouse RPE live imaging methodology, and follow-up on three proteins of interest: the Arp2/3 complex, mDia1, and Myosin 7a.

INTRODUCTION

The current state of RPE phagocytosis

Photoreceptor-RPE interaction is fundamentally important for long term maintenance of proper visual functioning, with deficits in this interaction, such as in Macular Degeneration, Retinitis Pigmentosa, and other retinopathies, leading to severe visual decline and eventually blindness (Gal et al., 2000; Duncan et al., 2003; Strauss, 2005; Esteve-Rudd et al., 2018; Inana et al., 2018). This interaction is based on the RPE's ability to phagocytose photoreceptor outer segments (POS or OS) regularly throughout life. The RPE forms an actin based structure, called a phagocytic cup, that extends up along the vertical outer segment and chews off pieces for ingestion (Almedawar et al., 2020; Kwon and Freeman, 2020; Umapathy et al., 2023). Previous work has shown the importance of actin in this ingestion process; actin morphology is predictive of phagocytic capacity (Müller and Finnemann, 2016; Müller et al., 2018a), a number of myosins have been found to be involved in the phagocytic process (Gibbs et al., 2003; Strick et al., 2009; Daniel et al., 2014; Zihni et al., 2022), and a range of Nucleation Promoting Factors (Shelby, 2012; Kwon and Freeman, 2020) and actin-associated Rho family GTPases (Nandrot and Finnemann, 2003; Mao and Finnemann, 2012, 2021) have also been shown to be involved. Fundamentally, actin structures are required for proper ingestion of outer segment material by the RPE.

Previous work in the lab (Umapathy et al., 2023) has established a new form of methodology to study 3D structure and protein interaction during ingestion – live cell imaging. We are the first to study ingestion through live cell imaging with fluorescent constructs of key proteins of interest, allowing us to create a more complete model for both the 3-D structure of the phagocytic cup as well as relative protein localization as it pertains to the phagocytosis process. In addition, the current state of live imaging technology has improved our ability to visualize this process providing unprecedented levels of spatial[1] and temporal[2] resolution. These recent advancements have uncovered a novel perspective on how the ingestion process should be viewed; generally, when RPE are fed POS in culture, ingestion does not result in an entire OS being fully engulfed, as in traditional phagocytosis. Instead, it is quite common for the apical actin cup to break off smaller pieces (median of 1.8μm in diameter [Umapathy et al., 2023]) from a larger OS, fully rupturing the target membrane, before engulfing these smaller pieces and trafficking them into the cell (Umapathy et al., 2023). In addition, *in vivo*, the organization of rod photoreceptors along the RPE is extremely tight, such that the peak rod density reaches about 28 rods/RPE cell in humans (Rapaport et al., 1995) and up to 216/RPE cell in mice (Volland et al., 2015; Keeling et al., 2020). Due to this organization, and the fact that outer segments do not shed when unassociated with RPE (Williams and Fisher, 1987; Guérin et al., 1993), the RPE likely excises a piece of the OS during the ingestion process. Traditionally, phagocytosis describes full engulfment of the target particle (Richards and Endres, 2014). However, in RPE, due to the rupture of the target membrane, this process realistically should be denoted as

---

[1] The primary improvement to spatial resolution lies in the Live-SR Module (Gataca Systems) which allows for resolution beyond light limits, without sacrificing temporal resolution

[2] Spinning Disk Confocal technology has improved significantly over the last decade, with the microscope used in this study (Yokogawa CSU-X1 Spinning Disk Field Scanning Confocal System) able to image up to 2000Hz

trogocytosis, coming from the latin '-trogo' or 'to gnaw or nibble', a subset of phagocytosis. While trogocytosis may share many features with traditional phagocytosis, there are likely specific differences regarding the scission event that require a distinct mechanism.

What actin nucleators and myosin(s) are required for successful ingestion?

Despite strong actin characterization of the phagocytic cup (Müller et al., 2018a; Umapathy et al., 2023), many of the actin associated proteins that facilitate cup structure are still unknown, notably the primary actin nucleators and relevant myosins. Actin monomers require accompanying proteins to organize into complex structural scaffolds to support cellular activity (Dominguez and Holmes, 2011). For example, profilin/cofilin regulate actin monomer availability (Dominguez and Holmes, 2011), spectrin-family proteins organize actin filament crosslinking, and BAR proteins link cytoskeletal dynamics with the membrane (Lee and Dominguez, 2010). The Arp2/3 complex, an actin nucleator, also plays such a role, by forming branched actin structures designed to stabilize and produce force (Goley and Welch, 2006; Ding et al., 2022). Formins, notably mDia1, act to nucleate actin assembly, induce processive elongation on the barbed end of actin filaments, and accelerate actin elongation (Pruyne et al., 2002; Goode and Eck, 2007; Breitsprecher and Goode, 2013). While it has been suggested that the Arp2/3 complex may play a role in RPE OS ingestion (Kevany and Palczewski, 2010; Kwon and Freeman, 2020), there is currently no direct evidence for this in the literature. In addition, while the Arp2/3 complex and mDia1 (as well as formins in general) have been implicated in other similar forms of phagocytosis such as in macrophages (Rotty et al., 2017; Jaumouillé et al., 2019) and Sertoli cells (Qian et al., 2013; Sakamoto et al., 2018), they have been almost entirely unexplored in the context of the retinal pigment epithelium.

Beyond actin nucleators, there must be some other protein, likely a myosin, to generate the force on the actin filaments required to rupture an external membrane (Houdusse and Sweeney, 2016; Robert-Paganin et al., 2020). In mouse, there are 7 myosins: myosin 1 (Myo1a-f, f-rs1), myosin II (MYH9, 10, 14), myosin V (Myo5a, b), myosin VI (Myo6), myosin VII (Myo7a, b, b-rs1), myosin IX (Myo9a, b), and myosin X (Myo10) (Hasson et al., 1996; Sellers and Heissler, 2019). Of these options, myosin II, myosin VI, and myosin VIIa seem the most likely to be involved in RPE phagocytosis. In more detail, myosin II is likely to be involved, as inhibition results in a reduction in phagocytosis (Strick et al., 2009; Zihni et al., 2022). However, the mechanism by which it acts is still unknown. Myosin VI has been implicated, both in the earlier stages of ingestion (Tan et al., 2023), as well as the later stages after the phagosomes have been trafficked into the cell (Daniel et al., 2014), but of the two manuscripts published on myosin VI and the RPE, neither has shown convincing evidence of scission activity at the apical region of the cup. Myosin 7a (of which mutations lead to Usher Syndrome 1B, a debilitating form of deaf-blindness [Usher, 1914; Weil et al., 1995; Williams, 2008]) has been clearly shown to be involved in the early stages of ingestion, as it associates with phagosomes in the apical region of the cell (Jiang et al., 2015), and primary RPE from shaker1 animals[3] are unable to traffic their phagosomes below this apical region (Gibbs et al., 2003). That said, the exact mechanism and localization of this protein, as

---

[3] *Myo7a*$^{4626SB/4626SB}$, Usher 1B model containing the 4626SB allele (Mburu et al., 1997; Gibbs et al., 2003).

well as whether or not it is involved in the scission process, is still unclear. In order to undergo a scission event during trogocytosis, a myosin is highly likely to be involved to generate force and excise the membrane, but which myosin (or myosins) is the important one?

Studying trogocytosis in RPE could provide new perspectives on old ideas

Understanding the actin nucleators' and myosins' involvements in the RPE ingestion process is valuable due to the nature of trogocytosis. Much of the phagocytosis literature relies on macrophages, which engage in full engulfment during ingestion, and so preliminary investigation into trogocytosis has relied on what has been found in that context. However, trogocytosis requires membrane rupture, a distinct mechanism from total engulfment, such that these proteins may be playing an entirely different role. By studying established actin-related proteins in this new system, we can explore what specifically delineates trogocytosis as distinct from traditional phagocytosis, investigate if there are novel actin-based roles in these processes that might be relevant for eye disease, and see if these long-studied proteins take on new roles in this system. In fact, much of the preliminary literature for trogocytosis comes from microglia, other immune cells, and parasitic bacteria, which use trogocytosis for a range of biological processes (Dance, 2019). Some cells use this process to prune synapses (Weinhard et al., 2018), while others use it for immune information exchange (Miyake and Karasuyama, 2021; Zhao et al., 2022), or even communal ingestion by parasitic bacteria (Dance, 2019; Uribe-Querol and Rosales, 2021); all of these cells utilize trogocytosis for very different purposes than the RPE. In addition, no one has explored the cytoskeletal mechanisms involved in this process and so it is unknown if these mechanisms are shared with traditional phagocytosis and full engulfment of the target particle. The only research published has focused on trogocytosis as a concept (Dance, 2019; Uribe-Querol and Rosales, 2021; Zhao et al., 2022), as well as eat-me signals (Hudrisier et al., 2007). Fundamentally, trogocytosis seems to have far more niche and specific roles when compared to phagocytosis as a whole. Understanding the elements that produce and facilitate the trogocytic process in RPE, the only epithelial cell, as well as the only immobile cell *in vivo*, that undergoes this type of ingestion, could provide highly valuable insights into eye disease. This is especially true with how necessary RPE phagocytosis is to vision: without it, we go blind.

Our goal with this investigation was to explore and characterize the phagocytic process, with a focus on how the Arp2/3 complex, mDia1, and Myosin 7a act in parallel to facilitate ingestion. In addition, we hope to create a better understanding of the 3D structure of the *in vivo* phagocytic cup by live cell imaging of this process *in vitro*. We show that mDia1 acts as the primary actin nucleator for growth and motility of the cup, the Arp2/3 complex is responsible for holding the OS and phagosome in their proper spatial location for ingestion and subsequent trafficking, and that Myosin 7a traffics the phagosome down the cup and into the cell. Deficits in actin remodeling can lead to immune dysregulation (Papa et al., 2021), which can in turn modify phagocyte behavior (Ronzier et al., 2022); by better understanding the biochemical mechanisms involved in RPE phagocytosis, we can create a strong basis of knowledge for studying actin related disease in the RPE and other phagocytes, and gain new insights into underlying causes of vision disease.

MATERIALS AND METHODS

Tissue Culture

ARPE-19 cells were grown and differentiated according to the protocols in Hazim et al. 2019. Undifferentiated ARPE-19 cells were fed with DMEM/F12 (Dulbecco's Modified Eagle Medium [DMEM]/F12 with GlutaMAX, 10% FBS, and 1% Penicillin/Streptomycin) while differentiated cells were fed with MEM-Nic (MEM alpha with GlutaMAX, 1% FBS, 1% Penicillin/Streptomycin, 1% NEAA, 1% N2 supplement, taurine [0.25 mg/ml], hydrocortisone [20 ng/ml], triiodo-thyronine [0.013 ng/ml], and 1M nicotinamide). Minimum Essential Medium (MEM) Alpha, DMEM/F12, certified-grade fetal bovine serum (FBS), nonessential amino acids (NEAA), and Penicillin/Streptomycin were obtained from Thermo Fisher Scientific. The N1 supplement, taurine, hydrocortisone, triiodothyronine, and nicotinamide were obtained from Sigma-Aldrich. ARPE-19 cells were obtained from ATCC (Lot Number 63478793) at their currently advertised passage number of 19, cultured in 6-well tissue culture plates for 2 weeks, trypsinized, and then differentiated on Ibidi µ-Slide 8 Well Glass Bottom (precoated with natural mouse laminin [Thermo Fisher Scientific]) for 2-6 more weeks before imaging, all in MEM-Nic. Primary mouse RPE was also plated on the Ibidi µ-Slide 8 Well Glass Bottom, fed with RPE GM with FBS and Penicillin/Streptomycin (DMEM high glucose 4.5 g/L, 1% NEAA, 1% Penicillin/Streptomycin, 1mM Sodium Pyruvate [Thermo Fisher Scientific], and 10% FBS), and were imaged 2-7 days after plating. All cells were maintained in 37°C, 5% CO_2.

Primary RPE Dissection and Mouse Eyecup Cryosection Preparation

All procedures conformed to institutional animal care and use authorizations. To prepare primary RPE we followed a previously described protocol (Gibbs and Williams, 2003; Gibbs et al., 2003), but plated final primary cells onto the Ibidi chamber slides as mentioned in the Tissue Culture section. Briefly, eyes were removed from p10-15 mice, washed in Primary RPE GM (see Tissue Culture), and incubated with 2% w/v dispase in GM at 37C° for 45min., with mixing every 10min. Eyes were then placed in GM supplemented with 10% Fetal Bovine Serum (FBS), 1% Pen/Strep, and 20mM HEPES (Thermo Fisher Scientific). The cornea, iris, and lens were dissected and removed, and the posterior eyecups were incubated at 37C° for 20min. The retina was then removed, and sheets of RPE were peeled off from Bruch's membrane, triturated, and then plated in GM with 10% FBS and 1% Penicillin/Streptomycin in Ibidi chamber slides. To control for sex, RPE was prepared from multiple mice at one time (all from the same litter), and the RPE was mixed and plated such that all cultures produced from a given dissection contained an equal amount of RPE from each animal of the litter, and therefore, on average, a mixture of cells from males and females. All primary RPE was prepared from WT C57BL/6, shaker1 (on a C57BL/6 background), or MERTK-null (B6;129-Mertk^{tm1Grl}/J) mice. To prepare CD-1 mouse eyecup cryosections, mice were housed in a 12:12 light cycle and harvested at +22.5hrs. First, mice were anesthetized with Isofluorane (Fluriso, Vet One) and sacrificed by cervical dislocation. Eyes were enucleated and placed into fresh PBS in a 35mm plate under a dissection scope. The anterior portion of the eye was punctured with a razor blade, and then the cornea, lens, and retina were dissected out gently, so as to not disturb the apical structure of the RPE. Eyes were then immediately placed in 4% PFA at room temperature for 30min., washed in PBS, and transferred to an increasing percentage (10, 20, 30%) sucrose solution approximately every 12 hours. Eyes were then embedded in OCT, frozen, sectioned on a cryostat (Epredia™ CryoStar™ NX70 Cryostat, Fisher Scientific) at 14 µm, and plated on slides for immunocytochemistry.

Photoreceptor Outer Segment Preparation

OS were isolated from C57BL/6J mice between 3 months and 1 year of age, with an even split of male and female mice. Animals were euthanized, and the retinas were removed and placed in 1mL of PBS. They were homogenized with a glass pestle on ice, and left for 5min. to gravity sediment the larger particles. The supernatant (containing the homogenized retina) was placed on a preformed 27-50% sucrose gradient (before pouring, each gradient sucrose solution was made up of 5mM Tris-base [Thermo Fisher Scientific], 2mM $MgCl_2$ [Thermo Fisher Scientific],13M NaCl [Thermo Fisher Scientific], and either 27% or 50% w/v sucrose [Thermo Fisher Scientific], pH 7.2), with a maximum of 15 retinas per gradient, and centrifuged in a SW-40 swinging bucket rotor at 38,000rpm, at 4C°, with slow acceleration and deceleration, for 1hr. and 5min. The rod fraction was collected, diluted 1:4 in PBS, and centrifuged in a SS-34 fixed angle rotor at 8000rpm, at 10C°, for 10min. The supernatant was decanted off, and the OS were resuspended in 1mL of primary RPE GM (see Primary RPE Dissection above) + 2.5% sucrose. OS quality was assessed and OS number was counted via hemocytometer under phase microscopy. OS were then either immediately frozen in aliquots of 2 million OS, or stained and fed to RPE cells.

pSIVA staining

For staining of detached retina, CD-1 mice were sacrificed shortly after light onset, eyes were enucleated, and the neural retina was dissected. Following a previously published protocol (Ruggiero et al., 2012), OS were stained with 10µg/mL CellMask (Thermo Fisher Scientific) in Hanks buffered saline (HBS), and with 10µg/mL pSIVA REAL-TIME Apoptosis Fluorescent Microscopy Kit (pSIVA; catalog #AP004, BIO-RAD) for 5min. at 37C°. Retinas were placed on glass slides and imaged with a laser-scanning confocal microscope (model FV1000, Olympus). Gradient-purified OS were stained with 5µg/mL CellMask and 15µg/mL pSIVA for 30min in PBS at 4C°, and imaged on a Spinning Disk Confocal Microscope.

Live Cell Imaging

For live cell imaging, previously isolated fresh or frozen Bovine (for ARPE-19, as they are easily available in large quantities, and are recognized by human RPE cells [Parinot et al., 2014]) or Mouse (for primary mouse RPE, prepared in-house using the protocol in the Photoreceptor Outer Segment Preparation section) POS were thawed and centrifuged at 10,000g for 10min. at 4C°. They were then resuspended in 0.1M Sodium Bicarbonate (Sigma-Aldrich) with a final concentration of 0.05mg/mL Alexa Fluor™ 488/647 (depending on the experiment) NHS Ester (Succinimidyl Ester) (Thermo Fisher Scientific) and incubated at 4C° for 30 minutes. POS were centrifuged at 10,000g for 5 min., washed in Ringer's solution, centrifuged again, and resuspended in 200µl culture media. The POS were then fed to the RPE (at 2 million mouse POS, or 3 million bovine POS, per chamber of an Ibidi live imaging slide [1.0 cm^2 surface area]), incubated for 30min.-1hr, washed 4X in culture media, and placed on the Nikon CSU X-1 Yokogawa Spinning Disk Field Scanning Confocal Microscope with a Live-SR Super

Resolution Module (Gataca Systems). Live cell movies were taken at either 3 minute movies with no delay between images to maximize framerate, or 10 minute movies with a 20 second delay between movies to maximize length of movie (as phagocytic cups last ~8-10 minutes). We have tested other frame rates and have found a 20 second delay between images to be optimal to maximize motion capture and minimize photobleaching. CK-666 was received from Sigma-Aldrich and used at 100μM (note that concentrations of 1μM, 10μM, 100μM, and 500μM were tested before settling on 100μM for experiments), and SMIFH2 was received from Sigma-Aldrich and used at 25μM. Cytochalasin D (Sigma-Aldrich) was used at 1μM, and cells were pulsed in Cytochalasin D for 1hr, before washing out and performing any experiments. 647-WGA was received from Thermo Fisher Scientific, and used at a final concentration of 4μg/mL; WGA was added into the culture media for 30min., and subsequently washed out, directly before feeding outer segments.

Constructs and Antibodies

The constructs used for transfection in live cell imaging included: RFP-Tractin and GFP-Tractin (kind gifts from Michael Schell, Uniformed Services University), LifeAct-TagRFP (Ibidi, in Lentiviral format), mEmerald-mDia1 (mEmerald-mDia1-N-14 was a gift from Michael Davidson [Addgene plasmid # 54157; http://n2t.net/addgene:54157; RRID:Addgene_54157]), pAAV-CMV-GFP-*MYO7A* tail (labelled as *MYO7A* Tail in Fig. 1-10, a gift from the Ramalho Lab at the University of Lisbon; this vector was cloned into a lentiviral backbone [pUltraHot; AddGene plasmid # 24130] using Gibson Assembly [NEBuilder HiFi DNA Cloning kit]), pUH-CBA-mCherry-*MYO7A* IF2 (the Myosin 7a rescue construct used in Fig. 1-10E, constructed in-house;

using Gibson Assembly, mCherry was fused at the N-terminus of *MYO7A* IF2 cDNA via a serine- and glycine-rich linker under the control of a shortened CAG promoter. This construct was cloned into the pUltraHot lentiviral backbone, again using Gibson assembly), and the control shRNA and mDia1 shRNA (sourced from Thompson et al. 2018 [a gift from Jordan Jacobelli, University of Colorado Anschutz Campus]). The backbone for the shRNA constructs was pSiren-RetroQ, used via transfection. The shRNA constructs also contained a ZsGreen reporter, for identification of transfected cells during live imaging. Sequences were verified by sanger sequencing (Laragen Inc; Culver City, CA).

Transfection was done with Lipofectamine 3000 (Invitrogen) and was used according to the manufacturer's protocol. In brief, Lipofectamine 3000, P3000, and the construct to be transfected were all added to Opti-mem, given 10-15 minutes for the DNA-liposome complex to form, and then directly added to cells. They were given ~12hrs to incubate before fresh media was added and were generally imaged on the afternoon of the following day. For the mDia1 shRNA, the plasmids were transfected the day after plating, were given 3 days for the shRNA to knock down the protein, and samples were imaged through live cell imaging, fed POS and fixed for immunocytochemistry, or fed and stained for a phagocytosis assay (see Immunocytochemistry and Phagocytosis Assays section).

The antibodies used for immunocytochemistry included: anti-rabbit O1 (made in-house), Alexa Fluor 647-1D4 conjugated antibody (anti-mouse 1D4 was purchased from Novus Biologicals and ester conjugated to Alexa Fluor 647 in-house), anti-rabbit mDia1 (Proteintech, 20624-1-AP), anti-rabbit Myosin 7a #454 (made in-house), anti-rabbit

Myosin 7a #615 (made in-house), anti-Mouse Myosin 7a from the Developmental Studies Hybridoma Bank (University of Iowa, 138-1), anti-rabbit Rab5 (Cell Signaling Technology, C8B1), anti-Rabbit Beta-Tubulin (Cell Signaling Technology, 9F3), anti-Rabbit Arp2 (Bioss, bs-12524R), and anti-rabbit ArpC2 (Proteintech, 15058-1-AP). The secondary antibodies used were goat anti-mouse and goat anti-rabbit IgG conjugated to Alexa Fluor 488, 594, or 647 (Thermo Fisher Scientific).

Other associated reagents used include: Alexa Fluor™ 488/647 NHS Ester (Succinimidyl Ester) (Thermofisher) to prestain POS, and 647/TRITC-Phalloidin (Sigma-Aldrich) to stain actin.

Immunocytochemistry and Phagocytosis Assays

For immunocytochemistry, cells were fixed in 4% PFA for 15 minutes at room temperature and then washed and left in PBS at 4C° for storage. Cells were placed in NDS Block (PBS Base, 5% NDS [Thermo Fisher Scientific], 0.25% Triton-X 100 [Sigma-Aldrich], 1% BSA [Sigma-Aldrich]) for 1 hour, and left in primary antibody overnight at 4C in a humid chamber. The next day they were washed 3X in blocking solution, placed in secondary antibody for 1 hour at room temperature, washed 3X, and mounted in either Vectashield (Vector Labs) for those in Ibidi chamber slides or Fluoro-Gel (Electron Microscopy Sciences) for those on microscope slides. Samples were then imaged on a Spinning Disk Confocal Microscope as in live cell imaging. For most experiments, cells were fed previously isolated and frozen POS for a 1hr. pulse before fixation. POS were usually prestained with Alexa Fluor™ 488/647 NHS Ester (Succinimidyl Ester), or in some cases were stained with antibodies against either O1 or 1D4.

For inside-outside phagocytosis assays, previously isolated and frozen mouse POS were thawed and prepared as in the Live Cell Imaging section of the methods. Cells were pretreated with DMSO, CK-666, or SMIFH2 (Fig. 1-5A) and these were maintained in the media during feeding; alternatively, cells were transfected with shRNA constructs on day 2 of plating and fed/fixed on day 5 (Fig. 1-8G). They were fed as normal, pulsed for 1hr, washed 4X in culture media, and fixed in 4% PFA for 15min. at room temperature. They were then stained similarly to standard immunocytochemistry, but with some minor differences to create the outside/inside phagosome staining pattern previously established in the lab (Hazim and Williams, 2018) (note that cells were plated on Ibidi chamber slides rather than Transwells, as written in the protocol). Briefly, OS were stained pre-permeabilization for 10 min. with an O1 primary antibody (to only target bound OS on the cell surface), washed, and then stained for a further 30min. with a secondary antibody compatible with O1. Then, the cells were permeabilized in 47.5% EtOh (Electron Microscopy Sciences), and stained with O1 again, this time using a differently colored secondary antibody to separate out bound OS from total. After staining, samples were placed on a Spinning Disk Confocal Microscope and 10-15 images of each sample were taken at random locations throughout the well. For analysis, images were placed into ImageJ (Rasband, W.S., ImageJ, U. S. National Institutes of Health, Bethesda, Maryland, USA, https://imagej.nih.gov/ij/, 1997-2018.), thresholded to match the expected size and shape of phagosomes from the original fluorescence image, and then particles were analyzed and counted (excluding particles outside of 0.1-3μm^2 in area) for both ‘outside’ and ‘all’. For both phagocytosis assays presented, the graphs show either 3 (for Fig. 1-5A) or 6 (for Fig. 1-8G) independent experiments, where ‘inside’ is calculated as ‘all’-‘outside’ for each independent image. Each individual experiment represents the mean of the 10-15 images taken per sample well.

Western Blot

Primary RPE was plated at 3 eyes per well of a 48-well plate, and grown in MEM-Nic + 10% FBS. Cells were given 3-6 days to grow, then were lysed in 200μl of Laemmli Lysis Buffer (100mM Tris-Cl [Thermo Fisher Scientific], 4% SDS [Sigma-Aldrich], 0.2% Bromophenol blue [Sigma-Aldrich]) with 5% beta-mercaptoethanol (Sigma-Aldrich). Samples were heated to 95C° for 5min., and then frozen at -20C°. 20μl of each sample was loaded into each well of a NuPAGE 4-12% Bis-Tris Gradient Gel [Thermo Fisher Scientific], the gel was run, and proteins were transferred onto a PVDF membrane using a wet transfer. Samples were blocked for 1hr. in Odyssey blocking buffer (LI-COR). Proteins were then probed with primary antibody in blocking buffer containing 0.1% Tween-20 [Sigma-Aldrich] at 1:1000 overnight at 4C°. Signal was detected by incubating the membrane with goat anti-rabbit or anti-mouse IRDye 800CW or IRDye 680RD (LI-COR) at 1:15000 in blocking buffer with 0.1% Tween-20 and 0.01% SDS for 1hr. at room temperature and then imaged. Images were taken using the Odyssey CLx Imaging System (LI-COR) and the Image Studio Ver5.2 software.

Computational Analysis/Statistics/Other

Live cell movies were analyzed and final images were taken in Imaris (Oxford Instruments). Unless otherwise specified, quantitative analysis was done with manual counting or automatic measurements within Imaris. Motility/speed/displacement measurements were done by 3D cropping the relevant region in Imaris, creating a Spots model (for Fig. 1-6E/F) or Surface Model (for Fig. 1-8F) of the pertinent fluorescence, and quantifying using Imaris' model statistics – each point on these graphs represents the statistical information of a different region of actin on a particular phagocytic cup. Phagosome diameter was measured in x-y. To create the composite images in Fig. 1-7F, we performed a Grouped Z-Project using either the Median or the Mean of 25 images of phagocytic cups, that were stained for Arp2/3, Phalloidin, and the OS; this was done in ImageJ. All computational statistics were done in Prism (GraphPad Software). For all datasets, we first used a Kolmogorov-Smirnov test to test for normality. For normal datasets, we used t-tests for direct comparisons, and one-way ANOVA with multiple comparisons for datasets with multiple groups. For non-normal datasets, we used a Mann-Whitney U test as a replacement for the t-test, and a Kruskal-Wallis test as a replacement for the one-way ANOVA. In the graphs, significance is shown via asterix: * = $P<0.05$, ** = $P<0.005$, *** = $P<0.0005$, **** = $P<0.00005$. All figures were created in GIMP (The GIMP Development Team), with the figure schematic (Fig. 1-12) and the introductory schematic (Fig. 1-1A/A') drawn in Procreate (Savage Interactive) and edited in GIMP. Note that Fig. 2-1, 2-12, and 3-8 were also drawn in Procreate and edited in GIMP.

Table 1-1: Replicate and sample size information for the presented figures

Figure Information	# Biological Replicates	# Technical Replicates	N Information	Pdf Page #s within Notebook	Relevant Methods Information
1-1B	3	~10-12 per mouse, 2 eyes from 2 mice each, and 1 eye from a third mouse	Staining for Phalloidin + OS repeated 26 times in cryosections	172, 176, 243, 251, 255, 263, 265, 416, 420	
1-2A/B	22 (individual Undiff ARPE-19 cultures)	N/A (one per Biological Replicate)	Live imaging of Untreated Undiff. ARPE-19 with RFP-Tractin repeated 22 times across experiments	11, 20-22, 31, 59-61, 69, 86, 99, 104, 107, 118, 123, 128, 131, 161, 189, 201	
1-2C/D	8 (individual Diff. ARPE-19 cultures)	N/A (one per Biological Replicate)	Live imaging of Untreated Diff. ARPE-19 with LifeAct repeated 8 times across experiments	64, 86, 93, 124, 155, 203, 311	
1-2E/F	23 (individual Primary RPE cultures, from different animals)	N/A (one per Biological Replicate)	Live imaging of Untreated Primary RPE with RFP-Tractin repeated 23 times across experiments	145, 163, 164, 165, 206, 233-234, 252, 257, 260, 294, 311, 348, 388, 403, 412	
1-2G	2 (Undiff./Diff. ARPE-19) or 3 (Mouse Primary RPE)		N = 15 for Undiff. ARPE-19, N = 8 for Diff. ARPE-19, and N = 12 for Primary RPE. Each data point represents a single movie of a phagocytic cup, spread across 2		

			(Undiff. ARPE-19, Diff. ARPE-19) or 3 (Mouse Primary RPE) experiments		
1-2H	2 (Undiff./Diff. ARPE-19) or 3 (Mouse Primary RPE)		N = 15 for Undiff. ARPE-19, N = 8 for Diff. ARPE-19, N = 66 for Primary RPE, and N = 16 for Mouse eyecup Cryosections. Each data point represents a single phagocytic cup, spread across 2-3 experiments		
1-3A/B	N/A	N/A	This is a published experiment (see Fig. 4 in the table) done by Antonio Paniagua, a postdoc in the lab. See the original publication for details		
1-3C/D	3 (2 using Sucrose, 1 using Percoll for isolation)	6 (2 each)	Each POS prep was split into two samples and stained with pSIVA separately	188, 190-191, 207	
1-3E	3	4 - each condition repeated 2 times with 1 biological replicate, and 1 time with 2 biological replicates	The number of OS counted (N) for Fresh/Frozen OS at the time points 10min., 15min., 20min., 25min., 30min., 40min., 50min., 60min., 75min., and 90min., are 39/40, 39/41, 39/40, 40/40, 40/40, 41/41, 40/40, 40/41, 41/40, and 41/40 respectively	376-377, 420	I plated each aliquot into a different well of an Ibidi chamber slide, and moved the scope every few minutes to image each well. This result was consistent when adding fresh/frozen OS to RPE in

					all of my live imaging experiments
1-4	See Umapathy et al. 2023, J. Neurosci for full replicate information		All the presented images in Fig. 4 are from the published manuscript. I performed the analyses in B-E, but did not perform experiments for A		
1-5A	3	N/A (one per Biological Replicate)	N=3 experiments, where each experiment is a composite of 10-15 images from each well of treated primary RPE	385	For each experiment I took 3 eyes, mixed the primary RPE together, and then plated into 3 wells. Each well was treated with DMSO, CK-666 or SMIFH2. Each of the three experiments was done on different days
1-5B/C	3	3 (Arp2 staining in eyecups repeated in eyes from 3 animals)		172, 416, 420	
1-5C'	3	3 (ArpC2 staining in eyecups repeated in eyes from 3 animals)		416, 420	
1-5D	3	3 (mDia1 staining in eyecups repeated in		172, 416, 420	

		eyes from 3 animals)			
1-6A/B	3	N/A (one per Biological Replicate)		145	
1-6C	3		Each data point represents a single experiment, made up of 2-4 live imaging movies		
1-6D	3		N = 10 for DMSO, and N = 8/9 for CK-666. Each data point represents a single phagocytic cup, spread across 3 different experiments		
1-6E/F	3		For all 4 graphs shown, N = 170 for DMSO, and 133 for CK-666. Each data point represents a specific actin Spot on the actin Spots model in Imaris. Each dataset is made up from 3 cups/condition (one cup per experiment)		
1-6G	2		N = 9 for DMSO, and N = 8 for CK-666. Each data point represents a single field of view of primary RPE, spread across two different experiments		
1-7A (Arp2)	2	3	3 western blots done, on two biological replicates	223, 227, 405	

			of primary RPE sample		
1-7A (ArpC2)	3	3		414, 418	
1-7B/B'	1	2 (1 for each fluorophore)		412	
1-7C-C''	9	N/A (one per Biological Replicate)	Note: 5 of the replicates are from untreated cells, 4 of the replicates are in treated/shaker/MERTK cells	363, 369, 372, 420	
1-7D-D''	3	N/A (one per Biological Replicate)		412, 420	
1-7E	3	N/A (one per Biological Replicate)		369, 420	
1-7G	2		N = 16 for DMSO, and N = 16 for CK-666. Each data point represents a single phagocytic cup, across 2 experiments		
1-8A/D/E	3 for the ctrl shRNA, and 2 for the mDia1 shRNA and the rescue	N/A (one per Biological Replicate)	Live imaged the ctrl shRNA 3 times on 3 different samples, and the mDia1 shRNA and the rescue experiment 2 times in 2 different samples	206, 233-234, 403	
1-8B	3	N/A (one per Biological Replicate)	Live imaging of mouse primary RPE with SMIFH2 treatment, while visualizing actin, repeated in 3 biological replicates	146	

1-8C	4	3 technical replicates of 1 sample, and 1 technical replicate of the 3 other samples		223, 227, 405, 414, 418, 419	
1-8F	2		Ordering the samples left to right, N = 45, 262, 254, 242, 206, 126, 173. Each data point represents a specific actin track on the actin Surface model in Imaris. Each dataset is made up from 3 cups/condition, split over 2 different experiments		
1-8G	6	N/A (one per Biological Replicate)	N = 6 experiments, where each experiment is a composite of 10-15 images of each well (Ctrl shRNA, and mDia1 shRNA) of treated primary RPE	233-234, 245	
1-8H	1	N/A (one per Biological Replicate)	Ordering the samples in the graph from left to right, N = 12, 11, 20, 10, 13, 17, 17. Each data point represents a single field of view of primary RPE, from a single experiment in each condition	397, 404	
1-9A	Same as 8C - see above				
1-9B	8	N/A (one per	Note: 5 of the replicates are from	363, 369, 372, 420	

		Biological Replicate)	untreated cells, 3 of the replicates are in treated/shaker/MERTK cells		
1-9C	4	N/A (one per Biological Replicate)		363, 369, 420	
1-9D	2		N=14 for WT, and N = 13 for SMIFH2. Each data point represents a single field of view of primary RPE, treated with either DMSO or SMIFH2, across 2 different experiments		
1-9E	2		N = 26 for DMSO, 34 for shaker, 19 for SMIFH2, and 20 for CK-666. Each data point represents a single phagocytic cup, spread across 2 different experiments and 10-12 fields of view per experiment		Cup height measured from the circumferential actin to the peak of the actin signal
1-9F	2		Ordering the samples left to right, N = 14, 14, 12, 12. Each data point represents a single field of view of primary RPE, treated with either DMSO or SMIFH2, across 2 different experiments		
1-9G	3	N/A (one per Biological Replicate)	2 of the biological replicates are from fixed tissue, and 1 is from live cell	394-395, 403, 412	

1-9H	2		N = 12 for DMSO and N = 10 for SMIFH2. Each data point represents a single field of view, across 2 different experiments		
1-9I	2		N = 40 for DMSO and N = 38 for SMIFH2. Each data point represents a single cup-associated phagosome, spread across 2 experiments and 10-12 fields of view		
1-9J	3	N/A (one per Biological Replicate)		369, 420	
1-9K	2		N = 33 for DMSO, 28 for CK-666, and 16 for SMIFH2. Each data point represents analysis of a single phagocytic cup across 2 experiments		
1-9L	3	N/A (one per Biological Replicate)		369, 420	
1-9M	2		N = 5 for DMSO, 54 for CK-666, and 40 for SMIFH2. Each data point represents analysis of a single phagocytic cup across 2 experiments		
1-9N	2		N = 32 for DMSO, 23 for CK-666, and 16 for SMIFH2. Each data point represents analysis of a single		

			phagocytic cup across 2 experiments		
1-9O	1			260, 372	
1-9P	1		N = 28 for DMSO (or 31 in right graph), and 36 for SMIFH2. Each data point represents a single phagocytic cup, from a single experiment		
1-10A	3 per antibody (454/615)	N/A (one per Biological Replicate)		251, 255, 263, 265, 416, 420	
1-10B	23 (individual Primary RPE cultures, from different animals)	N/A (one per Biological Replicate)	Live imaging of Untreated Primary RPE with RFP-Tractin repeated 23 times across experiments	145, 163, 164, 165, 206, 233-234, 252, 257, 260, 294, 311, 348, 388, 403, 412	
1-10C	4	N/A (one per Biological Replicate)	Live imaging of shaker1 Primary RPE with RFP-Tractin repeated 4 times across experiments	241, 259, 260, 372	
1-10D	2		N = 12 for WT, and 10 for shaker for total movies, and N = 10 for WT, and 16 for shaker for total cups analyzed. Each data point represents a single field of view (top) or phagocytic cup (bottom two) across 2 experiments		
1-10E	3	N/A (one per Biological Replicate)	Rescue experiment repeated in 3 biological replicates	241, 420	

1-10F	N/A (One specific movie, quantified)		Representative example of the actin/OS height as it changes over a single specific movie		
1-10G-G'	3	N/A (one per Biological Replicate)		164, 203, 388	
1-10H-H'	4	8	Note: 4 of the replicates are from untreated cells, 4 of the replicates are in treated cells	260, 369, 372, 420	
1-10I	2	N/A (one per Biological Replicate)	Repeated in both shaker Primary RPE and in shaker eyecup cryosections	259, 263	
1-10J	2		N = 17. For both graphs, they are made up of 17 cups across 2 different experiments		
1-11A-A'	3	N/A (one per Biological Replicate)		369, 420	
1-11B	3		N = 26 for DMSO, 46 for shaker, 19 for SMIFH2, and 20 for CK-666. Each data point represents a single phagocytic cup across 2 different experiments		
1-11C	3	N/A (one per Biological Replicate)		369, 420	
1-11D	3			372, 420	
1-11E	1			369	

RESULTS

RPE Phagocytosis is based on an actin protrusion that extends above the apical region of the cell.

To initially confirm the presence of actin cups *in vivo*, we removed the retina from an eye of an albino CD-1 animal, fixed the eye in formaldehyde, and embedded in OCT at ZT22.5[4]; recent work in our lab has found that the period shortly before light onset corresponds to a maximal ingestion rate, and so we chose ZT22.5 to maximize the number of phagocytic cups. We collected cryosections of these eyecups, and stained for Actin (via Phalloidin) as well as any lingering outer segments that remained bound to the RPE during the retinal detachment; OS that were in the process of active ingestion were more likely to remain bound, rather than being pulled off of the RPE, during the retinal detachment. Removing the retina allowed us to visualize the full actin structure of the cup, as there is little extracellular space between the RPE and the OS *in vivo*[5]. Increasing the extracellular space by detaching the retina leaves only the RPE and the choroid, and allows for proper visualization of phagocytic cups. After performing this

---

[4] ZT refers to Zeitgeber Time, where "lights on" starts at ZT0, and "lights off" starts at ZT12 in a 24hr. light cycle (Eckel-Mahan and Sassone-Corsi, 2015). ZT22.5 corresponds to 1.5hrs. before light onset.

[5] We have attempted experiments immunostaining cryosections of fully intact eyecups, with neural retina, but had difficulty analyzing these samples. The OS antibody was not defined enough to delineate individual outer segments, and the RPE actin signal at the OS-RPE interface was blurred due to the depth of the cryosection and the microvilli density. We were unable to confidently identify phagocytic cups in that context, so we decided to detach the retina.

experiment, we were able to identify individual actin cups along the eyecup cryosections (Fig. 1-1B/B’, cyan arrowhead). Phagocytic cups (both here, and throughout the remainder of the dissertation) were defined as an actin density that associated with an OS, and that protruded >3μm apically as measured in Z from the circumferential actin of the cell. While measurement from the circumferential actin may not always be a true representation of the height of the cup due to a variable domed apical membrane[6], it is the most consistent method that we have found to calculate this measure. In addition, RPE cells have apical actin-based microvilli that extend above the cell, but never beyond 3μm past the circumferential actin; our measurement ensures that the structure is indeed an actin protrusion independent from the microvilli.

In our cryosections, we found 6.15 ± 1.37 cups per $0.1mm^2$ (N = 4 experiments [2 eyes each from 2 different animals], each made up of 8-10 images across 3-4 sections, Mean ± SEM). As a comparison, there are 100-400 phagosomes ingested each day by a single RPE cell (Young, 1971). Using 400 phagosomes/day/RPE cell, each RPE cell ingests 0.046 phagosomes per 10 minute period, the approximate time for an ingestion event to occur. Since the area of the average mouse RPE cell is approximately $275μm^2$ (Kim et al., 2021), we expect to see about 1.67 phagosomes/$0.1mm^2$ being ingested in a given fixed snapshot. While this calculation is an average over the course of the day,

---

[6] Different cell lines portray different levels of curvature in their apical domed membranes. Primary mouse RPE, the main model used in this study, has little apical curvature and is more likely to be flatter than other RPE culture models. While this may be less accurate to the *in vivo* condition, it allows for better consistency in measuring the height of the cup.

we chose a time point with an high expected level of ingestion, and ingestion rates vary significantly throughout the day (Paniagua et al., 2023), so it is not surprising that we found more cups than expected in our cryosections (6.15 ± 1.37 vs. 1.67).

While this strategy allowed us to visualize cups *in vivo*, fixed cryosections have some important limitations. First, removal of the retina caused clear disruption to the apical structure of the RPE in some cryosections, so each section must be carefully analyzed to ensure that any cups present are indeed real cups. In some cases, the actin structure of the RPE may have been torn apically during the detachment, which could result in mislocalized actin structures (and therefore mislocalized antibody staining for cup related proteins), and reduce the number of cups that could be analyzed per region of tissue. Second, cryosections are limited in their ability to be experimentally manipulated, as the tissue must come from a live mouse and must be fixed shortly after enucleation. Third, fixed samples can be useful for understanding structural organization of a cup, but not the dynamics; live imaging is therefore required to understand the kinetics and dynamic movement of actin as the cell engages in the ingestion process. To compensate for these limitations, we decided to explore a few different RPE models that can be used in live cell imaging.

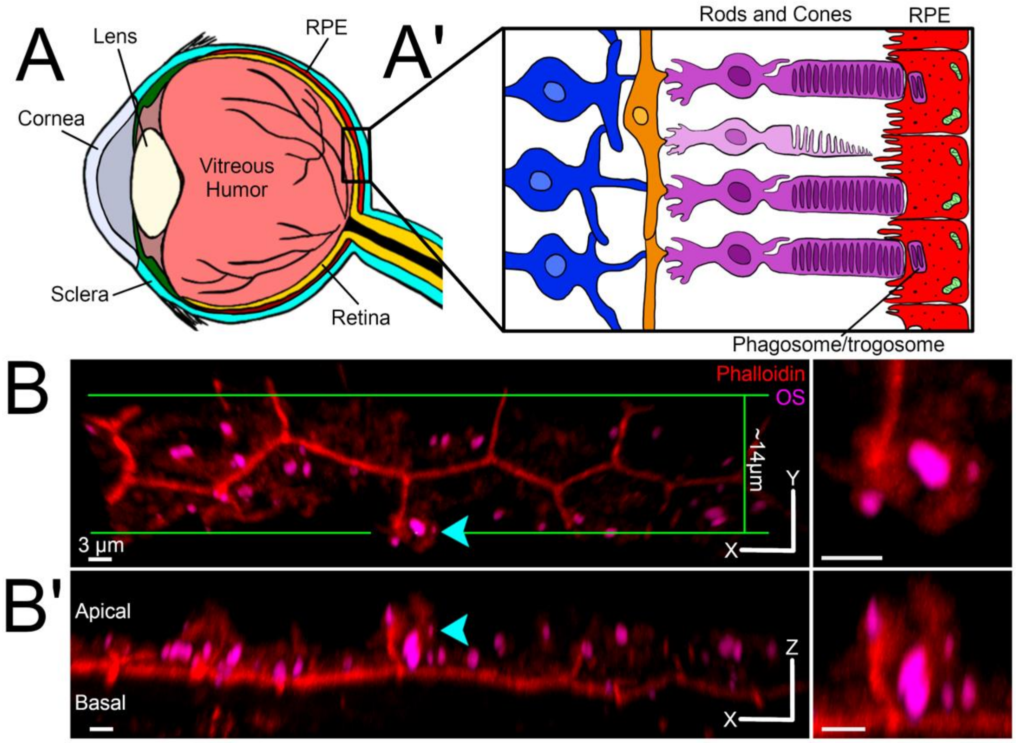

Figure Legend - Figure 1-1: RPE Phagocytosis is based on an actin protrusion that extends above the apical region of the cell. **A.** Illustrated schematic showing the structures of the eye, and the location of the retina (yellow) and RPE (red). **A'.** A magnified look at the back of the eye. Rods (dark pink) and cones (light pink) interface with the RPE at the outer segment, and create synaptic contacts with horizontal cells (orange) and rod bipolar cells (dark blue) at the rod spherule on the opposite end. Mitochondria are shown in green. **B/B'.** *En face* (B) and side view (B') of a 14µm width eyecup cryosection, after the retina has been detached. In B, the green lines outline the edges of the cryosection, and the magnified image on the right shows the phagocytic cup pointed out by the cyan arrowhead. In B', the magnified image on the right shows that same cup from a horizontal view.

Scale Bars: B-B': 3µm.

Investigation of three RPE culture models, within the context of RPE phagocytosis.

Due to the practical difficulties of manipulating or imaging this system *in vivo*, we tested three commonly used RPE cell culture models (Dunn et al., 1998; Gibbs and Williams, 2003; Gibbs et al., 2003; Kauppinen et al., 2012; Hazim et al., 2019; Umapathy et al., 2023) to investigate which would be the most effective for studying the actin dynamics of RPE phagocytosis. To act as an effective model, the phagocytic cup must be tall enough to distinguish the different regions of the cup that a fluorescent construct might be acting on, and must also engage in enough scission events to capture the necessary data to better understand this process. We initially investigated undifferentiated ARPE-19, a model that has been in use in the field for nearly 30 years (Dunn et al., 1996) and has over 2000 reports (Pfeffer and Fliesler, 2022). After transfecting with RFP-tractin, the unpolarized cells showed a lack of clear circumferential actin, and instead showed a light fuzz of actin signal all across the cell (Fig. 1-2A’). These cells were quick to ingest, producing 4-6 cups/cell at any given moment during the first hour of imaging, and relied on chaotic high-motility engulfment by independent actin protrusions (Fig. 1-2B, white arrowheads). Due to the unpolarized nature of these cells, these structures were likely not the microvilli that we see in the polarized condition. Similar structures in RPE have been previously coined as pseudopodia (Matsumoto et al., 1987; Kwon and Freeman, 2020). Filopodia are a subset of pseudopodia that are thin spine-like actin-based cell surface protrusions (Horsthemke et al., 2017) that have been shown to act as phagocytic ‘tentacles’ and pull phagosomes into the cell (Kress et al., 2007). Based on this, we decided to call these structures filopodia. While these cells did produce cups of a sufficient height, they rarely engaged in trogocytic scission events (Fig. 1-2G, 0.4 ± 0.2 events/movie, see Table 1-1 for sample size information, Mean ± SEM), a characteristic that represents the *in vivo* state. These cells instead tended to ingest the OS in full, an action that is more akin to macrophages than RPE cells, and is therefore not necessarily an effective model to better understand RPE *in vivo*.

Recently, this unpolarized cell line has been differentiated into a more *in vivo*-like state, with significantly improved epithelial cobblestone morphology, as a strategy to improve the model (Hazim et al., 2019). Evidence of this can be seen when comparing Fig. 1-2A' and C'; both images show a singular cell covering a similar field of view, but the cell in A' showed a light red diffuse signal all across the entire cell, while the cell in C' showed clear circumferential actin with only a few stress fibers down the middle of the cell. When polarized, it was more difficult to identify cups[7], however the few cups that did form engaged in 2.38 ± 0.38 scission events per 10min. movie (Fig. 1-2G, see Table 1-1 for sample size information, Mean ± SEM). Unfortunately, these cups were fairly short (Fig. 1-2H), and were difficult to identify visually during live imaging. In addition, it is practically impossible to transfect these polarized cells and so we had to rely on lentiviral transduction of relevant constructs rather than transient transfection of

---

[7] The apical surface of polarized ARPE-19 is filled with dense microvilli. Phagocytic cups on these cells do not extend far beyond the microvilli, and, looking through the oculars of a microscope, the actin density that denoted a cup did not look visually different to the microvilli. Due to this, each individual cup needed to be confirmed through 3-D reconstruction of a confocal z-stack rather than direct identification by eye.

plasmids (hence the use of lentiviral LifeAct, rather than transfection of RFP-tractin, to visualize actin). This problem made preliminary investigation quite difficult, as the process to create a lentivirus from a genetic construct can be time consuming. While the cups produced in this cell line seemed quite relevant for study, these practical issues made experimental manipulation and sampling difficult.

The last model tested, primary mouse RPE, produced tall cups (Fig. 1-2H) with a distinct rim, middle, and base, and engaged in a relatively high level of scission (Fig. 1-2G, 2.83 ± 0.64 events/movie, see Table 1-1 for sample size information, Mean ± SEM), precisely the characteristics that are useful for studying RPE phagocytosis. Primary mouse RPE are easy to transfect and experimentally manipulate, similar to undifferentiated ARPE-19, but engage in much more scission. In addition, the height of the cup and the spread of cup height variability of primary mouse RPE matched closely with the height of the cup in the *in vivo* cryosections (Fig. 1-2H), providing consistency for this model. Another benefit of primary mouse RPE and differentiated ARPE-19 is that, observationally speaking, a majority of cups in both of these polarized models presented near circumferential actin in X-Y, and those closer to cortical actin seemed to grow taller and were visually more motile; it is likely that the circumferential actin structure plays a role in facilitating phagocytosis, emphasizing the need to use polarized cells when studying ingestion in RPE[8]. In our investigation, we determined that primary

---

[8] It is important to specify that, moving forward, the field should aim to investigate differentiated cells when exploring RPE phagocytosis. Due to a lack of sophisticated models, the RPE field has been relying on undifferentiated RPE cells (generally ARPE-19) for decades, but the clear

mouse RPE was the most useful model for studying RPE phagocytosis. Now that we have established our culture model, we must ensure that our previously isolated OS are effective in modeling OS *in vivo*.

---

differences in cup structure in Fig. 1-2 show that the entire structure of the cup changes after proper differentiation.

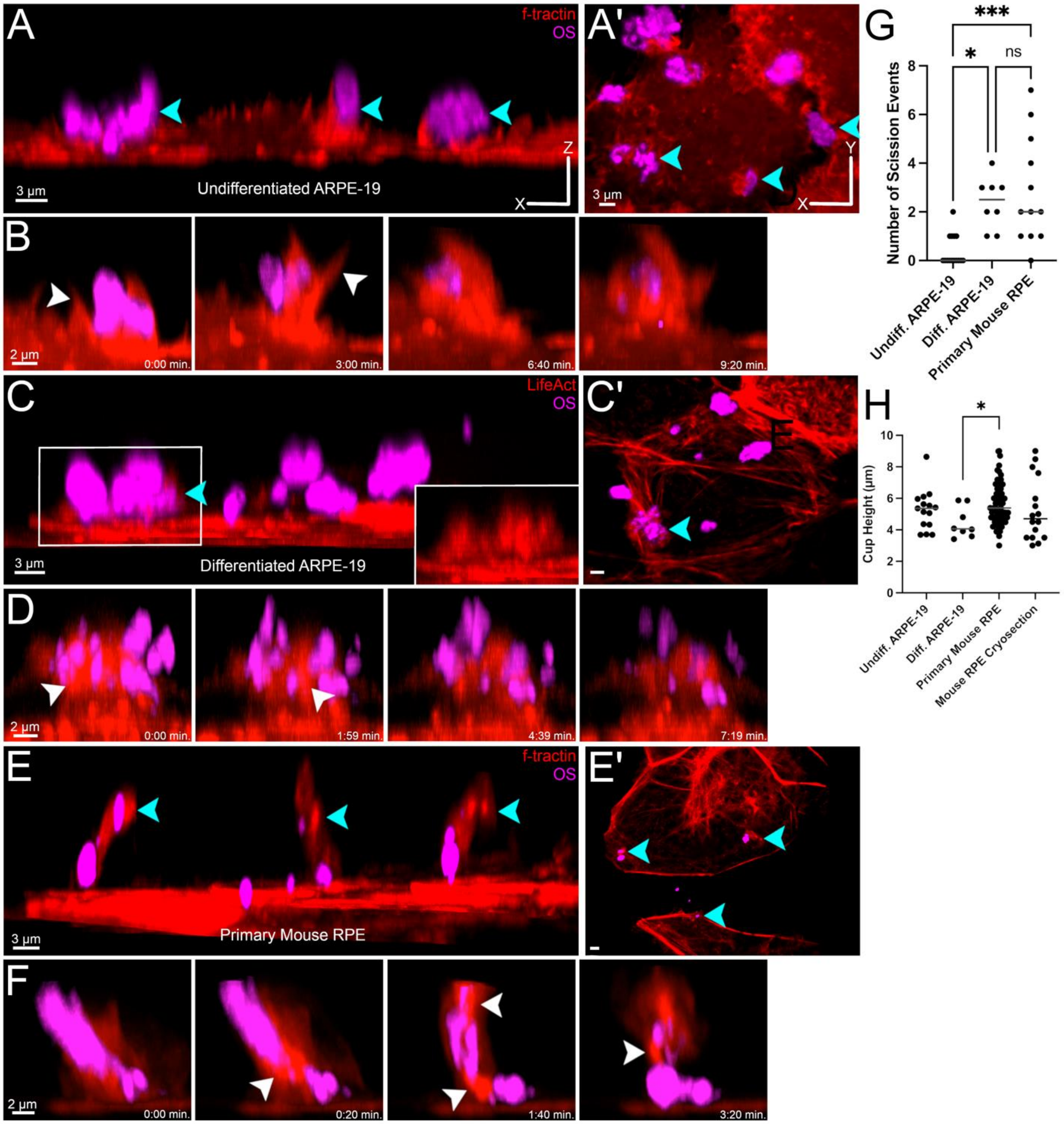

Figure Legend - Figure 1-2: Investigation of three RPE culture models, within the context of RPE phagocytosis. **A/A'.** Side (A) and *en face* (A') views of a particular undifferentiated ARPE-19 cell, previously transfected with RFP-Tractin, showing multiple phagocytic cups (cyan arrowheads). **B.** A time series from a 10min. movie of a phagocytic cup in undifferentiated ARPE-19. Note the filopodia that extent up and around the OS (white arrowheads). **C/C'.** Side (C) and *en face* (C') views of a particular differentiated ARPE-19 cell, stably transduced with LifeAct-RFP, showing a single phagocytic cup (cyan arrowhead). The box on the bottom right shows the same cup within the box on the left, but with only the phalloidin signal visible. **D.** A time series from a 10min. movie of a phagocytic cup in differentiated ARPE-19. Note the mobile actin densities that move and act to break apart the OS pieces and traffic them down into the cell (white arrowheads). **E/E'.** Side (E) and *en face* (E') views of a particular primary mouse RPE cell, showing multiple phagocytic cups (cyan arrowheads). **F.** A time series from a 10min. movie of a phagocytic cup in primary mouse RPE. Note the actin densities that act to break off pieces of the long OS and traffic them down the cup (white arrowheads). **G.** The number of scission events that each model underwent during a 10min. movie of a phagocytic cup. Each point represents a single phagocytic cup in a single movie. **H.** The height of the phagocytic cup in each model, as measured from the circumferential actin to the peak of the actin signal of the cup in Z.

Scale Bars: A-A': 3µm, B: 2µm, C-C': 3µm, D: 2µm, E-E': 3µm, F: 2µm.

Understanding PS localization and maintaining structural organization of previously isolated outer segments when feeding live to RPE.

When feeding previously isolated OS to plated RPE, it is important to optimize the structure of the OS and understand the molecular cues that are in place within these cells after removal from the retina, to ensure *in vivo* relevance. In the literature, Phosphatidyl Serine (PS), an anionic signaling phospholipid, has been shown to flip to the outer leaflet of the plasma membrane at the tips of rod OS in detached retina (Ruggiero et al., 2012). PS is, generally speaking, an 'eat-me' signal (Fadok et al., 1992; Krahling et al., 1999), so much of the literature that has followed has referred to PS as the 'eat-me' signal at the tip of the rod OS. In fact, at the time of light onset, the PS signal extends ~1.5µm down the tip of the outer segment (Ruggiero et al., 2012), approximately the size of a single phagosome, implying that PS may indicate the region of the OS that will be bitten off. We repeated this experiment (Fig. 1-3A/B[9]), confirmed their findings, and then explored whether our gradient-purified OS also contained PS localized purely to the tip. After removal from the retina, sucrose gradient purification, and staining with pSIVA and CellMask to identify PS signal and the overall rod shape respectively, we found that these rods contained PS on the outer leaflet all across the entire cell (in 96.6% of gradient-purified OSs, n = 264 across 6 experiments), and did not show tip-localized PS in a vast majority of cases (Fig. 1-3C/D). The size of the phagosome *in vitro* with fully-stained PS (as all experiments performed in both this

---

[9] The images in Fig. 1-3A-D are reproduced from Umapathy et al. 2023. Fig. 1-3A/B were collected by Dr. Antonio Paniagua.

thesis, and in Umapathy et al. 2023, utilized OS where a vast majority contained PS all along the entire cell body), was comparable to that of *in vivo* with, presumably, one-sided PS (Umapathy et al., 2023). This describes that, while PS may still act as an eat-me signal, it is not responsible for determining the size of the phagosome.

When feeding OS to RPE, it is also important that the cylindrical structure of the OS is maintained to ensure that the ingestion mechanism is as similar to the *in vivo* state as possible, where a rod would rest vertically on the RPE cell. Previous work in the literature has shown that there are mechanistic differences in the way that particles are engulfed based on their shape (Champion and Mitragotri, 2006; Tollis et al., 2010; Paul et al., 2013), and so by optimizing methodology to select for maintenance of the cylindrical structure of the OS we can ensure a greater *in vivo* relevance. When preparing OS, we would either gradient-purify them and immediately feed to RPE cells, or we would freeze them after purification, and thaw later for experiments. While fresh purification and feeding seems more ideal, freezing OS allowed for a higher overall yield and prevented excess mouse lives from being expended: >5 retinas are needed to visualize an OS band on the sucrose gradient, but only OS from 1-2 retinas could be utilized on a given experiment day. We observationally noticed that frozen OS were, on average, rounder than fresh OS; we decided to test whether utilizing fresh OS would be more consistent in producing movies with cylindrical OS undergoing ingestion. We prepared fresh and frozen gradient-purified OS, stained them as per standard protocol (see Methods), plated on chamber slides, and took an image every 5 minutes. We found that while the fresh OS did initially have a higher quality rating (Fig. 1-3E), this initial benefit sharply declined within the first 20-30 minutes. It should be noted that the pulse before the initiation of an imaging session is 30 minutes, and so by the time that the cells would be taken to the microscope, the benefit of using fresh OS has already been greatly diminished. In addition, frozen OS tended to maintain their structure that they were frozen in, regardless of what that structure was. Due to this, while there were few frozen OS that looked like clear rods, much more of them did maintain a relatively cylindrical structure over a 1+ hour imaging session; fresh OS instead rounded up into circles after about 30min., which would likely be ingested by a different mechanism than a fresh vertical rod. To optimize OS cylindrical structure, we opted to perform fresh OS purification and direct feeding for live experiments, where sampling is an issue, to ensure that the first 2-3 movies of a given experiment will contain a high quality rod. For fixed experiments, where we can capture many cups and pick and choose those with higher quality OS for imaging and quantification, we opted to use frozen OS.

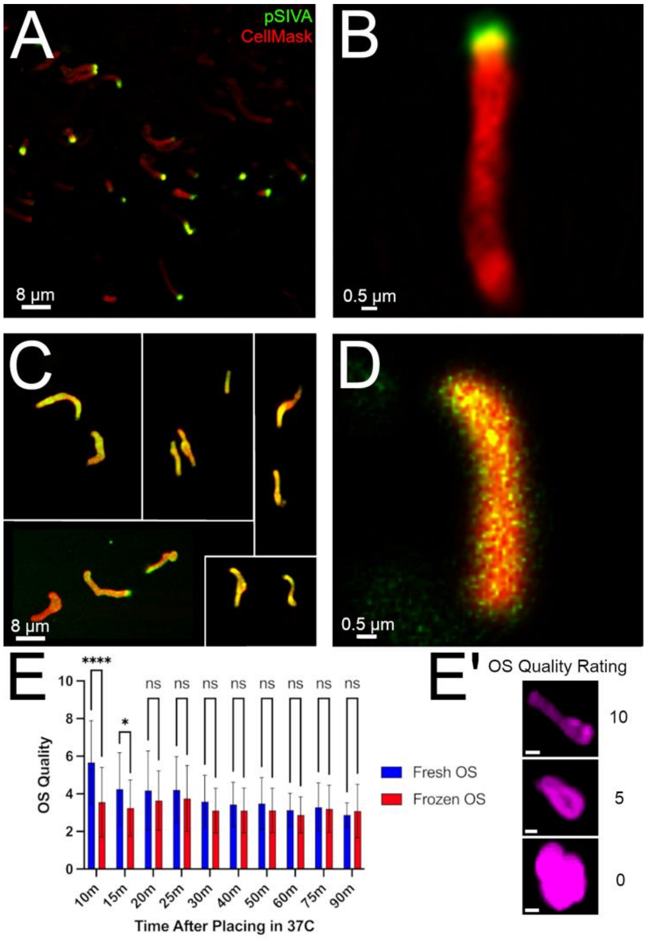

Figure Legend - Figure 1-3: Understanding PS localization and maintaining structural organization of previously isolated outer segments when feeding live to RPE. **A.** pSIVA and CellMask stained retina from an animal sacrificed shortly after light onset. CellMask stained the rod photoreceptor plasma membrane, and pSIVA stained phosphatidylserine on the outer leaflet of the membrane. **B.** A specific representative example of an OS from a detached retina, that shows the one-sided PS signal. **C.** A number of examples of fresh gradient-purified OS, stained with pSIVA and CellMask. **D.** A specific representative example of the PS staining seen in gradient-purified OS. **E.** The cylindrical quality of outer segments, either fresh or frozen, after standard live cell imaging staining with the Alexa Fluor 647 NHS Ester Dye (see Methods), and imaging at 37C° every 5 minutes. The number of OS counted (sample size) for Fresh/Frozen OS at the time points 10min., 15min., 20min., 25min., 30min., 40min., 50min., 60min., 75min., and 90min., are 39/40, 39/41, 39/40, 40/40, 40/40, 41/41, 40/40, 40/41, 41/40, and 41/40 respectively, across 3 biological replicates. The error bars depict standard deviation. **E'.** Representative examples of the OS quality at each rating.

Scale Bars: A: 8μm, B: 0.5μm, C: 8μm, D: 0.5μm, E': 3μm.

RPE engage in trogocytosis, a subset of phagocytosis, by utilizing actin as a fundamental regulator.

RPE trogocytosis has been investigated in detail in a previous publication from the lab – Umapathy, Torten et al. 2023[10]. *In vitro*, once one end of an outer segment has fallen onto a cell and has bound to a growing actin-based cup, trogocytosis begins. The actin cup grows up the base of the OS, and forms a tube, holding the OS in place (Fig. 1-4A, 0:40min. and 1:40min. time points). Actin densities work to push trogosomes down the cup (Fig. 1-4A, yellow arrowhead), and create new trogosomes by pressing actin densities into larger OS pieces (Fig. 1-4A, white arrowheads). The example in Fig. 1-4A shows a particular trogocytic cup as it performed a series of scission events on an OS resulting in 4 separate trogosomes (Fig. 1-4A, ‘1’, ‘2’, ‘3’, and ‘4’). The actin and OS densities can be quantified (Fig. 1-4B/C) by measuring the signal intensity down the center of the cup; actin formed intensities directly above each individual trogosome as they were trafficked down the cup (Fig. 1-4B/C).

Another major finding from this manuscript was that ingestion kinetics and phagosome size was tightly linked to actin polymerization. Treating these cells with Cytochalasin D, a drug that inhibits actin polymerization, completely eliminated cup formation. Instead, treating with Cytochalasin D, and then washing this drug out directly before imaging, enabled us to slow down the speed of ingestion significantly (Fig. 1-4E).

---

[10] The Umapathy et al. 2023 manuscript was a joint effort by a group of researchers at the Williams lab, including myself. For more information, please see the Preface of Chapter 1 or the original manuscript (https://pubmed.ncbi.nlm.nih.gov/36878726/)

With actin polymerization slowed down, the size of the phagosomes were consistently smaller (Fig. 1-4D, 1.8µm in DMSO treated and 1.2µm in Cytochalasin D washout, N = 30 for DMSO and N = 68 for Cyto D across 6 experiments, Median), describing that ingestion is fundamentally regulated by actin. Simply by manipulating the rate at which actin polymerizes, we can change the size of the phagosome and, presumably, the way that the cup takes a bite.

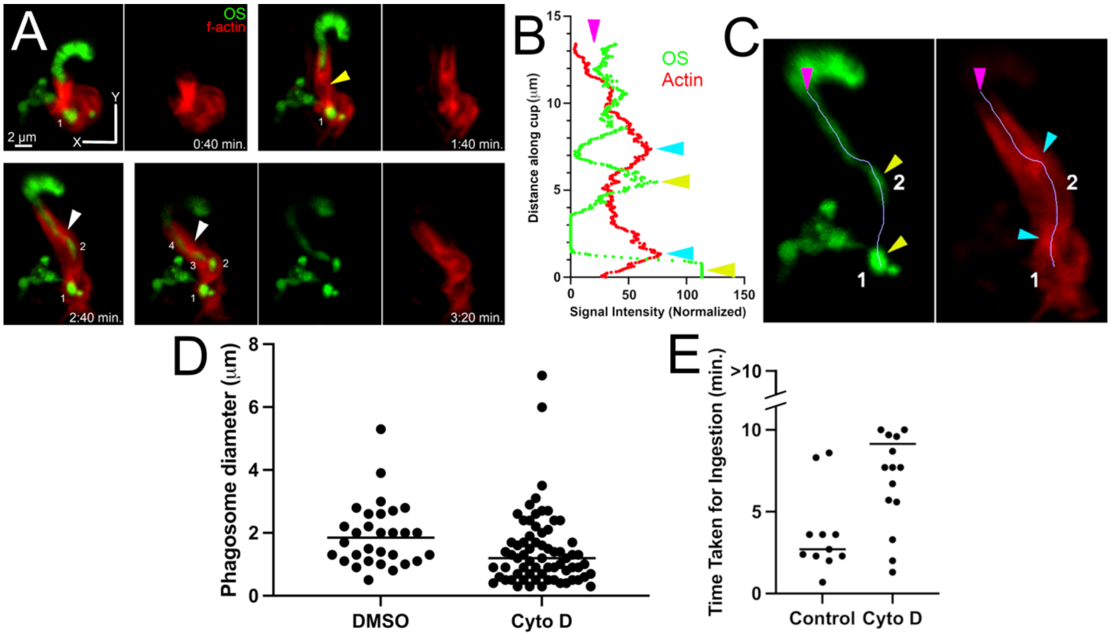

Figure Legend - Figure 1-4: RPE engage in trogocytosis, a subset of phagocytosis, by utilizing actin as a fundamental regulator. The images in this figure were adapted from Umapathy et al., 2023. **A.** Time series from a 10min. movie showing a trogocytic cup engage in multiple scission events and subsequent actin-based trafficking of trogosomes into the cell. **B/C.** Quantification of the actin and OS signals along the cup (along the grey line shown in C) at the 2:40min. time point from the movie in A. Cyan arrowheads depict high actin intensities, and yellow arrowheads depict high OS intensities. The pink arrowhead represents the starting location for measurement. **D.** The phagosome diameter measured in DMSO treated cells and Cytochalasin D treated cells (post washout). Each data point represents a single phagosome (N = 30 for DMSO, N = 68 for Cytochalasin D; data was aggregated from 6 independent experiments). The line depicts the median. **E.** The time before the first scission event in a given 10min. movie, in either DMSO or Cytochalasin D treated cells (post Cytochalasin D washout). Each data point represents a single cup. The line depicts the median.

Scale Bars: A: 2μm

Actin nucleators mDia1 and the Arp2/3 complex are present at the phagocytic cup *in vivo*, and significantly reduce ingestion when inhibited.

Now that we understand the events that occur during trogocytosis, it is important to explore what other actin-associated proteins are involved and investigate what role they may play. Due to the fact that actin produces strong intensities that assist with scission and trafficking, actin nucleation is highly likely to be occurring to mobilize actin and help produce those forces. We began by investigating actin nucleators, specifically the Arp2/3 complex and mDia1. To see whether these proteins play a role in this system, we performed an inside-outside phagocytosis assay with inhibitors of the Arp2/3 complex (CK-666) and formins (SMIFH2). This assay involves feeding primary mouse RPE for 1hr., fixing in 4% PFA, and then staining for OS pre-permeabilization for 10min., followed by a secondary antibody, in order to stain only the OS that are bound to the RPE. Then, cells are treated with the same primary antibody after permeabilization, but then followed up with a different secondary antibody. This allows us to separate bound OS from total OS (and therefore ingested OS as well, by subtracting bound from total). To validate that this experiment worked successfully, we can look at merged images of the phagosomes and identify 2 distinct populations made up of red phagosomes (All, Fig. 1-5A, orange arrowheads) and yellow (both red and green) phagosomes (Bound, Fig. 1-5A, pink arrowheads). While this experiment does provide a general idea of the ingestion characteristics of these cells during drug treatments, it does have a large limitation: it is difficult to control for degradation. We used a 1hr. pulse to minimize active degradation and focus on the early stages of ingestion, but even within 1hr. there is still degradation occurring. It takes approximately

20-30min. for the OS to land on the cells, and another 10min. for a full ingestion event to take place; 1hr is a compromise between ensuring ingestion happens enough to see differences in kinetics, and fixing quickly enough to prevent skewing the number of internalized phagosomes due to degradation. All that said, inhibition of these proteins with CK-666 (an Arp2/3 complex inhibitor) or SMIFH2 (a general formin inhibitor) resulted in a significant reduction of ingestion by 77.2 ± 8.2% for CK-666 and 90.8 ± 3.0% for SMIFH2 (Fig. 1-5A, N = 3 experiments [see Methods for details], Mean ± SEM). Clearly, the Arp2/3 complex, as well as formins, are acting on the phagocytic cup in some capacity.

Next, we wanted to confirm that these proteins are indeed present at the phagocytic cup *in vivo*, to ensure that they are in the proper place to interfere with ingestion when inhibited. It is possible that inhibition of these proteins interferes with the actin stability of the entire cell and is therefore resulting in a reduction in ingestion due to structural changes rather than direct action of these proteins. We immunostained the cryosections as shown in Fig. 1-1 with antibodies targeting Arp2, ArpC2[11], and mDia1. These three proteins were present at the cup *in vivo*, and appeared all throughout the actin cup (Fig. 1-5B, C, C', D). Arp2 and ArpC2 manifested differently, where Arp2 appeared as enriched regions throughout the cup, while ArpC2 looked more diffuse (See Fig. 7 Results for validation of these antibodies and antibody quality review). See Supplemental Figure 1-2 for more images of cups stained in this way in other biological replicates. Due to aforementioned potential apical structure problems (see Fig. 1-1

---

[11] Arp2 and ArpC2 are two components of the Arp2/3 complex, that localize together to nucleate branched actin.

Results), it is not prudent to take spatial information from these experiments as fact. Without corroborating with other data, these cryosections can only tell us that these proteins are present at the cup, but not where within the cup they may be, or what they might be doing. However, they do provide a good start by showing that these proteins are where they need to be to interact with and facilitate ingestion *in vivo*.

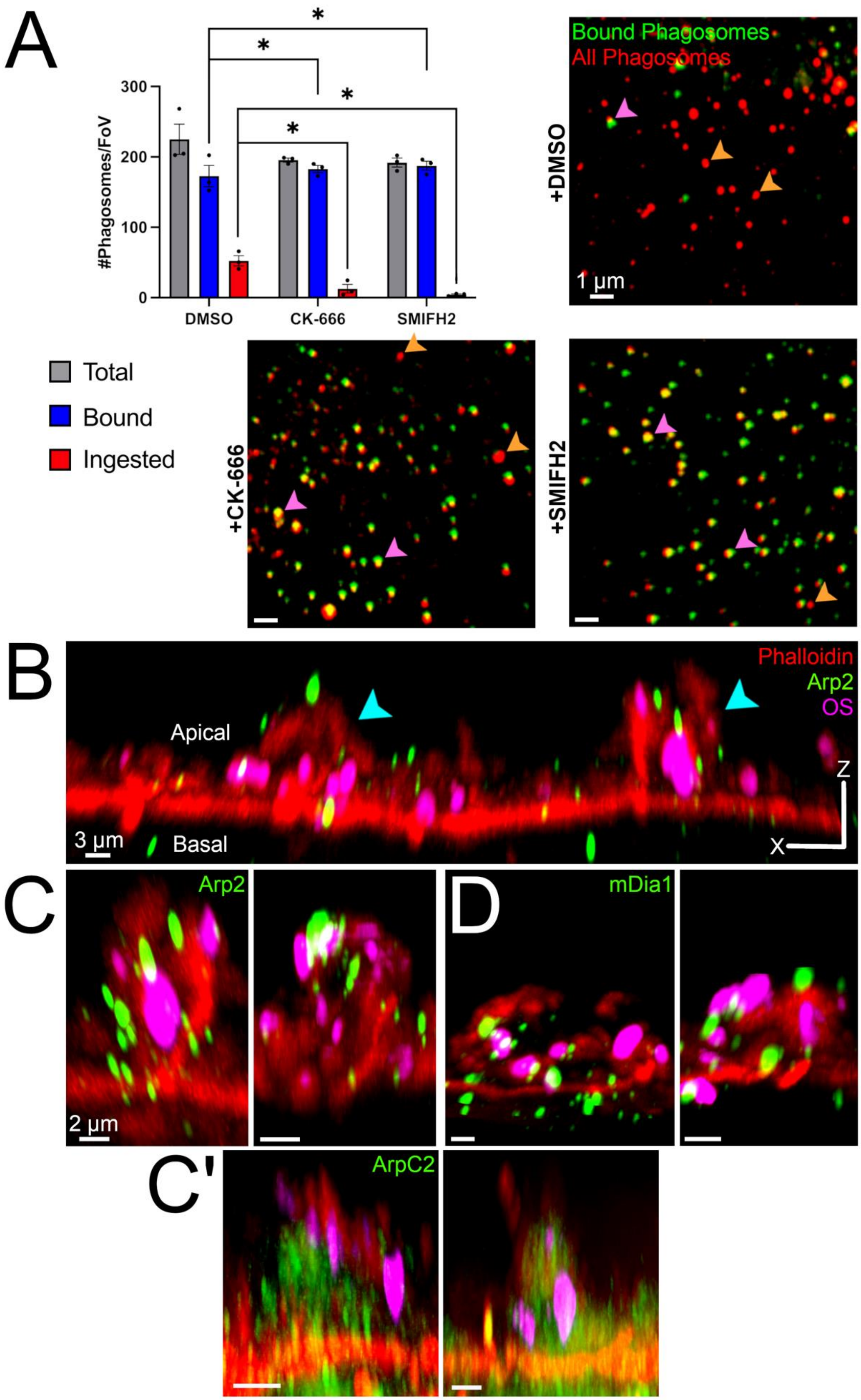
A
*
*
*
*
300
200
100
0
#Phagosomes/FoV
DMSO
CK-666
SMIFH2
Total
Bound
Ingested
Bound Phagosomes
All Phagosomes
+DMSO
1 µm
+CK-666
+SMIFH2
B
Phalloidin
Arp2
OS
Apical
Basal
3 µm
Z
X
C
Arp2
2 µm
D
mDia1
C'
ArpC2

Figure Legend - Figure 1-5: Actin nucleators mDia1 and the Arp2/3 complex are present at the phagocytic cup *in vivo*, and significantly reduce ingestion when inhibited. **A.** Inside-outside phagocytosis assay with primary mouse RPE cells, with a 1hr. pulse, pretreated (and maintained in the media) with DMSO, CK-666, or SMIFH2. Each data point represents a single experiment (made up of 10-12 images per well), and the images are high magnification representative images from this assay (made up of 50% of the area of the total FOV). Red phagosomes (orange arrowheads) represent both Bound and Ingested phagosomes, while yellow phagosomes (both red and green, pink arrowheads) represent Bound phagosomes. Error bars depict Mean ± SEM. **B.** Side view of a cryosection, as in Fig. 1-1, immunostained for Arp2 and the OS, and stained with Phalloidin. Cyan arrowheads point out two cups present on this cryosection. **C/C'/D.** Examples of phagocytic cups on cryosections, stained for Arp2 (C), ArpC2 (C'), or mDia1 (D).

Scale Bars: A: 1µm, B: 3µm, C/D: 2µm.

Inhibition of the Arp2/3 complex results in cups that fail to retain contact with the OS and initiate trogocytosis.

To investigate the role of the Arp2/3 complex at the cup, we pretreated RPE cells with CK-666 for 1hr., fed OS, and then performed live imaging with CK-666 maintained in the media. After inhibiting the Arp2/3 complex, we found something quite striking: the cells exhibited a difficulty in taking the initial trogocytic bite. With the Arp2/3 complex inhibited, and a lack of branched actin, the cups frequently dropped the OS onto the membrane of the cell (Fig. 1-6A/B, white arrows); they exhibited a failure to retain contact with the OS. In some cases, such as the movie shown in Fig. 1-6A, the cup was unable to create a proper rim to hold on to the outer segment, and so the OS simply fell out of the cup and onto the membrane of the cell. When it landed, the cell released a rippled wave of actin (Fig. 1-6A, white arrowheads), similar to dropping a stone in water, that extended out away from the cup. Actin waves similar to this have been seen in Dictyostelium and were thought to be a strategy for a phagocyte to scan a surface for particles to be engulfed (Gerisch et al., 2009). Once the OS was dropped, the cell had to scan its surface to find where the OS landed, and subsequently move the actin cup appropriately. In other cases, such as in Fig. 1-6B (a movie from a different biological replicate), the cup is able to recapture the OS once having dropped it. In Fig. 1-6B, the OS fell out of the cup by 5 minutes, and landed on the cell. The actin cup then moved rightward (the central grey line is static across the time series) and scooped up the OS, using an actin density to get underneath the OS and push it back to the top of the cup structure, into its proper location for a scission event to occur. A third cup from another biological replicate is shown in Supplemental Figure 1-3; this cup portrayed the slowed actin movement seen with CK-666 treatment (Fig. 1-6E), and was unable to initiate trogocytosis, despite a full actin cup structure completely surrounding one end of the OS for a 10+ minute period. Importantly, these cells failed to engage in scission and maintain the OS at the rim of the cup; the cups dropped the OS in 61.1 ± 5.6% (Fig. 1-6C, N = 3 experiments, Mean ± SEM) of 10-minute movies.

Once the cup was able to trogocytose a piece of the OS, ingestion proceeded normally. Comparing CK-666 treated cells to vehicle (DMSO) treated cells, there was no significant difference between the time taken between OS-cup association and the first scission event[12]. However, when comparing based on the time to the first scission event after the initiation of the movie, there was a significant increase in the CK-666 treated sample (Fig. 1-6D, left/middle). This describes that while it does take significantly longer for the cup to organize the OS in the proper location for ingestion, and initial immediate scission is inhibited, the ingestion process does proceed normally once the cup has managed to place the OS in the proper location. Further evidence of that fact is that the number of scission events per movie does not change when the Arp2/3 complex is inhibited (Fig. 1-6D, right).

To further study this phenotype, we then used an Imaris Spots model to quantify different metrics. Imaris is able to create a model of the actin signal, computationally choose points along the actin surface, and track them as they move throughout the movie. Imaris can then produce statistical data about the tracks and movements of

---

[12] In this context, a cup-OS association was defined as an overlap in signal of the OS and the high-intensity actin cup. In a majority of movies, the OS was already associated with the cup at the initiation of the movie. In many cases during CK-666 treatment, the OS was dropped and recovered before initiation of trogocytosis.

these points. CK-666 treated cells had a significant reduction in both Mean and Max track speed (Fig. 1-6E, the mean or max speed of a specific actin point along the movie), describing that these cups move slower both on average and when they are at their maximum speed. These cells also had a significant reduction in both Track Length (the distance that a particular actin point travelled over the movie) and Track Displacement (the total displacement that a particular actin point moved over the movie). This describes that when the Arp2/3 complex is inhibited, cups will move slower and travel less. We have previously shown that actin polymerization rates, and therefore actin speed, greatly affect cup dynamics (Fig. 1-4D, [Umapathy et al., 2023]), so slower actin movement implies that inhibition of Arp2/3 produced a cup that was less capable of normal ingestion.

Interestingly, there was a 77.2 ± 8.2% (Fig. 1-5A, N = 3 experiments, Mean ± SEM) reduction in ingestion in the phagocytosis assay when treated with CK-666, and in 61.1 ± 5.6% (N = 3 experiments, Mean ± SEM) of movies, there was an OS drop; it would not be surprising if these values are connected. If 60-80% of cups are unable to take a bite from their OS, it would logically follow that there would be a 60-80% reduction in ingestion. Due to the fact that these cups still act normally once the phagosome is ingested, it seems likely that significantly extending the chase time of the phagocytosis assay may eventually even out the amount of ingestion. However, extending chase times allows for extensive degradation, introducing a new significant variable, and so this validative experiment is practically difficult to complete.

One potential concern with inhibition of the Arp2/3 complex is that this treatment may impair the cell’s natural actin structures, resulting in changes to the ingestion process that are independent of Arp2/3 action at the cup. However, when quantified, the number of cups/FoV in CK-666 treated cells was not significantly different from that of untreated cells (Fig. 1-6G), describing that even though the cups themselves engage in trogocytosis differently than in DMSO-treated cells, there are still the same number of cups; CK-666 is not preventing cup formation. In addition, in all the live imaging and immunofluorescence images presented, CK-666 was only added acutely (<4hrs, 1hr. pretreat + 2-3hrs. imaging). There was no observable difference between untreated cells and those that were treated for 2hrs. in terms of actin morphology or organization (Supplemental Fig. 1-1A/B) and, observationally, there was no change in these actin structures comparing movies taken early to those taken late in the imaging experiment. Presumably, these cells would start showing effects over longer treatment times, but that was not seen at <4hrs of treatment as observed both in live imaging and fixed immunofluorescence assays.

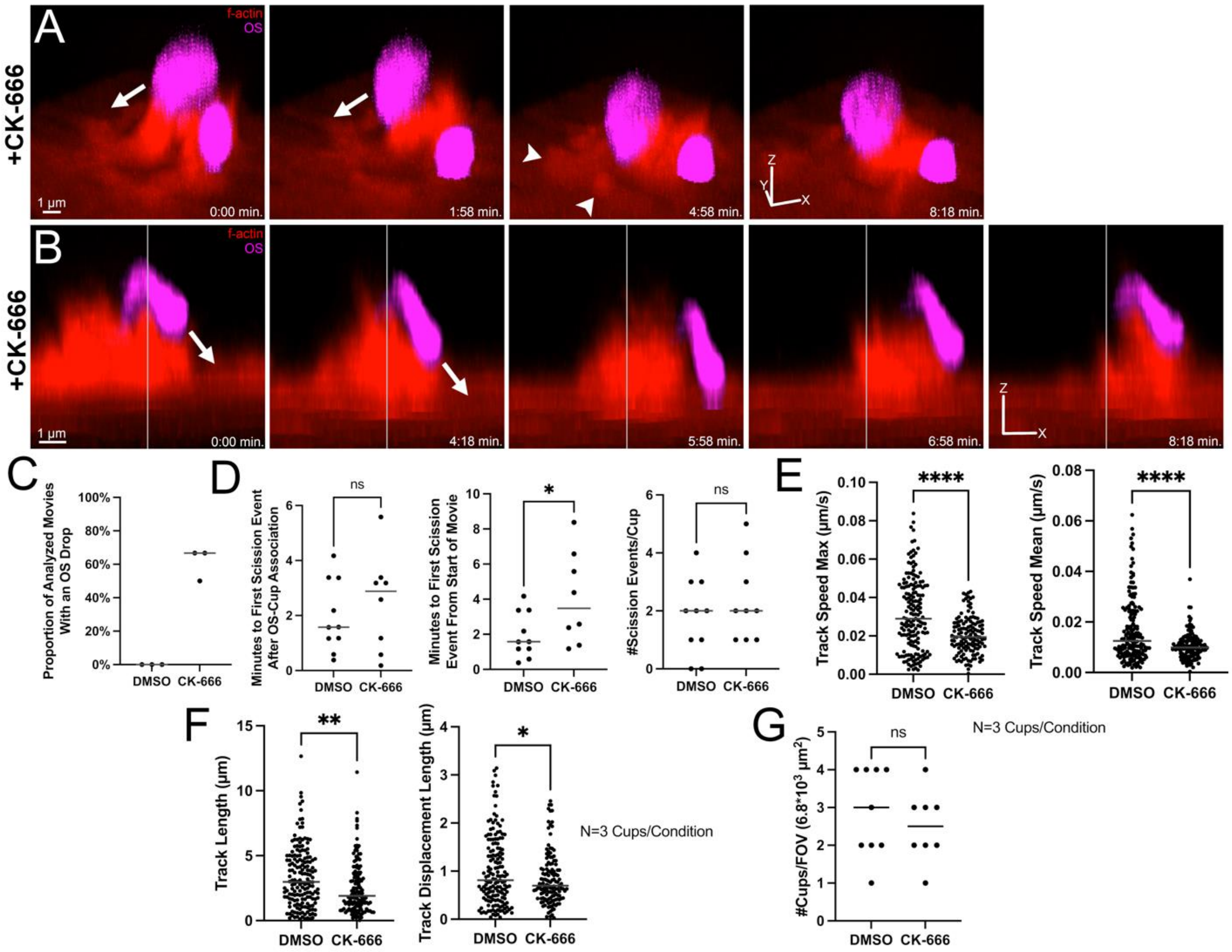

Figure Legend - Figure 1-6: Inhibition of the Arp2/3 complex results in cups that fail to retain contact with the OS and initiate trogocytosis. **A/B.** Two time series from 10min. movies of primary mouse RPE cells (originating from different biological replicates) unable to hold on to the OS and engage in proper trogocytosis, when treated with CK-666. White arrows show directional movement of the OS, and white arrowheads depict the actin ripples that appear after the OS lands on the cell. In B, the grey median line does not move throughout the time series, to show the rightward movement of the cup. **C.** The percentage of movies within a given experiment that showed an OS drop. Each data point represents a single experiment, made up of 3-4 movies. **D.** Quantification of a range of features regarding the OS drop during CK-666 treatment. Each data point represents a single phagocytic cup in a given movie. **E.** Quantification of the Mean and Max Track Speed in DMSO or CK-666 treated cells, as quantified by a Spots models in Imaris. Each data point represents a specific Spot on a Spots model, and the data was collected over 3 cups/condition, each from a different experiment. **F.** Quantification of the Track Length and Track Displacement Length in DMSO or CK-666 treated cells, as quantified by a Spots models in Imaris. Each data point represents a specific Spot on a Spots model, and the data was collected over 3 cups/condition, each from a different experiment. **G.** Quantification of the number of cups per field of view, comparing DMSO treated cells to CK-666 treated cells.

Scale Bars: A-B: 1μm

Arp2/3 localizes to the rim of the cup, and occasionally to the base of trogosomes.

Now that we have seen that Arp2/3 complex inhibition resulted in an immediate lack of OS retention/scission, we then investigated where the Arp2/3 complex was located within the cup. We fed normal primary Mouse RPE with OS, pulsed for one hour, then fixed in 4% PFA. We immunostained for the Arp2/3 complex with an Arp2 antibody (Fig. 1-7C/C'/C''), one of the proteins that makes up the Arp2/3 complex. The 7 proteins of the Arp2/3 complex act in concert (Goley and Welch, 2006), and so we expected that they would localize together, and that each protein staining would act as a representative location for the whole complex. Our IF results were quite striking: the Arp2/3 complex consistently localized to the rim of the cup, surrounding the base of the outer segment. In some cases, it also localized to the base of trogosomes within the cup. While the Arp2/3 complex did always appear at the rim, there was variability in the exact locations that this signal appeared throughout the cup. Sometimes, Arp2/3 was only at the rim[13], with minor signal through the rest of the cup (Fig. 1-7C, yellow arrowheads, Supplemental Fig. 1-4A [bottom]/B [top]); the cyan box on the left shows a z-slice through the image in C, along the cyan line. The numbered yellow arrowheads in the cyan box correspond to the numbered yellow arrowheads in the merged image in C.

---

[13] The rim is generally defined as the upper portion of the cup, where the actin structures surround the base of the outer segment. The rim defines a region that is associated specifically with the outer segment, and not with trogosomes. The measurement in Fig. 1-7G was made by measuring, in X, the horizontal distance between one end of the actin signal and the other through the center of the OS (or along the opening of the actin signal, if the actin rim was clear in 3-D) at the top of the cup. Examples of this measurement can be seen in Supplemental Fig. 1-4A/C, shown by blue lines crossing the rim of the actin signal in the third column.

Other times, it was present more around phagosomes, generally on either side of them (Fig. 1-7C'', orange arrowheads, Supplemental Fig. 1-4A [top/bottom]). In one particular cup, we found an outer segment that had folded over onto itself, and landed with both ends of the OS on the apical surface of the cell. In this case, Arp2/3 formed multiple separate extensions surrounding the rim of each end of the OS[14] (Fig. 1-7C', yellow arrowheads); as in C, the right cyan box shows a z-slice along the cyan line in C', and the numbered yellow arrowheads correspond to each of those in C'. The cell will create an Arp2/3 branched actin structure anywhere that an OS lands and activates the ingestion process, regardless of what the OS looks like and how it lands on the cell. Another interesting note was that the Arp2/3 complex did not fully surround the phagosome, but tended to create branched actin on 3 sides of the phagosome (cyan boxes, Fig. 1-7C/C'), usually forming a triangular support structure[15].

---

[14] As a side note, this image provides further evidence that 1-sided phosphatidylserine is not required for ingestion, as Arp2/3 signal at the phagocytic cup can appear on either end of an OS and is not side specific.

[15] It is difficult to tell why the Arp2/3 complex might organize in this triangular way. From a dynamic perspective, it seems possible that the three regions of branched actin are prepared to respond to OS movement. When the OS falls or leans too far to one side of the cup, the Arp2/3 complex might create more branched actin on that side to support it and prevent the OS from falling out of the cup. Creating three branched actin densities allows for dynamic changes to keep the OS in place, without needing to recruit very large amounts of the Arp2/3 complex proteins. That said, without live imaging with a high quality Arp2/3 fluorescent construct, something that we have been unable to find despite experimental testing, this remains speculation.

One potential concern was that the antibody signal for Arp2 in both cryosections (Fig. 1-5C) and fixed primary RPE (Fig. 1-7C-C’’) appeared as enriched globular regions throughout the cup; it is not uncommon for antibodies to aggregate, resulting in an artificially large globular signal that is simply an artifact of immunofluorescence staining. Our Arp2 staining did appear in globular enrichments, in a way that may have been artifactual. To ensure that this localization was not an artifact, we performed a number of controls, and stained with a different antibody targeting another protein that makes up the Arp2/3 complex as we did in cryosections: ArpC2. We validated our antibodies by western blot (Fig. 1-7A, N = 2 for Arp2, N = 3 for ArpC2) and performed secondary controls for the two Alexa Fluors that were used in these experiments (Fig. 1-7B, B’). We found that both primary and secondary antibodies were highly specific. The ArpC2 staining nearly phenocopied the Arp2 staining, showing ArpC2 present primarily at the rim of the cup (Fig. 1-7D, D’, D’’, yellow arrowheads, Supplemental Fig. 1-4C [first and third image]) as well as, in some cases, associating with phagosomes (Fig. 1-7D’, D’’, orange arrowheads). In one case, we found that the ArpC2 signal appeared as a tube, creating a path down the cup for multiple phagosomes to move through (Fig. 1-7D’’). The presence of the Arp2/3 complex at the rim of the cup was consistent across both antibodies (Fig. 1-7C/C’/D, Supplemental Fig. 1-4A/B/C); more examples from other biological replicates can be found in Supplemental Fig. 1-4A/B/C. While Arp2 and ArpC2 did manifest differently (i.e. enriched regions vs. smoother diffuse signal), they were still consistently present in the same location: beneath the outer segment at the rim, and, in some cases, around phagosomes.

Another validation step that we pursued was exploring the literature to see how our Arp2/3 signal compares to others. Unfortunately, investigating the Arp2/3 complex at such high resolution is not something that many labs invest in. The immunofluorescence stainings in the literature tended to focus on large scale cellular changes, rather than topics that require sub-micron spatial resolution, and so many of the images in the literature are of whole cell Arp2/3 signal (Zhao et al., 2020 p.1; Shi et al., 2021) which is not particularly useful as a comparison. That said, the images from those manuscripts that did stain for the Arp2/3 complex were consistent with our results, from what we were able to gather based on the published data. In addition, we did find two manuscripts that stained for Arp2, and also found the globular enrichments that we saw in our data (Fig. 1-7C-C''). Hubert et al., 2011 immunostained for ArpC1, Arp2, Arp3, and ArpC5 in HEK293T cells; Fig. 1A of that manuscript shows that the signal for Arp3 and ArpC5 are fairly specific, in that the signal to noise ratio of the antibody compared with the rest of the cell is quite high, and that excess non-specific signal appears light and diffuse, rather than globular. However, the Arp2 signal (as well as the ArpC1 signal), did appear with many enriched globular regions, similar to our results. This experiment also showed that while the signal localization of the Arp2/3 complex is similar with antibodies targeting different Arp2/3 proteins (i.e. at the pericentriolar matrix, in the case of Hubert et al. 2011, or the rim of the cup, in our experiments), it is not surprising for antibodies targeting these different proteins to manifest differently in terms of signal-to-noise ratio and the appearance of the signal itself. Aggarwal et al., 2012 also immunostained for Arp2 in dendritic cells infected with HIV, and showed that the

Arp2 signal appeared entirely as globular enrichments all across the cell (Fig. 4G in Aggarwal et al., 2012), highly similar to our results.

A final validation step we pursued was to create a composite average of the phagocytic cup images, to see how consistent the localization of the Arp2/3 complex was. To do this, we took the green (Arp2/ArpC2), red (Phalloidin), and pink (OS) signals from 25 Arp2/ArpC2 immunostained phagocytic cups and performed a Grouped Z-Project in ImageJ, either based on the Median (Fig. 1-7F, red and green signal) or the Mean (Fig. 1-7F, pink signal). Fig. 1-7F (red) shows a median actin signal for a phagocytic cup. The Arp2/3 signal (Fig. 1-7F, green, yellow arrowhead) shows that the Arp2/3 complex was consistently present in the central/upper portion of the cup. While the median image was not able to show the Arp2/3 signal on individual phagosomes, it does show that the Arp2/3 signal overlapped significantly with the upper half of the cup and all throughout the upper half of the OS signal. In addition, the Arp2/3 signal created a small cup shape (yellow arrowhead) that surrounded the base of the outer segment (OS pointed out by white arrow).

Lastly, we were interested to see if this localization changed when the Arp2/3 complex was inhibited; we found that the Arp2/3 complex did not change localization when inhibited, and still contained signal that associated with the outer segment, as well as with the phagosomes (Fig. 1-7E, yellow and orange arrowheads). For more examples from other biological replicates, see Supplemental Fig. 1-4D. Interestingly, however, CK-666 treated phagocytic cups had wider rims (Fig. 1-7G). Under the idea that the Arp2/3 complex produces branched actin at the rim of the cup, it logically follows that inhibition of the Arp2/3 complex would result in a less structured rim that is wider and larger than normal. This provides consistency to the result that Arp2/ArpC2 localized heavily to the rim of the cup (Fig. 1-7C/D, Supplemental Fig. 1-4A/B/C). In addition, this likely is also relevant for the 'lack of OS retention' phenotype seen in live cell imaging (Fig. 1-6A/B). A rim that is wider than the OS, and therefore not as tightly contoured to the OS membrane, would presumably be less able to prevent the OS from falling out of the cup.

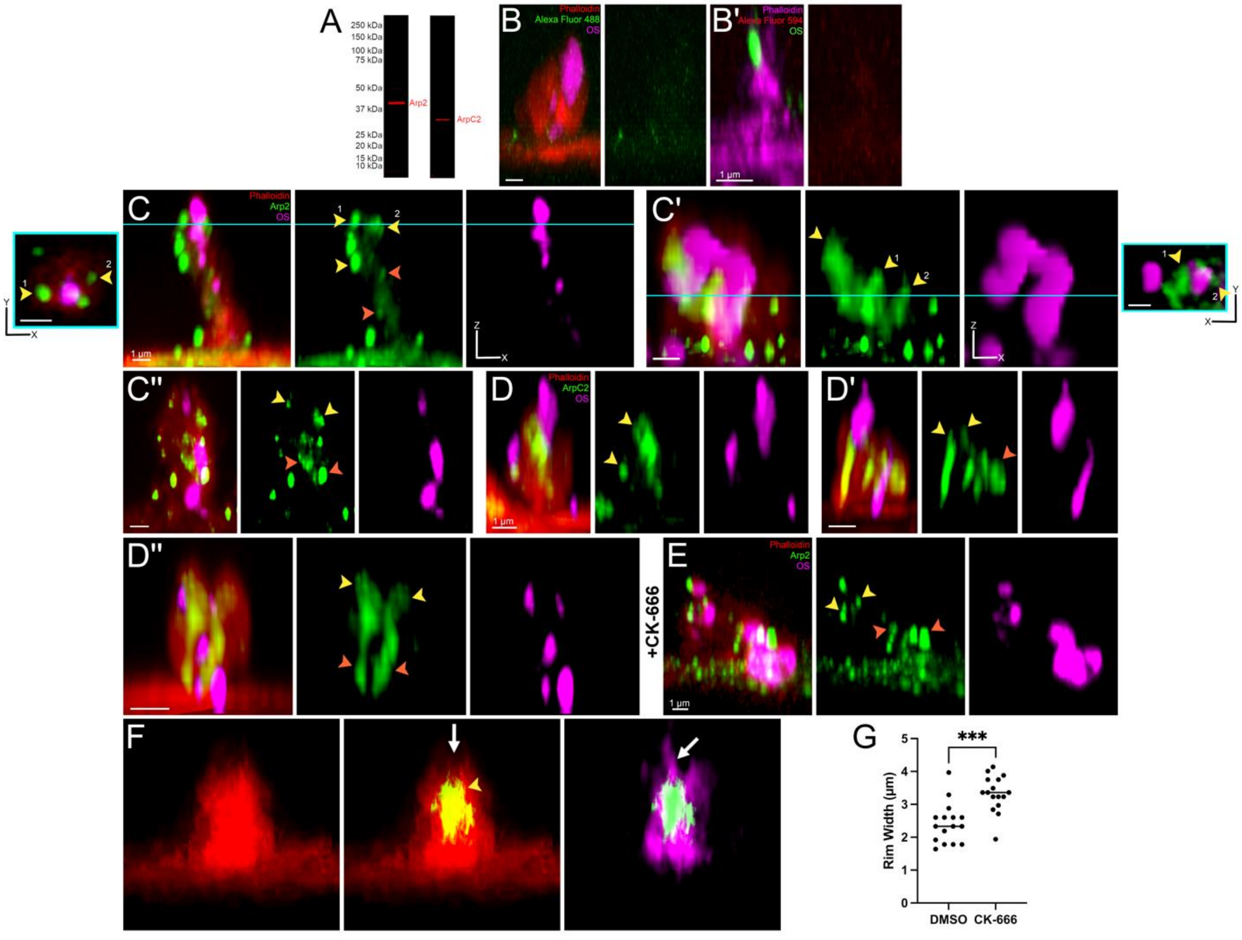

Figure Legend – Figure 1-7: Arp2/3 localizes to the rim of the cup, and occasionally to the base of trogosomes. **A.** Western blots validating the Arp2 (left) and ArpC2 (right) antibodies (N = 2 for Arp2, N = 3 for ArpC2). **B/B’.** Secondary controls for Alexa Fluor 488 and 594, the two secondary antibodies used in the presented immunofluorescence experiments (note that all immunofluorescence images shown within Chapter 1 use these secondary antibodies). Note the absence of green (left) and red (right) signal at the cup. **C/C’/C’’.** Three examples of the staining pattern of the Arp2 antibody at the phagocytic cup. Yellow arrowheads point out Arp2/3 signal at the rim of the cup, surrounding the OS, and orange arrowheads point out Arp2/3 signal within the cup at the base of phagosomes. The cyan boxes on the left (for C) and right (for C’) show z-slices through the image along the cyan line. The yellow arrowheads numbered ‘1’ and ‘2’ in the cyan boxes correspond to the numbered yellow arrowheads in the main image. **D/D’/D’’.** Three examples of the staining pattern of the ArpC2 antibody at the phagocytic cup. As in G, yellow arrowheads point out Arp2/3 signal at the rim, and orange arrowheads point out Arp2/3 signal associating with phagosomes. **E.** A representative example of a cup treated with CK-666 and stained for Arp2; there is no change in Arp2 localization after CK-666 treatment. **F.** A composite image made up of 25 individual images of phagocytic cups that have been immunostained for either Arp2 or ArpC2. The red (Phalloidin, left) and green (Arp2 or ArpC2, middle and right) signal are Median Grouped Z-Projections, while the pink (OS, right) signal was a Mean Grouped Z-Projection (the median image for the pink signal was nonexistent, because an OS could appear anywhere along the cup, and did not appear in the center of the cup consistently enough for a proper visible signal). These images do not have a scale bar as they are a composite of many images with slightly varying scales. The yellow arrowhead points out the Arp2/3 signal present on the top half of the cup, surrounding the base of the OS.

The white arrow points to the location of the OS that has its’ base surrounded by Arp2/3 signal. **G.** Quantification of the rim width in fixed immunostained cultures as shown in C/D.

Scale Bars: B-E: 1µm

mDia1 is necessary for cup formation.

Clearly, the Arp2/3 complex is involved in the ingestion process, but what about mDia1? To begin, we pretreated cells with SMIFH2, a general formin inhibitor, fed with OS, and imaged live (while maintaining SMIFH2 in the media). With this experimental setup, we found a lack of any apparent actin-based structures that resembled cups (Fig. 1-8B, Supplemental Fig. 1-5B). A lack of formin activity completely inhibited actin-based cup formation during live imaging. However, while SMIFH2 is easy to work with, it is not an ideal inhibition strategy. SMIFH2 is a general formin inhibitor, so it does inhibit all formins and not just mDia1. SMIFH2 also has been seen to inhibit some Myosins (Nishimura et al., 2021), so it is important to genetically knock down mDia1 to confirm that this lack of actin-based cups is due to inhibition of mDia1 specifically. To genetically knock down mDia1, we used a mouse mDia1 shRNA (Thompson et al., 2018) and found that it phenocopied SMIFH2 treatment: no actin-based cups whatsoever (Fig. 1-8D, Supplemental Fig. 1-5C). To ensure the quality of the shRNA sequence and construct, we then reintroduced human mDia1 (in the form of mEmerald-mDia1) to shRNA treated cells. With this, we were able to rescue this phenotype and consistently saw actin-based cups present on dually-transfected cells (mDia1 shRNA + mEmerald-mDia1[16], Fig. 1-8E, Supplemental Fig. 1-5D). Supplemental Figure 1-5 shows further examples from other biological replicates of these experiments.

---

[16] To identify dually transfected cells, we were able to use the reporters of these two constructs. The mDia1 shRNA contained a ZsGreen reporter, which appeared as large globular enrichments throughout the cell. The mEmerald-

To validate this finding, we performed a number of other assays and analyses with this same experimental setup. To begin, we performed an actin speed analysis to ensure that there was a true lack of movement, rather than just a reduction. As we did previously in CK-666 treated cells (Fig. 1-6E/F), we quantified the speed of individual actin points, this time on a Surface model[17], over 3 phagocytic cups/condition and found that there was a measurable amount of actin speed beyond baseline (i.e. no cups) only 'at the cup' in Ctrl shRNA treated cells, and in the rescue experiment (mDia1 shRNA + mEmerald-mDia1)(Fig. 1-8F). In all other scenarios, where mDia1 was inhibited or knocked down, or the cell was analyzed away from an OS, there was no movement and therefore no actin-based structures that resembled cups. One minor note is that the speed of the cup in the rescue seemed to vary (ranging from 4.29 - 73.15nm/s, N = 3 cups/condition each from different experiments) much more than in the control (ranging from 22.90 - 57.51nm/s, N = 3 cups/condition, each from a different experiment). We expect that this is likely just a consequence of the experimental setup. Our intervention does not regulate the amount of mDia1 that is knocked down, and the mDia1 over expression construct uses a CMV promoter which introduces variability in the mDia1 expression level of individual cells (Qin et al., 2010). Both of these together likely

---

mDia1 overexpression construct manifested as a diffuse signal all across the cell. Cells with both a diffuse light signal, as well as specific enriched globular regions, were easily identifiable by eye.

[17] We used a surface model here rather than a spots model because the Imaris surface model was better able to capture the lack of movement. Spots contained more variability between points, and so even visually unmoving regions quantified to have higher than expected speed.

resulted in some cells with greater or lesser mDia1 quantity, which could cause some cups to move slower or faster depending on the cell.

We further validated this phenotype with an inside-outside phagocytosis assay using the mDia1 shRNA. For our phagocytosis assay (Fig. 1-8G), there was a 84.4 ± 5.3% (N = 6 experiments, Mean ± SEM) reduction in ingestion, corroborating the SMIFH2 phenotype (Fig. 1-5A, 90.8 ± 3.0% reduction in ingestion, N = 6 experiments, Mean ± SEM). In addition, there was a reduction in the total number of phagosomes by 28.5 ± 3.5 (N = 6 experiments, Mean ± SEM). When looking at the phagocytosis assay in Figure 1-5, there was also a reduction in the total number of phagosomes by a mean of 33 (N = 3 experiments): nearly identical. This initially might seem a surprise, but it is likely that this is simply a result of trogocytosis. A lack of cups results in a lack of trogocytosis, and therefore no increase in the overall number of phagosomes within the cell, provided that there is no phagosome degradation (as trogocytosis will increase the total number of phagosomes by splitting an OS into multiple pieces). In both 1hr. pulse phagocytosis assays, done in equivalent ways, we see a drop by ~30 phagosomes in the treated condition – describing that about 30 phagosomes were produced as a result of the trogocytic activity, seeing as how all the wells were fed with the same starting content. Further evidence of this point is that in CK-666 treated cells (Fig. 1-5A), where there was also a reduction in trogocytosis, there was also a reduction in total phagosome number by about 30 phagosomes. A discrepancy with this experiment was that the total number of phagosomes, in both control and shRNA treated conditions, was much lower than the phagocytosis assay shown in Figure 1-5 (225.2 ± 21.6 in Fig. 1-5A DMSO [N = 3 experiments], 50.2 ± 2.7 in Fig. 1-8G DMSO [N = 6 experiments];

Mean ± SEM). This could be due to a number of reasons. To start, primary RPE vary heavily in their level of differentiation, with more polarized cells being more resistant to transfection. When transfecting in these constructs, the cells that are more likely to be transfected will be those that are larger and less polarized. When imaging, we chose transfected cells based on a green reporter, and so on average, the cells chosen were larger and less polarized. It was previously found that RPE that were less polarized and contained more stress fibers had a lower phagocytic capacity (Müller et al., 2018b). The fact that our transfected RPE was more likely to be less polarized is presumably a significant reason why we saw fewer overall phagosomes present in the phagocytosis assay. In addition, our lab has observationally found that transfected cells have a lower overall phagocytic capacity, and so it is not surprising that these cells (which needed to be transfected with the shRNA, either control or mDia1) interacted with significantly fewer phagosomes. This result was quite surprising, so we performed this experiment 6 separate times, and found highly consistent results. Importantly, there was a distinct significant reduction in ingestion in the mDia1 shRNA treated cells, and a complete lack of actin-based cups.

A final quantification method to validate this phenotype was to count cups/FOV in fixed immunostained cultures (Fig. 1-8H). This quantification validated our results, showing that cups will only form in cells that are DMSO treated, Ctrl shRNA treated, mDia1 shRNA + mEmerald-mDia1 treated, and mEmerald-mDia1 treated. We also utilized primary RPE from MERTK knockout mice[18], a traditional model for a lack of

---

[18] MERTK knockout mice (Lu et al., 1999) are a mouse model lacking the Mer Tyrosine Kinase receptor, a receptor required for engulfment of outer segment material by actin (Almedawar et al., 2020; Kwon and Freeman, 2020).

cups (Strauss et al., 1998; D’Cruz et al., 2000; Almedawar et al., 2020), as a negative control for this phenotype. Interestingly, we still found some actin-based cups in this culture, however, the number of cups was still a significant reduction when compared to DMSO treated, and was not significantly different from SMIFH2 treatment. Without mDia1 present in the cell, actin-based cups will simply not form.

As with CK-666, one potential concern with inhibition of mDia1/formins is that this treatment may impair the cell’s natural actin structures, resulting in changes to the ingestion process that are independent of formin activity at the cup. However, the speed of the actin signal (as quantified by Imaris) was not different with SMIFH2 treatment, at regions away from the cup (Fig. 1-8F). This describes that while SMIFH2 clearly prevented cup mobilization, it did not change actin kinetics away from the cup. In addition, in all the live imaging and immunofluorescence images presented, SMIFH2 was only added acutely (<4hrs, 1hr. pretreat + 2-3hrs. imaging). There was no observable difference between untreated cells and those that were treated for 2hrs. in terms of actin morphology or organization (Supplemental Fig. 1-1A/C) and, observationally, there was no change in these actin structures comparing movies taken early to those taken late in the imaging experiment. Presumably, these cells would start showing effects over longer treatment times, but that was not seen at <4hrs of treatment as observed both in live imaging and fixed immunofluorescence assays.

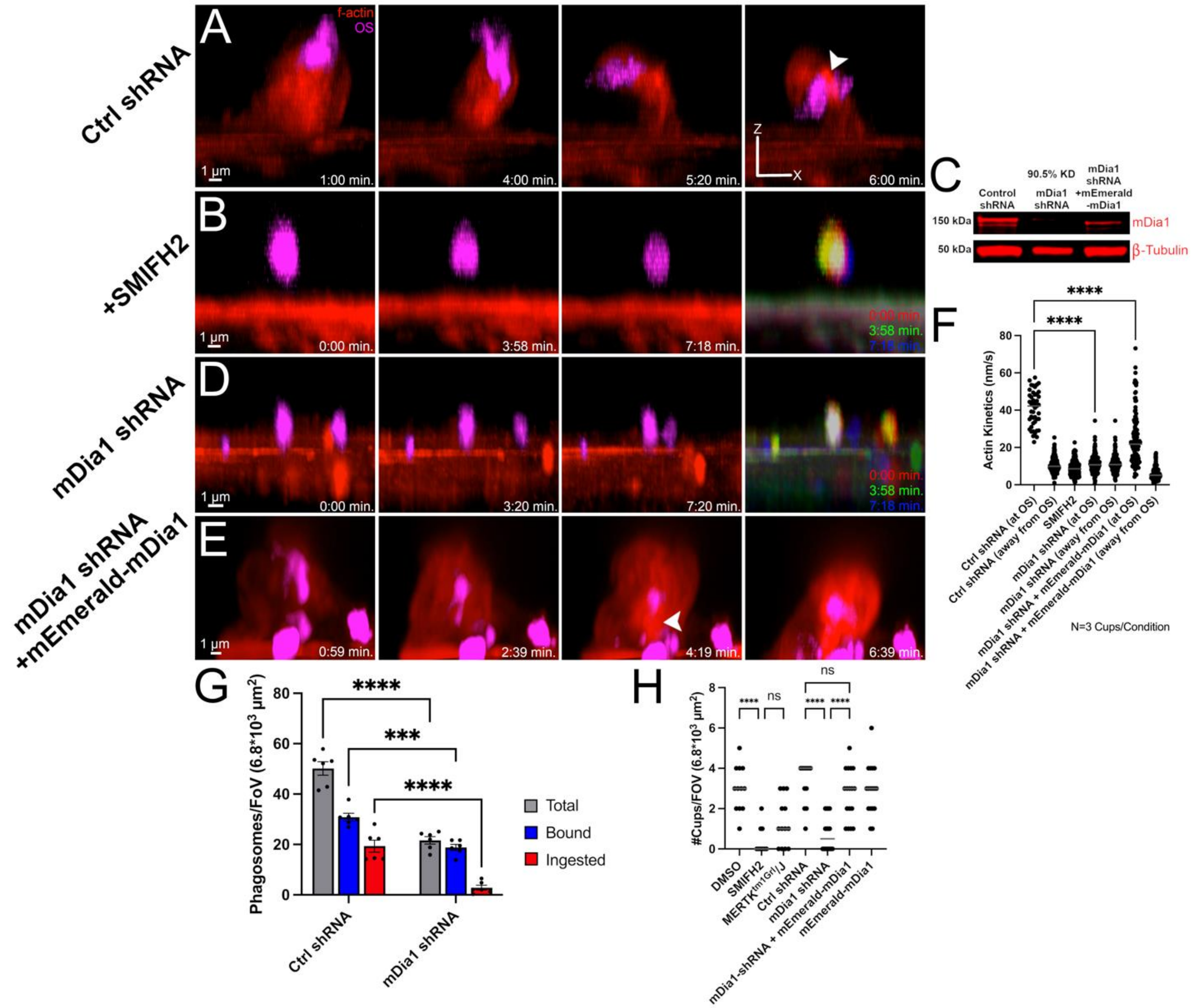

Figure Legend - Figure 1-8: mDia1 is necessary for cup formation. **A.** An example movie of a phagocytic cup in a Control shRNA transfected cell; this cup exhibited normal trogocytosis. The white arrowhead points out an actin density that worked to break apart the outer segment. **B.** A movie of a given OS on the apical surface of the RPE, during SMIFH2 treatment. The 4th image is a composite of red/green/blue-toned versions of the previous 3 time points. Note the lack of an apparent actin cup, and the lack of any motion over the course of the movie. **C.** A western blot validating the mouse mDia1 shRNA knockdown, as well as the recovery of mDia1 protein in the rescue, in primary mouse RPE (N = 4). **D.** A movie of a given OS on the apical surface of the RPE of a cell transfected with a mDia1 shRNA. As in B, the fourth image is a red/green/blue-toned composite of the previous 3 time points; note the lack of an apparent actin cup or any motion over the course of the movie. **E.** A movie of a phagocytic cup on a cell transfected with plasmids for both mouse mDia1 shRNA and human mEmerald-mDia1, rescuing the ‘no actin cup’ phenotype. The white arrowhead points out an actin density that worked to trogocytose the larger OS piece. **F.** Speed quantification of actin, based on an Imaris surface model, quantified in Imaris, in a range of conditions and locations. ‘Away from OS’ describes a region of actin that is >10µm away from an OS or the cortical actin in X-Y. ‘At OS’ describes a region where an OS was present and a phagocytic cup should be expected in normal conditions. Each data point represents the Mean Track Speed in Imaris of a specific point, on a specific cup, in a specific movie. Three movies were analyzed per condition, and the lines mark the median. **G.** An inside-outside phagocytosis assay with cells transfected with either a Control shRNA, or the mDia1 shRNA. The surface area of the transfected cells were measured in ImageJ based on the ZsGreen reporter of the plasmid, and the phagosome count was scaled up based on this value such that the Phagosomes/FOV represented the entire field of view. Each data point represents an individual experiment, and the error bars depict Mean ± SEM. **H.** Quantification of the number of cups per field of view that were visible in a range of conditions. Each data point represents a single field of view, and the lines mark the median.

Scale Bars: A-E: 1µm

Formin inhibition results in the formation of precups, that lack actin but contain other relevant ingestion proteins.

mDia1 was clearly involved in cup formation, but the complete lack of cups was a much more extreme phenotype than expected, so we followed up on this protein through immunofluorescence experiments to explore its localization. When validating the mDia1 antibody, which should stain the ~150 kDa mDia1 protein, we unexpectedly found that there were 5 separate bands in our western blot (Fig. 1-9A, N = 4). However, all of these bands disappeared, or were significantly reduced in signal, after treatment with the mDia1 shRNA, confirming that this antibody was specific to mDia1. The 75 kDa band likely represented a fragment of 150 kDa mDia1 protein, something that has been seen in the literature (Kim et al., 2015) and by the developers of the antibody. The three bands between 37-50 kDa likely represented the three mouse mDia1 isoforms 1, 2, and 3, which, based on the NIH GenBank, are 1264, 1255, and 1220 amino acids respectively[19] (Clark et al., 2016). However, it is unclear what the ~100 kDa band represented. It clearly disappeared after mDia1 shRNA treatment, but this size does not match any known mouse mDia1 isoforms. This band was still present with the addition of protease inhibitors during lysis, so it therefore is not a degradation product. It also disappeared with mDia1 shRNA treatment, so it is unlikely to be non-specific binding. It seems possible that mDia1 could undergo changes in the RPE that are unique when

---

[19] An estimate of the kDa weight of these protein isoforms places them within the 37-50 kDa region. These isoforms have been shown through transcripts within the NIH GenBank, but have not been shown by western blot in the literature.

compared to other cell types, and so there may be new isoforms that are unique to the RPE (that would not be found in a Gene Bank, unless it was RPE specific). That said, all of these bands did disappear during mDia1 shRNA treatment, so the antibody was specific to mDia1.

We first stained for mDia1 in primary mouse RPE, to understand its localization within the cup. mDia1 signal was present all along the cup in its entirety (Fig. 1-9B, Supplemental Fig. 1-6A); regardless of the number of cups analyzed, the imaging experiment, and changes to the intensity histogram, this signal almost always appeared even and spread throughout the cup (29/33 analyzed cups, across 2 experiments, showed a relatively smooth signal filling the entire cup). While this was not particularly exciting, we found something interesting when inhibiting formins with SMIFH2 and then staining for the Arp2/3 complex. While we previously saw that this resulted in a lack of cups, a phenotype that was consistent here, we did still see Arp2 at a region where the rim of the cup would normally be, should there be actin present (Fig. 1-9C, Supplemental Fig. 1-6B). The cells formed what we have decided to call ‘precups’, containing the relevant biochemical players for ingestion but without any actin structures. When we compared the number of cups present in DMSO treated cells, to the number of these precups in SMIFH2 treated cells, we found no significant difference (Fig. 1-9D). This implies that each of these events was intended to be a normal trogocytic cup, but the lack of actin structure prevented trogocytic events and subsequent ingestion; this is in line with our previous finding that SMIFH2 treatment drastically reduced ingestion (Fig. 1-5A).

The presence of Arp2 within these precups was quite a surprise - how does the Arp2/3 complex localize near the OS when the OS is seemingly bound and not actually inside the cell? We performed the same experiment, but this time we prestained the membrane with WGA, a dye that stains lectins and acts as a marker for the plasma membrane (Chazotte, 2011). This experiment showed that the OS were indeed technically inside the cell, despite no actin-based engulfment. WGA showed organized membrane structures that very tightly contoured the edge of these phagosomes in SMIFH2 treated cells (Fig. 1-9G, Supplemental Fig. 1-6C/D). Another example from live cell imaging in Supplemental Fig. 1-6D/D' shows a partially membrane-encapsulated OS with no actin present at or near the OS, describing that the membrane can indeed surround bound outer segments without actin structures. These phagosomes were always stuck in the apical portion of the cell, and were completely surrounded by membrane; these phagosomes were also consistently larger than in vehicle treated cells (1.73 ± 0.11µm diameter in DMSO treated cells [N = 40 across 2 experiments], compared to 2.21 ± 0.15µm in SMIFH2 treated cells [N = 38 across 2 experiments], Fig. 1-9I), likely contributing to their inability to enter the cell, as well as providing further evidence that trogocytosis was not occurring (as that would result in more smaller trogosome pieces). As before, when we counted the number of cups in DMSO treated cells to the number of membrane cups in WGA-dyed SMIFH2 treated cells, we found no difference (Fig. 1-9H), again describing that these were supposed to be true trogocytic cups, but lacked the actin structure to fulfill their function appropriately. Another relevant finding was that, based on the height of the Arp2 signal off of the circumferential actin in Z, SMIFH2 treated precups were shorter than regular cups (Fig. 1-9E). This is logically not surprising, as formins act to elongate the barbed end of actin – in this case, formins acted to extrude the actin cup apically away from the membrane. Without mDia1 activity, there was no actin, and no ability to extend the cup structures apically.

Another interesting question we explored was whether the Arp2/3 complex and mDia1 were working together, something that has been seen in other systems during ingestion processes (Naj et al., 2013; Isogai et al., 2015; Velle and Campellone, 2018; Cao et al., 2020). To do this, we treated cells with either SMIFH2 or CK-666 and stained for the non-inhibited protein. When treating with CK-666 and staining for mDia1, we found that mDia1 was no longer present as a diffuse signal all across the entire cup. mDia1 began to form enriched regions of signal located all throughout the cup: at the outer segment, at phagosomes, and away from OS material (Fig. 1-9J, cyan arrowheads, see Supplemental Fig. 1-6E for further examples). In addition, when the overall mDia1 signal intensity was normalized to the height of the cup, there was no significant difference between the signal intensity in the control and in the CK-666 treated cells (Fig. 1-9N). This describes that the cups did not lose any mDia1 content, but that it was instead reorganized. This result implies that mDia1 was associating with the branched actin structures that the Arp2/3 complex was helping to produce.

When staining for mDia1, but also inhibiting mDia1, we found a surprisingly similar phenotype. This experimental setup also resulted in mDia1 changing its signal to enriched regions across the cup (Fig. 1-9L, Supplemental Fig. 1-6F). These enriched regions were larger than during CK-666 treatment (Fig. 1-9M), but also did not portray any signal intensity change when the intensity was normalized to the height of the cup (Fig. 1-9N). While this result was a bit more surprising, there is evidence in the literature that mDia1 will change its localization based on its activity (Seth et al., 2006). In Seth et al. 2006, they showed that active mDia1 localizes to the membrane, but will localize to the cytoplasm when the FH2 domain is autoinhibited by the association of the DAD domain with the N-terminus (Alberts, 2001; Li and Higgs, 2003). When this autoinhibition is removed (by removing the DAD domain), mDia1 returns to the plasma membrane (Seth et al., 2006). Our results are likely an indication of this: normally mDia1 localizes in a diffuse pattern all along the membrane, but when it is inhibited by SMIFH2 (which acts by inhibiting the FH2 domain of mDia1 [Rizvi et al., 2009; Innocenti, 2023]), mDia1 localizes to the cytoplasm and so it instead is enriched in localized regions across the cytoplasm of the cup.

Looking later in the ingestion process, we also wanted to explore how downstream degradative components of phagocytosis were involved in these early steps. Specifically, we were interested to see if Rab5, an early endosome marker (Huotari and Helenius, 2011) that is associated with the first steps in the degradative process (Kwon and Freeman, 2020), was present within the cup and associated with phagosomes. Immunostaining showed that Rab5 was indeed present within the cup, and it extended 59.3 ± 2.5% (N = 1 experiment, Mean ± SEM) of the way up the cup from the circumferential actin (Fig. 1-9O/P). There was no significant difference in this extension during SMIFH2 treatment. An interesting note to make was that when we measured the raw µm up the cup that Rab5 extended into, rather than the percentage of the cup, there was a significant decrease in SMIFH2 treated cells. However, because the percentage quantification was not significant, this further describes that these cups are simply shorter when treated with SMIFH2 (Fig. 1-9E). Rab5 endosomes were able to travel significantly up the cup and associated with phagosomes very early during the ingestion process.

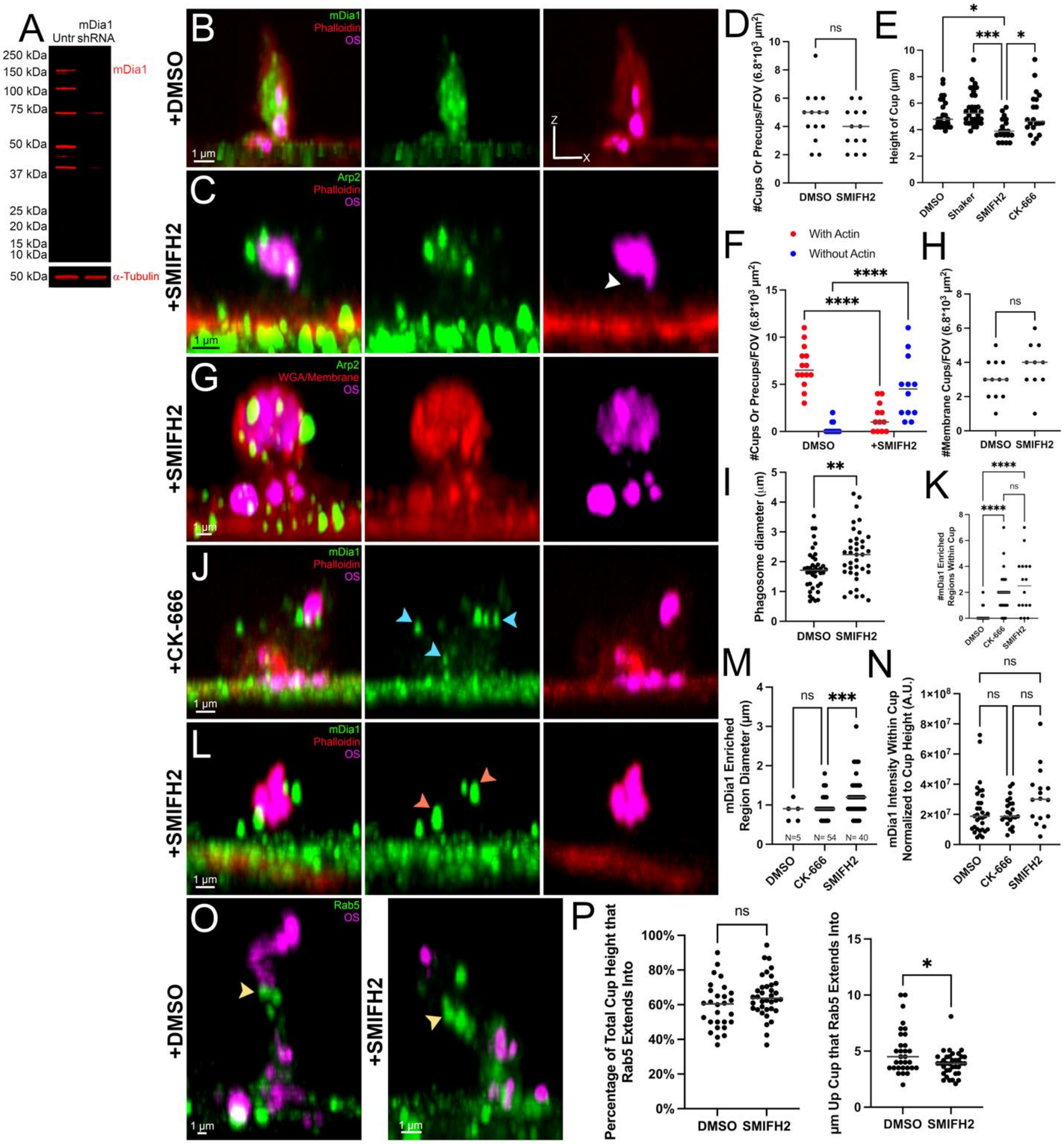

Figure Legend - Figure 1-9: Formin inhibition results in the formation of precups, that lack actin but contain other relevant ingestion proteins. **A.** A western blot validating the mDia1 antibody in primary mouse RPE (N = 4). **B.** A phagocytic cup immunostained for mDia1, that showed a diffuse signal all along the cup. **C.** A precup, treated with SMIFH2, that showed Arp2 signal next to the OS despite a complete lack of an actin cup. The white arrowhead points out the lack of actin beneath the OS. **D**. The number of cups (or precups, in the case of SMIFH2) per field of view in DMSO and SMIFH2 treated cells. Each data point represents a single field of view. **E.** The height of the phagocytic cup, as measured from the circumferential actin to the peak height of the Arp2 signal of the cup, in a variety of experimental conditions. **F.** Quantification of the number of actin-based cups and precups (i.e. no actin, but with Arp2 present) in each field of view. Each data point represents the total number of cups with or without actin in a single field of view. **G.** A precup during SMIFH2 treatment, with the membrane stained by WGA, showing the tightly organized membrane that surrounded the OS despite a lack of actin. **H.** The number of membrane cups surrounding OS in each field of view, based on WGA staining, in cells treated with either DMSO or SMIFH2. **I.** The diameter of phagosomes, as measured in X-Y, in DMSO or SMIFH2 treated cells. **J.** A phagocytic cup during CK-666 treatment, immunostained for mDia1. Note that the mDia1 signal became distinct enriched regions that were spread all throughout the cup: near the OS, next to phagosomes, and away from OS material (cyan arrowheads). **K.** Quantification of the number of mDia1 enriched regions within the cup in DMSO, CK-666, and SMIFH2 treated cells. **L.** A SMIFH2-treated precup, stained for mDia1. Note that mDia1 became distinct enriched regions (orange arrowheads), rather than a diffuse signal. **M.** The diameter of the mDia1 enriched regions in DMSO, CK-666, and SMIFH2 treated cells. **N.** The mDia1 signal intensity within the cup normalized to cup height, to show that the overall amount of mDia1 per cup does not change, just the organization. **O.** Rab5 signal within a phagocytic cup in either DMSO or SMIFH2 treated cells. Rab5 signal extends over halfway up the cup (yellow arrowheads), which does not change after SMIFH2 treatment. **P.** Quantification of the localization of Rab5 signal both by μm and by percentage. In all graphs, the grey line depicts the median.

Scale Bars: B-C, G, J, L, O: 1μm

Lack of Myosin 7a results in an inability to traffic trogosomes basally down the cup; Myosin 7a is present in the central region of the cup and associates with trogosomes.

Beyond actin nucleators, myosins are highly likely to also play a role in this system. Mutations in Myosin 7a have been historically shown to cause Usher Syndrome 1B (Ch, 1914; Liu et al., 1997; Williams, 2008), and previous work in the literature has found that *Myo7a* null primary mouse RPE had a distinct deficit with regards to the ingesting phagosome (Gibbs et al., 2003). In these cells, the phagosomes remained very apical, and the OS had consistent difficulty in passing through the cortical actin of the RPE and entering the cell body. However, a lack of technology, notably live cell imaging, has prevented this from being studied in more detail. Here, we utilized the new technology of live cell imaging to study this old problem.

To ensure that Myosin 7a is present at the phagocytic cup *in vivo*, we first stained for it in cryosections as we have done with the Arp2/3 complex and mDia1. Myosin 7a was present as a smear of signal all across the apical region of the RPE (Fig. 1-10A, Supplemental Fig. 1-7A/B), consistent with what has been shown in the literature (Jiang et al., 2015). We then plated shaker1 primary RPE (the mouse model lacking *Myo7a*), transfected with RFP-Tractin, fed outer segments, and performed live cell imaging. In wild type cells, the OS was bitten into smaller pieces, and each of these pieces was shuttled down the cup and into the cell (Fig. 1-10B); in Fig. 1-10B, the cup was formed, it ingested OS material, and it folded back into the membrane within the 10min. movie. However, in shaker1 RPE this is no longer the case. Trogosomes were still bitten off (Fig. 1-10C, cyan arrow), however they remained immobile and did not traffic down the length of the cup. Instead, they stayed localized near to the initial OS and, at some point, cup closure was initiated. Normally, the trogosomes would traffic into the cell, and the actin cup would subsequently fold back into the membrane (Fig. 1-10B, 6:50 and 9:47 time points). However, cups from *Myo7a*-null cells were unable to traffic the trogosomes, failed, and rather than pulling the trogosomes in one at a time, would instead enclose all the outer segment material into an actin spherule. This actin structure compacted, and remained tight against the apical region of the cell, such that the trogosomes and the OS were both stuck in a spherule of actin (Fig. 1-10C, C', white arrowhead, Supplemental Fig. 1-7C'). These actin/OS enclosures remained on the apical surface for an extended period of time; in some cases they were present even 30-40 minutes after the movie was taken (Fig. 1-10C', F, Supplemental Fig. 1-7C'). Examples from other biological replicates are shown in Supplemental Fig. 1-7C/C'. Supplemental Fig. 1-7C shows a cup that managed to hold on to an outer segment, but the cup, rather than shuttling the trogosomes down the cup and into the cell, remained stuck and was unable to close or shuttle the trogosomes basally throughout the 10 minute movie. The cup in Supplemental Fig. 1-7C' (from another biological replicate) shows a similar activity, with a cup that created an actin enclosure around the OS material, but, even after 40 minutes, remained unable to ingest any trogosomes. To explore whether the lack of Myosin 7a was affecting cup kinetics or trogocytic activity, we quantified the number of cups per field of view, the number of scission events per cup, and the minutes to the first scission event of a given movie; in shaker1 cells, all three were found to be not significantly different from wild type cells (Fig. 1-10D).

To validate this finding, we then performed a rescue experiment by adding back in lentiviral human *MYO7A*[20]. This construct was effectively able to rescue this phenotype, such that the cup was able to trogocytose the OS, ingest all of the outer segment material, and close the actin cup within a 10 minute period (Fig. 1-10E/E'). Two more examples from other biological replicates are shown in Supplemental Fig. 1-7D/D'. Note how in all three movies the cup successfully ingested the OS material and closed shortly after, all within the span of the 10 minute movies. For the movies in Fig. 1-10C/E, we quantified the height of the peak actin signal from the cortical actin, as well as the height of the center of the OS from the cortical actin, and graphed how these changed over the course of a movie (Fig. 1-10F). While the first 3 minutes appeared similar in kinetics and motion, when comparing the shaker1 cells to the rescue, there was a sharp difference after the 3 minute mark. While the rescue began to close the actin cup and trafficked the trogosomes into the cell quickly after the first 3 minutes of scission, the shaker1 cells plateaued. Eventually, after about 7 minutes, the OS/cup enclosure stabilized and remained stuck on the apical surface of the cell. By this point in time, the rescued cup had trafficked the trogosome to the level of the circumferential actin, and the actin cup was in the process of closing (Fig. 1-10F).

To investigate Myosin 7a activity through a different lens, we used a *MYO7A* tail construct (see Methods) containing only the cargo binding domain, and not the motor domain, of Myosin 7a. This construct effectively localizes to Myosin 7a cargo. This

---

[20] This construct was designed in-house by Dr. William Blake Gilmore, and is made up of Myosin 7a Isoform 2 fused to a mCherry fluorophore. See Methods for more details.

construct presented in two different ways depending on the cell. The *MYO7A* tail appeared either as a few large enrichments throughout the cell (as in Fig. 1-10G), or as many small globular enrichments (as in Fig. 1-10G'). In the movie in 9G, a large enrichment of *MYO7A* tail travelled rightwards towards a phagosome. The *MYO7A* tail travelled to the phagosome, past it, and localized directly beneath it. In 9G', another movie of the same construct (from a different biological replicate), we see that the *MYO7A* tail again localized directly beneath the OS (Fig. 1-10G', orange arrowhead in the 0:59min. time point). As the OS was trogocytosed between the first two frames presented (Fig. 1-10G', cyan arrowhead points out the nascent trogosome), the *MYO7A* tail began to travel upwards towards the next trogosome that needed to be trafficked, forming a ladder-like structure (Fig. 1-10G', orange arrowheads in the 3:39 and 5:19 time points). This subsequent trogosome began to traffic down the cell once it had associated with a halo of the *MYO7A* tail (Fig. 1-10G, orange arrowheads in the 5:19 time point).

As we have done with the Arp2/3 complex and mDia1, we then stained for Myosin 7a in normal primary mouse RPE cells. Myosin 7a consistently localized to the central region of the cup, where phagosomes are trafficked basally towards the cell body. This signal was incredibly high, frequently saturating the detector even with low laser power, such that it completely overshadowed the Myo7a present in the cell body. Fig. 1-10H shows the native signal with a lower intensity, while Fig. 1-10H'' shows the same image with a much higher signal intensity level; there was Myo7a throughout the cell body, but at a significantly lower quantity than at the cup. Another example of the saturating signal within the cup is shown in Fig. 1-10H'. Three examples from 3 other biological replicates are shown in Supplemental Fig. 1-7E-G; these three examples corroborate Myosin 7a presence in the center of the cup region, and show its relation to other relevant ingestion proteins (Supplemental Fig. 1-7E: Rab5, Supplemental Fig. 1-7F: Arp2, Supplemental Fig. 1-7G: mDia1). We quantified the position of Myosin 7a in 2 ways: by its relation to actin, and by its relation to the outer segment. By measuring from the circumferential actin (in Z) to the start of the Myosin 7a signal, to the end of the Myosin 7a signal, to the top of the actin cup, we found that Myosin 7a was positioned in the middle 30.6 ± 2.6% - 84.1 ± 3.2% (N = 17 cups across 2 experiments, Mean ± SEM) of the cup (Fig. 1-10J, left). When comparing to the outer segment, Myosin 7a signal was seen with an OS above it 76.5% of the time, and was seen with a trogosome below it 88.2% of the time (Fig. 1-10J, right, N = 17 cups across 2 experiments). Together, this describes that Myosin 7a was present when there were trogosomes to be trafficked; it was extremely rare for a cup to have Myosin 7a signal, but not also be undergoing active scission and ingestion. To ensure the quality of the antibody, we also stained for Myosin 7a in shaker1 primary RPE (Fig. 1-10I). In this experiment, there was no signal within any cups, effectively validating our antibody. Myosin 7a localized to the center of the cup, overlapping with actin densities that pushed trogosomes down the cup, and seemed to play a role in trafficking trogosomes basally.

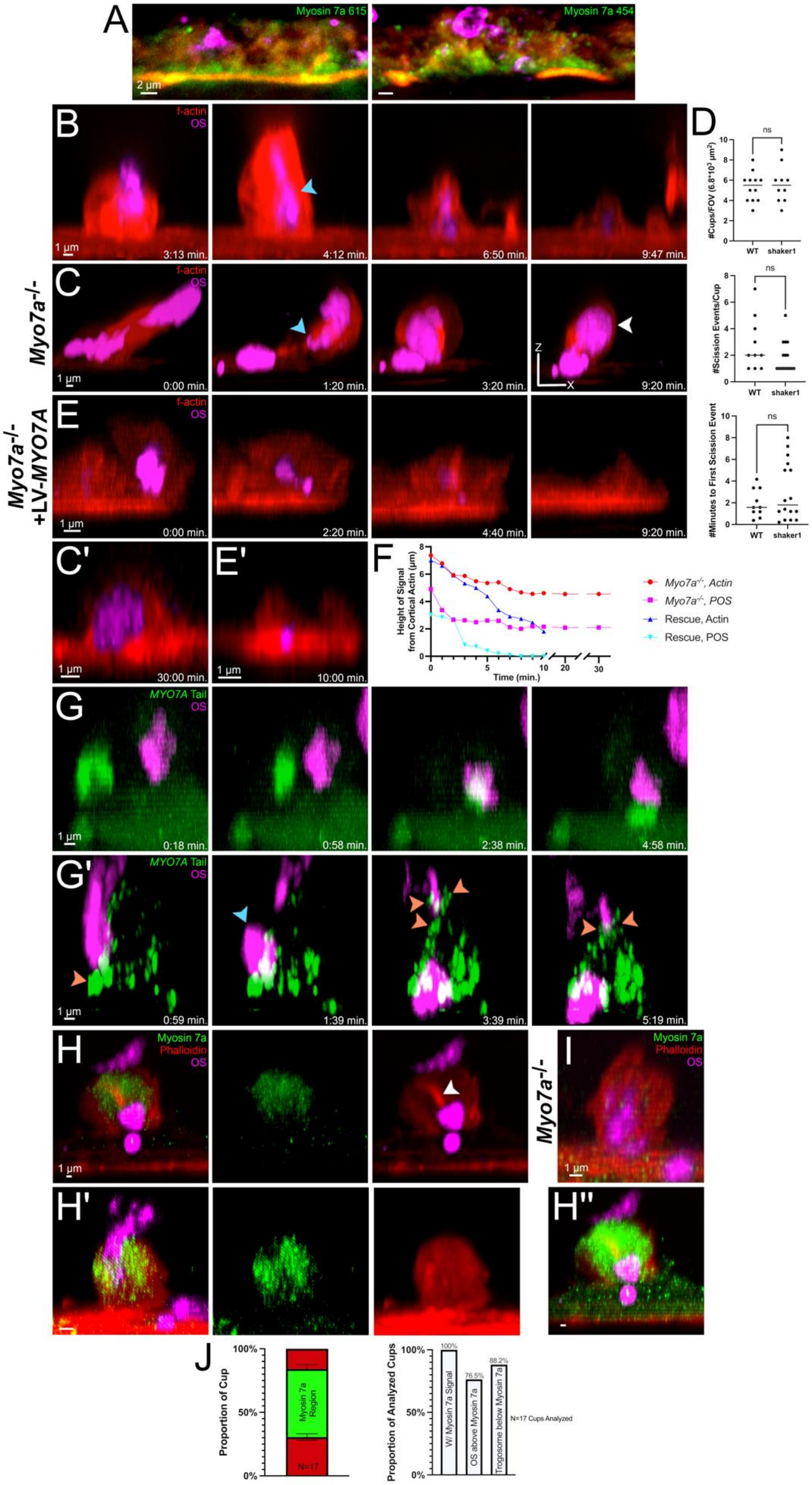
A
Myosin 7a 615
Myosin 7a 454
2 µm
B
f-actin
OS
1 µm
3:13 min.
4:12 min.
6:50 min.
9:47 min.
Myo7a-/-
C
f-actin
OS
1 µm
0:00 min.
1:20 min.
3:20 min.
Z
X
9:20 min.
Myo7a-/- +LV-MYO7A
E
f-actin
OS
1 µm
0:00 min.
2:20 min.
4:40 min.
9:20 min.
C'
1 µm
30:00 min.
E'
1 µm
10:00 min.
D
ns
#Cups/FOV (6.8*10³ µm²)
0
2
4
6
8
10
WT
shaker1
ns
#Scission Events/Cup
0
2
4
6
8
WT
shaker1
ns
#Minutes to First Scission Event
0
2
4
6
8
10
WT
shaker1
F
Height of Signal from Cortical Actin (µm)
0
2
4
6
8
0
5
10
20
30
Time (min.)
Myo7a-/-, Actin
Myo7a-/-, POS
Rescue, Actin
Rescue, POS
G
MYO7A Tail
OS
1 µm
0:18 min.
0:58 min.
2:38 min.
4:58 min.
G'
MYO7A Tail
OS
1 µm
0:59 min.
1:39 min.
3:39 min.
5:19 min.
H
Myosin 7a
Phalloidin
OS
1 µm
Myo7a-/-
I
Myosin 7a
Phalloidin
OS
1 µm
H'
H''
J
Proportion of Cup
100%
50%
0%
Myosin 7a Region
N=17
Proportion of Analyzed Cups
100%
50%
0%
100%
76.5%
88.2%
W/ Myosin 7a Signal
OS above Myosin 7a
Trogosome below Myosin 7a
N=17 Cups Analyzed

Figure Legend - Figure 1-10: Lack of Myosin 7a results in an inability to traffic trogosomes basally down the cup; Myosin 7a is present in the central region of the cup and associates with trogosomes. **A.** Mouse retina-detached eyecup cryosections immunostained for Myosin 7a, using one of two different antibodies (615 or 454). Phalloidin signal is shown in red and OS signal is shown in pink. **B.** Normal trogocytic ingestion in primary RPE. The actin signal increased in intensity at the scission event (cyan arrowhead); the cup was formed and closed fully within a 10 minute period. **C.** An ingestion event in shaker1 primary RPE. While actin densities did form and acted to excise pieces of the OS (cyan arrowhead), those pieces remained close together and folded into an actin enclosure (white arrowhead). **C'.** The same actin enclosure as shown in Supplemental Fig. 1-7C', but after a 30 minute time period. The OS material remained apical and enclosed in actin. **D.** Quantification of the cup dynamics of shaker1 primary RPE. **E.** A trogocytic movie in a shaker1 cell that has been transfected with lentiviral human *MYO7A,* to rescue the phenotype. Note that while all other images shown use RFP-tractin, E/E' used GFP-tractin, as the *MYO7A* rescue construct contained a mCherry fluorophore. **E'.** The same cup as in E, but after 10 minutes. Compare to C' which shows that the rescue was able to effectively ingest the outer segment material within a 10 minute period while the mutant was not. **F.** Time series graph showing the height of the actin (from the circumferential actin to the peak of the actin signal) and the height of the OS (from the circumferential actin to the center of the OS) as they progress through the phagocytic events from the movies in Supplemental Fig. 1-7C' (shaker1) and Fig. 1-10E (rescue). **G.** A phagocytic cup in WT mouse primary RPE, in a cell transfected with a *MYO7A* tail construct that contained only the cargo-binding domain, and not the motor domain, of MYO7A. Note how the enriched region of *MYO7A* Tail trafficked to the phagosome and positioned directly beneath it. **G'.** A second movie, from a different biological replicate, showing the organization of the *MYO7A* tail beneath an outer segment (orange arrowhead, 0:59min time point), and the movement up towards the next trogosome once the first has been cleaved (orange arrowheads, 3:39 and 5:19min. time points). The cyan arrowhead points to a trogosome that has been excised from the OS between 0:59 and 1:39min., and is subsequently trafficked down into the cell. **H/H'/H''.** WT primary mouse RPE, fed with OS, fixed, and immunostained for Myosin 7a. The white arrowhead points to an actin density that pushed the trogosome down the cup, and that overlapped with the Myosin 7a signal. H' is a second example of the Myosin 7a localization. H'' shows an over-saturated version of the image in H, to show that Myo7a was still present within the cell body, albeit at much lower levels than at the cup. **I.** A control for the Myosin 7a antibody, stained for Myosin 7a at a cup in shaker1 primary RPE. **J.** Left: Quantification of the localization of Myosin 7a within the cup (as measured from the circumferential actin, to the bottom of the Myosin 7a signal, to the top of the Myosin 7a signal, to the top of the actin signal of the cup). Right: Quantification of the positional associations of Myosin 7a with OSs and trogosomes.

Scale Bars: A: 2μm, B-C', E-E', G-I: 1μm

Arp2/3 signal extends down the entire cup, rather than remaining in the upper region of the cup, in *Myo7a*-null primary RPE.

Earlier, we showed that the Arp2/3 complex and mDia1 act together to facilitate ingestion. Next, we tested to see if there was any other protein cooperation by staining for each of the three proteins, in the absence of each protein (using SMIFH2/CK-666/shaker1 RPE and staining for mDia1/Arp2/Myosin 7a). While many of these experiments did not result in any noticeable changes to the immunofluorescence signal of these proteins, one particular combination did stand out: Arp2/3 localization in shaker1 cells. While the Arp2/3 complex normally only extended 2.31 ± 0.18μm (N = 26 cups across 3 experiments, Mean ± SEM) down the cup, it extended 4.59 ± 0.29μm down the cup in shaker1 cells (Fig. 1-11A, A', B, N = 46 cups across 3 experiments, Supplemental Fig. 1-8A). Visually, Arp2/3 no longer appeared consistently as distinct regions of signal, and became much more interconnected (Fig. 1-11A). It also clearly extended all the way down the cup reaching the cortical actin, something that was never seen in the control. In response to a lack of Myosin 7a, the Arp2/3 complex travelled further down the cup as trogosomes were trafficked downwards.

While Arp2/3 did show a difference in localization in shaker1 cells, many of the combinations did not result in changes. Specifically, CK-666 treatment did not change Myosin 7a localization (Fig. 1-11C, Supplemental Fig. 1-8B), and mDia1 did not appear differently in shaker1 cells (Fig. 1-11D, Supplemental Fig. 1-8C). In addition, Rab5 did not change in its localization in shaker1 cells, indicating that a lack of Myosin 7a does not interfere with the ability of the degradative components to enter the cup and begin the degradative process early on (Fig. 1-11E).

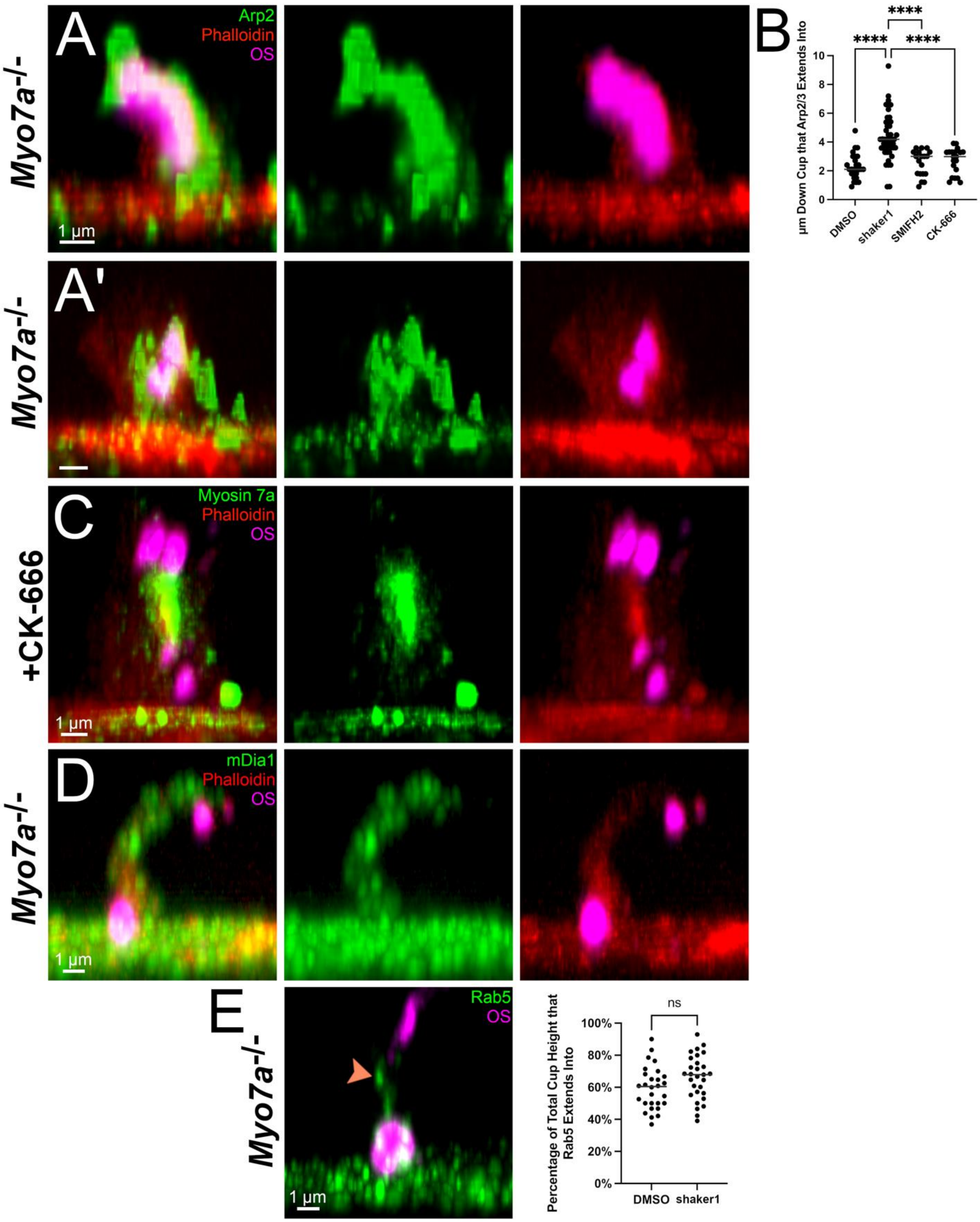
A
Arp2
Phalloidin
OS
Myo7a-/-
1 µm
B
µm Down Cup that Arp2/3 Extends Into
****
****
****
10
8
6
4
2
0
DMSO
shaker1
SMIFH2
CK-666
A'
Myo7a-/-
C
Myosin 7a
Phalloidin
OS
+CK-666
1 µm
D
mDia1
Phalloidin
OS
Myo7a-/-
1 µm
E
Rab5
OS
Myo7a-/-
1 µm
Percentage of Total Cup Height that Rab5 Extends Into
ns
100%
80%
60%
40%
20%
0%
DMSO
shaker1

Figure Legend - Figure 1-11: Arp2/3 signal extends down the entire cup, rather than remaining in the upper region of the cup, in *Myo7a*-null primary RPE. **A/A'.** Two examples of phagocytic cups from shaker1 primary mouse RPE, fed with OS, fixed, and immunostained for Arp2. **B.** Quantification of the µm down the cup that the Arp2 antibody signal extended from the rim in different experimental conditions, as measured from the peak of the Arp2 signal to the bottom of the Arp2 signal within the cup (in cups where the Arp2 signal extended fully to the cortical actin in Z, the extension measured was equal to the height of the cup). **C.** A phagocytic cup from primary mouse RPE pretreated with CK-666, fed OS (with CK-666 maintained in the media), fixed, and immunostained for Myosin 7a. **D.** A cup from shaker1 primary mouse RPE fed, fixed, and immunostained for mDia1. **E.** A cup from shaker1 primary mouse RPE fed, fixed, and immunostained for Rab5 (left). Quantified percentage of total cup height that Rab5 extends into (right) as measured from the circumferential actin in Z to the peak of the Rab5 signal.

Scale Bars: A-A', C-F: 1µm

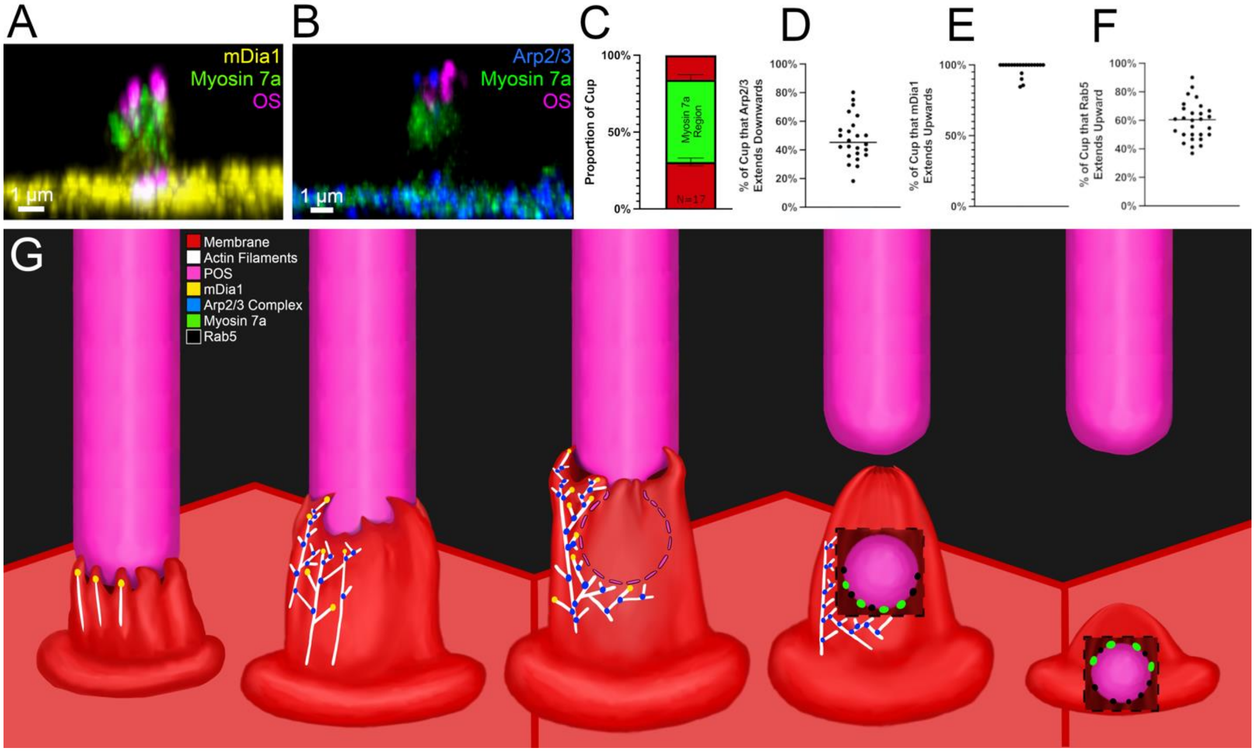

Figure Legend – Figure 1-12: During RPE trogocytosis, mDia1 acts as the primary actin nucleator, the Arp2/3 complex acts at the rim to hold the OS and trogosomes in their proper locations, and Myosin 7a traffics the trogosome down the cup once it has been excised. **A.** A phagocytic cup from primary mouse RPE, immunostained for mDia1, Myosin 7a, and the OS, to illustrate their localization. **B.** A phagocytic cup from primary mouse RPE, immunostained for Arp2, Myosin 7a, and the OS, to illustrate their localization. **C-F.** Quantifications describing the localization of Myosin 7a (C), Arp2/3 (D), mDia1 (E), and Rab5 (F). **G.** Schematic illustrating the RPE trogocytosis model, based on our results. First, mDia1 (yellow dots) attaches to the barbed end of actin filaments (white lines) and helps elongate the cup apically towards the OS (pink). Once the ingestion process has initiated, the Arp2/3 complex (blue dots) creates branched actin near the rim, supporting the OS and holding it in place. A scission event occurs, and the Arp2/3 complex/branched actin maintains association with the trogosome as it traffics down the top half of the cup. After the trogosome has travelled further basally, Myosin 7a attaches to the trogosome and traffics it into the cell, as the Arp2/3 branched actin surrounding the trogosome breaks down. Cup closure is initiated, and the actin structures fold back into the membrane. Rab5 endosomes associate with the trogosome in the bottom half of the cup and begin the degradation process. Note that this image is not drawn to scale, and does not include multiple scission events for ease of visualization. In normal trogocytosis there would be >1 scission event (Fig. 1-2G). Also note that the actin structures have only been drawn on the left half of the cup, for visualization purposes.

DISCUSSION

Conclusions

In this chapter, we investigated the actin dynamics of RPE trogocytosis and explored the role of three distinct actin-associated proteins or protein complexes during the ingestion process: the Arp2/3 complex, mDia1, and Myosin 7a. Based on our results, we speculate the following model as depicted in Figure 1-12G, which shows how the different proteins interact over a time series of 5 cup images. Actin dynamics are initiated through Rac1 signaling (Nandrot and Finnemann, 2003; Mao and Finnemann, 2012), causing a range of actin-associated proteins to traffic to the site of the cup; based on our results, these proteins include mDia1 (Fig. 1-9B, yellow dots in Fig. 1-12G), the Arp2/3 complex (Fig. 1-7C/C'/C'', blue dots in Fig. 1-12G), and Myosin 7a (Fig. 1-10H/H'', green dots in Fig. 1-12G). mDia1 is necessary for actin recruitment and growth of the cup, and so mDia1, along with the Arp2/3 complex, is trafficked to the site of the OS first and helps to elongate actin filaments apically to form the cup (Fig. 1-12G, yellow dots mark mDia1 and white lines mark actin filaments); lack of mDia1 results in a lack of actin structure within the cup (Fig. 1-8D). The Arp2/3 complex must also traffic to the cup region early on in the ingestion process, as Arp2/3 can be seen in precups without mDia1/actin (Fig. 1-9C), but must wait for mDia1 activity before it is able to create branched actin within the cup. Arp2/3 (marked by blue dots in Fig. 1-12G) traffics to the rim and creates branched actin structures surrounding the incoming outer segment and holding it in place for scission. As the branched actin is formed, mDia1 associates with the tips of the branched actin, likely to ensure that any vertical growth required for scission and OS manipulation can be completed. The first two cups in the time series of images in Fig. 1-12G show cup formation through mDia1 activity, and Arp2/3 localization to the rim of the cup. In the third cup image in Fig. 1-12G, the actin cup presses onto the OS as another protein, likely a myosin, reaches the top of the cup, excises a piece of the OS to form a trogosome, and the Arp2/3 complex associated branched actin holds the trogosome in place within the center of the cup and supports its movement down the upper region of the cup. When Myosin 7a is not present, Arp2/3 continues to make branched actin to ensure the trogosome remains in the center of the cup, where actin can apply mechanical force downwards. Presumably this is why the Arp2/3 complex extends to the base of the cup in shaker1 cells (Fig. 1-11A, A', B): there is likely some signaling mechanism to stop the OS-association of branched actin once Myosin 7a has associated with the trogosome. In WT cells (and in our 4th cup image in Fig. 1-12G), Myosin 7a (marked by green dots in Fig. 1-12G) associates with the trogosome once it has been excised and traffics it down the cup and into the cell, triggering the breakdown of branched actin around that trogosome. Some signaling mechanism informs the cell that the trogosomes have been ingested, and actin disassembly proteins traffic to the cup and break down its' structure, as it folds into the membrane (the last cup image in Fig. 1-12G).

What is needed to make RPE trogocytosis happen?

Based on this model and the current state of the field, there are likely to be many proteins that are still unknown with regards to RPE trogocytosis. To start the ingestion process, an OS will activate MERTK and $\alpha v\beta 5$ Integrin (Finnemann and Nandrot, 2006; Almedawar et al., 2020; Kwon and Freeman, 2020), and the RPE will interact with whatever unknown 'eat-me' signals (possibly phosphatidylserine [Ruggiero et al., 2012]) are present on the OS, triggering a biochemical cascade to initiate cup formation. First, to regulate actin nucleation activity, actin assembly proteins such as profilin (Pantaloni and Carlier, 1993), which has been shown to modulate Arp2/3 activity (Rotty et al., 2015), are required to increase and control actin polymerization rates (Krishnan and Moens, 2009) and support the creation of the actin filaments that will form the cup. To create the stability of the cup, there are likely to be actin bundling proteins, such as fimbrin or α-actinin (Cooper, 2000), to ensure a stable base for force generation into the OS. To form the branched actin structure, there may be larger actin crosslinking proteins such as Filamin (Cooper, 2000); if the Arp2/3 complex is indeed supporting scission activity, proteins like Filamin are needed on the branched actin to stabilize the structure and produce that force. Presumably, there is also some signaling mechanism to stop the cup from growing further once it has reached its' peak height; whatever this might be, it seems critical, as this mechanism is likely how the size of the trogosome is determined.

We chose to investigate mDia1 because diaphanous formins make up the largest subset of formins (Breitsprecher and Goode, 2013), have been strongly suggested to play a role in phagocyte cortical architecture (Mylvaganam et al., 2021), and had easily obtainable genetic constructs (shRNA sourced from Thompson et al., 2018, mEmerald-mDia1 sourced from Addgene). When studying mDia1 however, it was surprising to see that the mDia1 antibody showed 5-6 bands on the western blot, that disappeared after mDia1 shRNA treatment (Fig. 1-9A). While the 75 kDa band has been seen in the literature and described to be a fragment of the 150 kDa mDia1 protein (Kim et al., 2015), and the three bands between 37-50 kDa likely represented the three mouse mDia1 isoforms (Clark et al., 2016), it is still unclear what the ~100 kDa band represented. This band is not a degradation product (as repeating the western blot with protease inhibitors resulted in no changes to this band) or non-specific binding (as adding a mDia1 shRNA removed this band), so it is likely a new unknown isoform of mDia1 that has not been seen in transcripts, likely because the GenBank is not specific to RPE tissue. No other study has investigated mDia1 in the context of RPE; it would not be surprising if RPE cells create multiple isoforms of mDia1 to tightly regulate actin dynamics at the cup, where the varied activity of each mDia1 isoform creates different effects on cup dynamics. Moving forward, this could be an interesting area of study to explore both formin biology as well as trogocytic mechanisms. While mDia1 is clearly essential for cup formation, there also are other formins that likely play a role during ingestion: FMNL1 (Naj et al., 2013), other diaphanous formins (Colucci-Guyon et al., 2005; Junemann et al., 2016), DAAM1 (Hoffmann et al., 2014), and DAAM2 (Xu et al., 2023) have all been seen to play a role in some form of cellular internalization. Many of our results utilize SMIFH2 as a general formin inhibitor which, of course, inhibits all formins and not just mDia1. As previously mentioned, SMIFH2 has been shown to also inhibit some myosins (Nishimura et al., 2021) as well as IFN-induced JAK-STAT signaling (Thoidingjam et al., 2022; Innocenti, 2023) and so without creating genetic knockdown strategies it is practically difficult to screen the 15 mammalian formins (Schönichen and Geyer, 2010) for cup activity. Some groups have attempted to produce specific formin inhibitors (Gauvin et al., 2009; Orman et al., 2022), however finalized chemical inhibitors were either rife with artifact issues (Gauvin et al., 2009) or were found to have improved potency but not specificity (Orman et al., 2022), and so nothing has been produced so far to facilitate these types of experiments. Due to the fact that SMIFH2 treatment and a mDia1 knockdown both result in a complete lack of cups, it is difficult to tease apart what role other formins may be playing; in other words, demolishing a building provides little insight into how the building was formed by its constituent parts.

Continuing on with the next stages of phagocytosis, the actin cytoskeleton must then have a way to tether to the plasma membrane to create force on extracellular materials. Trogocytosis likely requires a large amount of specific directed force to rupture a membrane on an extracellular object, and so the actin architecture would presumably be tightly linked to the plasma membrane. While FAK, Vinculin, and Talin seem to be the most likely options (Finnemann, 2003; Kwon and Freeman, 2020; Zihni et al., 2022) there are plenty of other possibilities that could also play this role. Generally, microvilli use lateral arms of myosin 1 and calmodulin to link actin to the plasma membrane (Cooper, 2000). In RPE, Ezrin plays this tethering role within microvilli (Bonilha et al., 1999). While it is still unclear whether the phagocytic cup is produced by fusing microvilli or is a *de novo* actin structure, it would not be surprising for the RPE to utilize similar actin-associated proteins as the microvilli, seeing as how the proteins are already nearby and do not need to be trafficked very far to be involved. A protein, likely a myosin, must then traffic up the cup and provide force for OS scission, as the Arp2/3 complex holds the OS and nascent trogosome in place. The scission motor is currently unknown, but there are a few potential candidates. Myosin II could be a possibility as it mobilizes to the site of OS ingestion (Strick et al., 2009) and inhibition by blebbistatin results in a significantly reduced phagocytic capacity (Zihni et al., 2022).

Korobova et al., 2014 also found that myosin II provides the force for mitochondrial fission, a scission event that involves rupturing a membrane. Myosin VI could also be an option, as it interacts with phagosomes (Daniel et al., 2014), inhibition results in the actin-microtubule transition to be delayed in macrophages (Yu et al., 2023), and it was recently claimed to execute RPE trogocytosis alongside optineurin (Tan et al., 2023). Based on the evidence in the literature, it is clear that Myo6 is involved in RPE phagocytosis in some capacity, but the data presented in Tan et al., 2023 are not clear enough to definitively show that Myo6 is indeed the scission motor. There are only two experiments in that manuscript that directly probed Myo6. The first was a single immunofluorescence image that showed very light dots of Myo6 antibody signal, in fixed cells, lightly present along a phagosome that is, presumably, already internalized. In this image, Phalloidin signal is shown very dimly, and only in a single z-slice: there is no clear evidence that this is an active trogocytic cup. The second experiment involved treatment with TIP, a Myosin 6 inhibitor, that showed reduced rhodopsin by western blot. While this is stronger evidence, a reduction in rhodopsin content could be a result of reduced overall ingestion independent of trogocytosis, or increased trogosome degradation. As shown in our phagocytosis assay (Fig. 1-5A), there was an increase in total trogosome number due to scission events, a strong piece of validating evidence that would not appear in a western blot, because the overall rhodopsin content is not changing, just splitting into more trogosomes. Optineurin clearly plays some role in scission based on their data, but as a receptor with over 8 reported targets in a range of tissue (Ying and Yue, 2012), there are many roles that Optineurin could be playing independent of Myosin 6 that lead to scission. Finally, Myosin 6 is a reverse motor

(Wells et al., 1999; Sweeney and Houdusse, 2010), meaning that it travels towards the minus end of actin filaments. How can a motor that moves away from the outer segment engage in trogocytosis? Perhaps, because Arp2/3 is at the rim and associates with the minus end of actin filaments, Myo6 moves towards the rim of the cup, towards the Arp2/3 structures on the minus end, to produce force on the outer segment. However, while possible, this seems less practical when compared to simply using a forward motor as there would need to be some strategy for the actin structure to push past the Arp2/3 branched actin structures present without disrupting them. In general, without knowledge of the actin filament orientation within the cup, it is difficult to make claims about this motor. Generally, it seems more likely that Myo6 interacts with phosphoinositide 3-kinase (PI3K) to alter lipid and protein content at the membrane of the cup to facilitate entry of the phagosome; this has been shown in the context of Myo6 facilitating pathogen entry of Salmonella (Brooks et al., 2017; Nambiar and Manjithaya, 2024). While Myo6 is clearly present in RPE and interacts with the trogosome in some manner, it requires more direct temporal evidence to definitively attribute its activity to scission events. A final potential option for the scission motor is Myosin 1e, as it localizes to the leading edge of the phagocytic cup in macrophages (Vorselen et al., 2021), was found to coordinate actin assembly and cargo trafficking during endocytosis (Cheng et al., 2012), has been implicated in membrane-cytoskeletal crosstalk during ingestion (Barger et al., 2019), and has been found to interact with dynamin, a ‘scission’ protein for endocytosis (Krendel et al., 2007; while dynamin likely isn’t playing a role in OS ingestion, the fact that Myo1e seems to engage in scission in some contexts of endocytosis is interesting). Importantly, Vorselen et al., 2021 also found that Myo1e acts to constrict the membrane, a required force for OS scission, alongside actin ‘teeth’ made up of Arp2/3 branched actin. The fact that we also see Arp2/3 present at the rim in our own data (Fig. 1-7C), precisely where Myosin 1e could act alongside Arp2/3 to engage in scission, seems too consistent to simply be a coincidence.

During the scission process, membrane curvature proteins such as Amphiphysin, FBP-17 (Umapathy et al., 2023), and other BAR proteins also interact with the membrane of the cup to induce curvature and stabilize rounded edges. How these proteins facilitate curvature in this context, as well as which other curvature proteins are involved, is still unknown. Once a trogosome is excised, Myosin 7a associates with the new trogosome and traffics it down the cup and into the cell, likely handing it off to KLC1 (Jiang et al., 2015) for further intracellular trafficking. Trafficking kinetics and dynamics change as phagosomes pass through the cortical actin and associate with microtubules (Yu et al., 2023); this transition is likely why the delayed degradation phenotype occurs in shaker1 cells (Gibbs et al., 2003). Myosin 7a is responsible for bringing the phagosome past the cortical actin and onto microtubules, but without that ability the OS material gets stuck in the cortical actin, resulting in changes to how it can be degraded. As the phagosome travels down, Rab5 endosomes move apically up the cup and immediately begin the degradation process (Fig. 1-9O). This is likely why shaker1 cells are still able to degrade phagosomes at all, as Rab5 endosomes can begin the degradative process even when OS material is still very apical (Fig. 1-11E). It is, however, much less efficient than trafficking them throughout the cell, so the process is delayed. Once the phagosomes have been ingested, the cell sends signals to trigger the breakdown of the cup. Actin disassembly proteins, such as cofilin (Ostrowska and

Moraczewska, 2017), are presumably recruited to break down the branched actin and the filaments that make up the structure of the cup. While cofilin is the most common and conserved mechanism of actin disassembly, many other proteins may take on this role in RPE such as GMF or coronin alongside a range of depolymerization supporting proteins (Kueh et al., 2008; Goode et al., 2023).The phagocytic cup then folds into the membrane, and the actin is redistributed as the phagosomes undergo degradation. The actin dynamics required to engage in this complex series of steps requires high levels of temporal accuracy and regulation of protein localization; in simple terms, there are a lot of moving parts and many unidentified proteins. Understanding how different actin-interacting proteins regulate and facilitate ingestion in RPE could provide insights into fundamental actin biology, and lead to discoveries that could be relevant for eye disease.

Why do actin-interacting proteins traffic to a precup with no actin?

One surprising phenotype we found was that the Arp2/3 complex (Fig. 1-9C) was still present at SMIFH2-treated precups. While we then found that there was simply a membrane tightly surrounding the precup (Fig. 1-9G), that the Arp2/3 complex is present within, why would the membrane form without an actin structure? Why would the Arp2/3 complex, a protein complex requiring actin filaments to perform its function, appear present in a region completely devoid of actin? There are 2 main pieces to this puzzle: 1) how does the OS get engulfed, and 2) why do these proteins go to the cup? To the first question, phagocytosis computational modeling has found that actin-driven force generation is not absolutely required for particle engulfment (Tollis et al., 2010), and so even without actin it is not impossible for the OS to become internalized by membrane. However, it is important to note that the OS simply gets stuck in that location because, without actin, it cannot undergo trogocytic events and the size of the enclosed OS is simply too large to be passed through the cortical actin without scission (1.73 ± 0.11μm diameter in WT [N = 40 across 2 experiments], compared to 2.21 ± 0.15μm in SMIFH2 treated cells [N = 38 across 2 experiments], Fig. 1-9I). Even if membrane internalization is possible, full ingestion and degradation is not (Fig. 1-5A). In addition, we experimentally observed many very small particles (<0.1μm^2 in area) present within cells during a phagocytosis assay (Fig. 1-5A). These particles were much smaller than phagosomes and were likely small OS fragments that broke off during the freeze-thaw cycle, that became internalized through this alternative mechanism. While this does lower the quality of the result in the phagocytosis assay, as it is not necessarily a true measure of trogocytosis[21], it is consistent with the idea that OS material can be internalized even without actin structures. It is interesting that Arp2/3 is unable to nucleate or recruit actin on its own, and this is likely due to the fact that the Arp2/3 complex requires preexisting "mother" filaments in some systems to create branched actin structures (Mullins et al., 1998; Svitkina, 2018a, 2018b); mDia1, which localizes to the tips of the branched actin structures during RPE phagocytosis, is likely producing this initial "mother" filament for the Arp2/3 complex to act on.

---

[21] For the phagocytosis assays, the area threshold in X-Y for phagosomes was 0.1-3μm^2. We hope that this compensates for these small particles, as well as large OS clumps on the surface of the cells, but this is still an important variable to keep in mind.

To the second question, why these proteins even go to the cup, there is likely some signaling mechanism that triggers actin-related proteins to traffic to the site of the OS, that is independent of actin recruitment. To rephrase, the same signal may call for mDia1 and actin recruitment as well as the recruitment of Arp2/3, Myosin 7a, and a host of other proteins, regardless of which of these actually make it to the cup. All these proteins will be trafficked to their appropriate location for ingestion regardless of the state of the cell. These proteins will act on any actin structures nearby, but without mDia1/actin recruitment they are trafficked appropriately but do not have any actin to work with and so they simply sit, inactive, at the precup. These proteins are likely primed to begin actin modulatory activity, should any actin filaments arrive at the precup region. Looking through the literature, most manuscripts show the Arp2/3 complex specifically localizing along actin intensities (Fattouh et al., 2015; Dhanda et al., 2018), however, some manuscripts do show it present in regions devoid of actin (See Fig. 1-4G in Aggarwal et al., 2012; see Fig. 1-1C in Wang et al., 2014). While not common, it is possible for this actin nucleator to localize where there is no actin. Alternatively, due to the sheer quantity of actin present at the base of the cup, it seems possible that there still is actin present in the Arp2/3 signal regions away from the phalloidin signal, but that the actin is drowned out by the signal intensity more basally within the cup. There may still be actin present, even if it is not visible/dim. Presumably, the Arp2/3 complex will remain in the cup region until the signaling mechanism that triggers cup closure signals them to pull away and be redistributed throughout the cell.

To further explain the presence of these proteins at the precup, actin protrusion and mobilization is such a canonical trait of phagocytosis (Jaumouillé and Waterman,

2020) that there is no reason to prevent the actin associated proteins from trafficking to the precup, as a lack of actin recruitment would only happen in mutation or experimental manipulation (such as during SMIFH2 treatment). In a vast majority of cases in nature, a precup is impossible, and so there is no evolutionary need to prevent these proteins from trafficking to the cup and wasting that metabolic energy. However, this scenario describes that the membrane is fully capable of surrounding OS material without actin. Without actin, how is force generated on the membrane such that it can protrude past the circumferential actin and create the precup? This also raises an interesting temporal question about when the actin and membrane begin producing apical structures. Does the membrane first reach apically up the OS independently (as we show that it can during SMIFH2 treatment [Fig. 1-9G]) before actin reaches the region, or does actin elongation push the membrane to form the cup structure? While the latter is more likely based on canonical traits of phagocytosis, it seems that the former is entirely possible.

What does the *in vivo* cup look like?

Ideally, imaging RPE phagocytosis *in vivo* would be the optimal strategy for studying this problem, as the unique interface of rod outer segments and RPE is practically impossible to replicate otherwise. However, there are a number of limitations that prevent *in vivo* live imaging. First, the apical portion of the cell must be imaged through either the basal RPE side or the apical retina side. Imaging through the RPE of an eyecup is simply impossible, as the laser needs to penetrate past the choroid and remaining sclera, a very thick region filled with pigment. Imaging through the retina is, while possible, practically very difficult, as the retina is quite thick, and obtaining good signal without the interference of light scattering through the retina requires a powerful microscope (one option could be a two-photon microscope, which has been previously used to study photoreceptor-RPE interaction [Maeda et al., 2014]). This strategy also requires a method to stabilize the location of both RPE and retina in culture (keeping in mind that these structures have nothing to adhere to while in culture), as movement of even 20μm is enough to push a given cup out of the field of view. In addition, both the RPE and the photoreceptors must be fluorescent to image, and so this is only even possible in a mouse model with both fluorescent RPE and fluorescent Rhodopsin. Simply establishing this methodology is a challenging prospect; this is why we decided to utilize culture models of RPE, and also why the field has been unable to visualize trogocytosis until now.

While live imaging of culture models has provided valuable insights into the structure of the *in vivo* cup, and has greatly improved our ability to understand the 3D spatiotemporal organization of the phagocytic process, we are only able to infer the *in vivo* cup structure while keeping in mind the limitations of our culture models. For example, in the eye, rod density peaks at about 216 rods/RPE cell in mice (Volland et al., 2015; Keeling et al., 2020) and so space may not even be available for the apical cup to engage in significant motility, implying that while we can understand biochemical mechanisms and protein involvement during phagocytosis *in vitro* it is difficult to tell how much the actin structures in our culture models visually resemble those in the eye. In addition, there is also variation in the appearance and structure of RPE apical processes (Burnside and Laties, 1976; Almedawar et al., 2020), where they could appear more ‘finger-like’ (McLaughlin et al., 1983) or more ‘leaf-like’ (Fisher and Steinberg, 1982) in part due to geographic variation but also due to whether they interact with rods or cones. On a related note, it is not clear whether the microvilli fuse together to form sheets (Almedawar et al., 2020) or whether the phagocytic cup is a true independent entity that arises between the microvilli. If the microvilli fuse then it follows that any differences in microvilli structure could heavily modify the phagocytic cups' appearance. Based on this, it's entirely possible that the phagocytic cup changes in structure based on geographic region within the eye.

Following up on the idea that RPE may ingest rods and cones differently, there was an interesting discrepancy within our results: the actin cup can be quite tall, averaging 5.65 ± 0.16μm (Mean ± SEM [N = 66 cups across 3 experiments], Fig. 1-2H) in height. The length of a rod OS in mice is approximately 24μm (Battelle and LaVail, 1978; Carter-Dawson and Lavail, 1979; Fu and Yau, 2007), and so if 5.65μm of outer segment material is ingested during each ingestion event, that would mean that every time phagocytosis occurs, 23.54% of the rod OS is ingested. This seems far too high, especially knowing that only ~10% of the OS is ingested each day (Besharse and Hollyfield, 1979; Paniagua et al., 2023). In addition, the rod OS is constantly closely associated with the RPE apical processes, and so it should not need to grow much to trogocytose a piece. An answer may lie in cones: cone cells sit much further from the RPE, and the RPE extends a much larger apical cup to reach the cone OS. This has been seen by EM (see 'cone sheaths' in Fig. 1A of Fisher and Steinberg, 1982). Based on this reasoning, there is likely some 'stop growing' signal that the RPE receives upon interacting with the OS. This signal is triggered almost immediately with rods *in vivo*, but takes apical expansion and association with a cone OS for it to happen with cones *in vivo*. *In vitro*, we are likely missing this signal, and so the cup simply grows until either it loses structural stability or it engages in enough of the ingestion process to still trigger this cup-closure response (assuming the ‘stop growing’ signal is related to phagosome degradation/association). Based on the literature and our *in vitro* results, it seems likely that phosphatidylserine acts as the ‘stop growing’ signal (and possibly as a trigger to initiate ingestion), determining the height of the cup, but not determining the size of the bite taken (Fig. 1-3A-D, [Umapathy et al., 2023]). It seems likely that all RPE is capable of ingesting outer segments from either rods or cones, and *in vitro* these cells have no way to regulate the size of the cup because they are presumably missing this ‘stop growing’ signal (or, at the very least, are not associating with it at the correct time). Due to this, they simply grow cups as tall as they can, until they receive the ‘stop growing’ signal from whatever OS material they begin to ingest. Whatever it may be, the ‘stop growing’ signal is clearly important and severely understudied.

So, if phosphatidylserine does not define the size of the phagosome, then what does? This is a difficult topic for experimental study as there is inherent variability in the size and shape of fed POSs *in vitro*, as, once introduced to 37C°, they tend to round up and clump together (Fig. 1-3E), a situation that is impossible *in vivo*. This makes feeding cylindrical rod-shaped outer segments, and performing live imaging where the rods remain completely vertical and do not lose their structure, practically difficult to achieve. While it is difficult to study this directly, trogocytosis is a heavily actin-based process and previous work indicates that trogosome size is directly related to actin polymerization (Fig. 1-4D, [Umapathy et al., 2023]). It seems likely that actin remodeling plays a significant role in deciding the size of the phagosome, but when and how does this decision get made? Do microvilli extend up along the rod and ‘choose’ a region to press their actin density into in order to break off pieces? Does the actin form one large tube of a constant size that funnels up the rod and simply breaks pieces off when it has reached the peak tube height? Or perhaps it is a mixture of RPE actin signals and photoreceptor ‘eat-me’ signals, where the localization of some molecule or protein corresponds to where the rod will be bitten off. These questions are still unclear, of which the answers will greatly clarify the true phagocytic cup structure.

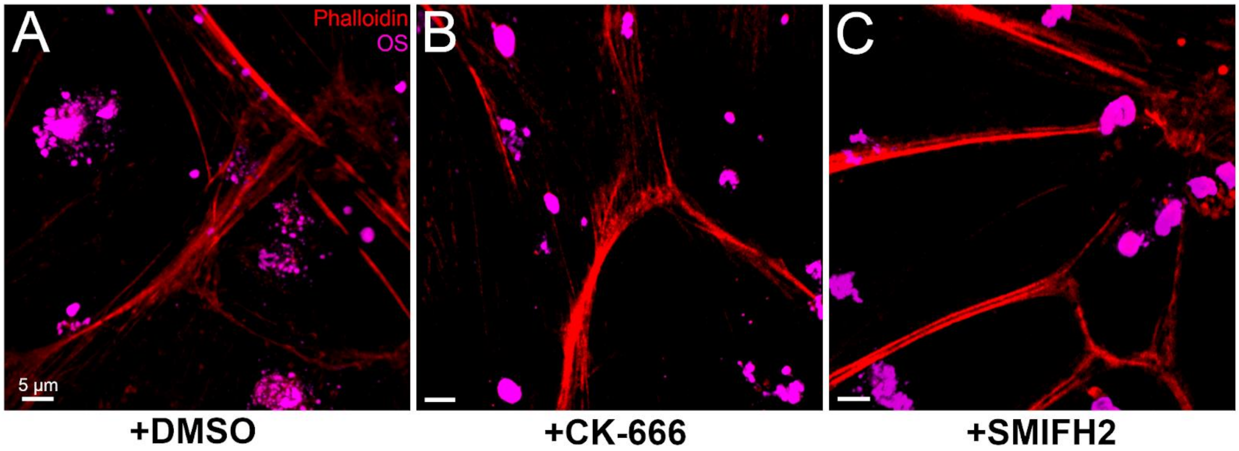

Figure Legend - Supplemental Figure 1-1: CK-666 and SMIFH2 treatment do not observationally change the actin structures of mouse primary RPE. **A.** A field of view of mouse primary RPE, *en face*, immunostained for Phalloidin and OS. **B.** A field of view of mouse primary RPE, *en face*, immunostained for Phalloidin and OS, after a 2hr. treatment (1hr. pre-feeding of OS, and 1hr. post-feeding of OS) of CK-666. **C.** A field of view of mouse primary RPE, *en face*, immunostained for Phalloidin and OS, after a 2hr. treatment (1hr. pre-feeding of OS, and 1hr. post-feeding of OS) of SMIFH2.

Scale Bars: A-C: 5μm

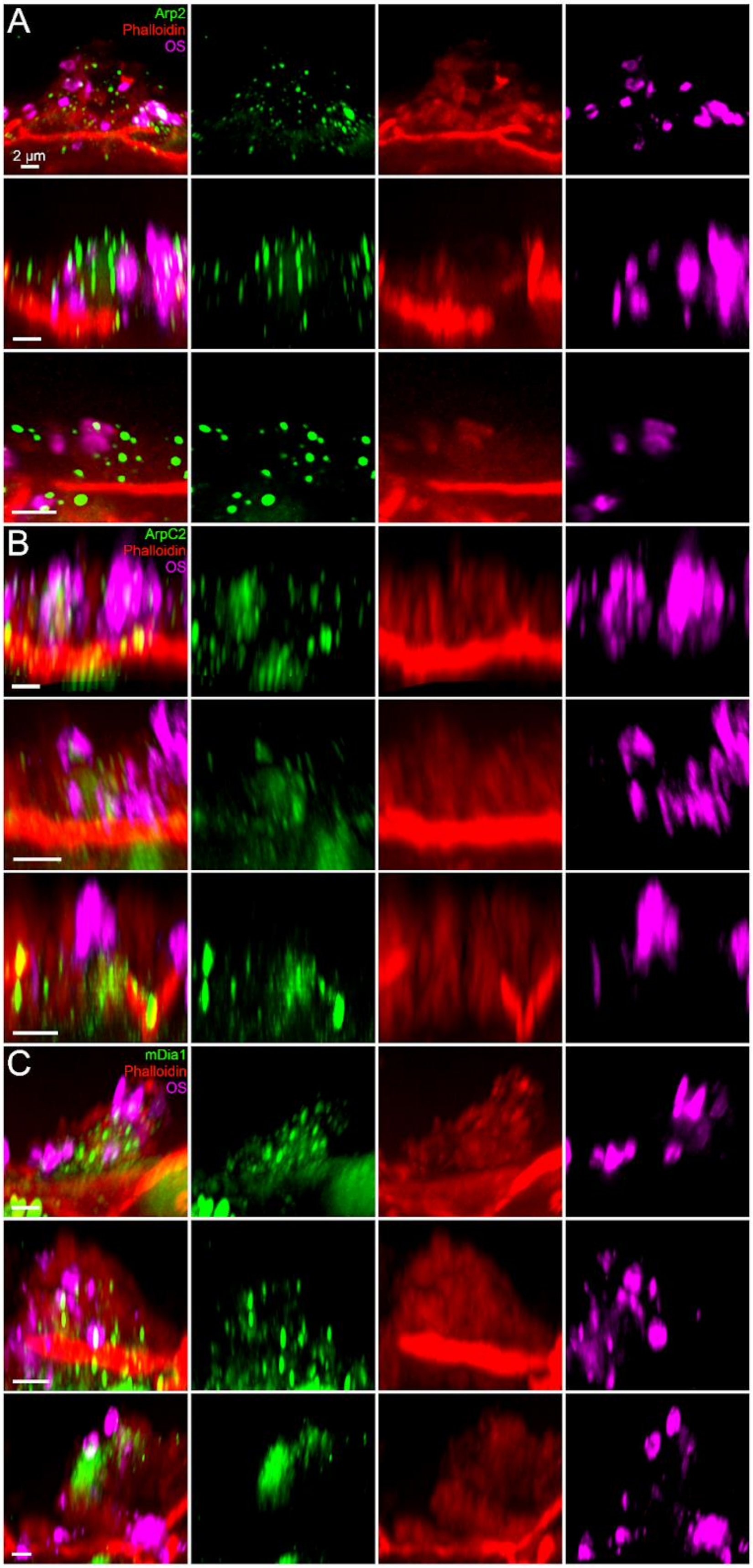
A
Arp2
Phalloidin
OS
2 µm
B
ArpC2
Phalloidin
OS
C
mDia1
Phalloidin
OS

Figure Legend - Supplemental Figure 1-2: Further data from biological replicates of experiments presented in Figure 1-5. **A.** Three phagocytic cups from eyecups with neural retina removed, immunostained for Arp2 and Phalloidin (with prestained OS), from 2 different biological replicates as those shown in Fig. 1-5. **B.** Three phagocytic cups from eyecups with neural retina removed, immunostained for ArpC2 and Phalloidin (with prestained OS), from 2 different biological replicates as those shown in Fig. 1-5. **C.** Three phagocytic cups from eyecups with neural retina removed, immunostained for mDia1 and Phalloidin (with prestained OS), from 2 different biological replicates as those shown in Fig. 1-5.

Scale Bars: A-C: 2μm

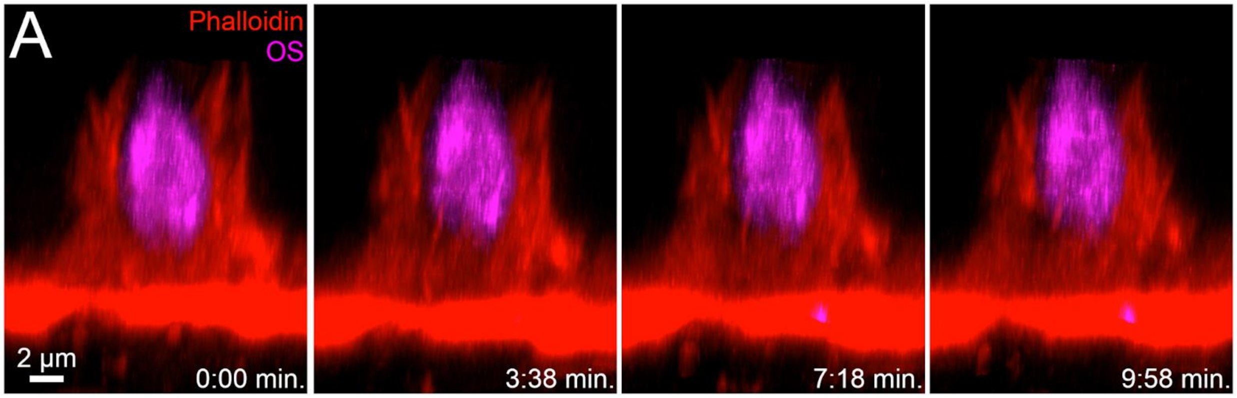

Figure Legend - Supplemental Figure 1-3: Further data from a biological replicate of experiments presented in Figure 1-6. **A.** A movie from a primary RPE cell, pretreated with CK-666 (and maintained in the media), from an additional biological replicate as those shown in Fig. 1-6A/B.

Scale Bars: A: 2μm

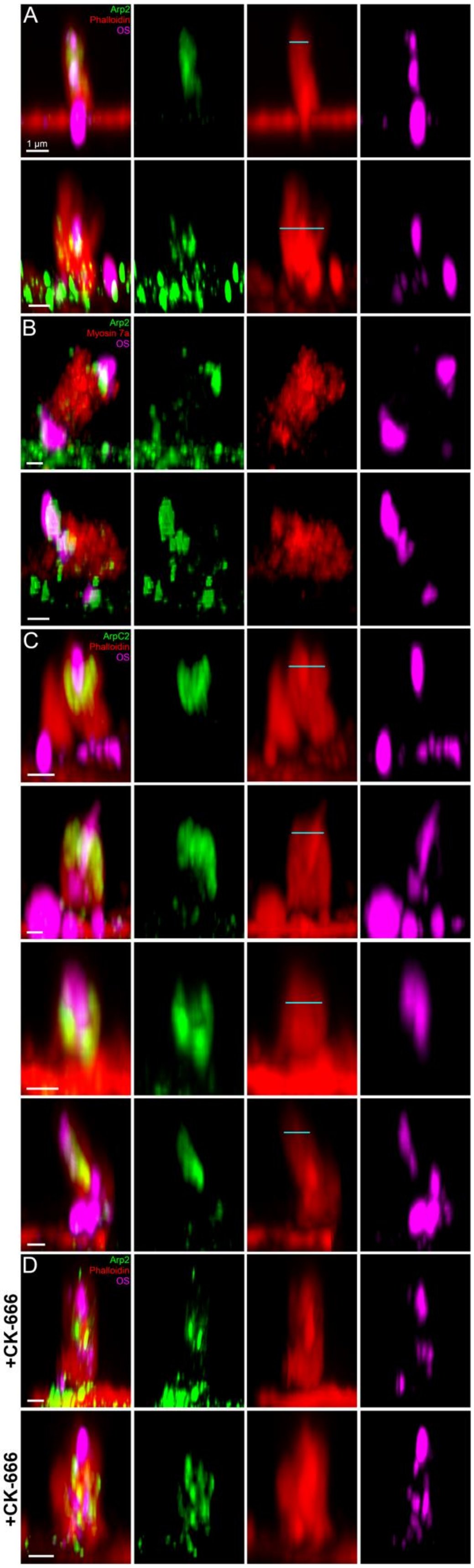
A
Arp2
Phalloidin
OS
1 µm
B
Arp2
Myosin 7a
OS
C
ArpC2
Phalloidin
OS
D
Arp2
Phalloidin
OS
+CK-666
+CK-666

Figure Legend - Supplemental Figure 1-4: Further data from biological replicates of the experiments presented in Figure 1-7. **A.** Phagocytic cups from primary RPE immunostained for Arp2, with Phalloidin, and prestained OS. Each image is from a different biological replicate. The cyan lines denote examples of the width measured for the rim of the cup, as quantified in Fig. 1-7G. **B.** Phagocytic cups from primary RPE immunostained for Arp2 and Myosin 7a, with prestained OS. Each image is from a different biological replicate. **C.** Phagocytic cups from primary RPE immunostained for ArpC2, with Phalloidin, and prestained OS. The first two images are from a different biological replicate as the second two images. The cyan lines denote examples of the width measured for the rim of the cup, as quantified in Fig. 1-7G. **D.** Phagocytic cups from primary RPE pretreated with CK-666 (and maintained in the media), immunostained for Arp2, with Phalloidin, and prestained OS. Each image is from a different biological replicate.

Scale Bars: A-D: 1μm

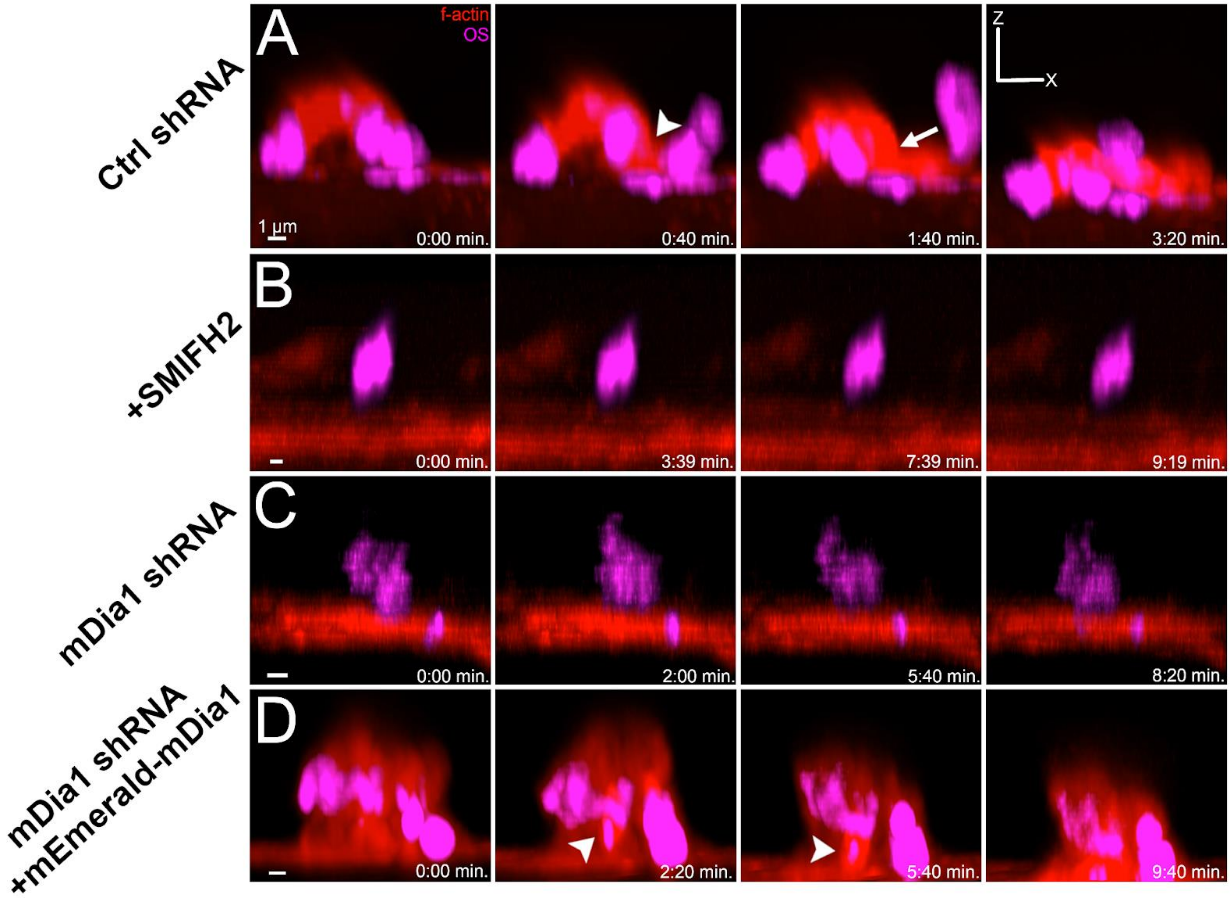

Figure Legend - Supplemental Figure 1-5: Further data from biological replicates of experiments presented in Figure 1-8. **A.** An example movie of a phagocytic cup in a Control shRNA transfected cell; this cup exhibited normal trogocytosis. The white arrowhead points out an actin density that trogocytosed the OS between the first and second presented frame. The arrow indicates the movement down the cup that the new trogosome travels between the last 2 time points presented. **B.** A movie of a OS on the apical surface of the RPE, during SMIFH2 treatment. Note the lack of an actin cup, and the lack of any motion over the course of the movie. **C.** A movie of an OS on the apical surface of the RPE of a cell transfected with a mDia1 shRNA. Note the lack of an actin cup and minimal motion over the course of the movie. **D.** A movie of a phagocytic cup on a cell transfected with plasmids for both mouse mDia1 shRNA and human mEmerald-mDia1, rescuing the ‘no cup’ phenotype. The white arrowheads point out actin densities that worked to trogocytose the larger OS piece and shuttle trogosomes basally into the cell.

Scale Bars: A-D: 1μm

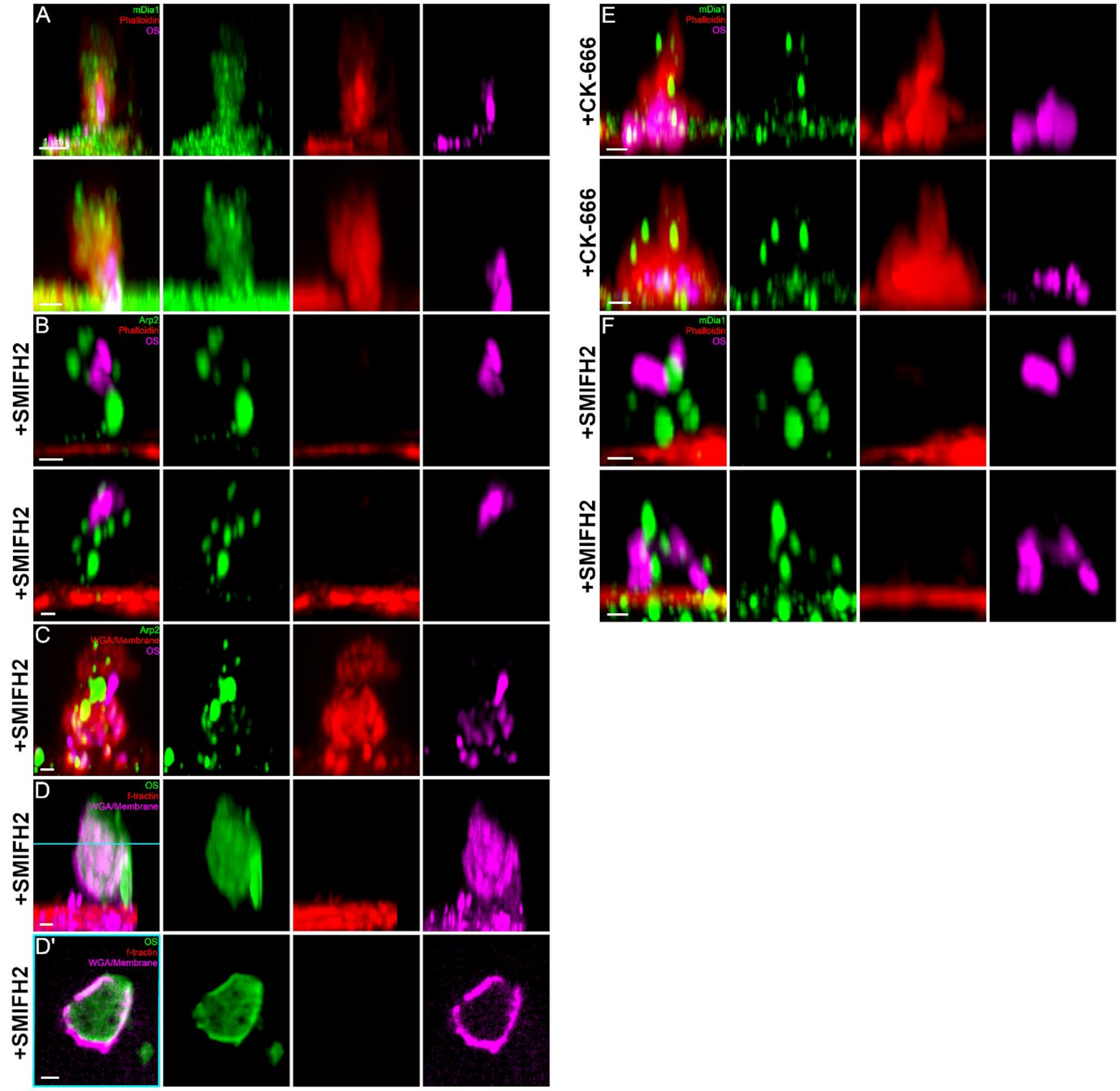

Figure Legend - Supplemental Figure 1-6: Further data from biological replicates of experiments presented in Figure 1-9. **A.** Phagocytic cups from primary RPE immunostained for mDia1, with Phalloidin, and prestained OS. Each image is from a different biological replicate. **B.** Phagocytic cups from primary RPE pretreated with SMIFH2 (and maintained in the media) immunostained for Arp2, with prestained OS. Each image is from a different biological replicate. **C.** A SMIFH2-treated precup from primary RPE immunostained for Arp2, with the membrane prestained with WGA, and with prestained OS. **D/D’.** Another precup as in C., but collected during live cell imaging in primary RPE transfected with RFP-Tractin and fed prestained OS. WGA was added to the media before feeding to stain the membrane. D’ is a cross section through the cyan line in D, showing the encapsulation of the partially surrounded OS by membrane. These are from different biological replicates as in Fig. 1-9. **E.** Phagocytic cups from primary RPE prestained with CK-666 (and maintained in the media), immunostained for mDia1, with Phalloidin, and prestained OS. Each image is from a different biological replicate. **F.** Precups from primary RPE prestained with SMIFH2 (and maintained in the media), immunostained for mDia1, with Phalloidin, and prestained OS. Each image is from a different biological replicate.

Scale Bars: A-F: 1µm

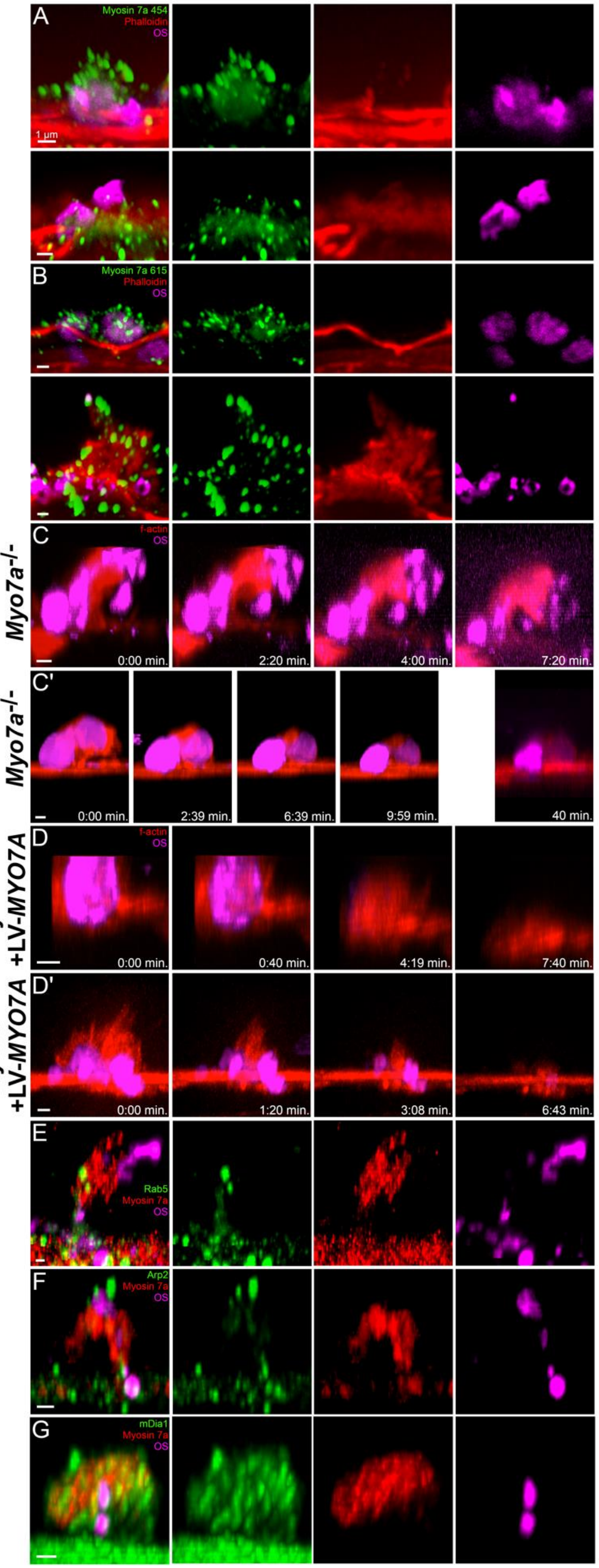
A
Myosin 7a 454
Phalloidin
OS
1 µm
B
Myosin 7a 615
Phalloidin
OS
C
f-actin
OS
$Myo7a^{-/-}$
0:00 min.
2:20 min.
4:00 min.
7:20 min.
C'
$Myo7a^{-/-}$
0:00 min.
2:39 min.
6:39 min.
9:59 min.
40 min.
D
f-actin
OS
$Myo7a^{-/-}$ +LV-MYO7A
0:00 min.
0:40 min.
4:19 min.
7:40 min.
D'
$Myo7a^{-/-}$ +LV-MYO7A
0:00 min.
1:20 min.
3:08 min.
6:43 min.
E
Rab5
Myosin 7a
OS
F
Arp2
Myosin 7a
OS
G
mDia1
Myosin 7a
OS

Figure Legend - Supplemental Figure 1-7: Further data from biological replicates of experiments presented in Figure 1-10. **A.** Two examples of phagocytic cups from mouse eyecups with neural retina removed, immunostained for Myosin 7a with the 454 antibody, from two different biological replicates than the images in Fig. 1-10A (left). **B.** Two examples of phagocytic cups from mouse eyecups with neural retina removed, immunostained for Myosin 7a with the 615 antibody, from two different biological replicates than the images in Fig. 1-10A (right). **C-C'**. Two examples of movies from live cell imaging in shaker cells from two biological replicates of the movie in Fig. 1-10C. In C', note that the cup was reimaged after 40 minutes; the image shown in Fig. 1-10C' depicts the 30 minute mark of this movie. **D-D'.** Two more examples of the Myosin 7a rescue experiment, from two biological replicates of the movie in Fig. 1-10E. The phagocytic cup trogocytoses an outer segment, and closes the cup within 6-8 minutes of initiating the movie. **E-G.** Three examples of Myosin 7a staining from three different experiments similar to Fig. 1-10H/H'. E shows Rab5 in green, F shows Arp2 in green, and G shows mDia1 in green, while all show Myosin 7a in red.

Scale Bars: A-G: 1μm

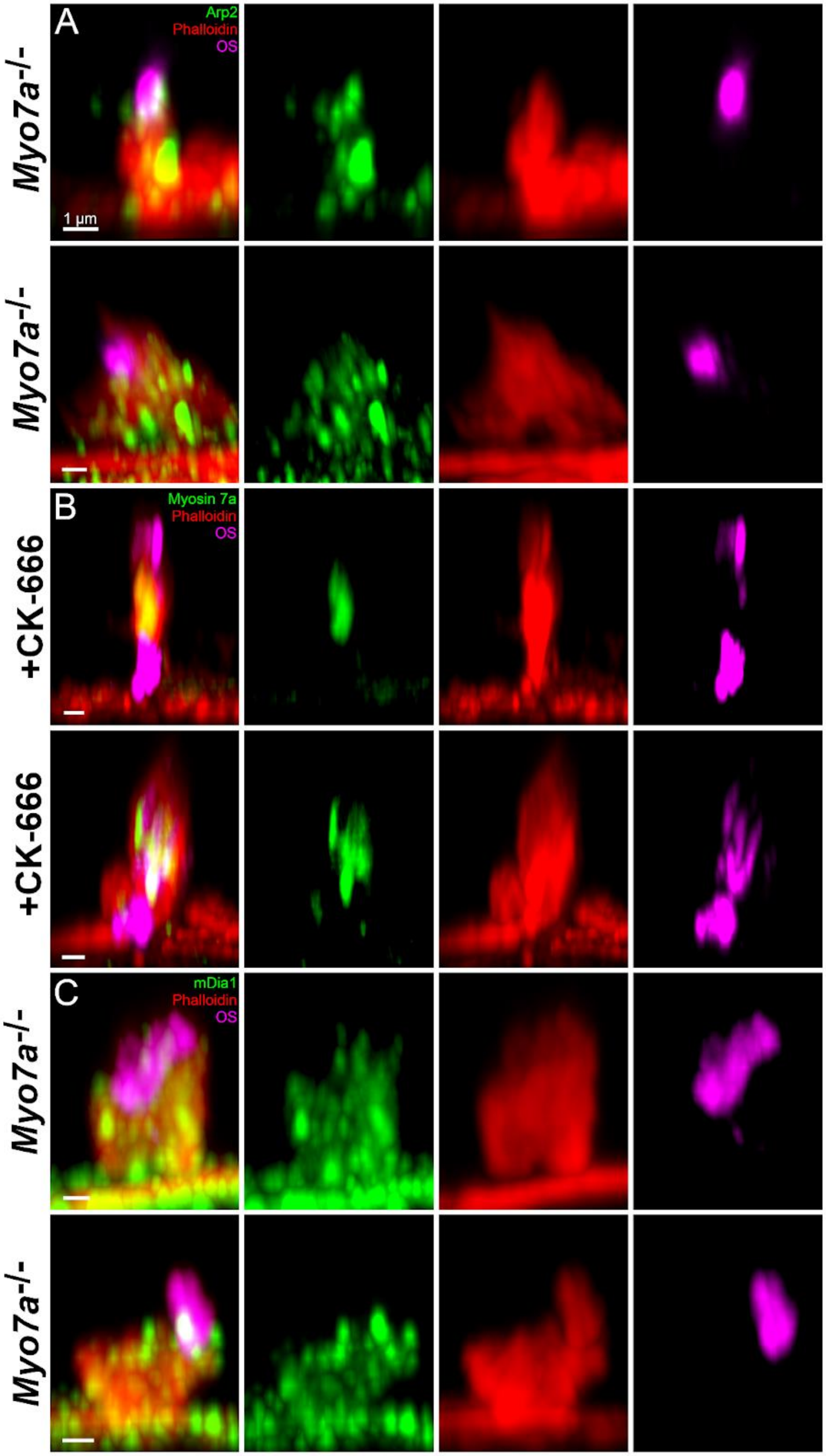
A
Arp2
Phalloidin
OS
$Myo7a^{-/-}$
1 µm
$Myo7a^{-/-}$
B
Myosin 7a
Phalloidin
OS
+CK-666
+CK-666
C
mDia1
Phalloidin
OS
$Myo7a^{-/-}$
$Myo7a^{-/-}$

Figure Legend - Supplemental Figure 1-8: Further data from biological replicates of experiments presented in Figure 1-11. **A.** Phagocytic cups from shaker1 primary RPE immunostained for Arp2, with Phalloidin, and prestained OS. Each image is from a different biological replicate. **B.** Phagocytic cups from primary RPE pretreated with CK-666 (and maintained in the media) immunostained for Myosin 7a, with prestained OS. Each image is from a different biological replicate. **C.** Phagocytic cups from shaker1 primary RPE immunostained for mDia1, with prestained OS. Each image is from a different biological replicate.

Scale Bars: A-C: 1μm

Chapter 2: What happens to the rod synapse during a 7 day retinal detachment (when POS ingestion stops)?

PREFACE

Trogocytosis of photoreceptor outer segments is a fundamentally important process for vision. When this process halts, there are many consequences to the photoreceptor, however, it is unknown what consequences the rod synapse faces during this period of stress. Rhegmatogenous retinal detachment is caused by a tear in the retina, resulting in fluid to accumulate in the subretinal space, separating the retina from the back of the eye. There are many degenerative outcomes to this such as physical damage to the rod plasma membrane, recruitment of immune cells, and, importantly, separation of rod photoreceptors from the RPE. To explore the ultrastructural changes that occur at the synapse, we performed electron microscope (EM) tomography of rod photoreceptor synapses (or rod spherules) in both normal cats and in cats that have undergone a 7-day retinal detachment. This work was fruitful, and resulted in the manuscript Torten et al., 2023; this manuscript is present in its entirety as Chapter 2 of this dissertation. In this preface, I will describe the path that led to this publication, and the contributions that each author made.

The tissue used in this study was initially collected for a previous study of retinal detachment: Erickson et al., 1983. This early study was the first to investigate the cellular effects of different lengths of retinal detachment, and provided fundamental knowledge about the consequences that the retina faces after a detachment. At this point, all the electron microscope data on the rod spherule that had been collected was in serial EM sections, and new technology, specifically EM Tomography, allowed for analyzing rod spherule ultrastructure at a level of resolution previously not possible. Utilizing this new technology, Kenneth Linberg and Dr. Steven Fisher collected many of the tomograms presented in the study, under the technical tomography assistance of Dr. Guy Perkins, and with resources contributed by Dr. Mark Ellisman at the University of California San Diego (UCSD). Dr. Steven Fisher created segmentations from many of the presented tomograms, with the remaining produced by Ken Linberg and Gabriel Luna. At this point, working with Mr. Linberg, Mr. Luna, Dr. Ellisman, and Dr. Perkins, Dr. Steven Fisher had collected many normal and 7-day detached tomograms of photoreceptor synapses, but, in order to produce a publication, lacked a number of tomograms from normal synapses, and required extra hands to write the manuscript. At this point, I had just started my Ph.D. at UCLA, and joined the project that had been in progress for nearly 50 years. I collected additional required control tomograms, which resulted in some fundamental points made in the manuscript regarding the tetrad organization of the postsynaptic processes. I performed all of the quantitative analysis of the tomograms, and troubleshot methodology regarding serial EM tomography, a strategy that was required to collect valuable data using the equipment at the Stein Eye Institute at UCLA. At this point, Dr. Fisher and I worked collaboratively to qualitatively analyze the data and create figures. Dr. Steven Fisher, Dr. David Williams, and I wrote the manuscript collaboratively. In terms of training, Dr. Antonio Paniagua taught me to section EM blocks, use the electron microscope, and perform EM tomography.

INTRODUCTION

Rod photoreceptor cells are highly sensitive light receptors that operate in dim light (i.e., scotopic vision). The synaptic terminal [rod spherule (RS)] of these cells is one of the most complex synapses in the mammalian CNS. It is uniquely structured to couple the high sensitivity of the rod cell with high temporal resolution of changes in the lighting environment (Rodieck, 1998). Rapid modulation of neurotransmitter release and rapid responses by its postsynaptic cells result from the presence of a presynaptic ribbon, molecular machinery that rapidly and precisely conveys synaptic vesicles to a presynaptic release site (Matthews and Sterling, 2008; LoGiudice and Matthews, 2009; Zampighi et al., 2011), and the presence of a synaptic invagination that encloses the postsynaptic processes within a tight, sequestered environment. The latter assures the ability of the cell to rapidly regulate glutamate concentration in the extracellular space (Sterling et al., 1987; Rao-Mirotznik et al., 1995; Rodieck, 1998).

The ultrastructure of rod synapses has been the focus of dozens of studies since the first by Sjöstrand, 1958. The first comprehensive description was by Missotten (1965), where he described two or three type 1 and 2 postsynaptic processes within the synaptic invagination (Fig. 2-1). These are now known to be rod bipolar (RB; Fig. 2-1, first type) dendrites and horizontal cell axon terminals (HCATs; Fig. 2-1, second type). The former transmits signals through the visual pathway ultimately to the ganglion cells, whose axons make up the optic nerve, whereas the latter integrates signals laterally across photoreceptors (Zampighi et al., 2011).

Although there is general agreement about RS structure, controversies remain about important details, such as the number and organization of the postsynaptic processes as well as the synaptic ribbon and arciform density. Accurate definitions of these features have implications for the flow of visual information through retinal pathways (Rodieck, 1998). The lack of agreement has arisen largely because of limitations for describing the 3-D ultrastructure of such a complex structure. Even serial section EM reconstruction (Missotten, 1965; Grünert and Martin, 1991; Rao-Mirotznik et al., 1995; Migdale et al., 2003) lacks sufficient *z*-axis resolution (~80–90 nm in past studies) to accurately define RS 3-D structure.

We used the high-resolution imaging capabilities of EM tomography to study the 3-D ultrastructure of the RS and changes it undergoes after retinal detachment. This approach allowed us to create high-resolution 3-D models (Kremer et al., 1996; Burette et al., 2012; Phan et al., 2017). It also reduces the number of sections required to reconstruct the synaptic invagination and improves *z*-resolution to ∼2–3 nm, thus revealing structural details with greater accuracy and precision.

Rhegmatogenous retinal detachment, in which there is a tear across the retina, is a relatively common cause of vision loss; it can occur by mechanical damage to the retina, in response to some inherited retinal diseases (Nash et al., 2021; Collin et al., 2022; Martin-Gutierrez et al., 2022), and in cultured retinal explants (Kung et al., 2017). Although retinal reattachment surgery can reverse outer segment degeneration, significant visual deficits often remain (Sørensen et al., 2020). Previous EM studies have shown dramatic remodeling of the RS in response to detachment (Erickson et al., 1983; Linberg et al., 2009) including changes in its shape, retraction from the outer plexiform layer (OPL) (Townes-Anderson et al., 2021), and retraction of RB dendrites from the synaptic invagination (Linberg et al., 2006a). However, details requiring higher resolution are not understood; for example, although the HCAT endings tend to remain within the invagination, little is known about changes they may undergo. Because of the precise regulation of glutamate release within the RS, it is likely that even modest structural remodeling of its invagination would have significant effects on neurotransmission to its postsynaptic neurons (Sørensen et al., 2020). Here, we describe changes in the RS and their postsynaptic processes after the first week of cellular remodeling induced by detachment.

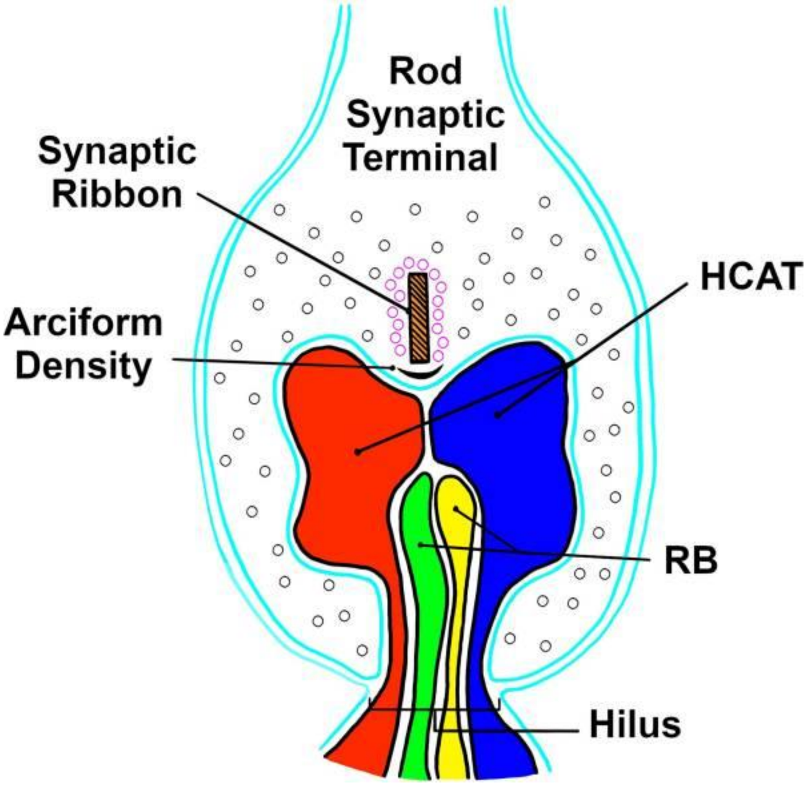

Figure Legend - Figure 2-1: Diagram of the rod spherule, showing the organization originally illustrated by Missotten (1965). In Missotten's description the synaptic ribbon was referred to as a “lamella”, the RBs as the “first type terminal buds”, and the HCATs as the “second type terminal buds”.

MATERIALS AND METHODS

All tissue used in this study was generated from female domestic cats, *Felis catus*, in a previous conventional EM study (Erickson et al., 1983), which describes the tissue preparation in detail. Briefly, following intracardiac perfusion with 1% glutaraldehyde and 1% formaldehyde in phosphate buffer, pH 7.1, eyes were enucleated, kept in the same aldehyde fixative overnight, postfixed for 1 h in 2% osmium tetroxide in phosphate buffer, dehydrated in an ethanol series, and embedded in Araldite. For the rhegmatogenous retinal detachment studies, the detachment surgery had been performed in one eye of each fully anesthetized animal 7 d before tissue fixation. As described in detail by the original study (Erickson et al., 1983), a small hole was made in the superior retina, through which 0.5% aqueous Healon (sodium hyaluronate) was injected into the subretinal space, thus creating a retinal detachment that radiated outward from the retinal hole toward the optic disk. Healon ensures that the retina stays detached for the duration of the experiment. Control retinas were prepared from animals that were not used in the detachment experiments. All animals had been maintained on a 12 h light/dark cycle and were killed midmorning.

Samples imaged at University of California, San Diego (UCSD) were sectioned at 400–500 nm, whereas samples imaged at University of California, Los Angeles (UCLA) were sectioned at 200 nm serially (four serial sections per tomogram); both were then counterstained with uranyl acetate followed by lead citrate. Colloidal gold particles (15 nm) were added to both sides of each section for fiducial alignment, and the sections were imaged on a custom JEOL JEM-4000EX IVEM using a specially constructed charge-coupled device camera with a pixel array of 1960 × 2560 (UCSD) or a JEOL

JEM-1400Plus (UCLA). The tilt series was acquired either manually (single-axis tomograms, −60°–60°, 1° increments; UCSD) or automatically through the program SerialEM (dual-axis tomograms, −65° to 65°, 1.5° increments; UCSD). The specimens were irradiated with electrons for ∼20 min to limit anisotropic specimen thinning during image collection before initiating a tilt series. During data collection, the illumination was held to near-parallel beam conditions, and the beam intensity was kept constant.

Tomograms were reconstructed, serial tomograms were joined, and 3-D models were generated using the software IMOD3D. Tomogram alignment and reconstruction were done in etomo, following the IMOD guide on the associated University of Colorado website (https://bio3d.colorado.edu/imod/doc/etomoTutorial.html). Briefly, image alignment was done using fiducial models based on added colloidal gold for both tilt axes. Dual-axis tomograms taken at UCLA were combined, and serial tomograms were stacked using etomo as well.

We used *z*-slice thickness to estimate *z*-axis resolution. The *z*-slice thickness was obtained from the total number of *z*-slices divided by the total depth of each tomogram. Within the presented tomograms, the number of *z*-slices ranged from 140 to 714, and the depth of the tomogram volume was either 800 nm (4 serial 200 nm tomograms at UCLA) or 400–500 nm (at UCSD), leading to a *z*-resolution of ∼2 nm (1.8 ± 0.1, mean ± SEM, $n = 14$). Segmentation of the tomograms was done by manually tracing contours for individual structural features using the IMOD drawing tools menu. In general, contours were traced on every three *z*-slices through the depth of the structure, although in some instances every *z*-slice was used. For scattered objects, the diameter was set in the object menu of IMOD. Each object was described as a closed or scattered (for vesicles) structure and assigned a specific color. Three-dimensional models were created using the mesh feature in IMOD, and in some cases the models were smoothed using the smoothsurf algorithm. Further image analysis was done in ImageJ for quantification of key structures.

During segmentation, HCATs were identified by the presence of intracellular vesicles of a larger size (~45 nm) than standard cytoplasmic synaptic vesicles. In control retinas, HCATs were also identified through their branching structure, and the extensive telodendria that extended from the main body of the process. RBs were identified by a lack of intracellular vesicles and membrane densification on the side of the RS membrane, apposed to the RB process. In detachment, these characteristics were maintained such that identification of these processes was straightforward in all but two cases; any processes lacking in both membrane densification and intracellular vesicles (see Fig. 2-9) were colored in cyan and are labeled with an asterisk in the figures. Previous conventional EM studies of this tissue by some of us (Linberg et al., 2009) indicated that the same criteria used to identify postsynaptic processes in the normal retina are valid in the detached retina.

Semithin sections of cat retinas were stained with Toluidine blue for 45 s before mounting with Permount (Thermo Fisher Scientific) and imaging with a Zeiss Axiophot microscope.

Statistical analyses

We performed quantification and analysis on 15 normal retina tomograms and 7 detached retina tomograms. Many tomograms contained two to three synapses, so in total, we analyzed 33 RSs (Table 2-1). In IMOD, the perimeter of the invaginating RS membrane was traced with the freehand selections tool, and values were measured within IMOD. In tomograms containing a hilus, the shape was closed with a straight line directly through the hilus. For quantification of area, perimeter, circularity, and solidity (see below for equations), the relative center of the invagination, in terms of *z*-depth, was selected to include most of the postsynaptic processes and branching complexity. These measurements were made using ImageJ software. To measure ribbon length, three points were taken, one at either end of the ribbon and one in the central point of the ribbon along its length. Lines were generated from each of the two end points to the center point, and the lengths of the two lines were summed. Although it is difficult to obtain a highly accurate measurement of length because of the variable 3-D structure of the ribbon, using two separate lines allows for reasonable quantification of straight, as well as heavily arced, ribbons. Synaptic vesicle density for each spherule (as well as the proportions of vesicle types in the detached condition for each spherule) was measured by counting the vesicles within a volume that included 20 consecutive *z*-slices, 200 × 200 nm in area, situated within 150 nm from the invagination in *X*-*Y*, and near the relative center of the invagination in *z*. To separate out vesicle types in the detached condition, vesicle diameters were binned from 20 to 35 nm (normal), 35.1 to 45 nm (medium), and >45 nm (large). Ribbon, HCAT, RB, and mitochondria quantities were counted across the entire *z*-stack. The coefficient of variability of intervesicular distance along the ribbon was determined. First, the distance between adjacent vesicles was independently measured for each condition, along each individual ribbon, using an ImageJ plug-in designed in house. This plug-in allows the user to select the center of consecutive vesicles along each ribbon, and then it automatically measures the distance between these points on each side of each ribbon. Then, the mean and SDs of these values were calculated, and the SD was divided by the mean for each individual ribbon.

In cases where the hilus was present but not fully captured (a common result in detachment), a relative diameter was assigned by assuming that the visible portion of the hilus would continue in an elliptical shape beyond the borders of the tomogram. If not enough of the hilus was present to make this estimate, then it was omitted from the quantification. In cases where the invagination was simplified to indentations during detachment, the hilus was measured as the distance across the area contacted by the postsynaptic processes. The diameter of the hilus neck was determined by measuring the narrowest region between the hilus and the main body of the invagination.

All measurements were taken manually, and the analyses were done blinded with respect to identification of the experimental groups; although, the extent of degeneration in the detached condition made it obvious whether a given tomogram was from a detached or normal retina. Significance was calculated first by performing a Kolmogorov–Smirnov test to ensure normality. Normally distributed datasets were analyzed with two-tailed Student's *t* tests, and non-normally distributed datasets (specifically #HC, #RB, #Ribbons, and #Mitochondria) were analyzed with the Mann Whitney U test. All analyses were done in Prism (GraphPad).

$$Circularity = \frac{4\pi(Area)}{(Perimeter)^2}$$

$$Solidity = \frac{Total\ Area}{Convex\ Area}$$

Table 2-1: List of tomograms from which figures were generated

Condition	Name of tomogram	Figure(s)	Number of sections	Section thickness	Pixel size (nm)	Location of image acquisition
Control	nCat414_01	2-10	1	400–500 nm	2.08	UCSD
	nCat414_02	2-2, 2-4, 2-10	1	400–500 nm	2.86	UCSD
	nCat414_03	2-3, 2-5, 2-7, 2-9, 2-10	1	400–500 nm	2.08	UCSD
	nCat414_04	2-11	1	400–500 nm	2.6	UCSD
	nCat414_12	2-7, 2-9	1	400–500 nm	2.08	UCSD
	nCat414_16	2-7	1	400–500 nm	1.3	UCSD
	nCat414_021621	2-6, 2-9, 2-10, 2-11	4	200 nm	0.847	UCLA
	nCat414_031121	2-8,2-10	4	200 nm	1.34	UCLA
	nCat414_102021	2-6	4	200 nm	0.847	UCLA
7d RD	7drd5	2-9	1	400–500 nm	2.21	UCSD
	7drd9	2-2, 2-4, 2-5, 2-9, 2-11	1	400–500 nm	2.42	UCSD
	7drd10	2-3, 2-5, 2-10	1	400–500 nm	2.42	UCSD
	7drd12	2-4, 2-11	1	400–500 nm	1.04	UCSD
	7drd14	2-9	1	400–500 nm	1.04	UCSD

Table 2-2: Color code for the 3-D models

Feature	**Color**
Rod spherule membrane	Cyan
Synaptic ribbon	Orange/gold
Mitochondria	Lavender
Cytoplasmic vesicles	Yellow
Ribbon-associated vesicles	Magenta
HCATs	Red and blue
RB dendrites	Green and yellow

RESULTS

General features, normal and 7 d detached retina (Figs. 2-2, 2-3)

There are multiple layers of RSs across the top two-thirds of the OPL in the rod-dominated feline retina. Figure 2-2*A* shows the photoreceptor layer in the normal feline retina used as the control in our study, Figure 2-2*B* shows this same layer in a retina detached for 7 d (Table 2-2). The vast majority of the RSs are referred to as type R1, which contain an axon (Li et al., 2016). A second type, referred to as R2 (Li et al., 2016), occurs when the rod cell body lies adjacent to the OPL, hence lacking an axon, so that the synaptic site is essentially incorporated into the basal region of the cell body. Although RSs may vary in shape, in agreement with Li et al., 2016, we observed common general characteristics; for example, both the R1 and R2 types contain a large population of free synaptic vesicles that nearly fill the synaptic cytoplasm (Figs. 2-2*C′*, 2-3*A′*, yellow spheres). Quantification of the tomograms indicates that synaptic vesicle density varies among RSs (across a threefold range). For example, compare the range of synaptic vesicle densities among the three different adjacent RSs in Figure 2-2*C′*, although all three are essentially the same size and reconstructed within the same tissue volume. Moreover, the RS model in Figure 2-3*A′* has even fewer synaptic vesicles, despite including more depth than those in Figure 2-2*C′* (234 vs 140 *z*-slices).

Consistent features among all normal RSs are the presence of synaptic ribbons (Fig. 2-2, white arrows), as well as mitochondria (Fig. 2-2*C*, m). The synaptic ribbon opposes the postsynaptic processes and is associated with its own population of synaptic vesicles (Fig. 2-2*C′*, magenta spheres). The ribbon forms an arc, so in some single sections the ends of the arc can give the impression of two separate ribbons (Fig. 2-2*C*, top RS, two white arrows). Single sections also normally depict the ribbon as a rather narrow structure. However, in Figure 2-3*A*, the ribbon (R) has been cut *en face*, illustrating a broader structure, which was validated by 3-D reconstruction (Fig. 2-4*A*,*B*, bottom). Note that this *en face* view still shows adjacent synaptic vesicles and that the ribbon is not bounded by a membrane (Fig. 2-3*A*). Transmission to second-order neurons occurs within the synaptic invagination, a pouch-like basal indentation of the RS membrane that contains closely organized postsynaptic processes. The immediate opening of the invagination denotes the hilus (Fig. 2-3*A*,*B*, red arrows); the invagination then narrows to form a neck (Fig. 2-3*A*, cyan arrows) that opens into the main body of the invagination. RB dendrites and HCATs enter the invagination through the hilus and are each identifiable by their characteristic features. In normal conditions, there are two HCATs per RS (Figs. 2-2, 2-3, red and blue processes). They branch deep within the invagination and contain apparent synaptic vesicles (Fig. 2-2*C′*, green spheres); their small branches are easily mistaken for multiple postsynaptic processes in single thin sections (Fig. 2-3*A*, white asterisk). In normal conditions, our data showed 2 RB dendrites per RS (Figs. 2-2, 2-3, green and yellow processes); however, they lack vesicles, and when RB dendrites lie adjacent to the RS membrane the membrane of the RS has an electron-dense coating (Vardi et al., 2000). This membrane densification is a quality that is used as a marker of sites opposed to mGluR6 receptors (Vardi et al., 2000; Migdale et al., 2003) and does not occur adjacent to the HCAT plasma membrane. In perinuclear synapses the invagination can dominate the volume of the cell basal cytoplasm (Fig. 2-3*A*). The invagination can also contain several profiles in individual sections that appear to be postsynaptic processes but instead are fingers of RS cytoplasm that extend into the invagination between postsynaptic processes (Fig. 2-3*A*, asterisk). These extensions have been termed diverticuli previously (Rao-Mirotznik et al., 1995), the terminology that is used here.

In 7 d detached retinas, both types of RS were still found, with the type R1 axonal synapses remaining the vast majority. However, both RS types undergo significant structural and organizational changes. The R2 type RS becomes smaller and more angular (Fig. 2-3*B*) with a significantly simplified invagination. Rather than penetrating deep into the cytoplasm, the invagination may be missing almost entirely or, if present, is much simpler and shallower and can even become just a simple indent into the cell membrane (Fig. 2-4*C*,*D*). The R1 type RS often appeared in an elongated teardrop shape (Fig. 2-2*D*), with electron-dense cytoplasm and a somewhat ruffled plasma membrane. Some of these axonal RSs had retracted into the outer nuclear layer (ONL) or had degenerated entirely, and their reduced number was made evident by the presence of expanded Müller cell (MC) processes that filled in the space normally occupied by adjacent spherules (Fig. 2-2*D*). In the normal retina, these processes form only thin layers of cytoplasm surrounding the RS (Fig. 2-2*C*, MC, blue arrow). The R1 synaptic invagination, when present, had a very modified organization (Fig. 2-4*C*,*D*). Remaining RSs still contained mitochondria and a population of synaptic vesicles. Indeed, no significant difference in the density of the synaptic vesicles, within the cytoplasm near to the invagination, was detected between normal and 7 d detached retinas (Fig. 2-3*E*). In summary, after 7 d of detachment, the RS structure has undergone significant degeneration, with a simplified invagination (if it is present at all), an elongated teardrop shape, and retraction from the OPL as Müller cells expand to fill up the missing space. For the remainder of the present study, we built on these general features by analyzing models from EM tomograms of the RS at higher magnification.

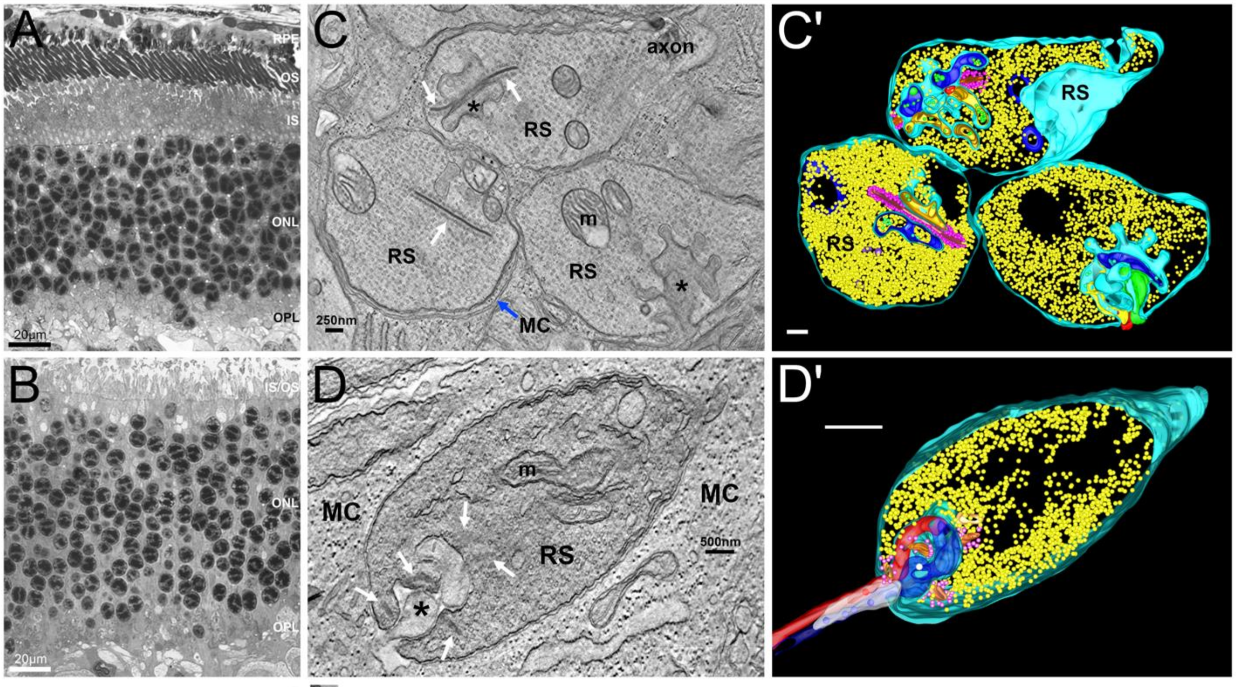

Figure Legend – Figure 2-2: *A*–*D*, Overview of axonal R1-type rod spherules in normal (*A*, *C*) and 7 d detached (*B*, *D*) cat retina. Toluidine blue stained semithin section showing the photoreceptor layer in a control retina (*A*) as it interfaces with the RPE. OPL, outer plexiform layer. ONL, outer nuclear layer. IS, photoreceptor inner segments. OS, outer segments. RPE, retinal pigment epithelium. *B*, Toluidine blue–stained semithin section showing the photoreceptor layer in a retina that has been detached for 7 d. Note the disruption in outer segment structure, the misorganized photoreceptor nuclei, and the lack of an associated RPE/Choroid. *C*, A single *z*-slice showing three adjacent RSs. The terminals are filled with synaptic vesicles, synaptic ribbons (white arrows) surrounded by their own population of synaptic vesicles, and postsynaptic processes (asterisk) in two. Several mitochondria (m) are present. The RS are surrounded by thin MC (Müller cell) processes (blue arrow). *C′*, Three-dimensional model derived from the tomogram in *C*. Spaces lacking vesicles are because of the presence of (unsegmented) mitochondria. *D*, A single *z*-slice from a tomogram of an RS from detached retina, with an elongated shape characteristic of degenerating R1 terminals. A simplified invagination is present with swollen HCATs (asterisk) surrounded by expanded extracellular space. Five separate synaptic ribbons occur around the invagination (white arrows), although only one of the four (bottom right arrow) is distinctly visible in this *z*-slice. Also present are two distorted mitochondria and a population of synaptic vesicles. The RS is surrounded by greatly expanded MC processes. *D′*, Three-dimensional model derived from the tomogram in *D* showing the presence of free synaptic vesicles, five shortened ribbons each with a population of surrounding vesicles (magenta spheres), and two truncated postsynaptic processes (red and blue).

Scale bars: *A*, *B*, 20 μm; *C*, *C′*, 250 nm; *D*, *D′*, 500 nm.

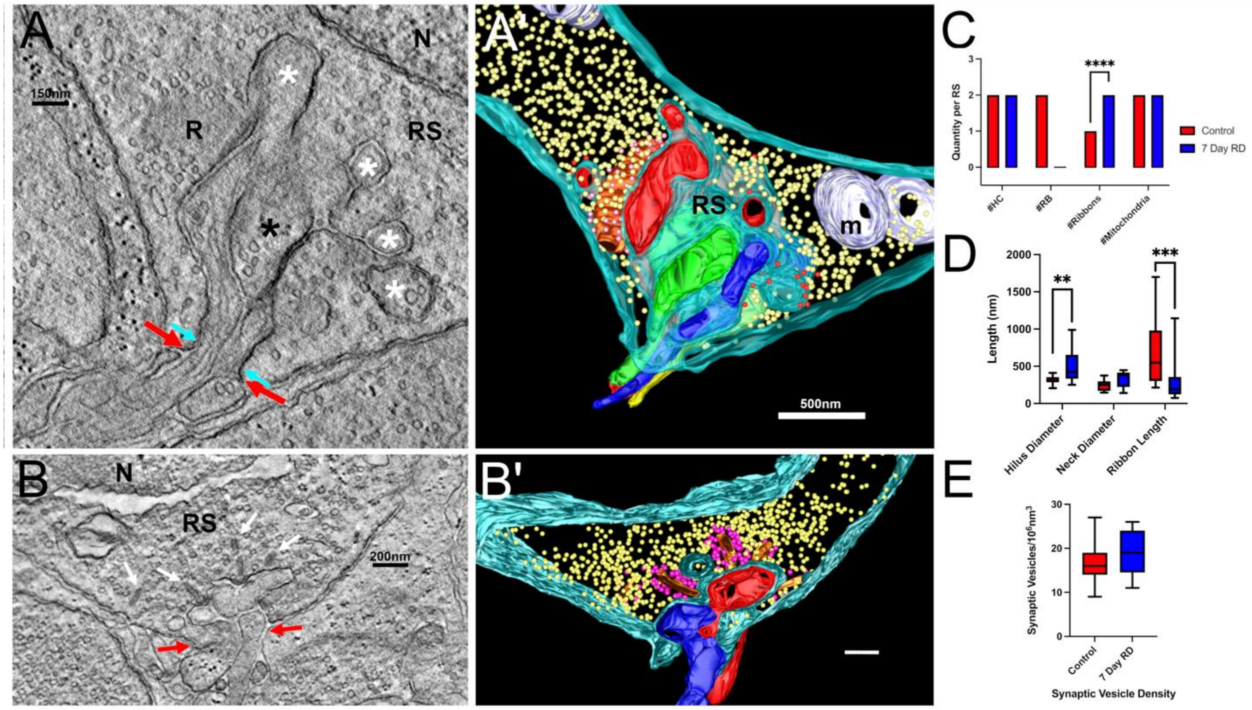

Figure Legend – Figure 2-3: ***A–B'***, Overview of perinuclear R2-type rod spherules in normal (***A***, ***A'***) and 7 d detached (***B***, ***B'***) cat retina. ***A***, A *z*-slice from a tomogram of normal retina. Note small terminal endings of the HCAT (white asterisks). A finger of cytoplasm from the RS membrane itself, or a diverticulum (black asterisk), occurs within the invagination. The hilus, or opening into the invagination, is shown between red arrows. The neck, where the hilus shrinks to its minimal diameter, is shown between cyan arrows. The synaptic ribbon (R) is cut *en face*. N, Nucleus. ***A'***, A 3-D model of the tomogram from ***A***. ***B***, A *z*-slice from a tomogram of a perinuclear RS from 7 d detached retina showing a shallow simplified invagination. There are four small synaptic ribbons (white arrows; ***B***). The hilus is indicated by red arrows. ***B'***, Three-dimensional model of the tomogram shows the presence of two HCATs (red and blue), free synaptic vesicles, and synaptic ribbons surrounded by their associated vesicles (magenta). ***C***, Quantity of different key structures across healthy and 7 d detached retinas. The medians are depicted, and a Mann Whitney *U* test was used to determine the probability of no significant difference. ***D***, Lengths (in nanometers) of key structures in healthy and detached retinas. Hilus and neck lengths were measured at the middle section of the hilus in terms of depth. ***E***, Number of synaptic vesicles in the cytoplasm adjacent to the invagination in a 200 nm square across 20 *z*-slices in the relative center of the invagination in terms of depth through the tomogram. Each *z*-slice was ~2 nm thick; small variations in this thickness would be highly unlikely to affect vesicle counts by more than ~10% (1–2 vesicles), as the vesicle diameter (20–30 nm) makes up much of the volume depth. Mann Whitney U tests (***C***) and two-tailed Student's *t* tests (***D***, ***E***) were used to determine the probability of no significant difference (see above, Materials and Methods for further statistical details); $^{**}p < 0.005$, $^{***}p < 0.0005$, $^{****}p < 0.00005$. Scale bars: ***A***, 150 nm; ***A′***, 500 nm; ***B***, ***B′***, 200 nm.

The synaptic invagination and hilus, normal and 7 d detached retina (Figs. 2-4, 2-5)

First, we modeled the rod synaptic invagination and the hilus, which is the opening through which postsynaptic processes must pass. Despite classical illustrations of the synaptic invagination appearing as a round and smooth indentation of the RS basal membrane (Missotten, 1965; Fig. 2-1), its structural organization is in fact quite complex. The RS membrane contoured the endings of the HC processes almost completely such that viewing the RS membrane independently, as in Figure 2-4, *A* and *B*, provided an accurate indication of the location of these processes. Thus, each of the pockets created in the RS membrane (Fig. 2-4*A*,*B*, white asterisks, ∼176 nm in diameter), reflects the smallest terminal branches of the HCAT telodendria, which appeared to be shaped like lollipops. The synaptic ribbon (Fig. 2-4*A*,*B*, orange) was positioned in a deep bifurcating ridge formed by two lobes of the invagination.

The hilus opens at the base of the spherule (Fig. 2-5*A*), where it measured 314 ± 13 nm in diameter (*N* = 17, ±SEM; Fig. 2-3*D*). Slightly farther into the RS, it constricts slightly to form a neck (246 ± 16 nm in diameter, *N* = 17, ±SEM; Fig. 2-3*A*, cyan arrows, *D*), and then fully opens to the main volume of the invagination. When viewed from the perspective of the OPL (Fig. 2-5*A*), the diverticuli of the RS membrane were visible (Fig. 2-5*A*, asterisks). Figure 2-5*B* shows four postsynaptic processes at the hilus. The processes narrow as they pass through it (Fig. 2-3*A*). Within the invagination, the processes expand and fill the entire invagination. There was no apparent difference in the structure of the invagination or hilus in the R1- or R2-type terminals.

After a 7 d detachment, the complex infoldings of the invagination was almost completely lost (Fig. 2-4*C*,*D*). The bulbous outgrowths that surround the HCAT telodendria had disappeared, and the invagination had a much simplified shape.
In Figure 2-4*C* the invagination remains but without its intricate infoldings. In Figure 2-4*D* the invagination is essentially absent, and the postsynaptic processes end in minor indentations along the base of the spherule (Fig. 2-4*D*, white arrows). Interestingly, we still observed associated synaptic ribbons (albeit modified) bifurcating these indentations despite the lack of a true invagination (Fig. 2-4*D*).

In 7 d detached retinas, the size of the hilus was greatly enlarged, 497 ± 85 nm (*N* = 8, ±SEM; Fig. 2-3*D*), compared with 314 ± 13 nm (*N* = 17, ±SEM; Fig. 2-3*D*) the control (compare Fig. 2-5*A*,*B* with Fig. 2-5*C*,*D*). The expansion and distortion of the hilus shown in Figure 2-5, *C* and *D*, occurred to the extent that it was difficult to define, allowing the remaining internal infoldings of the invagination to be visible. In less extreme cases, the hilus appeared relatively normal, although there were only two postsynaptic processes extending through it, both identified as HCATs (Fig. 2-5*E*).

In general, important features of the normal RS, that is, tightly packed postsynaptic processes, the presence of RB dendrites and highly branched HCAT, a narrow hilus, and a singular synaptic ribbon had disappeared at 7 d of retinal detachment. In the RS of detached retinas, there was significantly more extracellular space surrounding the remaining postsynaptic processes (see Fig. 2-9*C*,*F*, asterisks). It was common to find only two processes, with general features of HCATs, and rather than branching to form the deep endings of telodendria, as in the normal RS, the HCATs had ended bluntly within the invagination (Figs. 2-2*D′*, 3*B′*). Expansion of the hilus, an increase in the circularity and solidity of the invagination, indicating the loss of its complex branched structure, are all general characteristics of the RS in detached retina (Figs. 2-3*D*, 2-4*F*).

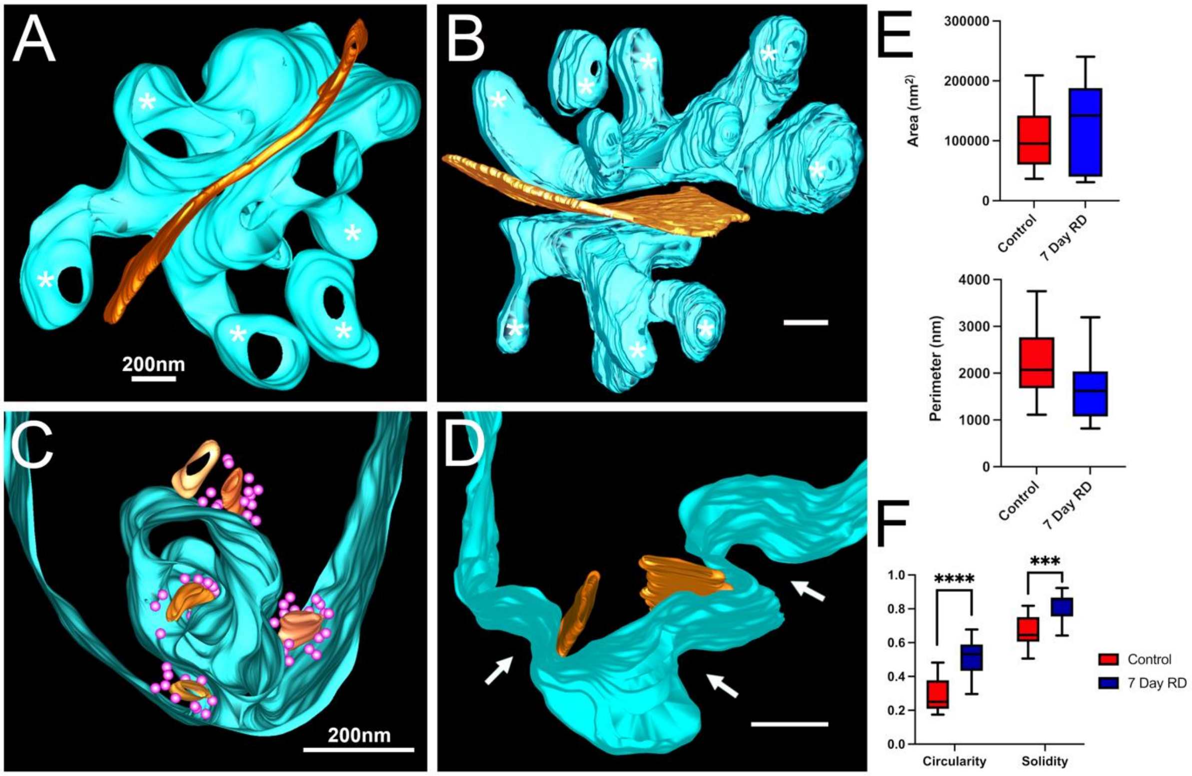

Figure Legend – Figure 2-4: ***A–D***, Organization of the synaptic invagination in normal (***A***, ***B***) and detached (***C***, ***D***) retinas. Three-dimensional models (***A***, ***B***) of the synaptic invagination in two normal RSs, illustrating how the presynaptic membrane contours the endings of the postsynaptic processes, shown from the perspective of the rod axon. Synaptic ribbons (gold) lie between two lobes of the invagination that outline the terminal branches of the HCAT (asterisk). Models of two invaginations from 7 d detached retinas (***C***, ***D***). In both cases, the deep branching of the invagination has been lost, resulting in extensive simplification. In ***C*** there are five independent synaptic ribbons (4 have a cloud of associated synaptic vesicles, magenta spheres), and in ***D*** there are two ribbons. In ***D*** there is no clearly definable invagination; instead, there are simple indentations of the plasma membrane (white arrows) opposite the postsynaptic processes (data not shown). ***E***, Area and perimeter of the invaginating structure shown as box and whisker plots. For these measures, a section in the relative center of the invaginating structure was chosen, and the invaginating RS membrane was traced; the shape was closed by a straight line through the hilus if present. ***F***, Circularity and solidity of the traced structure as drawn in ***E***, shown as box and whisker plots. Student's *t* tests were used to determine the probability of no significant difference (see above, Materials and Methods for further statistical details); $^{**}p < 0.005$, $^{***}p < 0.0005$, $^{****}p < 0.00005$. Scale bars: 200 nm.

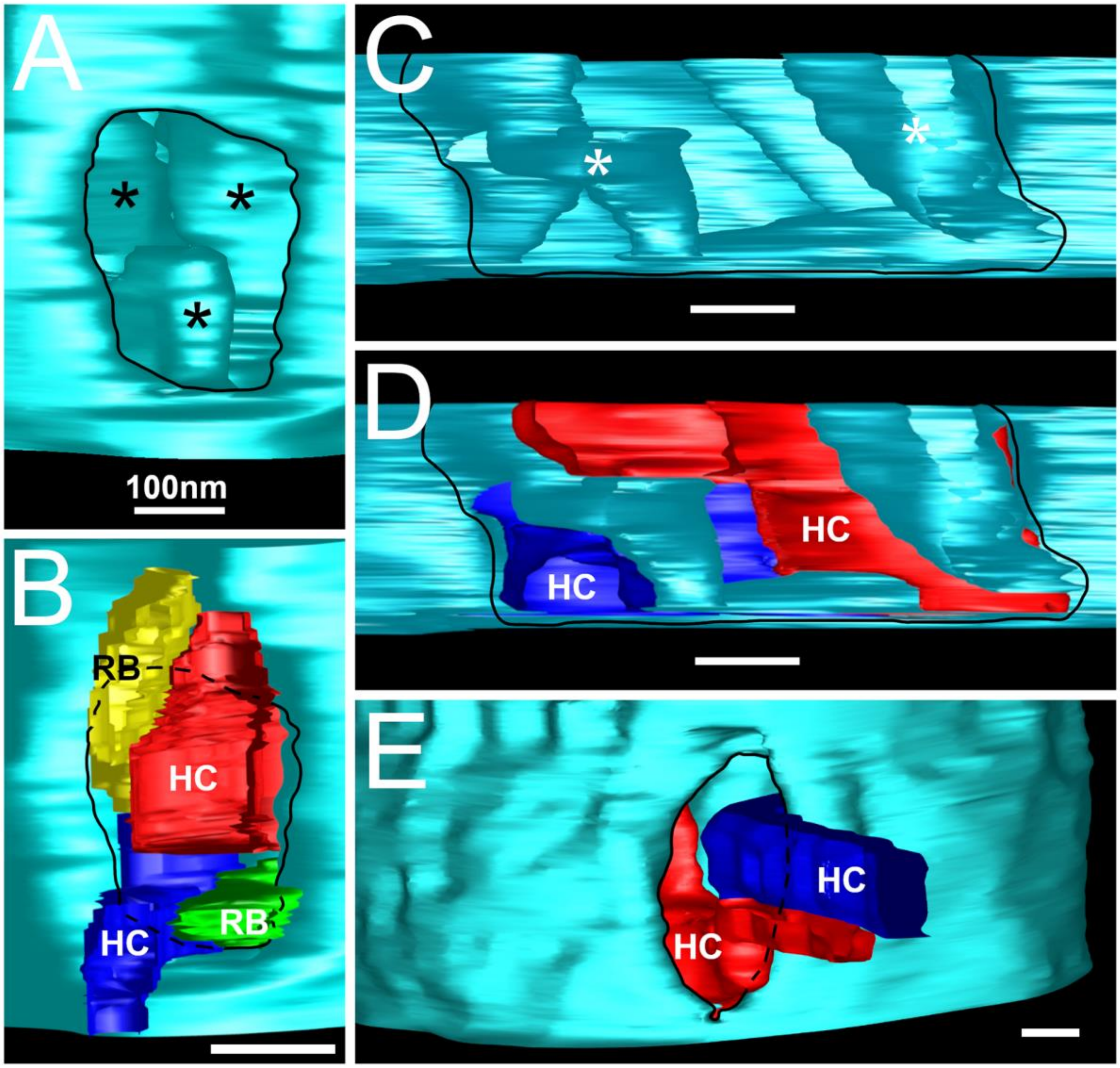

Figure Legend – Figure 2-5: The hilus, the opening into the synaptic invagination, plays an important role in regulating the environment of the invagination and expands greatly during detachment. The perspective in each image is from the outer plexiform layer into the synaptic invagination. ***A***, ***B***, Model of the hilus (black outline; dashed line in ***B*** indicates the hilus edge behind the postsynaptic processes) in a normal RS. In ***B***, postsynaptic processes are shown. In ***A*** the interior of the invagination reveals the diverticuli (asterisks), which reside between postsynaptic processes. In ***B*** note that the postsynaptic processes fill the hilus. ***C–E***, Models of the hilus (black outline; dashed line in ***E*** indicates the hilus edge behind the postsynaptic processes) in two 7 d detached retinas. In ***C*** and ***D*** the hilus is greatly enlarged and could not be imaged completely in a single 400-nm-thick section. In ***C***, diverticuli, often absent in detached RS, are present (white asterisk). In ***D***, two HCATs (red and blue) are visible and do not fill the entire hilus. A relatively normal hilus (***E***) from a 7 d detached RS but only two postsynaptic HCs (red and blue) enter the hilus with significant extracellular space normally occupied by RB dendrites. Scale bars: 100 nm.

Organization of postsynaptic processes in the normal retina

Models derived by segmentation of the tomograms also illustrate the organization of postsynaptic processes within the invagination. Examples are shown in Figure 2-6, which shows the detailed organization of the postsynaptic processes; Figure 2-6, *A* and *C*, show selected *z*-slices from two tomograms, illustrating the appearance of the postsynaptic complex in single sections. In Figure 2-6*A*, there appear to be two ribbons (R) with three postsynaptic processes opposite each, one rod bipolar dendrite (RB1, RB2), and two horizontal cell processes (H1, H2). Diverticuli from the RS (asterisk) lie between them. In this plane, the top H1 process can be seen to have a few synaptic vesicles, and the RS membrane opposite the RB dendrites is lined with densification (small arrows), defining characteristics for each. RB processes are typically devoid of vesicles. Figure 2-6*C* shows another example, in this case only one ribbon (R) is evident, and the hilus of the RS is visible between the black arrowheads. Figure 2-6, *B* and *B′* show two views of the 3-D model constructed from the tomogram in Figure 2-6*A*. In Figure 2-6*B* the model is clipped to show data from selected *z*-slices that reflect the structures shown in Figure 2-6*A*. In this case the synapse appears to have two triadic arrangements of postsynaptic processes opposite two ribbons. Figure 2-6*B′* shows the full model showing that there is in fact one long arching ribbon behind two horizontal cell processes and two rod bipolar dendrites. In Figure 2-6*C′* the model shows a similar arrangement of the postsynaptic processes. Within each model, diverticuli (asterisks) fill in space between the postsynaptic processes.

The configuration of the postsynaptic processes of the RS is often described as a triad in nonprimate mammals. Figure 2-6 demonstrates the importance of comprehensive 3-D reconstruction to understand their organization. Figure 2-6*A* shows a 2-D view, which appears to illustrate two such triads, each composed of two HCAT endings (H1, H2) and a single RB dendrite opposite a synaptic ribbon. Figure 2-6*B* reinforces this interpretation by partial reconstruction of the synapse. However, Figure 2-6*B′* shows the complete reconstruction of these processes as they terminate beneath the synaptic ribbon. The two ribbons in Figure 2-6, *A* and *B*, are in fact endings of the same arch-shaped ribbon, and the HCAT and RB endings form a complex of four postsynaptic processes (two from each cell type) associated with it. This same configuration can be seen in a single *z*-slice selected from another tomogram (Fig. 2-6*C*,*C′*) where the two HCAT and RB dendrites terminate beneath the ribbon. Of nine complete tomograms, seven had a clear tetrad, one also contained an unidentified postsynaptic process (see Fig. 2-8), and one seemed likely to be a tetrad but lacked sufficient membrane resolution to be unambiguous. Therefore, images of complete reconstructions support a tetradic arrangement of the postsynaptic processes rather than a triadic one.

Additional models of the postsynaptic processes are shown in Figure 2-7. The architecture of the two types of processes were found to vary greatly once inside the invagination. RB processes appeared relatively narrow as they enter the invagination and terminated one- to two-thirds of the way within the invagination relative to the HCAT (Fig. 2-7*B*). They expanded slightly to form a slab-like blunt ending; they were never observed to branch. HC processes on the other hand expanded greatly within the invagination and curved to fill space just below the ribbon. They also branched to form readily identifiable small telodendria that terminate deep within the RS cytoplasm (Figs. 2-3*A*, 2-4*A*,*B*, 2-7*A*,*C*, white asterisks). As mentioned earlier, this prominent branching is readily identifiable by segmenting just the plasma membrane of the RS (Figs. 2-4*A*,*B*, 2-7*B*,*C*). The main body of the HCAT terminates directly adjacent to the synaptic ridge beneath the synaptic ribbon (Figs. 2-6, 2-7*A*, 2-8), whereas the small lollipop endings terminate deep in the RS cytoplasm. The organization of the HCATs can be complex within the invagination as they parallel the synaptic ribbon (Fig. 2-7*C*). The 3-D models show the extent of the small lollipop endings. HCATs can form up to four to five of these terminal endings from the main HCAT volume. Overall, although RB dendrites are simple in their organization, HCATs are more complex in organization and structure than previously appreciated; some HCATs extend up to six independent lollipop endings, of which the functional implications are not clear.

Our tomography data from the normal cat has revealed an unexpected variation within some RSs. Figure 2-8*A* shows a single *z*-slice through the postsynaptic process of a RS, with the typical two HCAT (H) and two RB dendrites. But there is also an additional process (Fig. 2-8*A*, asterisk). In most *z*-slices, this process had the characteristics of a diverticulus. However, here, and in one other RS, it did not connect to the RS cytoplasm but rather entered the invagination through the hilus, where it terminated bluntly beneath the ribbon. When reconstructed, this process (Fig. 2-8*B*, white area) stands out as distinct from the HCAT and RB processes. In addition to the presence of vesicles (Fig. 2-8*B*, cyan spheres), these processes have membrane densification opposite the RB dendrites (Fig. 2-8*A*, black arrows), thus making it distinct from any other postsynaptic processes. Hence, we have identified an additional postsynaptic process in two RSs that arise from an unknown cell type.

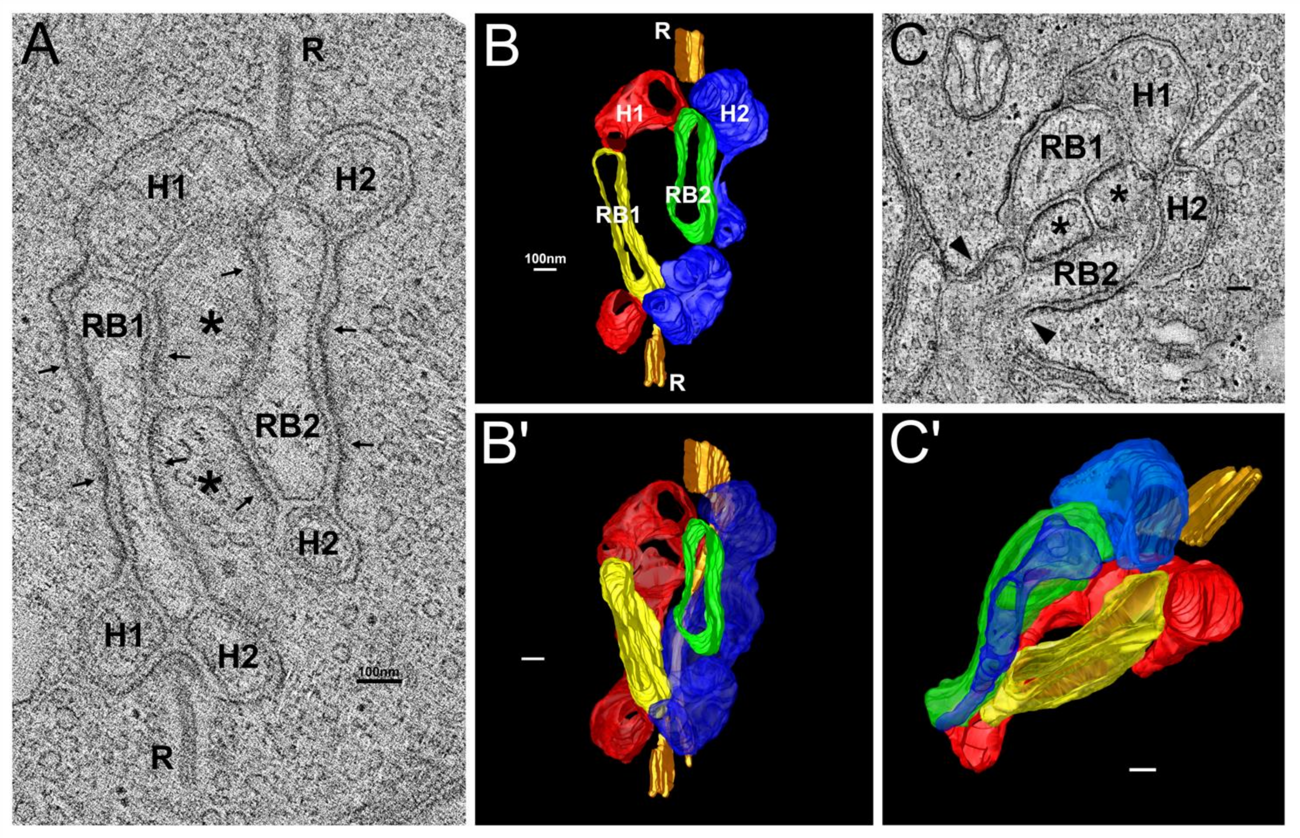

Figure Legend – Figure 2-6: The organization of postsynaptic processes reveals a tetrad as the fundamental organizing unit. ***A***, A *z*-slice of a tomogram selected to show an arrangement of two HC processes (H1, H2) and two rod bipolar processes (RB1, RB2) opposite apparent synaptic ribbons (R). The image also shows two of the diverticuli of RS cytoplasm (asterisks), which reside between postsynaptic processes, one of which (bottom) is still contiguous with the RS cytoplasm, and the other (top) appears independent in this plane. Densification of the RS plasma membrane occurs opposite the RB dendrites (small arrows). ***B***, ***B'***, Segmentation of the tomogram in ***A***. In ***B*** several *z*-slices have been omitted to show two characteristic triads around two apparent synaptic ribbons as shown in ***A***. ***B'***, however, shows segmentation of the full volume indicating a simple arrangement of four postsynaptic processes opposite one synaptic ribbon. ***C***, ***C'***, A second example from another tomogram of the four postsynaptic processes opposite one ribbon. In ***C*** the asterisks indicate the diverticuli between the postsynaptic processes. The hilus is indicated by black arrowheads. Scale bars: 100 nm.

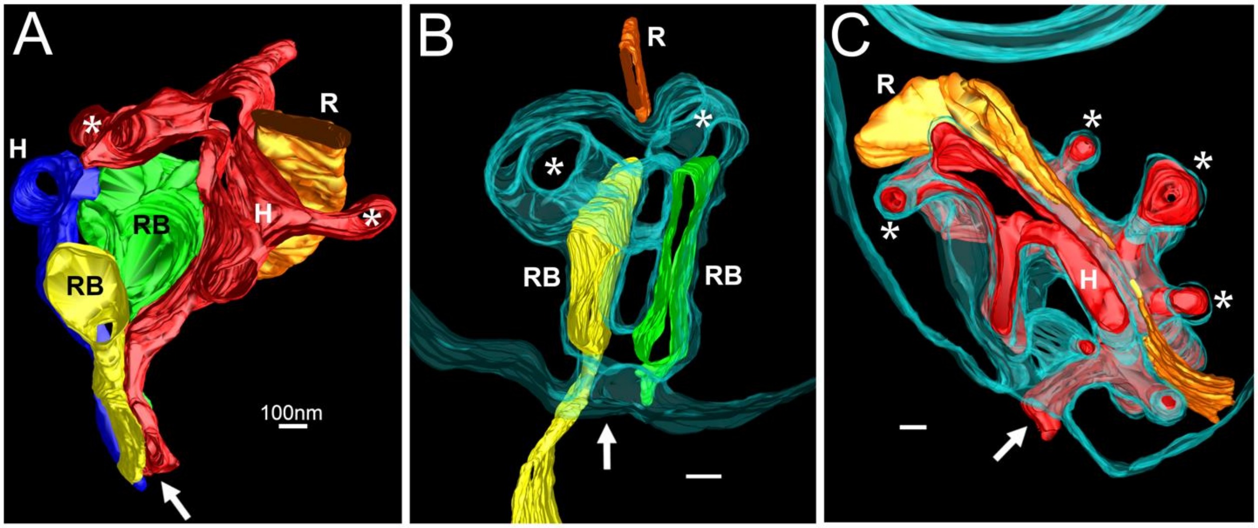

Figure Legend – Figure 2-7: Structural organization of the different postsynaptic processes in normal retina. ***A***, The postsynaptic processes and synaptic ribbon from a healthy RS invagination. Note the complexity of the red HCAT as it branches around the ribbon giving rise to two of the lollipop-shaped endings (asterisk) on either side of the ribbon (R). Both RB cell dendrites end bluntly more distant from the ribbon. Only a portion of the blue HCAT was within the volume. ***B***, The synaptic invagination of a healthy RS, with only the RBs, the ribbon, and the RS membrane visible. The cyan plasma membrane of the RS is made transparent to show how the RB dendrites expand within the invagination to unbranched slab-like endings that terminate distant from the ribbon. Asterisks mark the location of HCAT adjacent to the ribbon (R). The arrows mark the hilus. ***C***, An RS invagination with just the ribbon, a singular HCAT, and a translucent RS membrane visible. In this image, the model is oriented to show the complex branching of the HCAT (red) adjacent to the synaptic ribbon (orange). Asterisks indicate the lollipop endings of the HCATs. The HCAT enters the invagination at the hilus (arrow). Scale bars: 100 nm.

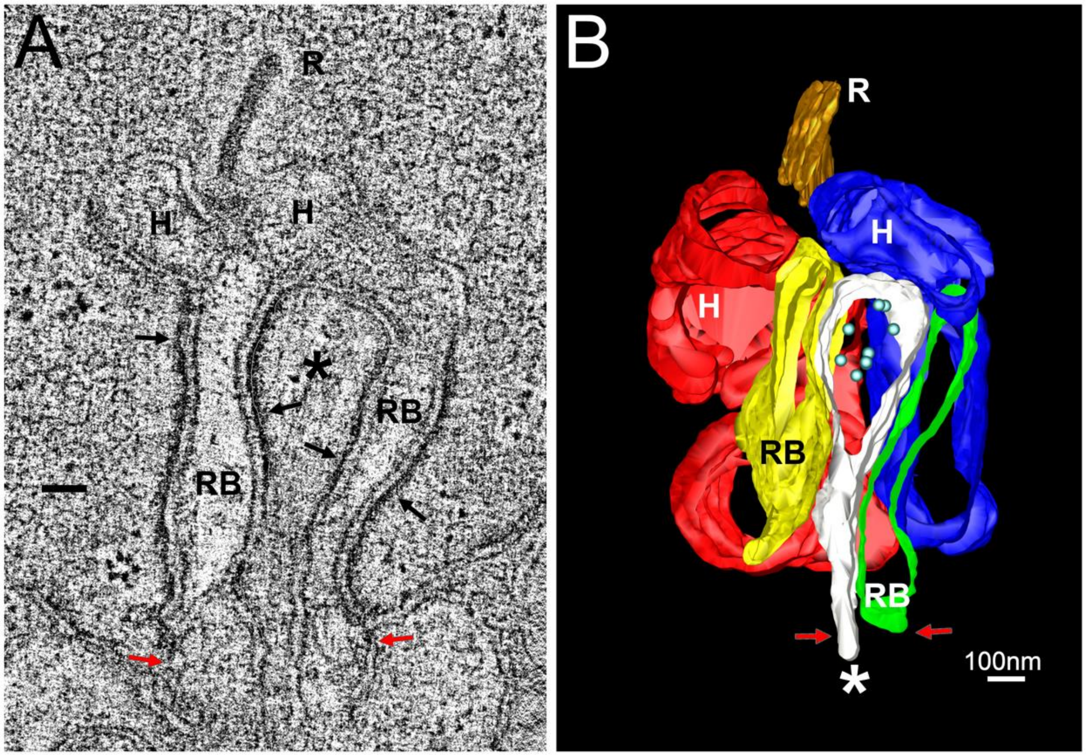

Figure Legend – Figure 2-8: An additional unidentified process occurs at some synapses. ***A***, ***B***, A representative *z*-slice from a tomogram of a normal RS showing an unidentified process (asterisk) terminating within the invagination (***A***). A segmentation of this tomogram (***B***) where two HCATs (H, red and blue) and two RB dendrites (yellow and green) were identified in addition to the unusual process (white asterisk). This process has ultrastructural characteristics of RS cytoplasm (membrane densification opposite the RB processes, black arrows in ***A***), and the presence of several intracellular vesicles (cyan spheres in ***B***). However, the process originates within the OPL and enters the invagination through the hilus (red arrows). Scale bars: 100 nm.

Organization of postsynaptic processes in the 7 d detached retina

Beyond the general changes in RS organization mentioned here (see below, Results), the most striking other change in the RSs of detached retinas was the complete lack of identifiable RB dendrites within the invagination (Fig. 2-3*C*). In contrast, HCATs were still present; their identification was usually straightforward because they contained cytoplasmic synaptic vesicles (even in detached retinas). However, they were extensively modified as they completely lack the complex branching characteristic of HCATs in normal retinas. Hence, the loss of RB dendrites and the complex branching of the HCATs creates excess extracellular space in the invagination in the RSs of 7 d detached retinas. Synaptic ribbons, albeit highly modified (see below), were still present and often lay in an identifiable bifurcation ridge that would typically separate the two HCATs (Fig. 2-9*A*,*A′*,*C*,*C′*,*F*,*F′*), even in RSs that did not have a clear invagination (Fig. 2-9*D*,*D′*).

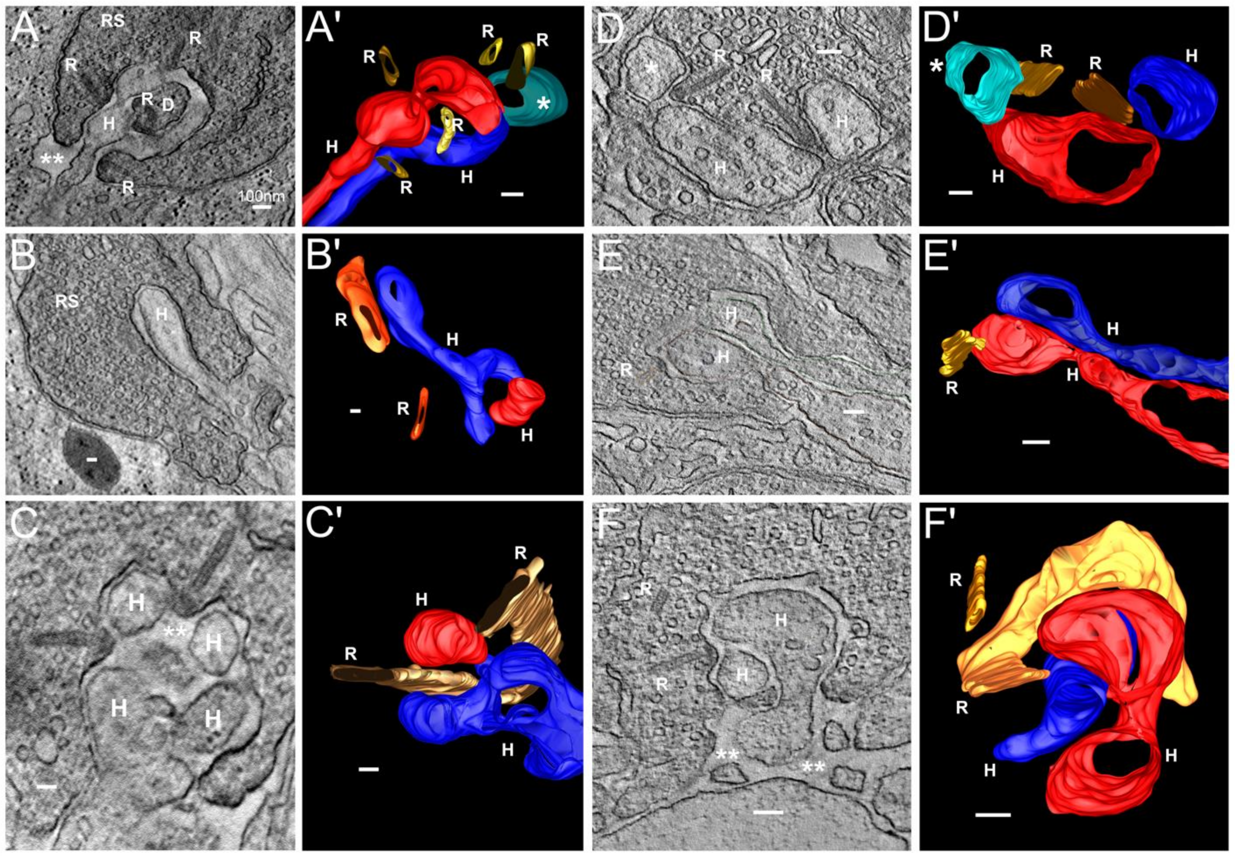

Figure Legend – Figure 2-9: Rod spherules after a 7 d detachment. They have a greatly simplified organization and show the loss of RB dendrites; HCATs have lost their complex branching, including the small lollipop endings, there are often multiple synaptic ribbons, and there is increased extracellular space within the invagination. ***A–F'***, Representative *z*-slices of tomograms (left, ***A–F***) and their 3-D models (right, ***A'–F'***). Simplistic HCATs lacking telodendria, with multiple synaptic ribbons (***A***, ***B***, ***E***). An additional unidentified process is evident in ***A***. All postsynaptic processes that were positively identified arose from HCATs. ***A'*** and ***D'*** each contain a process that could not be positively identified as an HCAT because of a lack of intracellular vesicles but were not able to be positively identified as RB dendrites either because of a lack of membrane densification (these processes are shown in cyan, labeled with a white asterisk). ***C*** and ***F*** depict extremely arced and distorted synaptic ribbons, a shrunken synaptic invagination, and a large amount of extracellular space (white double asterisks). ***D*** contains an RS that lacks an invagination entirely and only has slightly indenting postsynaptic processes that lie between multiple bifurcating synaptic ribbons. Extracellular space not found in normal RS is indicated by white double asterisks in ***A***, ***C***, and ***F***, and a diverticulum (white D) is shown in ***A***. Scale bars: 100 nm.

The synaptic ribbon and vesicle populations in the normal retina

In single sections, the synaptic ribbon can appear as a typical straight-line structure (Fig. 2-10*A*); however, when adequately reconstructed, they formed a long arc that folded over a synaptic ridge opposite the postsynaptic complex (Figs. 2-10*B*, 2-11*A*). However, there was variation in the size and shape of the ribbon; we found ribbon lengths ranging from 214 to 1700 nm in the normal RS. We found convincing evidence for only a single ribbon per RS in all of our tomograms from normal feline retina.

The arciform density is a structural feature lying directly beneath the ribbon, within the synaptic ridge adjacent to the HC processes (Fig. 2-10*B*,*E*). It has been described as a V-shaped trough in which the ribbon sits (Zampighi et al., 2011). In our reconstructions, the arciform density was a continuous structure extending the full length of the ribbon (Fig. 2-10*B*,*E*). Like the ribbon, it is not a membrane-bound organelle. Zampighi et al. (2011) described pentamer structures that extend from the edges of the arciform density toward the ribbon. Here, we observed similar electron-dense structures ~25 nm in size extending along the full length of the arciform density with a spacing of 35–45 nm (Fig. 2-10*E*, white arrows). Fundamentally, the arciform density appeared as a continuous structure that lined the entire extent of the ribbon. This observation contrasts with the previous reports of two separate arciform densities at each synapse (Migdale et al., 2003; Tsukamoto and Omi, 2022).

In normal RSs, there are three different states that synaptic vesicles of typical size (~25 nm) can occur in—free throughout the cytoplasm, associated with the synaptic ribbon (Fig. 2-10*A*–*C*, magenta spheres). and fused to the RS membrane.

Although data from single ultrathin sections have suggested that the vesicle population across RS is quite similar, our tomographic reconstructions, capable of showing three to four times the volume of an ultrathin section, suggested that there may be variability from one RS to the next, as shown in comparison of the left RS and the two right RSs in Figure 2-2*C′*. Ribbon-associated vesicles generally pattern the synaptic ribbon along its length. In single sections these can appear to be uniformly and evenly spaced (Fig. 2-10*A*,*C*) and have generally been depicted in this configuration. However, our tomographic reconstructions show that they are not necessarily evenly distributed over the surface of the ribbon (Figs. 2-10*B*, 2-11*A*). Many vesicles can be seen clearly fused with the RS membrane (Fig. 2-10*D*, green arrows), engaging in active synaptic transmission. Interestingly, although vesicular fusion events do occur near the synaptic ribbon, the assumed site of synaptic transmission, a large number of fused vesicles were also observed far away from this region, primarily adjacent to the small HCAT telodendria (Fig. 2-10*F*, red spheres). Zampighi et al. (2011) also described vesicle fusion in regions other than at the synaptic ribbon and suggested they may be involved in transmitter release or alternatively as sites of vesicular membrane recovery.

An identifying feature of HCATs is the presence of intracellular vesicles. Although similar to traditional synaptic vesicles, they are typically larger in diameter (∼45 vs ∼25 nm) and with more variation in size and shape (Fig. 2-11*A*,*B*). They were generally scattered throughout the HCAT but were aggregated in the lollipop endings (Fig. 2-11*A*, cyan arrow). We also found dense core vesicles (DCVs) in the HCAT processes (Fig. 2-10*D*, black arrow; Fig. 2-11*B*, large spheres in the red HCAT). DCVs have been reported to occur near neuronal synapses where they most likely participate in some form of a paracrine type of response affecting neurons differently than the vesicles participating in typical neuronal signaling (Kuznetsov and Kuznetsov, 2017; Trueta, 2021). However, their exact role at the rod synapse is not clear.

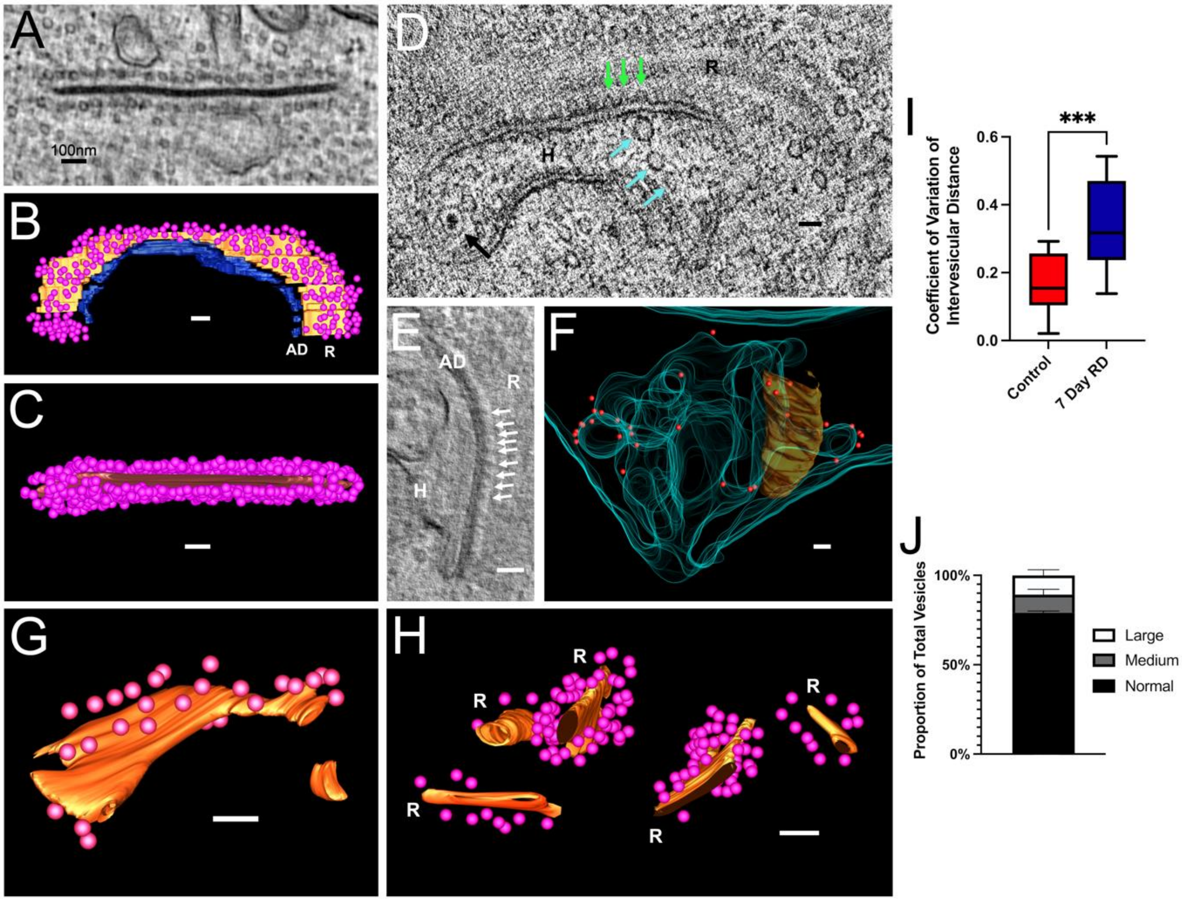

Figure Legend – Figure 2-10: Synaptic ribbons and vesicles in normal and 7 d detached retina. ***A***, A representative *z*-slice from a tomogram of a normal synaptic ribbon with characteristic patterning of synaptic vesicles along its length. ***B***, A model derived from the segmentation of a synaptic ribbon (orange) with its associated vesicles and arciform density (blue); the arciform density is a thin layer that underlies the length of the ribbon. Note that vesicles are scattered over the surface of the ribbon. ***C***, The same model as in ***B*** but viewed from top-down angle where vesicles appear uniformly clustered on the ribbon. ***D***, A representative *z*-slice from a tomogram of a normal synaptic ribbon (R) arcing around an HCAT (H). Synaptic vesicles are fused to the RS membrane opposite the HCAT (green arrows). Also shown are intracellular HCAT vesicles (cyan arrows), as well as a characteristic dense core vesicle (black arrow). ***E***, A z-slice from a tomogram showing electron dense projections (white arrows) extending from the arciform density toward the synaptic ribbon (R) which is sectioned *en face*. ***F***, A normal synaptic invagination with its membrane (cyan) made semitransparent. The synaptic ribbon is in orange (dimly lit, behind the RS membrane), and nonribbon associated vesicles fused to the RS membrane are red spheres. ***G***, ***H***, Models of synaptic ribbons from 7 d detached retina, showing ribbon fragments with sparse and often unorganized associated vesicles. ***I***, Analysis of the spacing of synaptic vesicles along the ribbon. The distance between ribbon-associated vesicles was measured, and the coefficient of variation (SD/mean) was plotted as a measure of variability on a box and whisker plot. Each data point represents the intervesicular spacing variability along a single ribbon. Student's *t* tests were used to determine the probability of no significant difference (see above, Materials and Methods for further statistical details). ***J***, The proportion of different types of cytoplasmic vesicles present in the 7 d detached rod spherules; $^{**}p < 0.005$, $^{***}p < 0.0005$, $^{****}p < 0.00005$. Scale bars: 100 nm.

The synaptic ribbon and vesicle populations in the 7 d detached retina

All the reconstructed RSs in 7 d detached retinas still had identifiable synaptic ribbons, and in single sections the morphology of some ribbons in detached retinas appeared similar to those in normal retinas. However, when viewed in tomographic volumes, it was clear that the organization of most ribbons was greatly altered by detachment. Most striking was their increase in number, decrease in size, and their altered location within the spherule cytoplasm (Figs. 2-4, 2-9, 2-10*G*,*H*). Many assumed a very different shape in comparison with those in normal retinas. For example, the two apparent ribbons in the *z*-slice shown in Figure 2-9*C* are the result of sectioning through the ends of a highly curved ribbon that is almost U shaped (Fig. 2-9*C′*). In a normal RS, the ribbon is not as highly curved. The larger ribbons shown in Figure 2-9, *C′* and *F′*, contain a clear twist. In a normal cat RS, there is always just one ribbon. In a 7 d detached retina, the number of independent ribbons can vary from one (Fig. 2-9*C′*,*E′*), to two (Figs. 2-9*B′*,*D′*,*F′*, 2-10*G*) or more (Figs. 2-3*B*, 2-4*C*, 2-9*A*, 2-10*H*). A major difference in the detached retina was the appearance of short ribbons, often lying close to, but not connected to, a larger more traditional ribbon, suggesting they had fragmented from the larger ribbon (Fig. 2-10*G*,*H*). The average ribbon length after retinal detachment decreased from 0.7 ± 0.09 μm (*N* = 22, ±SEM) in the normal retina to 0.3 ± 0.07 μm (*N* = 18, ±SEM) in the detached retina (Fig. 2-3*D*; *p* = 0.0003), and the ribbon quantity per spherule doubled (Fig. 2-3*C*; *p* = 0.00,008). Sometimes, these smaller ribbons had no vesicles associated with them (Fig. 2-4*C*, top ribbon). In detached retinas, ribbons that maintained their proximity to postsynaptic processes (i.e., adjacent to the RS membrane) had an identifiable arciform density (Figs. 2-3*B*, 2-9*C*,*E*,*F*), whereas those that lay free in the cytoplasm did not.

In the normal RS, vesicles lay adjacent to the entire ribbon at a defined distance and relatively uniform distribution (Fig. 2-10*A*–*C*). In detachment, this association appeared looser, with vesicles sometimes forming a sparsely populated cloud around the ribbons (Fig. 2-10*G*,*H*). Although segmentation of these vesicles in a normal RS is relatively straightforward, it was difficult to assign vesicle locations relative to the ribbon in the detached retina. This is further described by the large increase in the coefficient of variation (SD/mean) of the distance between ribbon-associated vesicles (Fig. 2-10*I*). The 7 d detached RS had more than twice the spacing variability compared with the control.

Although vesicles associated with synaptic transmission were still observable in the detached retina—free in the RS cytoplasm, associated with the synaptic ribbon, and in the HC processes—major differences appeared in vesicle fusion, the appearance of large swollen cytoplasmic vesicles, and their distribution within the HC processes. Despite being easily found in the control, we were unable to identify a single vesicle fused to the RS plasma membrane in the detached condition. Within degenerating RSs we also found the presence of two new vesicle morphologies, those slightly larger than synaptic vesicles (~45 nm; Fig. 2-11*C*, blue arrows) and much larger swollen vesicles (Fig. 2-11*C*, red arrows; Fig. 2-10*J*). The intracellular HCAT vesicles also have some slight changes; they were usually fewer in number and more scattered throughout the process (Fig. 2-11*D*) where it enters the invagination.

Hence, 7 d of retinal detachment results in a greater number of synaptic ribbons, a reduction in consistency of synaptic vesicle association with the synaptic ribbons, and a complete lack of vesicle fusion along the membrane, indicating that synaptic transmission after detachment is likely significantly impaired.

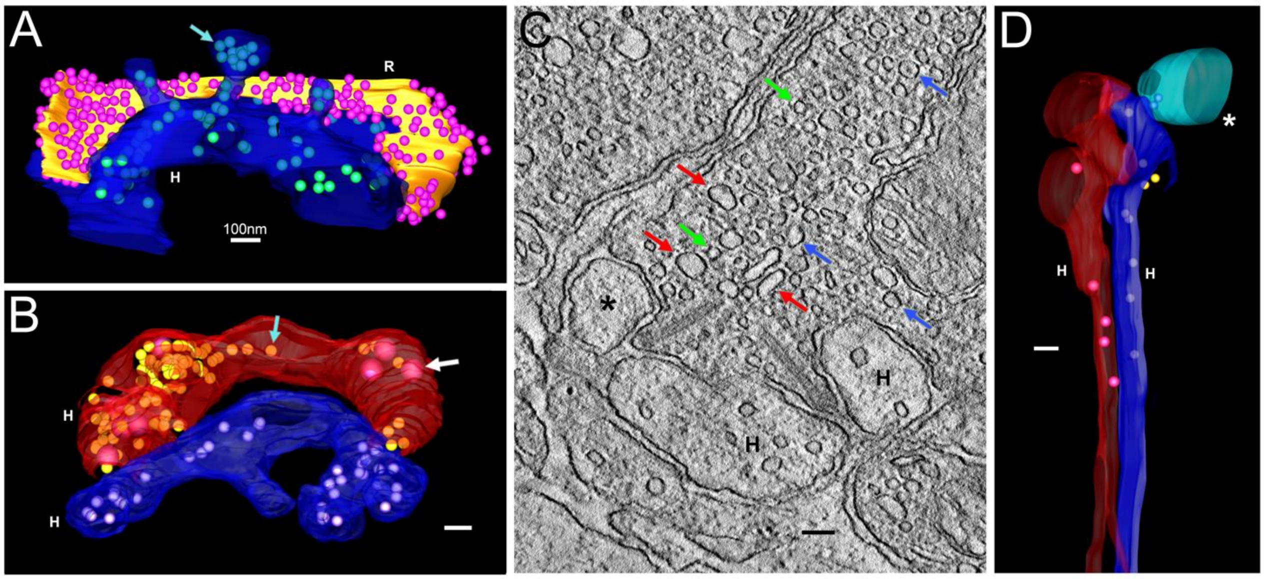

Figure Legend – Figure 2-11: Retinal detachment leads to changes in cytoplasmic and intracellular vesicles. ***A***, An HC process (blue) in normal retina opposite its synaptic ribbon (orange). The HCATs often have large numbers of intracellular vesicles, with special accumulation in the lollipop endings (cyan arrow). ***B***, Another pair of HCATs in normal retina depicting both a large population of typical synaptic vesicles (cyan arrow) as well as a number of larger dense-core vesicles (white arrow). ***C***, A *z*-slice from a tomogram of 7 d detached RS containing a range of intracellular vesicles. There is a large number of typical synaptic vesicles (green arrows), a few vesicles of larger size (blue arrows), and a few swollen vesicles that are of variable shape and size (red arrows). ***D***, A model showing two HCATs (H, red and blue) in a 7 d detached retina with a reduced population of intracellular vesicles. The process marked with the asterisk was unidentified. Scale Bars: 100 nm.

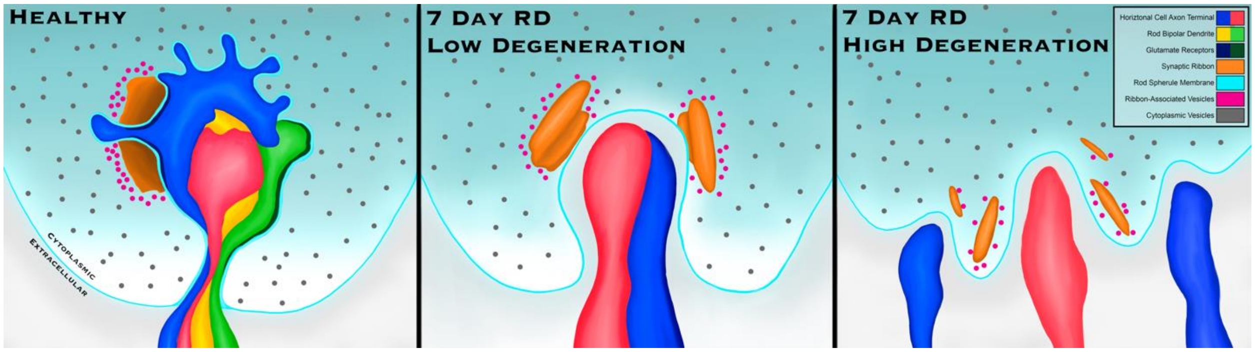

Figure Legend – Figure 2-12: Schematic figure describing the key ultrastructural changes occurring in the rod spherule during a retinal detachment. There is variation in the extent of degeneration from one spherule to the next, and so we have depicted two different levels of degeneration within RS. Left, In the healthy RS, there are four (occasionally 5) postsynaptic processes made up of two horizontal cell axon terminals and two rod bipolar cell dendrites. A synaptic ribbon surrounds the HCATs along the edge of the invagination as the spherule membrane tightly contours these postsynaptic processes. Middle, In lower levels of degeneration, the complex contours of the invaginating membrane are lost, leaving a heavily simplified structure. Bipolar cell processes generally retract, leaving only HCATs that are left surrounded by large amounts of extracellular space. The hilus greatly expands, and the synaptic ribbons fragment resulting in two or more synaptic ribbons with sparse and variable vesicle associations. Right, In the most highly degenerated synapses, the postsynaptic cells no longer enter the hilus and simply lie as indents along the spherule membrane. The ribbon often fragments and in some cases is present with no associated vesicles. The entire synaptic structure falls apart, likely leading to a complete inability to send synaptic signals.

DISCUSSION

By exploiting the high *z*-resolution of EM tomography, we have added significantly to our knowledge of the RS, the first synapse of scotopic vision and one of the most complex synapses in the CNS. In particular, we have shown the extent and complexity of the synaptic invagination and have provided new evidence for interpreting the organization of the postsynaptic processes. Our results have shown that tomography is valuable in resolving contradictory descriptions for the organization of this synapse. Additionally, we have provided the first high-resolution description of changes these synapses undergo during retinal injury in the context of a 7 d retinal detachment, where the organization of the RS breaks down significantly.

Organization of the postsynaptic processes

The organization and especially the number and types of cells contributing to postsynaptic processes in the RS is fundamental to retinal circuitry. Yet, there has been confusion over these processes since their earliest descriptions by Sjöstrand (1958) and Missotten (1965). A triadic organization has been commonly reported, consisting of two lateral HC processes and a centrally located RB dendrite (Mariani, 1984; Maslim and Stone, 1986). However, Rao-Mirotznik et al. (1995) described the processes as a tetrad in cat, and Migdale et al. (2003) described them as organized into two synaptic units in cat, monkey, and human, with each unit having two lateral elements and one or more central elements. Tsukamoto and Omi (2022) described 10 different types of pattern in Macaque RS and one type (a tetrad) in mouse. The limited *z*-axis resolution in reconstructions from conventional EM serial sections has contributed to these different interpretations. As shown in Figure 2-6, the arc shape of the synaptic ribbon can easily lead to the conclusion that the processes occur in two triadic arrangements. However, our tomographic reconstructions suggest that the tetrad is the most accurate description in cat. It is likely that high-resolution reconstruction of this synapse in other species will also show the tetrad to be the most common fundamental organizational unit in mouse and other nonprimate mammals. Signaling from a rod spherule to two RB cells (as in a tetrad) rather than just one (as in a triad) might be a way of countering intrinsic noise in the RB cells.

The number of synaptic ribbons remains controversial, in large part because of their very large size and arcuate shape. On full reconstruction of large 3-D volumes, we identified only one ribbon in each RS. This conclusion is in agreement with Migdale et al.'s (2003) conclusion for cat retina; however, they concluded there were two arciform densities associated with each ribbon, defining two synaptic units for each RS. Tsukamoto and Omi (2022) identified one or two ribbons and two arciform densities in each mouse RS. In our high-resolution reconstructions we found no evidence for a break in the continuity of the arciform density, suggesting there is only one long site of transmitter release associated with each synaptic ribbon. Thus, our results are most compatible with a simple grouping of four postsynaptic processes opposite a single ribbon and single arciform density. Moreover, our imaging of the normal hilus (Fig. 2-5) shows that four synaptic processes (two HCs and two RBs) enter the invagination, indicating that terminal branching does not underlie the appearance of four processes within the invagination.

We also found 2 of 14 normal synapses that had a third type of postsynaptic process (Fig. 2-8). A process with this shape and location within the invagination was identified as a HCAT in Kolb, 1970 and as an RB dendrite (https://webvision.med.utah.edu/book/part-iii-retinal-circuits/circuitry-for-rod-cells-through-the-retina/). Its ultrastructural characteristics most closely match those of the diverticuli that enter the invagination as internal branches of the spherule itself (i.e., the presence of both synaptic vesicles and membrane densification), but in both cases it enters the invagination through the hilus from the outer plexiform layer. To our knowledge, there is no known candidate cell type reported in the literature of mammalian retinas that could account for this process.

Major ultrastructural degeneration in 7 d detachment

As suggested previously (Linberg et al., 2009), 7 d of retinal detachment resulted in most RSs showing ultrastructural signs of severe degeneration. Here, we show that this includes a remodeling of the complex contour of the invagination itself, in some cases proceeding to only minor indentations of the RS base. In the degenerating RS, the greatly simplified HCATs remained associated with the terminal, even when the invagination was almost entirely lost (Figs. 2-9, 2-11). RB dendrites, however, were lost from every postdetachment RS we examined, consistent with results from previous studies (Linberg et al., 2006b, 2009; Townes-Anderson et al., 2021). The synaptic ribbon appeared to become fragmented into small ribbons, which often appeared free in the RS cytoplasm, seemingly no longer anchored to a synaptic site, an observation never seen in normal retinas. The approximate doubling in the number of ribbons, together with the halving of ribbon length, implies that overall ribbon length per spherule was nevertheless conserved. Ultrastructurally, the small ribbons appeared best described as fragments of the original ribbon (Figs. 2-9, 2-10*G*,*H*), but we cannot rule out the possibility that they were synthesized *de novo* (Fig. 2-12).

We also identified, in normal retinas, 25 nm projections that extended toward the synaptic ribbon from the arciform density. Bassoon, a large 420 kDa protein, vitally important for anchoring the ribbon to the invagination (Dick et al., 2003), is a likely candidate for forming these projections (Brandstätter et al., 1999). The arciform density was difficult to study in degenerated synapses because of its small size and the disorganization of the synapse, but our limited observations suggest that these features were indeed maintained but only associated with ribbons that remained closely apposed to the presynaptic membrane (Figs. 2-3*B*, 2-9*C*,*E*,*F*). Ribbon fragments that were not in close apposition to the membrane appeared to float in the cytoplasm without an arciform density.

Remodeling of the hilus in the detached retina was profound and would likely have important functional ramifications. The normal hilus was filled with the processes from postsynaptic neurons (Fig. 2-5*A*,*B*). In most degenerating RSs the hilus became greatly enlarged (Figs. 2-5*C*,*D*; Linberg et al., 2009), and, even when its size was maintained, it was no longer filled with neurites because of the retraction of RB dendrites (Fig. 2-5*E*). The remodeling of postsynaptic processes also greatly increased the extracellular space within the invagination. Thus, the normally compact, isolated internal environment of the synaptic invagination was lost and became continuous with the extracellular space of the outer plexiform layer. Presumably, any glutamate released from the photoreceptors would no longer be confined to the synaptic invagination; it would be free to diffuse into the retina and may account for the spike in retinal glutamate suggested to occur during the first 3 d after a retinal detachment in cat (Marc et al., 1998). Glutamate is a potent excitotoxin that can cause rod photoreceptor cell death (Charles-Messance et al., 2020) and changes in the inner retina (Bringmann et al., 2013), including gliosis of Müller cells (Ji et al., 2012) and degenerative changes in neurons (Yang, 2004; Yee et al., 2018; Milla-Navarro et al., 2021). Detachment produces rapid photoreceptor cell death (Cook et al., 1995), gliotic responses in Müller cells (Lewis et al., 2010), as well as aberrant sprouting of neurites from RB, horizontal, and ganglion cells (Lewis et al., 1998; Coblentz et al., 2003; Linberg et al., 2006b) possibly induced by excess glutamate in the retinal environment.

In normal retinas, synaptic vesicles fused to the RS plasma membrane at both the active zone and far from it, usually opposite the lollipop-shaped endings of the HCAT (Fig. 2-10). Evidence suggests that vesicle release at these two locations use different synaptotagmins and that the nonribbon release plays a more modulatory role (Mesnard et al., 2021) that is currently not well understood. In detached retinas, we found no evidence for vesicle fusion at either site in detached retina, a further indication that detachment interrupts the flow of information into the rod pathway. We did, however, observe that ribbon-associated vesicles remained, even in association with very small ribbons (Fig. 2-10*H*). The population of free vesicles was highly heterogenous with the inclusion of many large vesicles (Fig. 2-11). There is evidence for vesicle-to-vesicle fusion that may occur before their fusion to the RS membrane as a mechanism for multiquantal release (Mesnard et al., 2021). In the degenerated state, there may be an imbalance in vesicle production and release resulting in a significant increase in the heterogeneity of the vesicle population.

The presence of a dense population of synaptic vesicles in the HCAT lollipop-shaped endings is congruent with physiological evidence for synaptic feedback from horizontal cells to rod photoreceptors (Thoreson et al., 2008). Only two studies, one in human and one in macaque, have found ultrastructural evidence for identifiable presynaptic sites in the HCAT (Linberg and Fisher, 1988; Tsukamoto and Omi, 2022). These sites are atypically small, but it seems unlikely we would have overlooked them in the tomograms, suggesting that the synaptic feedback in many species is nontraditional in form. Interestingly, we found that HCATs continued to express these vesicles even in a highly degenerated state and after the loss of their lollipop-shaped endings.

The changes we have identified in RS in detached retina likely have profound effects ranging from loss of the primary pathway for sending signals to the inner retina, to a disturbance in glutamate homeostasis. Based on our results and those from previous studies (Linberg et al., 2006b, 2009), within the 7 d detachment time period, the RB dendrites withdraw, leaving behind significant extracellular space (Figs. 2-2*D*, 2-3*B*) within the synaptic invagination and an open hilus, and the HCATs remodel, losing their small lollipop-shaped terminals and ending bluntly within the invagination. Thus, recovery of this synapse would seem to have several challenges, including virtually the complete rebuilding of the rod–RBC pathway. Indeed, there is now evidence that photoreceptor synapses may have very limited capacity for recovery (Townes-Anderson et al., 2021), stressing the need for early intervention or therapeutics that will enhance recovery.

Chapter 3: What is the degenerative progression of the rod spherule over the first 3 days of retinal detachment?

PREFACE

Following up on the Torten et al., 2023 manuscript, I performed EM tomography on RSs in cat retina that had undergone a retinal detachment for a range of time points within the first three days. The samples used in Chapter 3 are from the same batch as those collected for Erickson et al., 1983 (as in Chapter 2). For this work, I performed the entirety of the tomogram collection, a large majority of the segmentation, and all of the writing. Previous undergraduates in the lab, Julie Chung and Olivia Mulry, created the remaining segmentations for this chapter that I did not create myself.

INTRODUCTION

The rod photoreceptor synapse (also called the rod spherule, or RS) is the first synapse in the mammalian visual pathway, and is one of the most complex synapses in the mammalian CNS. This synapse is either adjacent to the nucleus in the rod cell body (Type 2), or, in its predominant form (Type 1), within a spherule at the end of the axon (Li et al., 2016). Within the rod spherule, there are a number of canonical features. The plasma membrane forms an invagination, of which, in cat, 4 postsynaptic processes enter. Two Type B Horizontal Cells Axon Terminals (HCAT) enter the invagination and line either side of the synaptic ribbon. The synaptic ribbon is an arc-shaped electron-dense structure that organizes synaptic vesicles for synaptic transmission, allowing for quick modulation of neurotransmitter release and rapid responses from postsynaptic cells (Matthews and Sterling, 2008; LoGiudice and Matthews, 2009; Zampighi et al., 2011). Two rod bipolar cell dendrites (RB) also enter the invagination, sit within the center of the spherule in the trough made by the ribbon and the HCATs, where they end bluntly within the first 2/3rds of the invagination opening (Torten et al., 2023). The rod bipolar cells transmit signals through the rod visual pathway to the brain, while the horizontal cells integrate signals across nearby photoreceptors (Zampighi et al., 2011). Together, the 2 RBs and 2 HCATs form a tetrad of postsynaptic processes (Torten et al., 2023).

In Chapter 2 (Torten et al., 2023), we explored the normal ultrastructure of this complex synapse, as well as the degenerative changes that this synapse underwent during 7 days of rhegmatogenous retinal detachment. RS appeared with a large number of synaptic ribbons, either free-floating or anchored to the invagination, and either associated with synaptic vesicles or completely free of them. Synapses that maintained an invagination no longer had rod bipolar cells present, and the invaginations that remained were heavily simplified in geometric structure, resulting in spherical invaginations that lacked the complex branching seen in the control (See Fig. 2-4A, B). However, a big question still remains: how long does it take for these changes to occur?

In contrast to the PNS, axonal regeneration is difficult to impossible to achieve in the CNS (Ramon y Cajal, 1928; Bradke, 2022), however, synaptic regeneration can still occur through different mechanisms (Cooke et al., 2022) and with support cells or therapeutic intervention (Purves et al., 2001; Akram et al., 2022; Costa et al., 2022). In order to fully regenerate a synapse like the rod spherule, it seems likely that there is some threshold of degenerative changes, such that, after this threshold has been reached, the synapse is no longer able to fully recover. Unfortunately, photoreceptor synapses may have an intrinsic limited ability to recover (Townes-Anderson et al., 2021), and other ribbon synapses such as in the hair cells of the cochlea do as well (Wan and Corfas, 2015; Chen et al., 2019), so this threshold may be sooner rather than later. Further evidence of that fact is that, even with full retinal reattachment, animals can still experience significant visual deficits (Sørensen et al., 2020), and, even with confirmed outer segment recovery, these issues often remain (Guérin et al., 1989, 1993). Previous work exploring reattachment methodology implied that this threshold lies between 1 and 3 days (Lewis et al., 2003), and Sothivannan et al., 2022 found evidence that early reattachments in patients, within 0-3 days, but ideally within 24hrs.[22], resulted in superior outcomes to those done at 4-7 days. It seems likely that degenerating synaptic structure plays a significant role here, especially with the result that the RBs, the second cell in the mammalian visual pathway, retracts by 7 days of detachment (Linberg et al., 2006b, 2009; Torten et al., 2023).

The results presented in Ch. 2 showed the value of EM tomography in creating high resolution 3-D models and resolving ultrastructural details up to a z-resolution of ~2-3nm (Kremer et al., 1996; Burette et al., 2012; Phan et al., 2017). In this study, we took samples, from the same sample set as in Chapter 2, but that were fixed after 30min., 1hr., 24hr., 48hr., and 72hrs. of detachment, and performed further EM tomography in order to study this early time scale. To explore how much time may represent a degenerative threshold, it is important to understand exactly how long it takes for each of these degenerative changes to occur, such that the retina can be clinically reattached before it is too late.

---

[22] While treating retinal reattachment surgery as urgent is ideal, there are practical concerns such as busy physician schedules, overtime costs, physician fatigue, and physician work-life balance that may delay surgery and prevent immediate reattachment (Lichter, 1992).

METHODS

The materials and methodology used in Chapter 3 are identical to those used in Chapter 2. Please see the Methods section in Chapter 2 for more details. Generally, there were only two differences in methodology between these chapters. First, rather than waiting a full 7 days after detachment before fixing the eye, animals were sacrificed and eyes were fixed after detachment times of 30min., 1hr., 24hrs., 48hrs., or 72hrs. Second, all the tomograms were collected at the University of California, Los Angeles (UCLA) using serial 200nm sections, following the methodology section of Chapter 2 as it pertains to tomograms collected at UCLA. In terms of analysis, there were no methodological differences between Chapters 2 and 3. RS/mm was measured by manually counting RS along a Toluidine Blue stained 500nm semithin section on a Zeiss Axiophot microscope, and dividing by the total length of the RS layer across the section. We decided to measure RS per mm of retina, rather than RS per mm^2 unit area because, observationally, the area of the RS region did not vary significantly across the retina.

Due to the nature of the tissue (i.e. cat tissue that was fixed in the early 1980's), there was only a single animal available per time point in each of the time points analyzed (see Table 3-1). In order to choose the retinal region to perform tomography on, I utilized Detachment charts present within the slide boxes, that described where the detachment was made along the retina as well as the general features and characteristics present within the eye. I analyzed the detachment charts and chose the 2-3 EM blocks that were collected across the detachment region. I then collected semithin sections of these blocks, stained with Toluidine Blue, and analyzed them for quality. Many of the blocks had structural damage due to repeated sectioning and aging, which made them break apart during sectioning. Others had fixation issues, or biological issues associated with the detachment, that made it practically difficult to find appropriate rod spherules for tomography. Due to these problems, there was only a single EM block for each time point that was structurally secure enough to take serial sections, that was a valuable region for imaging, and that also overlapped with the detachment region. To compensate for this issue, we took wide sections, and performed tomography in varied regions along the section.

Table 3-1: List of tomograms from which figures were generated

Condition	Name of Tomogram	Figure(s)	Number of Sections	Pixel Size (nm)
30min.	Cat55714_1	3-2, 3-7	1	16.71
	Cat55714_2	None (Quantification)	1	11.23
	Cat55714_3	None (Quantification)	1	11.23
	Cat55714_4	3-2	1	11.23
	Cat55714_5	None (Quantification)	1	11.23
	Cat55714_071921	3-2	3	4.376
	Cat55714_081621	3-2, 3-6	3	4.376
1hr.	Cat09613_1	None (Quantification)	1	11.23
	Cat09613_2	None (Quantification)	1	16.71

	Cat09613_3	None (Quantification)	1	11.23
	Cat09613_4	3-7	1	11.23
	Cat09613_5	3-6	1	11.23
	Cat09613_010421	3-2, 3-6	3	13.37
	Cat09613_070821	None (Quantification)	4	16.71
	Cat09613_071221	None (Quantification)	3	8.465
24hrs.	Cat32464_1	3-3	1	13.37
	Cat32464_2	3-7	1	11.23
	Cat32464_3	None (Quantification)	1	11.23
	Cat32464_4	3-3	1	8.465
	Cat32464_5	3-3	1	11.23
	Cat32464_080822_4sec	3-3	4	13.37
	Cat32464_080822_1sec	3-3, 3-6	1	13.37
	Cat32464_080922	3-3	4	8.465

48hrs.	Cat32232_120621	3-4	3	11.23
	Cat32232_120721	3-4, 3-6	3	13.37
	022224_48hrRD	None (Quantification)	3	16.71
	022624_48hrRD	None (Quantification)	3	16.71
72hrs.	Cat09612_082520_1	3-5, 3-7	1	8.465
	Cat09612_082520_2	None (Quantification)	1	13.37
	Cat09612_080122	3-5	5	13.37
	Cat09612_072822	3-5	4	11.23
	Cat09612_120820_Serial1	3-5	2	13.37
	Cat09612_120820_Serial2	3-5	2	11.23

Table 3-2: Color code for the 3-D models

Feature	**Color**
Rod Spherule Membrane	Cyan
Synaptic Ribbon	Orange
Ribbon-Associated Vesicles	Magenta
HCATs	Red and Blue
RB Dendrites	Green and Yellow

RESULTS

The feline retina portrays signs of degeneration during early retinal detachments

To validate the presence of the detachment in the sectioning region, and to understand the larger scale changes that occur, we first imaged semi-thin sections on a light microscope to visualize the health and state of the retina after early detachments of 30min., 1hr., 24hrs., 48hrs., and 72hrs.[23]. RS retraction is a canonical characteristic of retinal degeneration after a retinal detachment, with the extent of retraction often used as a metric for extent of degeneration in this context (Linberg et al., 2009; Townes-Anderson et al., 2017, 2023; Halász et al., 2021). Despite no statistically significant change to the number of RS/mm at 30 minutes of detachment (Fig. 3-1A/B, orange arrowheads point out RSs), 1 hour of detachment resulted in a reduction of rod spherules visible in the OPL from 382.9 ± 25.2 at 30min. to 261.9 ± 27.3 RS/mm at 1hr. (Mean ± SEM, N = 3, Fig. 3-1B). The RS/mm continued to decrease and plateaued at 24hrs. (Fig. 3-1B). In later time points, other signs of degeneration began to appear in these semi-thin sections. At 48hrs. of detachment, retinas contained holes and gaps where nuclei would normally sit (Fig. 3-1A, green arrows) as well as nuclei with very condensed chromatin (Fig. 3-1A, pink arrows), a common sign of apoptosis

---

[23] Cat Outer Nuclear Layer (ONL) thickness varies significantly across the area centralis (Mischi et al., 2022), and, observationally, structural organization/extent of degeneration varied across the retina in longer detachment times. Due to this, finding a location along the retina at each detachment time point with a consistent ONL size and organization was quite difficult. We have chosen regions where the inner segments appeared clear and aligned (when present), and have chosen average representative images with regards to the extent of degeneration.

(Oberhammer et al., 1994; Burgoyne, 1999). By 72hrs., Müller cells encroached into the ONL (Fig. 3-1A, yellow arrowhead), something we also saw at 7 days (See Fig. 2-2D). We did not see any significant difference between mitochondrial number in each spherule (Fig. 3-1C); any variability in mitochondrial number is likely due to a lack of depth, as we aimed to capture the majority of the invagination rather than the entire rod spherule and therefore may be missing some mitochondria.

Li et al. 2016 stratified rod spherules by Type 1 (positioned away from the rod cell body by an axon) and Type 2 (attached to the cell body, adjacent to the nucleus). In our investigation, both at a retina-level and an ultrastructural level, we have found no discernible differences between the ways that these two types of RS degenerate. Due to this, we have decided to analyze these two types of spherules together.

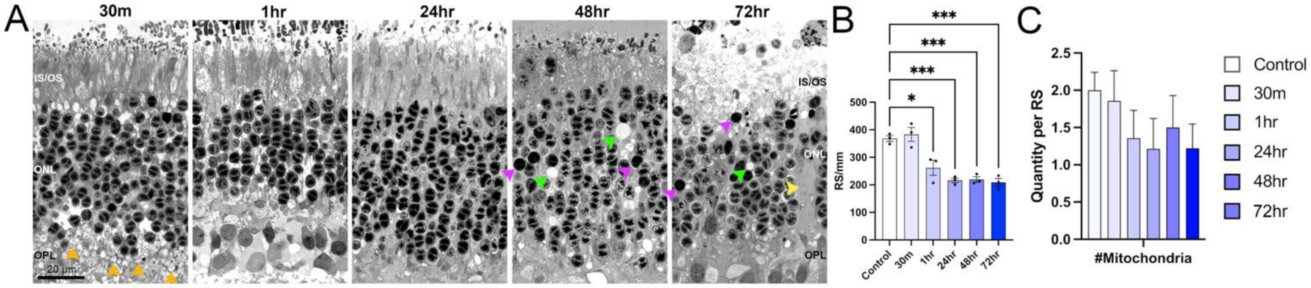

Figure Legend - Figure 3-1: The feline retina portrays signs of degeneration during early retinal detachments. **A.** Semi-thin sections of feline retina at varying time points of retinal detachment. Orange arrowheads point to rod spherules, pink arrowheads point to black/pigmented nuclei, green arrowheads point to gaps in the retina where nuclei should lie, and the yellow arrowhead points to a Müller Cell. **B.** Quantification of the number of rod spherules visible in semi-thin sections at 63X on a Zeiss Axiophot microscope. Each data point represents a single counted section from a different retinal region. Mean ± SEM is depicted. **C.** Quantification of the number of mitochondria visible across the entire tomogram in a single RS. The sample sizes (# of analyzed synapses) for each of the time points for C were as follows: Control, 24; 30min., 7; 1hr., 14; 24hrs., 14; 48hrs., 6; 72hrs., 9. Mean ± SEM is depicted.

Scale Bars: A: 20μm

Ultrastructural remodeling occurs even within 30 minutes to 1 hour of detachment

30 minutes of retinal detachment resulted in synapses that showed early signs of degeneration and remodeling. The synapse in Fig. 3-2A, while normal in terms of postsynaptic process organization, showed some increased extracellular space (‘X’ in Fig. 3-2A). Fig. 3-2B shows a synapse that, again, looks fairly healthy, but contained a ribbon that arced horizontally, and not just vertically as in the control[24]; while only two densities of ribbon appear in the z-slice in Fig. 3-2B, the depth in the tomogram confirmed that they originated from a single arcing ribbon. Fig. 3-2C shows a segmentation from a RS in a retina detached for 30 minutes. Generally, it does appear to have the tetrad arrangement (Torten et al., 2023): a synaptic ribbon, 2 HCATs (red and blue) that line either side of the ribbon, and 2 RBs (green and yellow) that sit in the central region of the synaptic complex, within the arc that is formed by the ribbon and the HCATs. However, the red HCAT formed a half circle on one end (Fig. 3-2C/C’, ‘#’), that surrounded a small density that appeared like a synaptic ribbon. By 30 minutes, some synapses already contained more than one ribbon, shown in Fig. 3-2C/C’ and Fig. 3-2D/D’. Unfortunately, neither of these tomograms contained enough depth to fully capture these ribbons, and so we cannot confirm that they are fully independent from

---

[24] As a comparison, see the linear ribbons shown in Fig. 3-2C’/G, and compare to the curving ribbons shown in Fig. 3-2B/F’’/H. All of these ribbons are shown from a similar perspective.

the main ribbon. However, due to the shape, size, and orientation[25] of these ribbons, we expect that they are indeed independent structures.

By 1 hour of detachment, the RS showed more significant remodeling in terms of postsynaptic process organization. In Fig. 3-2E/E'/E'', and 3-2F/F'/F''[26] we show two different synapses that were present within the same tomogram, and therefore came from the exact same region of the retina. Fig. 3-2E/E'/E'' shows a fairly normal looking synapse. A single synaptic ribbon arched over the invagination, 2 HCATs lined the synaptic ribbon, and 2 RBs sat within the trough formed by the arcing synaptic ribbon and the HCATs. Fig. 3-2F/F'/F'', on the other hand, shows a synapse that has undergone some degenerative remodeling. In this synapse, the red HCAT did not extend all the way along the far side of the ribbon, and the green RB process appeared to pull away in a perpendicular direction from the ribbon (Fig. 3-2F''). The ribbon was curved in space and elongated, as if it had attempted to maintain contact with the green RB that was (presumably) retracting from the invagination. At this point, while the blue HCAT in Fig. 3-2F/F'/F'' had maintained its complex branching structure as seen in the control (see Fig. 2-7A/C), the red HCAT appeared much simpler. Not all synapses at 1 hour of detachment portrayed this extensive remodeling, but many did.

---

[25] The second ribbon in Fig. 3-2D/D' appeared nearly perpendicular to the primary ribbon, making it highly unlikely for these two ribbons to be part of the same larger ribbon.

[26] For Fig. 3-2E/F: E/F are representative slices from the tomogram, E'/F' are views of the segmentation angled from the synaptic ribbon side, and E''/F'' are views of the segmentation angled from the postsynaptic process side (flipped 180°).

At 30min. of detachment, the structure of the invagination membrane heavily simplified. At 1hr., some of the bulbous outgrowths, caused by HCAT telodendria, and also seen in the control (see Fig. 2-4B, and 2-7A/C), were maintained (Fig. 3-2G/H/I), but, these synapses appeared much rounder and smoother (Fig. 3-2K). In a general sense, the area, perimeter, circularity, and solidity of the invagination all increased significantly after a detachment (Fig. 3-2J/K). While area and perimeter stayed fairly consistent after this initial change through the first 3 days, the circularity and solidity significantly increased again at 48hrs. (Fig. 3-2K). It should be noted that, while these values all indeed increased, they all still exceeded the increase that we saw at 7 days of detachment (compare Fig. 3-2J/K to Fig. 2-4E/F); after the significant increase by 72hrs., all of these values likely slowly decrease to match the results at 7 days.

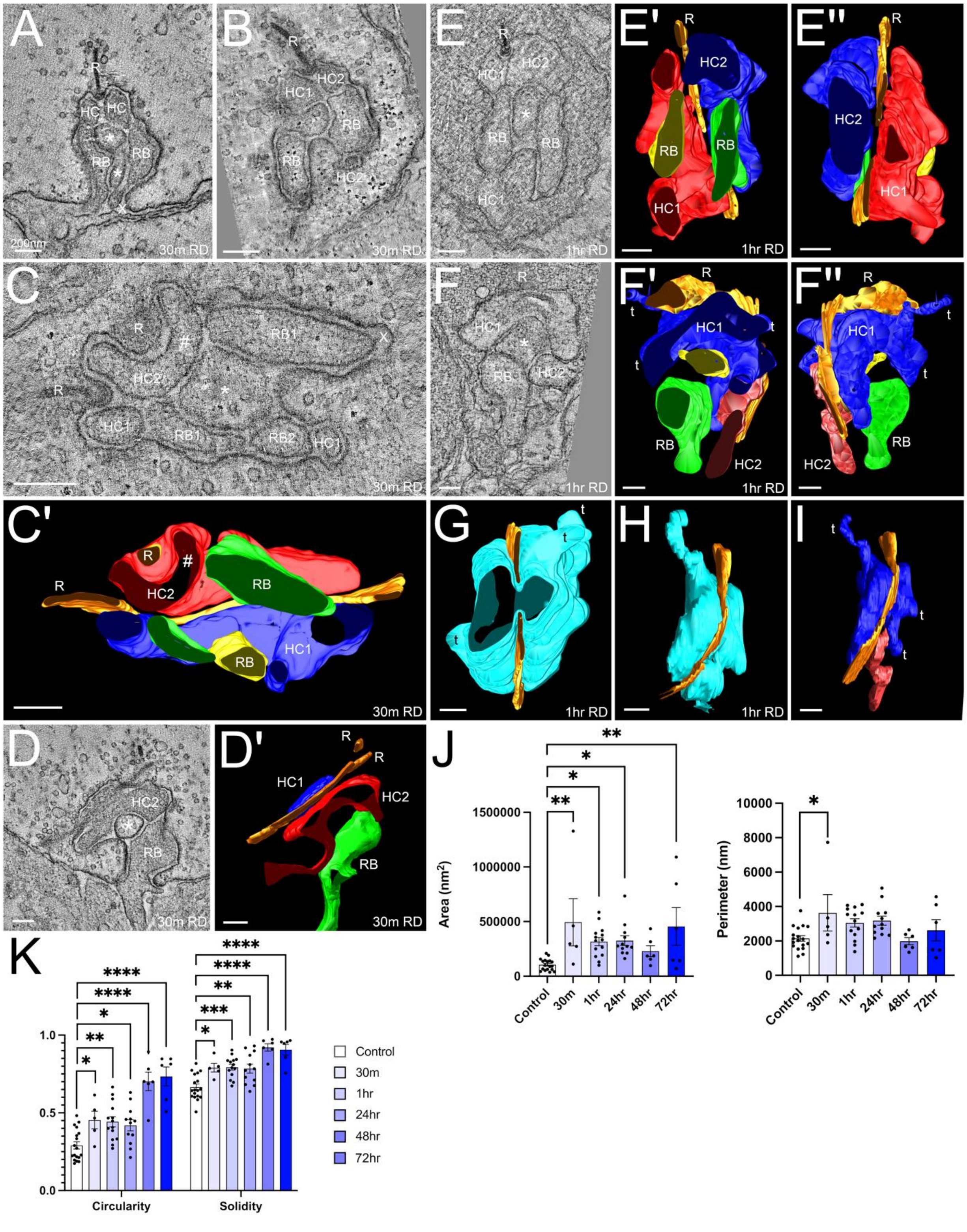

Figure Legend - Figure 3-2: Ultrastructural remodeling occurs even within 30 minutes to 1 hour of detachment. **A.** A representative z-slice from a tomogram of a particular synapse after 30min. of detachment. This synapse showed minor increased extracellular space (‘X’), but an otherwise normal organization. **B.** Another example of a fairly normal synapse at 30min. of detachment, featuring a curving synaptic ribbon. **C/C’.** An example of a synapse that had a normal organization, but showed changes in the red HCAT as well as the presence of a new ribbon. C’ shows the segmentation for the tomogram in C, with red and blue HCATs, green and yellow RBs, and an orange synaptic ribbon. Extracellular space is pointed out by the ‘X’. **D/D’.** Another tomogram from 30min. of detachment showing a second ribbon present directly next to, and nearly perpendicular to, the primary ribbon. **E/E’/E’’.** Three views of a specific synapse at 1hr. of detachment. This synapse appeared fairly normal in organization. E’ shows the segmentation from the view of the postsynaptic processes, while E’’ flips the model 180° and shows the segmentation from the view of the ribbon. HCATs are shown in red and blue, RBs are shown in green and yellow, and the synaptic ribbon is shown in orange. **F/F’/F’’.** Another 1hr. RD synapse, this time showing remodeling of the postsynaptic processes. As in E, F’ shows the model from the view of the postsynaptic processes, while F’’ shows the model from the view of the ribbon. The color scheme remains the same as in E. **G.** The segmentation from the synapse in E, but with just the ribbon and the plasma membrane visible, in order to show the simplification of the plasma membrane. **H/I.** An invagination that appeared mildly simplified but still contained the bulbous extensions produced by HCAT telodendria (t). H shows the model with only the plasma membrane and synaptic ribbon visible, while **I** shows the model with only the red and blue HCATs and the synaptic ribbon visible. **J.** Quantification of the area and perimeter of the invagination space in 2-D at the largest and most complex z-slice.

Mean ± SEM is depicted. **K.** Circularity and solidity of the invagination space, as in J. In both J and K, each data point represents a single invagination of a single RS. The sample sizes (# of analyzed invaginations) for each of the time points for the graphs in J and K were as follows: Control, 18; 30min., 5; 1hr., 14; 24hrs., 12; 48hrs., 6; 72hrs., 6. Mean ± SEM is depicted.

Scale Bars: A-I: 200nm

24 hours of retinal detachment results in significant ultrastructural remodeling of the rod spherule, including postsynaptic process reorganization, RB retraction, and the presence of large curving ribbons

At 1 hour of detachment, there was minor remodeling, but many synapses still had plenty of normal characteristics. At 24hrs., we no longer found any synapses that could be considered normal. All synapses showed signs of degeneration including elongated synaptic ribbons (Fig. 3-3B, G, K), significant postsynaptic process remodeling (Fig. 3-3C/D/D’, H, I, J, K), an expanded hilus (Fig. 3-3A, B, L, N), and in extreme cases, enlarged HCATs and multiple ribbons (Fig. 3-3L).

Figure 3-3A-D’ shows a specific 24hr. RD synapse. This synapse contained a very large arcing ribbon (Fig. 3-3B) that appeared as 3 separate densities in a z-slice (Fig. 3-3A); this twisting shape is incredibly unique, and is one of the most extreme variant ribbons found. Also note that that the invagination structure itself (Fig. 3-3B, cyan) appeared very simple, and nearly like a spherical indent into the membrane. In C, only the ribbon and the postsynaptic processes are visible. From this view, note how closely the HCATs still associate with the ribbon, but rather than each HCAT associating on either side of the ribbon, the HCATs interface with the ribbon entirely on one side. In this synapse, the postsynaptic processes, in a general sense, organize perpendicularly to the ribbon, rather than parallel as seen in Fig. 3-2C’ and Fig. 3-2E’. This is shown more clearly when this synapse is viewed from a top-down angle as in Fig. 3-3D/D’. In those views (and the z-slice shown in Fig. 3-3A), it becomes clear that the RB dendrites sat at the very base of the invagination and were positioned further away from the ribbon than they would normally be in a healthy control, indicating that they were likely in the process of retraction (white arrows in Fig. 3-3A and black arrows in Fig. 3-3D' indicate presumed movement direction of the retracting RBs[27]).

Looking at another synapse (shown in Fig. 3-3E-H), we see a similar trend in terms of remodeling. In F, the RS plasma membrane is shown translucently, along with the ribbon. While most of the ribbon forms a normal arc over the invagination, the end of the ribbon, the portion that primarily associates with the postsynaptic processes at this synapse, has split into three distinct regions (Fig. 3-3G, bottom, white arrowheads). In addition, the invagination had simplified and appeared nearly as an oval (Fig. 3-3G, top). Surprisingly, when viewing just the postsynaptic processes (Fig. 3-3H), the blue and red HCATs still laid along either end of the ribbon. However, this synapse is entirely missing one RB, and the other RB (Fig. 3-3H, green) associated with the ribbon on just the singular convoluted end, and not within the arc of the ribbon as in the control.

Generally, the key features of a 24hr. RD synapse included an elongated ribbon, 1 or 2 RBs (at least one RB was missing in 8/11 analyzed 24hr. RD synapses), and mislocalized processes, with one of the RBs retracting perpendicularly from the ribbon. These characteristics can also be seen in other synapse examples (Fig. 3-3I-L). The

---

[27] It is important to note that we cannot definitively say that these RB processes are moving in the direction of the arrows without temporal data. However, in previous time points we see the RBs penetrate much further into the invagination and associate much more closely with the ribbon. In later time points, we see a complete lack of RB dendrites. Together, this information describes that 24hrs. of detachment represents an intermediary time point when the RBs are in the process of retracting.

synapse in Fig. 3-3L shows 2 distinct ribbons[28] (visually appearing as 4 densities in the z-slice) along with a hypertrophic HCAT that filled nearly the entire invagination; these two features are consistent characteristics of synapses at 48hrs. of detachment, but can be seen by 24hrs. in more degenerated synapses. In addition, the hilus expanded in diameter (Fig. 3-3N, can be seen clearly in Fig. 3-3A, E, L) and this change became statistically significant after 48hrs. of detachment.

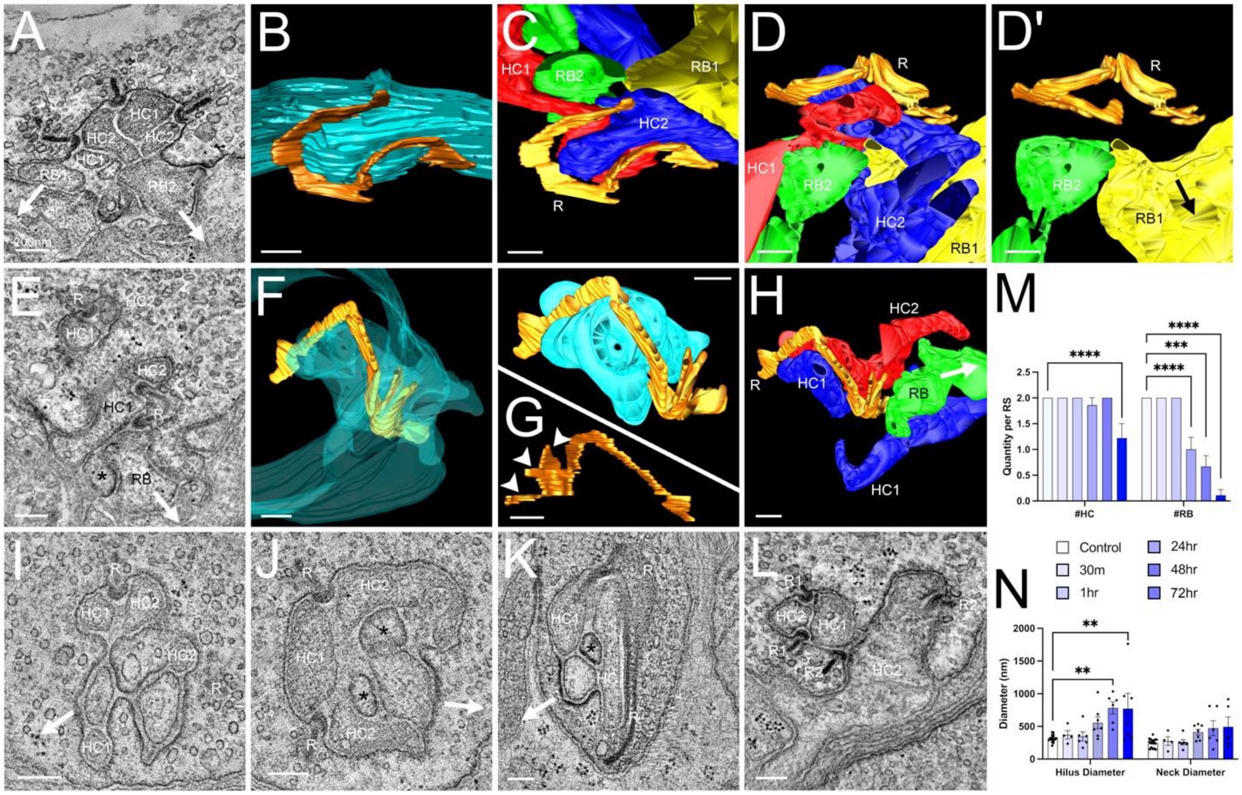

Figure Legend - Figure 3-3: 24 hours of retinal detachment results in significant ultrastructural remodeling of the rod spherule, including postsynaptic process reorganization, RB retraction, and the presence of large curving ribbons. **A-D'.** A

---

[28] Confirmed by tomogram depth.

tomogram from 24hrs. of detachment. A shows a representative z-slice, while B-D’ show the segmentation from this tomogram. B shows the model with only the simplified plasma membrane (cyan) and large curving synaptic ribbon (orange) visible, while C shows just the ribbon with the four postsynaptic processes (HCATs in red and blue, RBs in green and yellow). D shows the model in C, but rotated 180° and looked directly down upon from above (relative to the perspective shown in B/C). D’ is the same as D, but with the HCATs not visible, showing the increased distance between the RBs and the ribbon. The white arrows in A and the black arrows in D’ indicate the speculative direction of retraction for the RB. **E-H.** Another tomogram from a 24hr. RD. E shows a z-slice from the tomogram, while F-H show the segmentation. F depicts only the plasma membrane (translucent cyan) and the ribbon (orange), to show how the ribbon still maintained the arc over the invagination. G (top) shows a top-down view (relative to the perspective in F) with a solid plasma membrane, while G (bottom) shows just the ribbon from a side view. White arrowheads point out three protruding sections of the ribbon on one end. H shows a similar perspective as in F, but with only the ribbon and postsynaptic processes visible. As in A, the white arrows in E and H indicate the speculative direction of RB retraction. **I-L.** Four different examples of synapses from a 24hr. RD with varying phenotypes in terms of organizational remodeling. Generally, I-K show a single RB retracting perpendicularly away from the ribbon (with presumed retraction direction pointed out by arrows), while L shows a very enlarged HCAT along with two distinct ribbons (that appear as 4 densities in the z-slice). **M.** The number of HCs and RBs present in a given invagination. The sample sizes (# of analyzed synapses) for each of the time points were as follows: Control, 24; 30min., 7; 1hr., 14;

24hrs., 14; 48hrs., 2; 72hrs., 9. Mean ± SEM is depicted. **N.** The diameter of the hilus and the neck of the invagination. The sample sizes (# of analyzed hilus/neck regions) for each of the time points for N were as follows: Control, 17; 30min., 4; 1hr., 6; 24hrs., 7; 48hrs., 6; 72hrs., 5. Mean ± SEM is depicted.

Scale Bars: A-L: 200nm

48 hours of detachment results in RS containing large hypertrophic HCATs and multiple ribbons

48hrs. of detachment resulted in the most severe level of degeneration that still contained some semblance of organization and structure. In other words, the spherule was actively degenerating, but had not plateaued to the degree of degeneration seen at 7 days. In 5/6 synapses analyzed, there was a single very large hypertrophic HCAT, and a smaller shrunken HCAT (Fig. 3-4B/D). All synapses at 48hrs. contained exactly 2 ribbons, neither of which resembled a healthy ribbon. Interestingly, when the ribbons were unable to position in a normal location, they still, in many cases, associated between two HCATs; this was not always possible, depending on the synapse. For example, the two ribbons in Fig. 3-4B showed this behavior. The rightmost ribbon in Fig. 4B does seem to curve in order to position between the blue and red HCATs (despite the fact that the blue HCAT is very small and not able to associate all along the ribbon). The leftmost ribbon in Fig. 3-4B also found a position where it could maintain an HCAT on either side, but those HCAT processes in this case originated from the same red cell (Fig. 3-4B, left ribbon). In cases where a RB was present, as in Fig. 3-4D/D', both ribbons organized such that each HCAT lined either side of the ribbon (Fig. 3-4D). However, the ribbon that was closer to the RB extended much further along the process such that the tip of the ribbon still maintained a close contact with the retracting RB (Fig. 3-4D', white arrow). In general, by 48hrs. of detachment, the invaginations themselves appeared very round and simple (Fig. 3-4B'). They still maintained a reasonably large area and perimeter (Fig. 3-2J), but showed a specific significant increase in both circularity (0.29 ± 0.02 in the control [N = 18], 0.42 ± 0.04 at 24hrs. [N = 12], and 0.70 ±

0.06 at 48hrs. [N = 6]) and solidity (0.67 ± 0.02 in the control [N = 18], 0.78 ± 0.03 at 24hrs. [N = 12], and 0.92 ± 0.02 at 48hrs. [N = 6])(Fig. 3-2K) to the point that many of the invaginations simply looked like spheres.

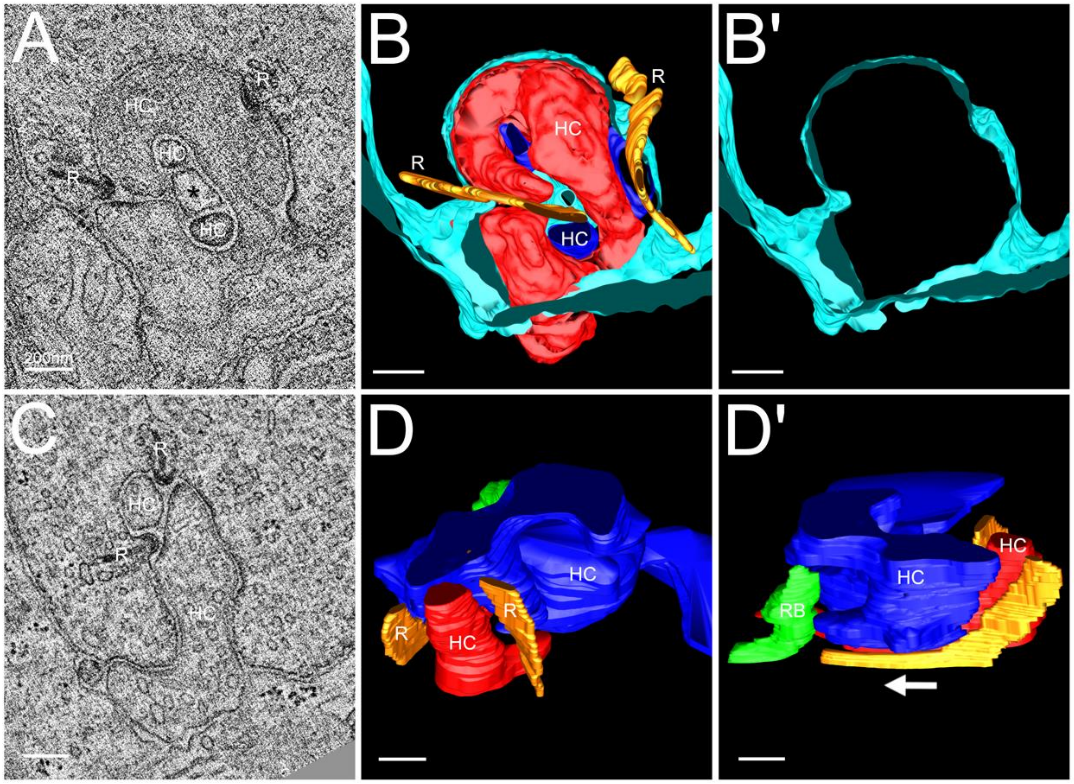

Figure Legend – Figure 3-4: 48 hours of detachment results in RS containing large hypertrophic HCATs and multiple ribbons. **A-B’.** A tomogram from a 72hr. RD. A is a representative z-slice from the tomogram. B is the segmentation of the tomogram showing two HCATs (large red and small blue), two synaptic ribbons (orange), and the plasma membrane (cyan). B’ shows the same image in B, but with just the plasma membrane showing, to visualize how simplified the invagination has become. **C-D’.** Another 72hr. RD tomogram, with a very large HCAT (blue) and a smaller HCAT (red) adjacent to it. Also shown are two synaptic ribbons and a single RB (green). D’ shows the same model in D, but rotated approximately 90° counter-clockwise. The arrow in D’ indicates the direction that the ribbon presumably had extended to keep close contact with the RB as it retracted.

Scale Bars: A-D’: 200nm

After 3 days of detachment, the RS undergoes significant degeneration and portrays degenerative characteristics similar to 7 days of detachment

By 72hrs. of detachment, only 1 out of 9 synapses contained identifiable rod bipolar processes. All analyzed RS at 72hrs. of detachment were significantly degenerated, and many synapses only contained a single HCAT process. Those that contained more tended to be highly simplified, and lacked standard organizational structure. Even in the healthiest synapse we found (Fig. 3-5A/B/B'), the invagination appeared completely round, there were no RB processes, and there were 2 ribbons, similar to synapses at 48hrs. of detachment. Many synapses contained only a single HCAT (Fig. 3-5C-D'', E/F/G, G') with an invagination that appeared as a circle around the HCAT (Fig. 3-5D, G). In these synapses there were usually 2 ribbons, and these ribbons formed small cages surrounding the HCAT process (Fig. 3-5F, G'). Some synapses lacked an invagination altogether (Fig. 3-5H/I), and the horizontal cells present were simply indented into the membrane (Fig. 3-5J). The synapse in Fig. 3-5H was particularly striking, as it very closely resembled the 7 day detached synapse in Fig. 2-9D/D'. Beyond simply matching in structure (i.e. lacking an invagination, with just two identifiable processes that indent into the membrane), what was also similar to that 7 day synapse was that this synapse also contained 2 processes that were unidentifiable. These processes (white and cyan in Fig. 3-5J') both contained vesicles, a characteristic of horizontal cell processes, and did not show any membrane densification apposed to the spherule membrane, a characteristic of rod bipolar cell processes. While not all synapses at 72hrs. of detachment appeared like those at 7 days of detachment, the most severely degenerated synapses did. This seems to be the latest stage of detachment: a vast majority of RS contained either a heavily simplified invagination with 1-2 HCATs, or simply a lack of any invagination at all (but with synaptic ribbons still floating in the cytoplasm).

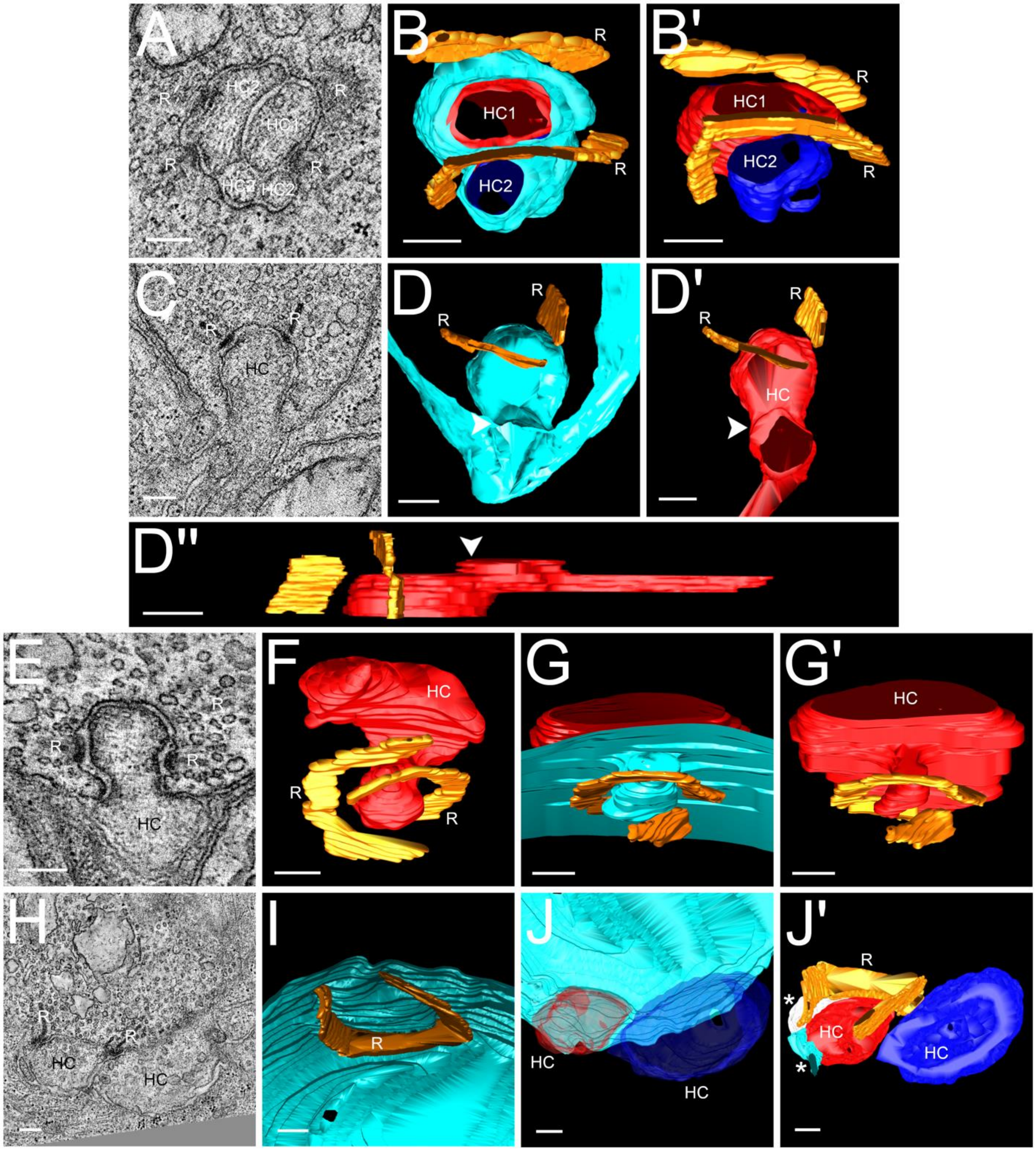

Figure Legend – Figure 3-5: After 3 days of detachment, the RS undergoes significant degeneration and portrays degenerative characteristics similar to 7 days of detachment. **A-B’.** A 72hr. RD tomogram of a relatively healthier synapse from this time point. A shows a representative z-slice from the tomogram, while B and B’ show the segmentation. B shows the model including the plasma membrane (cyan), while B’ shows the model without it. **C-D’’.** An average 72hr. RD tomogram, featuring just a single HCAT (red) and two ribbons (orange). D shows the model with the plasma membrane, while D’ shows it without. D’’ is a side view of the model in D’. The white arrowhead points out the hilus. **E-F.** E is a z-slice from a tomogram showing a heavily simplified invagination with just a single HCAT, and F is a model of this tomogram. **G-G’.** A segmentation from a 72hr. RD tomogram showing a very simplified invagination either with (G) or without (G’) the plasma membrane (cyan). **H-J’.** A 72hr. RD tomogram depicting significant degeneration and a complete lack of an invagination. I shows the model from the inside of the RS, where there is no invagination at all, but merely light indents into the membrane (cyan) on the inside of the arc of the synaptic ribbon (orange). J shows the outside of this RS, where the blue and red HCATs are shown translucent to see the light indents they make against the cyan plasma membrane. J’ shows the same orientation and perspective as J, but with no plasma membrane, and other unidentified processes also segmented. The white and cyan process in J’ were not identifiable as either HCATs or RBs.

Scale Bars: A-J’: 200nm

Ribbons elongate and subsequently fragment over the first 3 days of detachment

Synaptic ribbons in the healthy rod spherule appear as a long arc that folds over a synaptic ridge opposite the postsynaptic complex (see Fig. 2-10A-C for a clear example). As mentioned earlier, presumable new ribbons began to appear after just 30 minutes of detachment (Fig. 3-2C, 3-2D, 3-6A-A''), with definitive independent ribbons clearly present by 1 hour (Fig. 3-6B, green arrowhead, 3-6C). Fig. 3-6A-A'' shows a segmentation of a 30min. RD synapse, showing either the plasma membrane (cyan) and the ribbons (orange) (A), the postsynaptic processes and the ribbons (A'), or just the ribbons alone (A''). This view illustrates that the main ribbon formed a smooth arc over the invagination, apposed to the postsynaptic complex, and appeared fairly normal, as the main ribbon did in all of the analyzed 30min. detached synapses. However, the second ribbon in Fig. 3-6A-A'' appears off to the side. The synaptic complex had seemingly made room for this new ribbon by curving the plasma membrane and HCAT around it. Fig. 3-6B shows a 1hr. RD synapse, again with a second ribbon adjacent to the first. In this case, however, the entire second ribbon was contained within the tomogram volume and confirmed to be independent (Fig. 3-6C shows a segmentation of the tomogram in B)

With increased detachment times came ribbons with strange distinct protrusions, visually appearing as if the ribbon was about to fragment into pieces (Fig. 3-3G, 3-6D), as well as longer arcing ribbons (Fig. 3-3B, 3-6E). By 72hrs., a majority of analyzed synapses contained more than one ribbon, even containing up to 4 distinct ribbons (Fig. 3-6G-J); the synapses with a larger number of ribbons tended to be those that lacked an invagination. It should be noted that at 7 days of detachment, there were synapses containing up to 5 distinct ribbons (see Fig. 2-4C, 2-9A, 2-10H), indicating a progression in ribbon degeneration.

When quantified, the number and length of the ribbons stood out. The number of ribbons per RS doubled from 1 in the control (N = 24) to 2 at 48hrs. (N = 6, Fig. 3-6K), and increased further to 2.8 ± 0.5 at 72hrs. (N = 9, Mean ± SEM). The length of the ribbon nearly doubled from the control (677.9 ± 94.8nm, N = 22, Mean ± SEM) to 30min. (1191.0 ± 154.2nm, N = 7, Mean ± SEM) but then decreases back near the average length of the control at 48hrs. (709.9 ± 158.4nm, N = 4, Mean ± SEM), and drops even further at 72hrs. (458.3 ± 52.7nm, N = 24, Mean ± SEM, Fig. 3-6L). Overall, this data implies that ribbon length was conserved, after an initial elongation of the ribbon after 30 minutes. With just the 7 day detachment data, it was difficult to make conclusions about ribbon fragmentation. Based on the fact that the ribbon length has a consistent inverse relationship with the ribbon number after 30min. (Fig. 3-6K/L), it seems highly unlikely that these ribbons are produced *de novo*, and are instead fragmented off from the primary elongated ribbon.

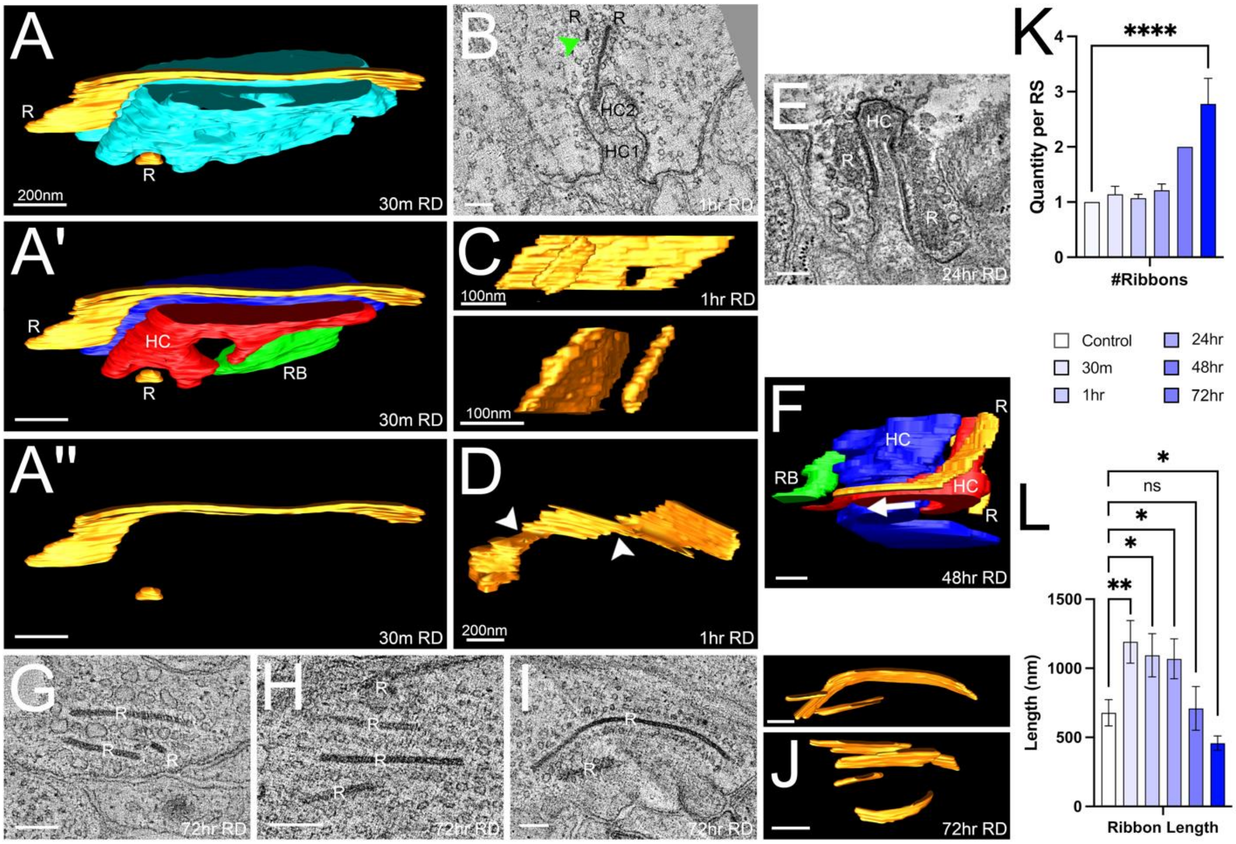

Figure Legend – Figure 3-6: Ribbons elongate and subsequently fragment over the first 3 days of detachment. **A-A''.** A 30min. RD synapse with the ribbon (orange) visible along with the plasma membrane (A, cyan), the postsynaptic processes (A', red/blue HCATs and green RB), or alone (A''). **B.** A synapse at 1hr. of detachment, showing a second ribbon (green arrowhead) adjacent to the main ribbon of the invagination. **C-D.** Examples of ribbons from a 1hr. detachment. C shows the same 2 ribbons from the synapse in B, from two different angles (top and bottom), to show that these are indeed two distinct ribbons. Note that the smaller ribbon in C is fully encapsulated by the tomogram. The ribbon in D shows three distinct densities of ribbon, separated by thin extensions (white arrowheads), which give the visual indication that these three may fragment in the near future. **E.** A synapse from a 24hr. detachment, showing a single long ribbon that arcs heavily around the invagination. **F.** A segmentation from a 48hr. detachment (the same model as in Fig. 3-4C-D'), showing two distinct ribbons, where one ribbon presumably elongated to maintain association with the RB process. **G-I.** Three example synapses from a 72hr. detachment that lacked an invagination, and only contained multiple synaptic ribbons. **J.** Segmentations of the tomograms in I (top) and H (bottom), showing only the ribbons. **K-L.** Quantification of the number of ribbons in each RS (K) and the length of each individual ribbon across RS (L). The sample sizes (# of analyzed synapses) for each of the time points in K were as follows: Control, 24; 30min., 7; 1hr., 14; 24hrs., 14; 48hrs., 6; 72hrs., 9. The sample sizes (# of analyzed ribbons) for each of the time points in L were as follows: Control, 22; 30min., 7; 1hr., 11; 24hrs., 17; 48hrs., 4; 72hrs., 24. Mean ± SEM is depicted.

Scale Bars: A-B: 200nm, C: 100nm, D-J: 200nm

Longer detachment times lead to dysregulation of vesicle size and patterning

Focusing on synaptic vesicles, one primary result stood out: there was a sharp drop in the synaptic vesicle density in the RS after 30min. of detachment (from 16.3 ± 0.9 vesicles/10^6nm^3 in the control [N = 21] to 6.7 ± 1.4 vesicles/10^6nm^3 at 30min. [N = 7], Fig. 3-7A, E). While this drop did recover somewhat by 1 hour (11.9 ± 1.2 vesicles/10^6nm^3 at 1hr. [N = 14], Fig. 3-7B, E), it was never able to reach healthy levels until 7 days (see Fig. 2-3E). Clearly, there was some significant acute response that the RS underwent that resulted in a massive reduction in synaptic vesicle content, that took time to recover from. It is not clear why this might have been the case.

As seen at 7 days of detachment, larger vesicles also began to appear starting at 24hrs. (Fig. 3-7A, C, D, white arrowheads and magenta spheres), filling the cytoplasm in some cases. The model in Fig. 3-7D is from the same tomogram as the image in Fig. 3-6G; in Fig. 3-6G these clear large vesicles were apparent all around the three synaptic ribbons. When quantifying the number of different vesicle sizes, there was a linear decrease in the number of normal vesicles along with a linear increase in the number of large vesicles in increasing detachment times (Fig. 3-7G). In addition, we also measured the coefficient of variation of intervesicular distance, to see how regularly spaced the synaptic vesicles were along the ribbon. At 7 days we found a large increase in this value (see Fig. 2-10I), and, validating that finding, here there was a consistent small linear increase in the coefficient of variation with increasing detachment time points (Fig. 3-7F). Over the first 3 days, retinal detachment resulted in an inability to consistently regulate vesicle content, which resulted in larger vesicles, and misregulated vesicles along the ribbon.

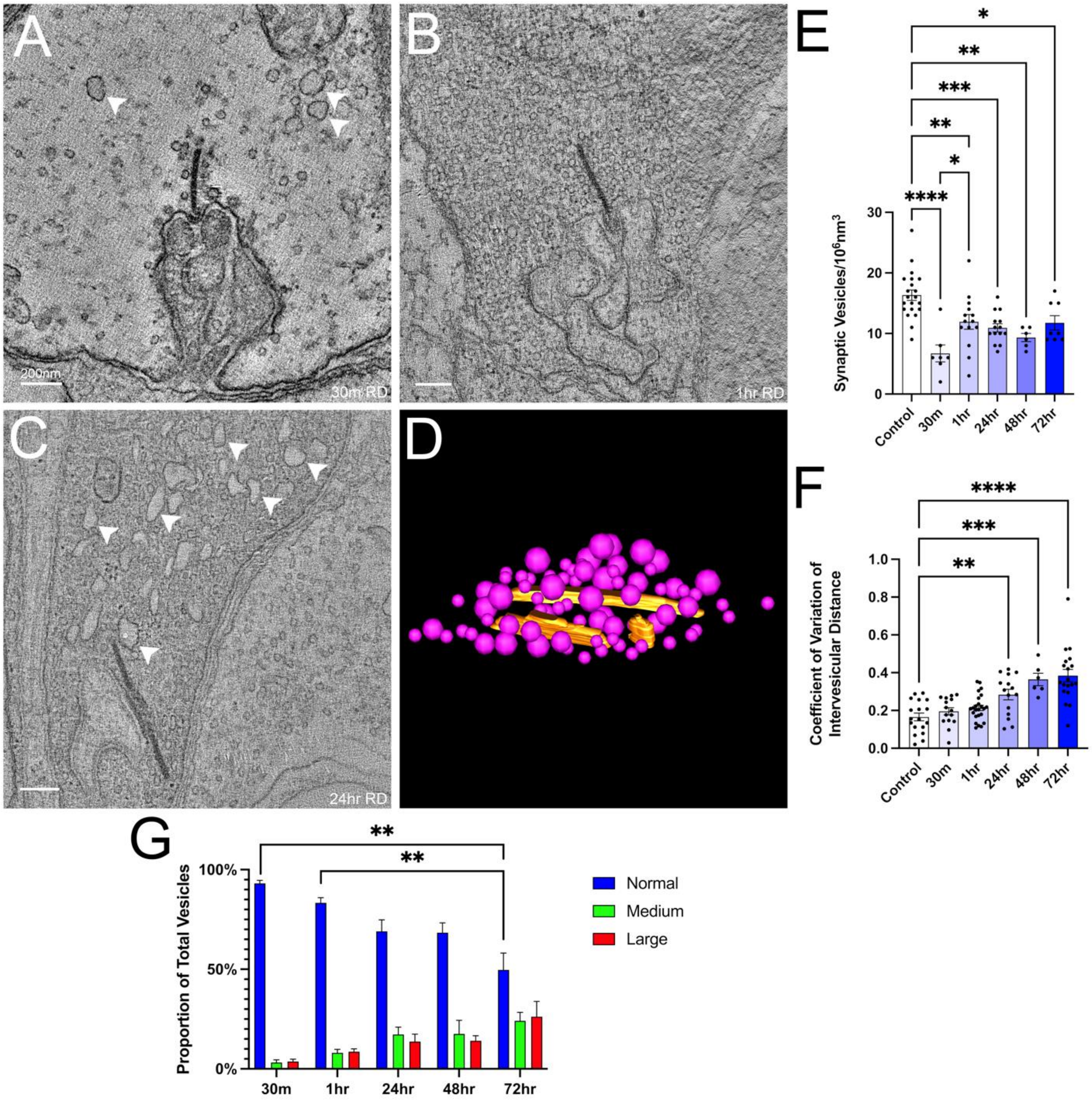

Figure Legend – Figure 3-7: Longer detachment times lead to dysregulation of vesicle size and patterning. **A.** A tomogram from 30min. of detachment, that showed a lack of overall vesicle content within the cytoplasm, and the presence of some large vesicles (white arrowheads). **B.** A tomogram from 1hr. of detachment that showed a significant recovery of the loss of synaptic vesicles seen at 30min. **C.** A tomogram from 24hrs. of detachment from a synapse with many large vesicles throughout the cytoplasm (white arrowheads). **D.** A segmentation from a 72hr. RD tomogram (the same tomogram as in Fig. 3-6G) from a synapse with many large vesicles completely surrounding the three synaptic ribbons. There is no invagination within this RS. **E.** The number of synaptic vesicles in the cytoplasm adjacent to the invagination in a 200nm square, across 20 z-slices in the relative center of the invagination in terms of tomogram depth. The sample sizes (# of analyzed synapses) for each of the time points were as follows: Control, 21; 30min., 7; 1hr., 14; 24hrs., 14; 48hrs., 6; 72hrs., 8. Mean ± SEM are depicted. **F.** The coefficient of variation (Standard Deviation/Mean) of the distance between adjacent synaptic vesicles along the synaptic ribbon. Each data point represents the coefficient of the vesicle spacing along a single ribbon. The sample sizes (# of analyzed ribbons) for each of the time points were as follows: Control, 18; 30min., 15; 1hr., 24; 24hrs., 15; 48hrs., 6; 72hrs., 19. Mean ± SEM are depicted. **G.** The proportion of different vesicle types across detachment time points. Each bar represents the Mean ± SEM of the analyzed synapses at each time point, made by counting 20-30 vesicles per RS and quantifying the percentage of each type. Vesicles were easily visibly identifiable into three categories (normal, medium, and large), and there were few to no vesicles of intermediate size between these three options. The sample sizes (# of analyzed synapses) for each of the time points were as follows: 30min., 8; 1hr., 14; 24hrs., 11; 48hrs., 3; 72hrs., 8.

Scale Bars: A-C: 200nm, D: 500nm

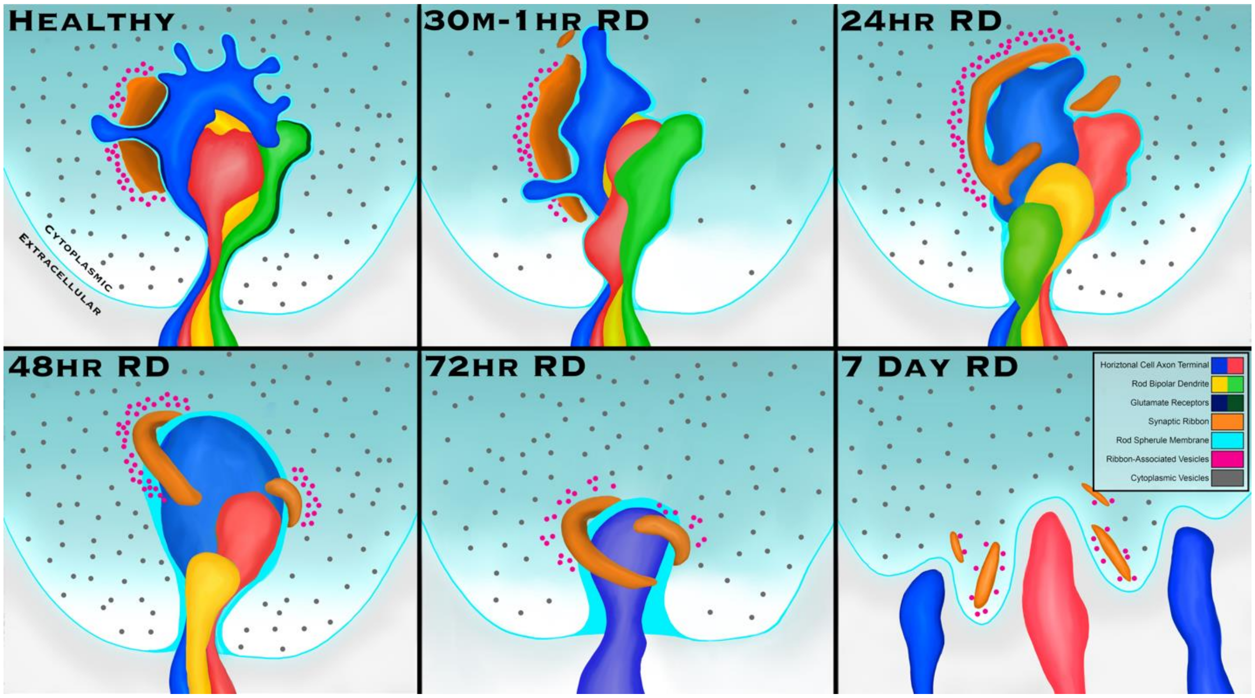

Figure Legend – Figure 3-8: Three days of retinal detachment results in significant remodeling and degeneration of the rod photoreceptor synapse. After just 30 minutes to 1 hour of detachment, there is a reduction in cytoplasmic synaptic vesicle content and early remodeling of the postsynaptic processes. The ribbon may fragment in some cases, but most often it will significantly elongate. By 24 hours, more significant remodeling occurs. The rod bipolar dendrites begin to retract from the center of the invagination, and move away from the ribbon as they start to leave the synaptic complex. HCATs simplify significantly, and the overall invagination structure becomes more rounded and smooth. By 48hrs., the synapse is missing at least one of the RBs, and one of the HCATs will expand to fill the extra space. There are generally two synaptic ribbons interfacing with the invagination. After 72hrs. have passed, the rod bipolar cells are entirely gone from the invagination. There are usually only 1-2 horizontal cell processes, and the remaining invagination is almost completely spherical.

The synaptic ribbons surround the invagination and form a cage around the remaining process(es). The most severely degenerated synapses at 72hrs. lack an invagination entirely, with many appearing very similar to those at 7 days of detachment.

DISCUSSION

Conclusions

In this study, we investigated the ultrastructure of the rod photoreceptor synapse during the first three days of rhegmatogenous retinal detachment. Over the course of the first 3 days, a range of degenerative characteristics appeared (Fig. 3-8). Within 30 minutes, new synaptic ribbons were present, small and directly adjacent to the primary ribbon (Fig. 3-2C, D). Within the first hour, minor remodeling occurred; one of the HCATs moved towards one end of the ribbon (Fig. 3-2F/F'/F'') and one of the RBs began to retract perpendicularly away from the ribbon (Fig. 3-2D/D', F/F'/F''). At 24hrs. a large majority of the degenerative changes have begun to occur, including large scale reorganization of postsynaptic processes (Fig. 3-3A-D', E-H, I-L) and complete retraction of at least a single RB process in a majority of tomograms (8 out of 12 analyzed synapses, Fig. 3-3M). At 48hrs., one of the HCATs in each synapse grew significantly in size (Fig. 3-4B, D), leaving the other one to compress into the remaining space. All synapses contained exactly two distinct ribbons at this time point (Fig. 3-6K). 72hrs. of detachment appeared similar to tomograms taken at 7 days of detachment (see Ch. 2) indicating that the degenerative peak occurs around 72hrs., with changes plateauing over the following few days. At 72hrs. of detachment, there were a range of degenerative levels. The least degenerated RSs still contained both horizontal cell processes and two ribbons (Fig. 3-5A-B'), while the most degenerated synapses didn't even contain an invagination (Fig. 3-5H-J'). In many cases, there was simply a single HCAT surrounded by a spherical invaginating membrane, and a cage of synaptic ribbons (Fig. 3-5C-G'). It seemed that there were two separate time points that represented a specific significant change in the RS. At 24hrs., significant remodeling began to occur, and the structural geometry (circularity/solidity) heavily simplified (Fig. 3-2K). At 48hrs., there was significant breakdown in the structural organization of the invagination and the maintenance of postsynaptic process organization. Circularity and solidity significantly increased (Fig. 3-2K), and, by 72hrs., no synapses contained rod bipolar cell processes (Fig. 3-3M). 48hrs. also represented a peak in hilus diameter (Fig. 3-3N), likely to allow space for the RBs to retract. Clearly, synaptic remodeling occurs even within a single day of retinal detachment, with more dramatic remodeling and RS breakdown over the next few days.

Consequences to the Visual Pathway

The rod bipolar cell is the first synapse in the mammalian visual pathway (Kolb, 2011), so therefore the lack of the rod bipolar dendrite within the rod spherule seems like it would fundamentally interrupt rod-based vision. Even with full retinal reattachment, animals can still experience visual deficits (Sørensen et al., 2020) and so it would not be surprising if that is due to the lack of the rod bipolar cell, which would prevent signal from transmitting through the rod visual pathway[29]. Without more specific electrophysiological investigation, it is difficult to know whether these cells are indeed able to still send proper signals. Interestingly, even in heavily degenerated synapses, the HCATs still remained. HCATs are generally responsible for lateral communication

---

[29] It should be noted that humans primarily use cones for day vision, and so, while a lack of rod signaling may impair scotopic vision, the more common visual deficits may be due to similar degenerative characteristics in cones. Follow-up studies exploring ultrastructure in cone synapses would be useful for exploring that possibility.

across photoreceptors resulting in improved signal diversity, enhanced sensitivity to ambient light, and improved spatial frequency tuning (Chaya et al., 2017). Without RBs, it seems strange that the HCATs remain, because the modified signal would still not necessarily pass to a rod bipolar cell and reach the brain. In addition, due to the retinal detachment, the photoreceptors would likely not be receiving the correct light information due to folds in the retina or bubbles in the subretinal space. What is the purpose of the remaining horizontal cell process(es) within the RS? One potential idea is simply that HCATs are a sturdier cell type. Single cell RNA-sequencing of retinas has shown that, from a transcriptomic perspective, in mouse, there are 15 types of bipolar cells (Shekhar et al., 2016; Peng, 2023) but only a single type of horizontal cell (Macosko et al., 2015; Peng, 2023). Horizontal cells may simply be hardier cells, able to maintain processes more easily due to their simpler signaling strategy compared to bipolar cells and their lack of extensive specialization. Another possibility is that HCATs are responsible either for the structural organization of the invagination, or for rod bipolar cell recruitment signaling, as Nemitz et al., 2019 found that ablation of horizontal cells prevented rod bipolar processes from entering the RS in a developmental context. A final possible option could be that the HCATs are maintained for the purpose of lateral signaling to RS that are away from the site of the detachment. They still may be able to communicate with attached retina, should the RS be localized near the edge of the detachment. Overall, many questions still remain as to the outcome of the visual pathway after a detachment, and by studying how the signals from these cells change we will likely uncover some fundamental properties of how they function during stress.

Beyond the postsynaptic processes, there was another result that brings up questions regarding synaptic activity and signal transmission: why does the synaptic vesicle content drop after 30 minutes? Rod photoreceptors are depolarized in the dark, constantly releasing synaptic vesicles, and halt vesicle release with light signal (Lamb and Pugh, 2006). The immediate reduction of synaptic vesicles at 30min., that recovers by 1hr., describes that there must be a large immediate neurotransmitter release, that coincides with a large lack of light signal, right as the detachment occurs. This could occur for a couple reasons. The first possibility is simply that the cat felt physiologically uncomfortable after the detachment surgery, and so they simply closed their eyes for the first 15-30 minutes post-surgery. This would result in an extended dark signal, that likely resolved by 1 hour after the animal had become used to the feeling in their eye and was able to open their eye before they were sacrificed[30]. While this idea is possible, it seems surprising that the vesicle density would change to such a significant degree simply from eye-closing. Another possibility is that the reagents that were injected (or simply inflammation and stress caused by the injection/surgery itself) during the detachment triggered off target effects that resulted in vesicle release from the RS, that recovered by 1hr. While the sodium hyaluronate used for the detachment has not been documented to have this effect (Abatangelo et al., 2020), inducing a retinal detachment introduces stress and inflammation in the animal and so the vesicle release may have simply been a stress response. Alternatively, the injected solution could dilute the natural content of the subretinal space, which could change ionic concentrations and

---

[30] Unfortunately, we do not have behavioral information about the cat after surgery. This possibility is speculation.

trigger this response in the RS. Overall, it is unclear why this drop in synaptic vesicle density occurs, and it would be interesting to see if this is consistent in other animal models and contexts.

Ribbon Fragmentation

Analyzing the graphs in Fig. 3-6K/L indicates conservation of ribbon length, after an initial elongation at 30min. Conservation of ribbon length over the detachment period, especially with the initial elongation at 30min., indicates a high likelihood that ribbons are elongated and subsequently fragmented, rather than produced *de novo*. Generally speaking, it seems that the ribbon has intrinsic signals that keep it in close contact with the invaginating membrane/postsynaptic processes, and in situations where the cell may be less healthy, and the postsynaptic processes are moving, the ribbon then changes to follow and maintain those connections. The protein that makes up the ribbon, Ribeye, is stable at the ribbon, but intrinsically dynamic such that the ribbon can change shape and localization (Chen et al., 2018). The ribbons initially elongate to maintain contact with the moving processes (as in Fig. 3-4D’, white arrow, and Fig.3-3H), but, at some point around 24-48hrs., the ribbon is unable to maintain contact with all the remodeling cells, especially with the retracting RB. In some cases, the end of the ribbon splits, likely in an attempt to increase surface area to make better contact with the retracting RB and the other postsynaptic processes (Fig. 3-3G). At some point, however, the ribbon is unable to maintain this elongated state, likely due to the dynamic nature of the Ribeye protein (Chen et al., 2018) preventing large stable structures. At that point, the ribbon fragments. While this logically follows based on what we understand about the ribbon, it does not explain why we first see small ribbons appear at 30min. (Fig. 3-2C, D), and 1hr. (Fig. 3-6B/C), but then no more very small ribbons until 72hrs. Perhaps these are transient intermediaries in the elongation process; the ribbon grows significantly between the control and the 30min. detachment period (677.9 ± 94.8nm in the control [N = 22], compared to 1191 ± 154.2nm at 30m. [N = 7], Mean ± SEM, Fig. 3-6L), and so perhaps these small ribbons break off from the main ribbon, but then fuse back creating a large elongated ribbon. Alternatively, the small ribbons may act to communicate structural information about the invagination. In that case, once degeneration initiates, these small ribbons are fragmented and might anchor to different parts of the invagination to explore whether the single ribbon is sufficient for synaptic transmission after postsynaptic process remodeling. In some cases, it may collect information that one of the processes is not close enough for proper transmission, and would then either elongate itself to maintain that contact (resulting in 2 larger ribbons as seen at 48hrs.), or fuse back into the primary ribbon to support its growth in that direction. The fact that there is more than one ribbon is more likely to be related to covering the full required surface area of the invagination for transmission as it undergoes remodeling, rather than any functional benefit of having two ribbons. The length of the ribbon, however, plays a very functional role in ensuring association with all the postsynaptic processes.

Another interesting result with regards to the ribbon was the ability of the ribbon to spontaneously organize with HCATs on either side. In every normal tomogram, the two HCATs lined either side of the ribbon, and as the processes remodeled during degeneration, that organization was maintained until it was impossible to maintain due to retraction of the HCAT. Even at 48hrs., where one of the HCATs had significantly shrunken in volume, the ribbon still associated with HCATs on either side – in the case of the left ribbon in Fig. 3-4B however, it was the same red HCAT that associated on either side of the ribbon. It seems likely that there is some organizing protein or structure that guides either the ribbon or the HCATs to associate in this particular way.

What is needed to make and maintain an invagination?

The structural organization of the rod spherule is very tight, such that there is little extracellular space present between the postsynaptic processes and the plasma membrane. During detachment, this close organization is lost, with increases in extracellular space in large part caused by remodeling of the internal processes. Presumably, glutamate present in the synaptic cleft could diffuse out of the invagination and into the rest of the retina, due to this increased extracellular space. Glutamate is an excitotoxin that can cause photoreceptor cell death (Charles-Messance et al., 2020), and lead to degenerative changes in neurons (Yang, 2004; Yee et al., 2018; Milla-Navarro et al., 2021); maintaining the interior of the invagination seems important in preventing degenerative changes from spreading to other parts of the retina. Energetically unstable structures like the invagination, however, cannot appear spontaneously and require protein and lipid structure to create and maintain. Lipid composition plays a significant role in controlling the rigidity and tension of the plasma membrane (Togo et al., 2000; Gauthier et al., 2011; Diz-Muñoz et al., 2013; Horn and Jaiswal, 2019). By changing the distribution and organization of different lipids, the cell can create significant curvature and structure. Within different regions of the RS invagination, there are likely lipids like sphingomyelin that, along with intercalating cholesterol, form lipid rafts (van Meer et al., 2008) to decrease the local membrane fluidity around straighter regions (Cebecauer et al., 2018; Horn and Jaiswal, 2019). There are also likely many cylindrical lipids, such as phosphatidylserine or dioleoylglycerol, all within the outer leaflet of the invagination in order to form an inward membrane curvature (Vamparys et al., 2013; Horn and Jaiswal, 2019) along heavily curved regions. The distribution and organization of different lipids within the plasma membrane of the invagination likely plays a significant role in its maintenance, however, lipids have been entirely unstudied in the context of the RS invagination. In addition, plasma membrane structure is highly variable (Mouritsen, 2011), and a vast majority of studies investigating invagination lipid structure explored it in the context of a fusing/forming vesicle; to our knowledge, lipid structure at a stable invagination like in the RS has never been investigated.

Beyond lipids, BAR and N-BAR proteins play a significant role in producing, controlling, and maintaining membrane curvature (Mim and Unger, 2012). There are also likely BAR domain proteins, presumably F-BAR (Frost et al., 2008) proteins, that associate all around the invagination membrane, especially the neck region (Zhao et al., 2013), to induce curvature. On a larger scale, another thing that likely supports invagination structure are the HCAT processes themselves. It was found that ablating HCAT processes prevented rod bipolar process recruitment to the RS during development (Nemitz et al., 2019); due to the extent that the HCAT processes enter the invagination, their complex branching structure, and the tendency for the plasma membrane to tightly contour the edges of the HCAT implies that the HCATs may be fairly responsible for preventing the invagination from collapsing. The HCAT may provide an outward force to ensure the invagination keeps its shape, and in contexts where the invagination breaks down, it is always preceded by a simplification of the HCATs within the invagination. Further evidence for this is shown in Fig. 3-5D/D’ and 3-5G/G’, where, after 72hrs. of detachment, only a single HCAT remained that was very tightly contoured by the spherical plasma membrane. It seems likely that, without the remaining HCAT, these invaginations would collapse and flatten with respect to the RS plasma membrane. In normal invaginations, with complex branching and organization (see Fig. 2-4A/B), there is very likely to be a large amount of protein and lipid modification to create such a complex structure.

Reattachment/regeneration and the clinic

Retinal detachment is a serious injury frequently requiring surgery for appropriate reattachment of the retina (Blair and Czyz, 2024). Even with confirmed anatomical reattachment, animals can still experience visual deficits (Sørensen et al., 2020), and, even with confirmed outer segment recovery, there still tend to be abnormalities with the outer segments in well regenerated regions (Guérin et al., 1989, 1993). A chief limitation to our study is that we only investigated detached samples, and not reattached ones, and so it is still unclear the timescale required for reattachment to ensure full recovery of the synapse. That said, we can make some speculative conclusions based on our results. Maintaining the rod bipolar process either at or near the invagination seems fundamentally important for recovery. If the RB dendrite retracts back to its original cell body, is it able to then regrow that dendrite and find the same photoreceptor synapse? If the RB does indeed retract back into its original cell, this may interfere and modify the structural synaptic proteins present on this process such as mGluR6 and TRPM1 (Martemyanov and Sampath, 2017). They would then need to be trafficked to a new developing process during healing, something that has only been seen during development (Anastassov et al., 2019). We were unable to identify the RB dendrite once it had retracted from the invagination, and so it is difficult to tell how far this process traveled after retraction. Since both RBs retracted from the synapse in some cases by 48hrs (in 2 of 6 synapses), but almost always by 72hrs (in 8 of 9 synapses), recovery would presumably be very difficult. By 48hrs., at least 1 RB dendrite left the invagination in every synapse analyzed, and so based on these results, we hypothesize that, in cat, a retina must be reattached within 24hrs. to ensure a full recovery. Further validation of this fact can be seen in the literature: Lewis et al., 2003 reattached a retina after 3 days of detachment, and found that, after 28 days of recovery, there were still degenerative issues across the retina. Sothivannan et al., 2022 found that patients who had retinal reattachments within 0-3 days, but especially within 24hrs., had better outcomes than patients with reattachments done at 4-7 days. Together, this information implies that 24hrs.[31] is likely the reattachment threshold to prevent long term synaptic damage. All that said, without investigating reattached samples, we cannot make any definitive conclusions. It's entirely possible that the RB is indeed able to search out and find the same photoreceptor synapse even after months of detachment (albeit, this situation is fairly unlikely). It is also possible that ribbons are unable to fuse back

---

[31] Technically, our evidence cannot determine when between 24hrs. and 48hrs. the RB dendrites retract, only that they do significantly retract in that time frame. 24hrs. is the final time point that we can state that all synapses still contained the required processes to recover.

together and so, even if all the other pieces of the invagination recover, having multiple ribbons may change the way signals are sent.

An important note to include is that ribbon synapses in other systems have problems regenerating from injury without external support. Ribbon synapses in hair cells in the cochlea have difficulty recovering from damage on their own (Martinez-Monedero et al., 2006; Maison et al., 2013), but are able to recover with support from macrophages (Manickam et al., 2023). Mammalian vertebrate hair cells are only able to recover from synaptic damage with some form of therapeutic support (Chen et al., 2019). It seems likely that the photoreceptor synapse can recover if it is reattached within 24hrs., but perhaps it can still recover from longer detachments with appropriate treatment. Recent work from Ellen Townes-Anderson has shown that ROCK inhibition during retinal detachment reduces RS retraction, protects cone synapses, (Townes-Anderson et al., 2023) and reduces functional damage to rod synapses (Halász et al., 2021). ROCK inhibition is a promising new therapeutic for preventing photoreceptor synaptic damage in injury, and could be a valuable addition to the current treatment dogma in minimizing synaptic damage during a retinal detachment.

Altogether, our investigation into the feline rod spherule during the first three days of retinal detachment has added significantly to our understanding of degeneration at one of the most complex synapses in the central nervous system. Now that we have a clear understanding of how this synapse degenerates during detachment, it is now important to explore reattached samples, to provide a therapeutic correlative to humans in the clinic.

References

Abatangelo G, Vindigni V, Avruscio G, Pandis L, Brun P (2020) Hyaluronic Acid: Redefining Its Role. Cells 9:1743.

Aggarwal A, Iemma TL, Shih I, Newsome TP, McAllery S, Cunningham AL, Turville SG (2012) Mobilization of HIV Spread by Diaphanous 2 Dependent Filopodia in Infected Dendritic Cells. PLoS Pathog 8:e1002762.

Akram R, Anwar H, Javed MS, Rasul A, Imran A, Malik SA, Raza C, Khan IU, Sajid F, Iman T, Sun T, Han HS, Hussain G (2022) Axonal Regeneration: Underlying Molecular Mechanisms and Potential Therapeutic Targets. Biomedicines 10:3186.

Alberts AS (2001) Identification of a carboxyl-terminal diaphanous-related formin homology protein autoregulatory domain. J Biol Chem 276:2824–2830.

Almedawar S, Vafia K, Schreiter S, Neumann K, Khattak S, Kurth T, Ader M, Karl MO, Tsang SH, Tanaka EM (2020) MERTK-Dependent Ensheathment of Photoreceptor Outer Segments by Human Pluripotent Stem Cell-Derived Retinal Pigment Epithelium. Stem Cell Reports 14:374–389.

Anastassov IA, Wang W, Dunn FA (2019) Synaptogenesis and synaptic protein localization in the postnatal development of rod bipolar cell dendrites in mouse retina. J Comp Neurol 527:52–66.

Barger SR, Reilly NS, Shutova MS, Li Q, Maiuri P, Heddleston JM, Mooseker MS, Flavell RA, Svitkina T, Oakes PW, Krendel M, Gauthier NC (2019) Membrane-cytoskeletal crosstalk mediated by myosin-I regulates adhesion turnover during phagocytosis. Nat Commun 10:1249.

Battelle B-A, LaVail MM (1978) Rhodopsin content and rod outer segment length in albino rat eyes: Modification by dark adaptation. Experimental Eye Research 26:487–497.

Besharse JC, Hollyfield JG (1979) Turnover of mouse photoreceptor outer segments in constant light and darkness. Investigative Ophthalmology & Visual Science 18:1019–1024.

Blair K, Czyz CN (2024) Retinal Detachment. In: StatPearls. Treasure Island (FL): StatPearls Publishing. Available at: http://www.ncbi.nlm.nih.gov/books/NBK551502/ [Accessed January 30, 2024].

Bonilha VL, Finnemann SC, Rodriguez-Boulan E (1999) Ezrin Promotes Morphogenesis of Apical Microvilli and Basal Infoldings in Retinal Pigment Epithelium. J Cell Biol 147:1533–1548.

Bradke F (2022) Mechanisms of Axon Growth and Regeneration: Moving between Development and Disease. J Neurosci 42:8393–8405.

Brandstätter JH, Fletcher EL, Garner CC, Gundelfinger ED, Wässle H (1999) Differential expression of the presynaptic cytomatrix protein bassoon among ribbon synapses in the mammalian retina. Eur J Neurosci 11:3683–3693.

Breitsprecher D, Goode BL (2013) Formins at a glance. J Cell Sci 126:1–7.

Bringmann A, Grosche A, Pannicke T, Reichenbach A (2013) GABA and Glutamate Uptake and Metabolism in Retinal Glial (Müller) Cells. Frontiers in Endocrinology 4 Available at: https://www.frontiersin.org/articles/10.3389/fendo.2013.00048 [Accessed August 11, 2022].

Brooks ABE, Humphreys D, Singh V, Davidson AC, Arden SD, Buss F, Koronakis V (2017) MYO6 is targeted by Salmonella virulence effectors to trigger PI3-kinase signaling and pathogen invasion into host cells. Proceedings of the National Academy of Sciences 114:3915–3920.

Burette AC, Lesperance T, Crum J, Martone M, Volkmann N, Ellisman MH, Weinberg RJ (2012) Electron tomographic analysis of synaptic ultrastructure. J Comp Neurol 520:2697–2711.

Burgoyne LA (1999) The mechanisms of pyknosis: hypercondensation and death. Exp Cell Res 248:214–222.

Burnside B, Laties AM (1976) Actin filaments in apical projections of the primate pigmented epithelial cell. Invest Ophthalmol 15:570–575.

Cao L, Yonis A, Vaghela M, Barriga EH, Chugh P, Smith MB, Maufront J, Lavoie G, Méant A, Ferber E, Bovellan M, Alberts A, Bertin A, Mayor R, Paluch EK, Roux PP, Jégou A, Romet-Lemonne G, Charras G (2020) SPIN90 associates with mDia1 and the Arp2/3 complex to regulate cortical actin organization. Nat Cell Biol 22:803–814.

Carter-Dawson LD, Lavail MM (1979) Rods and cones in the mouse retina. I. Structural analysis using light and electron microscopy. Journal of Comparative Neurology 188:245–262.

Cebecauer M, Amaro M, Jurkiewicz P, Sarmento MJ, Šachl R, Cwiklik L, Hof M (2018) Membrane Lipid Nanodomains. Chem Rev 118:11259–11297.

Ch U (1914) On the inheritance of retinitis pigmentosa;with note of cases. Royal London Opthalmol Hosp Rep 19:130–236.

Champion JA, Mitragotri S (2006) Role of target geometry in phagocytosis. Proceedings of the National Academy of Sciences 103:4930–4934.

Charles-Messance H, Blot G, Couturier A, Vignaud L, Touhami S, Beguier F, Siqueiros L, Forster V, Barmo N, Augustin S, Picaud S, Sahel J-A, Rendon A, Grosche A, Tadayoni R, Sennlaub F, Guillonneau X (2020) IL-1β induces rod degeneration through the disruption of retinal glutamate homeostasis. Journal of Neuroinflammation 17:1.

Chaya T, Matsumoto A, Sugita Y, Watanabe S, Kuwahara R, Tachibana M, Furukawa T (2017) Versatile functional roles of horizontal cells in the retinal circuit. Sci Rep 7:5540.

Chazotte B (2011) Labeling membrane glycoproteins or glycolipids with fluorescent wheat germ agglutinin. Cold Spring Harb Protoc 2011:pdb.prot5623.

Chen Y, Zhang S, Chai R, Li H (2019) Hair Cell Regeneration. In: Hearing Loss: Mechanisms, Prevention and Cure (Li H, Chai R, eds), pp 1–16 Advances in Experimental Medicine and Biology. Singapore: Springer. Available at: https://doi.org/10.1007/978-981-13-6123-4_1 [Accessed January 24, 2024].

Chen Z, Chou S-W, McDermott BM (2018) Ribeye protein is intrinsically dynamic but is stabilized in the context of the ribbon synapse. J Physiol 596:409–421.

Cheng J, Grassart A, Drubin DG (2012) Myosin 1E coordinates actin assembly and cargo trafficking during clathrin-mediated endocytosis. Mol Biol Cell 23:2891–2904.

Clark K, Karsch-Mizrachi I, Lipman DJ, Ostell J, Sayers EW (2016) GenBank. Nucleic Acids Res 44:D67–D72.

Coblentz FE, Radeke MJ, Lewis GP, Fisher SK (2003) Evidence that ganglion cells react to retinal detachment. Exp Eye Res 76:333–342.

Collin GB, Shi L, Yu M, Akturk N, Charette JR, Hyde LF, Weatherly SM, Pera MF, Naggert JK, Peachey NS, Nishina PM, Krebs MP (2022) A Splicing Mutation in Slc4a5 Results in Retinal Detachment and Retinal Pigment Epithelium Dysfunction. Int J Mol Sci 23:2220.

Colucci-Guyon E, Niedergang F, Wallar BJ, Peng J, Alberts AS, Chavrier P (2005) A Role for Mammalian Diaphanous-Related Formins in Complement Receptor (CR3)-Mediated Phagocytosis in Macrophages. Current Biology 15:2007–2012.

Cook B, Lewis GP, Fisher SK, Adler R (1995) Apoptotic photoreceptor degeneration in experimental retinal detachment. Invest Ophthalmol Vis Sci 36:990–996.

Cooke P, Janowitz H, Dougherty SE (2022) Neuronal Redevelopment and the Regeneration of Neuromodulatory Axons in the Adult Mammalian Central Nervous System. Frontiers in Cellular Neuroscience 16 Available at: https://www.frontiersin.org/articles/10.3389/fncel.2022.872501 [Accessed January 24, 2024].

Cooper GM (2000) Structure and Organization of Actin Filaments. In: The Cell: A Molecular Approach. 2nd edition. Sinauer Associates. Available at: https://www.ncbi.nlm.nih.gov/books/NBK9908/ [Accessed November 17, 2023].

Costa G, Ribeiro FF, Sebastião AM, Muir EM, Vaz SH (2022) Bridging the gap of axonal regeneration in the central nervous system: A state of the art review on central axonal regeneration. Frontiers in Neuroscience 16 Available at:

https://www.frontiersin.org/articles/10.3389/fnins.2022.1003145 [Accessed February 2, 2024].

Dance A (2019) Core Concept: Cells nibble one another via the under-appreciated process of trogocytosis. Proc Natl Acad Sci U S A 116:17608–17610.

Daniel R, Nagata B, Altman D (2014) A Role for Myosin VI in Retinal Pigment Epithelium Phagocytosis. Biophysical Journal 106:178a.

D’Cruz PM, Yasumura D, Weir J, Matthes MT, Abderrahim H, LaVail MM, Vollrath D (2000) Mutation of the receptor tyrosine kinase gene Mertk in the retinal dystrophic RCS rat. Hum Mol Genet 9:645–651.

Dhanda AS, Vogl AW, Albraiki SE, Otey CA, Beck MR, Guttman JA (2018) Palladin Compensates for the Arp2/3 Complex and Supports Actin Structures during Listeria Infections. mBio 9:10.1128/mbio.02259-17.

Dick O, tom Dieck S, Altrock WD, Ammermüller J, Weiler R, Garner CC, Gundelfinger ED, Brandstätter JH (2003) The Presynaptic Active Zone Protein Bassoon Is Essential for Photoreceptor Ribbon Synapse Formation in the Retina. Neuron 37:775–786.

Ding B, Narvaez-Ortiz HY, Singh Y, Hocky GM, Chowdhury S, Nolen BJ (2022) Structure of Arp2/3 complex at a branched actin filament junction resolved by single-particle cryo-electron microscopy. Proceedings of the National Academy of Sciences 119:e2202723119.

Diz-Muñoz A, Fletcher DA, Weiner OD (2013) Use the force: Membrane tension as an organizer of cell shape and motility. Trends Cell Biol 23:47–53.

Dominguez R, Holmes KC (2011) Actin Structure and Function. Annu Rev Biophys 40:169–186.

Duncan JL, LaVail MM, Yasumura D, Matthes MT, Yang H, Trautmann N, Chappelow AV, Feng W, Earp HS, Matsushima GK, Vollrath D (2003) An RCS-Like Retinal Dystrophy Phenotype in Mer Knockout Mice. Investigative Ophthalmology & Visual Science 44:826–838.

Dunn KC, Aotaki-Keen AE, Putkey FR, Hjelmeland LM (1996) ARPE-19, a human retinal pigment epithelial cell line with differentiated properties. Exp Eye Res 62:155–169.

Dunn KC, Marmorstein AD, Bonilha VL, Rodriguez-Boulan E, Giordano F, Hjelmeland LM (1998) Use of the ARPE-19 cell line as a model of RPE polarity: basolateral secretion of FGF5. Invest Ophthalmol Vis Sci 39:2744–2749.

Eckel-Mahan K, Sassone-Corsi P (2015) Phenotyping Circadian Rhythms in Mice. Curr Protoc Mouse Biol 5:271–281.

Erickson PA, Fisher SK, Anderson DH, Stern WH, Borgula GA (1983) Retinal detachment in the cat: the outer nuclear and outer plexiform layers. Invest Ophthalmol Vis Sci 24:927–942.

Esteve-Rudd J, Hazim RA, Diemer T, Paniagua AE, Volland S, Umapathy A, Williams DS (2018) Defective phagosome motility and degradation in cell nonautonomous RPE pathogenesis of a dominant macular degeneration. Proc Natl Acad Sci USA 115:5468–5473.

Fadok VA, Voelker DR, Campbell PA, Cohen JJ, Bratton DL, Henson PM (1992) Exposure of phosphatidylserine on the surface of apoptotic lymphocytes triggers specific recognition and removal by macrophages. J Immunol 148:2207–2216.

Fattouh R, Kwon H, Czuczman MA, Copeland JW, Pelletier L, Quinlan ME, Muise AM, Higgins DE, Brumell JH (2015) The Diaphanous-Related Formins Promote Protrusion Formation and Cell-to-Cell Spread of Listeria monocytogenes. J Infect Dis 211:1185–1195.

Finnemann SC, Nandrot EF (2006) MERTK ACTIVATION DURING RPE PHAGOCYTOSIS IN VIVO REQUIRES αVβ5 INTEGRIN. Adv Exp Med Biol 572:499–503.

Fisher SK, Steinberg RH (1982) Origin and organization of pigment epithelial apical projections to cones in cat retina. J Comp Neurol 206:131–145.

Frost A, Perera R, Roux A, Spasov K, Destaing O, Egelman EH, De Camilli P, Unger VM (2008) Structural Basis of Membrane Invagination by F-BAR Domains. Cell 132:807–817.

Fu Y, Yau K-W (2007) Phototransduction in mouse rods and cones. Pflugers Arch - Eur J Physiol 454:805–819.

Gal A, Li Y, Thompson DA, Weir J, Orth U, Jacobson SG, Apfelstedt-Sylla E, Vollrath D (2000) Mutations in MERTK, the human orthologue of the RCS rat retinal dystrophy gene, cause retinitis pigmentosa. Nat Genet 26:270–271.

Gauthier NC, Fardin MA, Roca-Cusachs P, Sheetz MP (2011) Temporary increase in plasma membrane tension coordinates the activation of exocytosis and contraction during cell spreading. Proc Natl Acad Sci U S A 108:14467–14472.

Gauvin TJ, Fukui J, Peterson JR, Higgs HN (2009) Isoform-selective chemical inhibition of mDia-mediated actin assembly. Biochemistry 48:9327–9329.

Gerisch G, Ecke M, Schroth-Diez B, Gerwig S, Engel U, Maddera L, Clarke M (2009) Self-organizing actin waves as planar phagocytic cup structures. Cell Adh Migr 3:373–382.

Gibbs D, Kitamoto J, Williams DS (2003) Abnormal phagocytosis by retinal pigmented epithelium that lacks myosin VIIa, the Usher syndrome 1B protein. Proc Natl Acad Sci U S A 100:6481–6486.

Gibbs D, Williams DS (2003) Isolation and Culture of Primary Mouse Retinal Pigmented Epithelial Cells. In: Retinal Degenerations (LaVail MM, Hollyfield JG, Anderson RE, eds), pp 347–352 Advances in Experimental Medicine and Biology. Boston, MA: Springer US.

Goley ED, Welch MD (2006) The ARP2/3 complex: an actin nucleator comes of age. Nature Reviews Molecular Cell Biology 7:713–726.

Goode BL, Eck MJ (2007) Mechanism and Function of Formins in the Control of Actin Assembly. Annual Review of Biochemistry 76:593–627.

Goode BL, Eskin J, Shekhar S (2023) Mechanisms of actin disassembly and turnover. J Cell Biol 222:e202309021.

Grünert U, Martin PR (1991) Rod bipolar cells in the macaque monkey retina: immunoreactivity and connectivity. J Neurosci 11:2742–2758.

Guérin CJ, Anderson DH, Fariss RN, Fisher SK (1989) Retinal reattachment of the primate macula. Photoreceptor recovery after short-term detachment. Invest Ophthalmol Vis Sci 30:1708–1725.

Guérin CJ, Lewis GP, Fisher SK, Anderson DH (1993) Recovery of photoreceptor outer segment length and analysis of membrane assembly rates in regenerating primate photoreceptor outer segments. Invest Ophthalmol Vis Sci 34:175–183.

Halász É, Zarbin MA, Davidow AL, Frishman LJ, Gombkoto P, Townes-Anderson E (2021) ROCK inhibition reduces morphological and functional damage to rod synapses after retinal injury. Scientific Reports 11:692.

Hasson T, Skowron JF, Gilbert DJ, Avraham KB, Perry WL, Bement WM, Anderson BL, Sherr EH, Chen ZY, Greene LA, Ward DC, Corey DP, Mooseker MS, Copeland NG, Jenkins NA (1996) Mapping of unconventional myosins in mouse and human. Genomics 36:431–439.

Hazim RA, Volland S, Yen A, Burgess BL, Williams DS (2019) Rapid differentiation of the human RPE cell line, ARPE-19, induced by nicotinamide. Exp Eye Res 179:18–24.

Hazim RA, Williams DS (2018) Cell Culture Analysis of the Phagocytosis of Photoreceptor Outer Segments by Primary Mouse RPE Cells. Methods Mol Biol 1753:63–71.

Hoffmann A-K, Naj X, Linder S (2014) Daam1 is a regulator of filopodia formation and phagocytic uptake of Borrelia burgdorferi by primary human macrophages. FASEB J 28:3075–3089.

Horn A, Jaiswal JK (2019) Structural and signaling role of lipids in plasma membrane repair. Curr Top Membr 84:67–98.

Horsthemke M, Bachg AC, Groll K, Moyzio S, Müther B, Hemkemeyer SA, Wedlich-Söldner R, Sixt M, Tacke S, Bähler M, Hanley PJ (2017) Multiple roles of filopodial dynamics in particle capture and phagocytosis and phenotypes of Cdc42 and Myo10 deletion. J Biol Chem 292:7258–7273.

Houdusse A, Sweeney HL (2016) How myosin generates force on actin filaments. Trends Biochem Sci 41:989–997.

Hubert T, Vandekerckhove J, Gettemans J (2011) Actin and Arp2/3 localize at the centrosome of interphase cells. Biochemical and Biophysical Research Communications 404:153–158.

Hudrisier D, Aucher A, Puaux A-L, Bordier C, Joly E (2007) Capture of Target Cell Membrane Components via Trogocytosis Is Triggered by a Selected Set of Surface Molecules on T or B Cells1. The Journal of Immunology 178:3637–3647.

Huotari J, Helenius A (2011) Endosome maturation. EMBO J 30:3481–3500.

Inana G, Murat C, An W, Yao X, Harris IR, Cao J (2018) RPE phagocytic function declines in age-related macular degeneration and is rescued by human umbilical tissue derived cells. Journal of Translational Medicine 16:63.

Innocenti M (2023) Investigating Mammalian Formins with SMIFH2 Fifteen Years in: Novel Targets and Unexpected Biology. Int J Mol Sci 24:9058.

Isogai T, van der Kammen R, Leyton-Puig D, Kedziora KM, Jalink K, Innocenti M (2015) Initiation of lamellipodia and ruffles involves cooperation between mDia1 and the Arp2/3 complex. Journal of Cell Science 128:3796–3810.

Jaumouillé V, Cartagena-Rivera AX, Waterman CM (2019) Coupling of β 2 integrins to actin by a mechanosensitive molecular clutch drives complement receptor-mediated phagocytosis. Nat Cell Biol 21:1357–1369.

Jaumouillé V, Waterman CM (2020) Physical Constraints and Forces Involved in Phagocytosis. Frontiers in Immunology 11 Available at: https://www.frontiersin.org/articles/10.3389/fimmu.2020.01097 [Accessed November 21, 2023].

Ji M, Miao Y, Dong L-D, Chen J, Mo X-F, Jiang S-X, Sun X-H, Yang X-L, Wang Z (2012) Group I mGluR-mediated inhibition of Kir channels contributes to retinal Müller cell gliosis in a rat chronic ocular hypertension model. J Neurosci 32:12744–12755.

Jiang M, Esteve-Rudd J, Lopes VS, Diemer T, Lillo C, Rump A, Williams DS (2015) Microtubule motors transport phagosomes in the RPE, and lack of KLC1 leads to AMD-like pathogenesis. J Cell Biol 210:595–611.

Junemann A, Filić V, Winterhoff M, Nordholz B, Litschko C, Schwellenbach H, Stephan T, Weber I, Faix J (2016) A Diaphanous-related formin links Ras signaling directly to actin assembly in macropinocytosis and phagocytosis. Proceedings of the National Academy of Sciences 113:E7464–E7473.

Kauppinen A, Niskanen H, Suuronen T, Kinnunen K, Salminen A, Kaarniranta K (2012) Oxidative stress activates NLRP3 inflammasomes in ARPE-19 cells—Implications for age-related macular degeneration (AMD). Immunology Letters 147:29–33.

Keeling E, Chatelet DS, Tan NYT, Khan F, Richards R, Thisainathan T, Goggin P, Page A, Tumbarello DA, Lotery AJ, Ratnayaka JA (2020) 3D-Reconstructed Retinal Pigment Epithelial Cells Provide Insights into the Anatomy of the Outer Retina. Int J Mol Sci 21:8408.

Kevany BM, Palczewski K (2010) Phagocytosis of Retinal Rod and Cone Photoreceptors. Physiology (Bethesda) 25:8–15.

Kim J, Waldvogel HJ, Faull RLM, Curtis MA, Nicholson LFB (2015) The RAGE receptor and its ligands are highly expressed in astrocytes in a grade-dependant manner in the striatum and subependymal layer in Huntington’s disease. J Neurochem 134:927–942.

Kim Y-K, Yu H, Summers VR, Donaldson KJ, Ferdous S, Shelton D, Zhang N, Chrenek MA, Jiang Y, Grossniklaus HE, Boatright JH, Kong J, Nickerson JM (2021) Morphometric Analysis of Retinal Pigment Epithelial Cells From C57BL/6J Mice During Aging. Invest Ophthalmol Vis Sci 62:32.

Kolb H (2011) Circuitry for Rod Signals Through The Retina by Helga Kolb – Webvision. Available at: https://webvision.med.utah.edu/book/part-iii-retinal-circuits/circuitry-for-rod-cells-through-the-retina/ [Accessed December 22, 2021].

Korobova F, Gauvin TJ, Higgs HN (2014) A Role for Myosin II in Mammalian Mitochondrial Fission. Current Biology 24:409–414.

Krahling S, Callahan MK, Williamson P, Schlegel RA (1999) Exposure of phosphatidylserine is a general feature in the phagocytosis of apoptotic lymphocytes by macrophages. Cell Death Differ 6:183–189.

Kremer JR, Mastronarde DN, McIntosh JR (1996) Computer visualization of three-dimensional image data using IMOD. J Struct Biol 116:71–76.

Krendel M, Osterweil EK, Mooseker MS (2007) Myosin 1E interacts with synaptojanin-1 and dynamin via its SH3 domain. FEBS Lett 581:644–650.

Kress H, Stelzer EHK, Holzer D, Buss F, Griffiths G, Rohrbach A (2007) Filopodia act as phagocytic tentacles and pull with discrete steps and a load-dependent velocity. Proc Natl Acad Sci U S A 104:11633–11638.

Krishnan K, Moens PDJ (2009) Structure and functions of profilins. Biophys Rev 1:71–81.

Kueh HY, Charras GT, Mitchison TJ, Brieher WM (2008) Actin disassembly by cofilin, coronin, and Aip1 occurs in bursts and is inhibited by barbed-end cappers. J Cell Biol 182:341–353.

Kung F, Wang W, Tran TS, Townes-Anderson E (2017) Sema3A Reduces Sprouting of Adult Rod Photoreceptors In Vitro. Invest Ophthalmol Vis Sci 58:4318–4331.

Kwon W, Freeman SA (2020) Phagocytosis by the Retinal Pigment Epithelium: Recognition, Resolution, Recycling. Frontiers in Immunology 11 Available at: https://www.frontiersin.org/article/10.3389/fimmu.2020.604205 [Accessed January 26, 2022].

Lamb TD, Pugh EN Jr (2006) Phototransduction, Dark Adaptation, and Rhodopsin Regeneration The Proctor Lecture. Investigative Ophthalmology & Visual Science 47:5138–5152.

Lee SH, Dominguez R (2010) Regulation of Actin Cytoskeleton Dynamics in Cells. Mol Cells 29:311–325.

Lewis GP, Chapin EA, Luna G, Linberg KA, Fisher SK (2010) The fate of Müller's glia following experimental retinal detachment: nuclear migration, cell division, and subretinal glial scar formation. Mol Vis 16:1361–1372.

Lewis GP, Linberg KA, Fisher SK (1998) Neurite outgrowth from bipolar and horizontal cells after experimental retinal detachment. Invest Ophthalmol Vis Sci 39:424–434.

Lewis GP, Sethi CS, Linberg KA, Charteris DG, Fisher SK (2003) Experimental retinal reattachment. Mol Neurobiol 28:159–175.

Li F, Higgs HN (2003) The mouse Formin mDia1 is a potent actin nucleation factor regulated by autoinhibition. Curr Biol 13:1335–1340.

Li S, Mitchell J, Briggs DJ, Young JK, Long SS, Fuerst PG (2016) Morphological Diversity of the Rod Spherule: A Study of Serially Reconstructed Electron Micrographs. PLoS One 11:e0150024.

Lichter PR (1992) The timing of retinal detachment surgery: patient and physician considerations. Ophthalmology 99:1349–1350.

Linberg KA, Fisher SK (1988) Ultrastructural evidence that horizontal cell axon terminals are presynaptic in the human retina. J Comp Neurol 268:281–297.

Linberg KA, Lewis GP, Fisher SK (2009) Retraction and remodeling of rod spherules are early events following experimental retinal detachment: an ultrastructural study using serial sections. Mol Vis 15:10–25.

Linberg KA, Lewis GP, Matsumoto B, Betts KE, Fisher SK (2006a) Changes in the Morphology and Connectivity of Rod Spherules After Experimental Retinal Detachment: An

Immunocytochemical and Ultrastructural Study. Invest Ophthalmol Vis Sci 47:4224–4224.

Linberg KA, Lewis GP, Matsumoto B, Betts KE, Fisher SK (2006b) Changes in the Morphology and Connectivity of Rod Spherules After Experimental Retinal Detachment: An Immunocytochemical and Ultrastructural Study. Invest Ophthalmol Vis Sci 47:4224–4224.

Liu X, Vansant G, Udovichenko IP, Wolfrum U, Williams DS (1997) Myosin VIIa, the product of the Usher 1B syndrome gene, is concentrated in the connecting cilia of photoreceptor cells. Cell Motility 37:240–252.

LoGiudice L, Matthews G (2009) The Role of Ribbons at Sensory Synapses. Neuroscientist 15:380–391.

Lu Q, Gore M, Zhang Q, Camenisch T, Boast S, Casagranda F, Lai C, Skinner MK, Klein R, Matsushima GK, Earp HS, Goff SP, Lemke G (1999) Tyro-3 family receptors are essential regulators of mammalian spermatogenesis. Nature 398:723–728.

Macosko EZ, Basu A, Satija R, Nemesh J, Shekhar K, Goldman M, Tirosh I, Bialas AR, Kamitaki N, Martersteck EM, Trombetta JJ, Weitz DA, Sanes JR, Shalek AK, Regev A, McCarroll SA (2015) Highly Parallel Genome-wide Expression Profiling of Individual Cells Using Nanoliter Droplets. Cell 161:1202–1214.

Maeda A, Palczewska G, Golczak M, Kohno H, Dong Z, Maeda T, Palczewski K (2014) Two-photon microscopy reveals early rod photoreceptor cell damage in light-exposed mutant mice. Proc Natl Acad Sci U S A 111:E1428–E1437.

Maison SF, Usubuchi H, Liberman MC (2013) Efferent Feedback Minimizes Cochlear Neuropathy from Moderate Noise Exposure. J Neurosci 33:5542–5552.

Manickam V, Gawande DY, Stothert AR, Clayman AC, Batalkina L, Warchol ME, Ohlemiller KK, Kaur T (2023) Macrophages Promote Repair of Inner Hair Cell Ribbon Synapses following Noise-Induced Cochlear Synaptopathy. J Neurosci 43:2075–2089.

Mao Y, Finnemann SC (2012) Essential diurnal Rac1 activation during retinal phagocytosis requires αvβ5 integrin but not tyrosine kinases focal adhesion kinase or Mer tyrosine kinase. Mol Biol Cell 23:1104–1114.

Mao Y, Finnemann SC (2021) Acute RhoA/Rho Kinase Inhibition Is Sufficient to Restore Phagocytic Capacity to Retinal Pigment Epithelium Lacking the Engulfment Receptor MerTK. Cells 10:1927.

Marc RE, Murry RF, Fisher SK, Linberg KA, Lewis GP (1998) Amino acid signatures in the detached cat retina. Invest Ophthalmol Vis Sci 39:1694–1702.

Mariani AP (1984) The Neuronal Organization of the Outer Plexiform Layer of the Primate Retina. In: International Review of Cytology (Bourne GH, Danielli JF, Jeon KW, eds), pp

285–320. Academic Press. Available at: https://www.sciencedirect.com/science/article/pii/S0074769608601813 [Accessed April 28, 2023].

Martemyanov KA, Sampath AP (2017) The Transduction Cascade in Retinal ON Bipolar Cells: Signal Processing and Disease. Annu Rev Vis Sci 3:25–51.

Martinez-Monedero R, Corrales CE, Cuajungco MP, Heller S, Edge ASB (2006) Reinnervation of Hair Cells by Auditory Neurons after Selective Removal of Spiral Ganglion Neurons. J Neurobiol 66:319–331.

Martin-Gutierrez MP, Buckley TM, MacLaren RE (2022) Chronic untreated retinal detachment in a patient with choroideremia provides insight into the disease process and potential therapy. Eur J Ophthalmol 32:NP30–NP33.

Maslim J, Stone J (1986) Synaptogenesis in the retina of the cat. Brain Res 373:35–48.

Matsumoto B, Defoe DM, Besharse JC (1987) Membrane turnover in rod photoreceptors: ensheathment and phagocytosis of outer segment distal tips by pseudopodia of the retinal pigment epithelium. Proc R Soc Lond B Biol Sci 230:339–354.

Matthews G, Sterling P (2008) Evidence That Vesicles Undergo Compound Fusion on the Synaptic Ribbon. J Neurosci 28:5403–5411.

Mburu P, Liu XZ, Walsh J, Saw D, Cope MJ, Gibson F, Kendrick-Jones J, Steel KP, Brown SD (1997) Mutation analysis of the mouse myosin VIIA deafness gene. Genes Funct 1:191–203.

McLaughlin BJ, Boykins LG, Seyfried RS (1983) Surface-replica topography of retinal pigment epithelium during phagocytosis. Experimental Eye Research 36:827–838.

Mesnard C, Hays C, Grassmeyer J, Barta CL, Hinz KK, Thoreson W (2021) Synaptotagmins 1 and 7 in vesicle release from rods and cones of mouse retina. Investigative Ophthalmology & Visual Science 62:2003.

Migdale K, Herr S, Klug K, Ahmad K, Linberg K, Sterling P, Schein S (2003) Two ribbon synaptic units in rod photoreceptors of macaque, human, and cat. J Comp Neurol 455:100–112.

Milla-Navarro S, Diaz-Tahoces A, Ortuño-Lizarán I, Fernández E, Cuenca N, Germain F, de la Villa P (2021) Visual Disfunction due to the Selective Effect of Glutamate Agonists on Retinal Cells. Int J Mol Sci 22:6245.

Mim C, Unger VM (2012) Membrane curvature and its generation by BAR proteins. Trends Biochem Sci 37:526–533.

Mischi E, Soukup P, Harman CD, Oikawa K, Kowalska ME, Hartnack S, McLellan GJ, Komáromy AM, Pot SA (2022) Outer retinal thickness and visibility of the choriocapillaris in four distinct retinal regions imaged with spectral domain optical coherence tomography in dogs and cats. Vet Ophthalmol 25:122–135.

Missotten L (1965) The ultrastructure of the retina. Brussels: Editions Arscia SA.

Miyake K, Karasuyama H (2021) The Role of Trogocytosis in the Modulation of Immune Cell Functions. Cells 10:1255.

Mouritsen OG (2011) Lipids, curvature, and nano-medicine. Eur J Lipid Sci Technol 113:1174–1187.

Müller C, Charniga C, Temple S, Finnemann SC (2018a) Quantified F-Actin Morphology Is Predictive of Phagocytic Capacity of Stem Cell-Derived Retinal Pigment Epithelium. Stem Cell Reports 10:1075–1087.

Müller C, Charniga C, Temple S, Finnemann SC (2018b) Quantified F-Actin Morphology Is Predictive of Phagocytic Capacity of Stem Cell-Derived Retinal Pigment Epithelium. Stem Cell Reports 10:1075–1087.

Müller C, Finnemann SC (2016) F-actin organization as potency indicator for high-quality, functional human RPE cell culture. Investigative Ophthalmology & Visual Science 57:239.

Mullins RD, Heuser JA, Pollard TD (1998) The interaction of Arp2/3 complex with actin: Nucleation, high affinity pointed end capping, and formation of branching networks of filaments. Proc Natl Acad Sci U S A 95:6181–6186.

Mylvaganam S, Freeman SA, Grinstein S (2021) The cytoskeleton in phagocytosis and macropinocytosis. Current Biology 31:R619–R632.

Naj X, Hoffmann A-K, Himmel M, Linder S (2013) The Formins FMNL1 and mDia1 Regulate Coiling Phagocytosis of Borrelia burgdorferi by Primary Human Macrophages. Infection and Immunity 81:1683–1695.

Nambiar A, Manjithaya R (2024) Driving autophagy - the role of molecular motors. J Cell Sci 137:jcs260481.

Nandrot EF, Finnemann SC (2003) Rac1 Activation by vß5 Integrin Receptor Signaling Is Required for OS Phagocytosis by the Retinal Pigment Epithelium. Investigative Ophthalmology & Visual Science 44:942.

Nash BM, Loi TH, Fernando M, Sabri A, Robinson J, Cheng A, Eamegdool SS, Farnsworth E, Bennetts B, Grigg JR, Chung S-K, Gonzalez-Cordero A, Jamieson RV (2021) Evaluation for Retinal Therapy for RPE65 Variation Assessed in hiPSC Retinal Pigment Epithelial Cells. Stem Cells Int 2021:4536382.

Nemitz L, Dedek K, Janssen-Bienhold U (2019) Rod Bipolar Cells Require Horizontal Cells for Invagination Into the Terminals of Rod Photoreceptors. Front Cell Neurosci 13:423.

Nishimura Y, Shi S, Zhang F, Liu R, Takagi Y, Bershadsky AD, Viasnoff V, Sellers JR (2021) The formin inhibitor SMIFH2 inhibits members of the myosin superfamily. J Cell Sci 134:jcs253708.

Oberhammer FA, Hochegger K, Fröschl G, Tiefenbacher R, Pavelka M (1994) Chromatin condensation during apoptosis is accompanied by degradation of lamin A+B, without enhanced activation of cdc2 kinase. J Cell Biol 126:827–837.

Orman M, Landis M, Oza A, Nambiar D, Gjeci J, Song K, Huang V, Klestzick A, Hachicho C, Liu SQ, Kamm JM, Bartolini F, Vadakkan JJ, Rojas CM, Vizcarra CL (2022) Alterations to the broad-spectrum formin inhibitor SMIFH2 modulate potency but not specificity. Sci Rep 12:13520.

Ostrowska Z, Moraczewska J (2017) Cofilin - a protein controlling dynamics of actin filaments. Postepy Hig Med Dosw (Online) 71:339–351.

Paniagua AE, Sabharwal HS, Kethu K, Chang AW, Williams DS (2023) Revisiting the Daily Timing of POS Phagocytosis. Adv Exp Med Biol 1415:515–519.

Pantaloni D, Carlier MF (1993) How profilin promotes actin filament assembly in the presence of thymosin beta 4. Cell 75:1007–1014.

Papa R, Penco F, Volpi S, Gattorno M (2021) Actin Remodeling Defects Leading to Autoinflammation and Immune Dysregulation. Frontiers in Immunology 11 Available at: https://www.frontiersin.org/articles/10.3389/fimmu.2020.604206 [Accessed December 7, 2022].

Parinot C, Rieu Q, Chatagnon J, Finnemann SC, Nandrot EF (2014) Large-Scale Purification of Porcine or Bovine Photoreceptor Outer Segments for Phagocytosis Assays on Retinal Pigment Epithelial Cells. J Vis Exp:52100.

Paul D, Achouri S, Yoon Y-Z, Herre J, Bryant CE, Cicuta P (2013) Phagocytosis Dynamics Depends on Target Shape. Biophys J 105:1143–1150.

Peng Y-R (2023) Cell-type specification in the retina: Recent discoveries from transcriptomic approaches. Current Opinion in Neurobiology 81:102752.

Pfeffer BA, Fliesler SJ (2022) Reassessing the suitability of ARPE-19 cells as a valid model of native RPE biology. Experimental Eye Research 219:109046.

Phan S, Boassa D, Nguyen P, Wan X, Lanman J, Lawrence A, Ellisman MH (2017) 3D reconstruction of biological structures: automated procedures for alignment and reconstruction of multiple tilt series in electron tomography. Adv Struct Chem Imaging 2:8.

Pruyne D, Evangelista M, Yang C, Bi E, Zigmond S, Bretscher A, Boone C (2002) Role of Formins in Actin Assembly: Nucleation and Barbed-End Association. Science 297:612–615.

Purves D, Augustine GJ, Fitzpatrick D, Katz LC, LaMantia A-S, McNamara JO, Williams SM (2001) Recovery from Neural Injury. In: Neuroscience. 2nd edition. Sinauer Associates. Available at: https://www.ncbi.nlm.nih.gov/books/NBK10856/ [Accessed January 24, 2024].

Qian X, Mruk DD, Wong EWP, Lie PPY, Cheng CY (2013) Palladin Is a Regulator of Actin Filament Bundles at the Ectoplasmic Specialization in Adult Rat Testes. Endocrinology 154:1907–1920.

Qin JY, Zhang L, Clift KL, Hulur I, Xiang AP, Ren B-Z, Lahn BT (2010) Systematic Comparison of Constitutive Promoters and the Doxycycline-Inducible Promoter. PLoS One 5:e10611.

Ramon y Cajal S (1928) Degeneration and regeneration of the nervous system. Oxford, England: Clarendon Press.

Rao-Mirotznik R, Harkins AB, Buchsbaum G, Sterling P (1995) Mammalian rod terminal: architecture of a binary synapse. Neuron 14:561–569.

Rapaport DH, Rakic P, Yasamura D, LaVail MM (1995) Genesis of the retinal pigment epithelium in the macaque monkey. Journal of Comparative Neurology 363:359–376.

Richards DM, Endres RG (2014) The Mechanism of Phagocytosis: Two Stages of Engulfment. Biophys J 107:1542–1553.

Rizvi SA, Neidt EM, Cui J, Feiger Z, Skau CT, Gardel ML, Kozmin SA, Kovar DR (2009) Identification and characterization of a small molecule inhibitor of formin-mediated actin assembly. Chem Biol 16:1158–1168.

Robert-Paganin J, Pylypenko O, Kikuti C, Sweeney HL, Houdusse A (2020) Force Generation by Myosin Motors: A Structural Perspective. Chem Rev 120:5–35.

Rodieck RW (1998) The First Steps in Seeing.

Ronzier E, Laurenson AJ, Manickam R, Liu S, Saintilma IM, Schrock DC, Hammer JA, Rotty JD (2022) The Actin Cytoskeleton Responds to Inflammatory Cues and Alters Macrophage Activation. Cells 11:1806.

Rotty JD, Brighton HE, Craig SL, Asokan SB, Cheng N, Ting JP, Bear JE (2017) Arp2/3 complex is required for macrophage integrin functions but is dispensable for FcR phagocytosis and in vivo motility. Dev Cell 42:498-513.e6.

Rotty JD, Wu C, Haynes EM, Suarez C, Winkelman JD, Johnson HE, Haugh JM, Kovar DR, Bear JE (2015) Profilin-1 serves as a gatekeeper for actin assembly by Arp2/3-dependent and -independent pathways. Dev Cell 32:54–67.

Ruggiero L, Connor MP, Chen J, Langen R, Finnemann SC (2012) Diurnal, localized exposure of phosphatidylserine by rod outer segment tips in wild-type but not Itgb5−/− or Mfge8−/− mouse retina. PNAS 109:8145–8148.

Sakamoto S, Thumkeo D, Ohta H, Zhang Z, Huang S, Kanchanawong P, Fuu T, Watanabe S, Shimada K, Fujihara Y, Yoshida S, Ikawa M, Watanabe N, Saitou M, Narumiya S (2018) mDia1/3 generate cortical F-actin meshwork in Sertoli cells that is continuous with contractile F-actin bundles and indispensable for spermatogenesis and male fertility. PLoS Biol 16:e2004874.

Schönichen A, Geyer M (2010) Fifteen formins for an actin filament: A molecular view on the regulation of human formins. Biochimica et Biophysica Acta (BBA) - Molecular Cell Research 1803:152–163.

Sellers JR, Heissler SM (2019) Nonmuscle myosin-2 isoforms. Curr Biol 29:R275–R278.

Seth A, Otomo C, Rosen MK (2006) Autoinhibition regulates cellular localization and actin assembly activity of the diaphanous-related formins FRLα and mDia1. Journal of Cell Biology 174:701–713.

Shekhar K, Lapan SW, Whitney IE, Tran NM, Macosko EZ, Kowalczyk M, Adiconis X, Levin JZ, Nemesh J, Goldman M, McCarroll SA, Cepko CL, Regev A, Sanes JR (2016) COMPREHENSIVE CLASSIFICATION OF RETINAL BIPOLAR NEURONS BY SINGLE-CELL TRANSCRIPTOMICS. Cell 166:1308-1323.e30.

Shelby SJ (2012) MERTK-mediated Signaling in the Retinal Pigment Epithelium: Insights into the Mechanism of RPE Phagocytosis. Available at: https://www.semanticscholar.org/paper/MERTK-mediated-Signaling-in-the-Retinal-Pigment-the-Shelby/5e966a830ef5a35f25d0a3a6e56dff766bd75376 [Accessed November 15, 2023].

Shi X, Wen Z, Wang Y, Liu Y-J, Shi K, Jiu Y (2021) Feedback-Driven Mechanisms Between Phosphorylated Caveolin-1 and Contractile Actin Assemblies Instruct Persistent Cell Migration. Front Cell Dev Biol 9:665919.

Sjöstrand FS (1958) Ultrastructure of retinal rod synapses of the guinea pig eye as revealed by three-dimensional reconstructions from serial sections - PubMed. Available at: https://pubmed.ncbi.nlm.nih.gov/13631744/ [Accessed August 30, 2021].

Sørensen NB, Christiansen AT, Kjær TW, Klemp K, Cour M la, Heegaard S, Warfvinge K, Kiilgaard JF (2020) Loss of retinal tension and permanent decrease in retinal function: a new porcine model of rhegmatogenous retinal detachment. Acta Ophthalmologica 98:145–152.

Sothivannan A, Eshtiaghi A, Dhoot AS, Popovic MM, Garg SJ, Kertes PJ, Muni RH (2022) Impact of the Time to Surgery on Visual Outcomes for Rhegmatogenous Retinal Detachment Repair: A Meta-Analysis. American Journal of Ophthalmology 244:19–29.

Sterling P, Cohen E, Freed MA, Smith RG (1987) Microcircuitry of the on-beta ganglion cell in daylight, twilight, and starlight. Neurosci Res Suppl 6:S269-285.

Strauss O (2005) The Retinal Pigment Epithelium in Visual Function. Physiological Reviews 85:845–881.

Strauss O, Stumpff F, Mergler S, Wienrich M, Wiederholt M (1998) The Royal College of Surgeons rat: an animal model for inherited retinal degeneration with a still unknown genetic defect. Acta Anat (Basel) 162:101–111.

Strick DJ, Feng W, Vollrath D (2009) Mertk Drives Myosin II Redistribution during Retinal Pigment Epithelial Phagocytosis. Investigative Ophthalmology & Visual Science 50:2427–2435.

Svitkina T (2018a) The Actin Cytoskeleton and Actin-Based Motility. Cold Spring Harb Perspect Biol 10:a018267.

Svitkina TM (2018b) ULTRASTRUCTURE OF THE ACTIN CYTOSKELETON. Curr Opin Cell Biol 54:1–8.

Sweeney HL, Houdusse A (2010) Myosin VI Rewrites the Rules for Myosin Motors. Cell 141:573–582.

Tan LX, Germer CJ, Thamban T, Cunza NL, Lakkaraju A (2023) Optineurin tunes outside-in signaling to regulate lysosome biogenesis and phagocytic clearance in the retina. Current Biology 33:3805-3820.e7.

Thoidingjam LK, Blouin CM, Gaillet C, Brion A, Solier S, Niyomchon S, El Marjou A, Mouasni S, Sepulveda FE, de Saint Basile G, Lamaze C, Rodriguez R (2022) Small Molecule Inhibitors of Interferon-Induced JAK-STAT Signalling. Angewandte Chemie International Edition 61:e202205231.

Thompson SB, Wigton EJ, Krovi SH, Chung JW, Long RA, Jacobelli J (2018) The Formin mDia1 Regulates Acute Lymphoblastic Leukemia Engraftment, Migration, and Progression in vivo. Frontiers in Oncology 8 Available at: https://www.frontiersin.org/article/10.3389/fonc.2018.00389 [Accessed January 28, 2022].

Thoreson WB, Babai N, Bartoletti TM (2008) Feedback from Horizontal Cells to Rod Photoreceptors in Vertebrate Retina. J Neurosci 28:5691–5695.

Togo T, Krasieva TB, Steinhardt RA (2000) A Decrease in Membrane Tension Precedes Successful Cell-Membrane Repair. Mol Biol Cell 11:4339–4346.

Tollis S, Dart AE, Tzircotis G, Endres RG (2010) The zipper mechanism in phagocytosis: energetic requirements and variability in phagocytic cup shape. BMC Syst Biol 4:149.

Torten G, Fisher SK, Linberg KA, Luna G, Perkins G, Ellisman MH, Williams DS (2023) Three-Dimensional Ultrastructure of the Normal Rod Photoreceptor Synapse and Degenerative Changes Induced by Retinal Detachment. J Neurosci 43:5468–5482.

Townes-Anderson E, Halász É, Sugino I, Davidow AL, Frishman LJ, Fritzky L, Yousufzai FAK, Zarbin M (2023) Injury to Cone Synapses by Retinal Detachment: Differences from Rod Synapses and Protection by ROCK Inhibition. Cells 12:1485.

Townes-Anderson E, Halasz E, Wang W, Zarbin M (2021) Coming of Age for the Photoreceptor Synapse. Investigative Ophthalmology & Visual Science 62:24.

Townes-Anderson E, Wang J, Halász É, Sugino I, Pitler A, Whitehead I, Zarbin M (2017) Fasudil, a Clinically Used ROCK Inhibitor, Stabilizes Rod Photoreceptor Synapses after Retinal Detachment. Transl Vis Sci Technol 6:22.

Tsukamoto Y, Omi N (2022) Multiple Invagination Patterns and Synaptic Efficacy in Primate and Mouse Rod Synaptic Terminals. Investigative Ophthalmology & Visual Science 63:11.

Umapathy A, Torten G, Paniagua AE, Chung J, Tomlinson M, Lim C, Williams DS (2023) Spatiotemporal Live-Cell Analysis of Photoreceptor Outer Segment Membrane Ingestion by the Retinal Pigment Epithelium Reveals Actin-Regulated Scission. J Neurosci 43:2653–2664.

Uribe-Querol E, Rosales C (2021) The Multiple Roles of Trogocytosis in Immunity, the Nervous System, and Development. Biomed Res Int 2021:1601565.

Vamparys L, Gautier R, Vanni S, Bennett WFD, Tieleman DP, Antonny B, Etchebest C, Fuchs PFJ (2013) Conical Lipids in Flat Bilayers Induce Packing Defects Similar to that Induced by Positive Curvature. Biophys J 104:585–593.

van Meer G, Voelker DR, Feigenson GW (2008) Membrane lipids: where they are and how they behave. Nat Rev Mol Cell Biol 9:112–124.

Vardi N, Duvoisin R, Wu G, Sterling P (2000) Localization of mGluR6 to dendrites of ON bipolar cells in primate retina. J Comp Neurol 423:402–412.

Velle KB, Campellone KG (2018) Enteropathogenic E. coli relies on collaboration between the formin mDia1 and the Arp2/3 complex for actin pedestal biogenesis and maintenance. PLoS Pathog 14:e1007485.

Volland S, Esteve-Rudd J, Hoo J, Yee C, Williams DS (2015) A Comparison of Some Organizational Characteristics of the Mouse Central Retina and the Human Macula. PLOS ONE 10:e0125631.

Vorselen D, Barger SR, Wang Y, Cai W, Theriot JA, Gauthier NC, Krendel M (2021) Phagocytic 'teeth' and myosin-II 'jaw' power target constriction during phagocytosis Lappalainen P, Pfeffer SR, Lappalainen P, Poincloux R, eds. eLife 10:e68627.

Wan G, Corfas G (2015) No longer falling on deaf ears: mechanisms of degeneration and regeneration of cochlear ribbon synapses. Hearing research 329:1.

Wang F, An G-Y, Zhang Y, Liu H-L, Cui X-S, Kim N-H, Sun S-C (2014) Arp2/3 Complex Inhibition Prevents Meiotic Maturation in Porcine Oocytes. PLoS One 9:e87700.

Weil D, Blanchard S, Kaplan J, Guilford P, Gibson F, Walsh J, Mburu P, Varela A, Levilliers J, Weston MD (1995) Defective myosin VIIA gene responsible for Usher syndrome type 1B. Nature 374:60–61.

Weinhard L, di Bartolomei G, Bolasco G, Machado P, Schieber NL, Neniskyte U, Exiga M, Vadisiute A, Raggioli A, Schertel A, Schwab Y, Gross CT (2018) Microglia remodel synapses by presynaptic trogocytosis and spine head filopodia induction. Nat Commun 9:1228.

Wells AL, Lin AW, Chen L-Q, Safer D, Cain SM, Hasson T, Carragher BO, Milligan RA, Sweeney HL (1999) Myosin VI is an actin-based motor that moves backwards. Nature 401:505–508.

Williams DS (2008) Usher syndrome: Animal models, retinal function of Usher proteins, and prospects for gene therapy. Vision Research 48:433–441.

Williams DS, Fisher SK (1987) Prevention of rod disk shedding by detachment from the retinal pigment epithelium. Invest Ophthalmol Vis Sci 28:184–187.

Xu J, Sang M, Cheng J, Luo C, Shi J, Sun F (2023) Knockdown of disheveled-associated activator of morphogenesis 2 disrupts cytoskeletal organization and phagocytosis in rat Sertoli cells. Mol Cell Endocrinol 563:111867.

Yang X-L (2004) Characterization of receptors for glutamate and GABA in retinal neurons. Prog Neurobiol 73:127–150.

Yee CW, Ivanova E, Toychiev AH, Willis DE, Sagdullaev BT (2018) Atypical expression and activation of GluN2A and GluN2B-containing NMDA receptors at ganglion cells during retinal degeneration. Neuroscience 393:61–72.

Ying H, Yue BYJT (2012) CELLULAR AND MOLECULAR BIOLOGY OF OPTINEURIN. Int Rev Cell Mol Biol 294:223–258.

Young RW (1971) THE RENEWAL OF ROD AND CONE OUTER SEGMENTS IN THE RHESUS MONKEY. J Cell Biol 49:303–318.

Yu Y, Zhang Z, Yu Y (2023) Timing of Phagosome Maturation Depends on Their Transport Switching from Actin to Microtubule Tracks. J Phys Chem B 127:9312–9322.

Zampighi GA, Schietroma C, Zampighi LM, Woodruff M, Wright EM, Brecha NC (2011) Conical tomography of a ribbon synapse: structural evidence for vesicle fusion. PLoS One 6:e16944.

Zhao H, Michelot A, Koskela EV, Tkach V, Stamou D, Drubin DG, Lappalainen P (2013) Membrane-Sculpting BAR Domains Generate Stable Lipid Microdomains. Cell Reports 4:1213–1223.

Zhao K, Wang D, Zhao X, Wang C, Gao Y, Liu K, Wang F, Wu X, Wang X, Sun L, Zang J, Mei Y (2020) WDR63 inhibits Arp2/3-dependent actin polymerization and mediates the function of p53 in suppressing metastasis. EMBO Rep 21:e49269.

Zhao S, Zhang L, Xiang S, Hu Y, Wu Z, Shen J (2022) Gnawing Between Cells and Cells in the Immune System: Friend or Foe? A Review of Trogocytosis. Frontiers in Immunology 13 Available at: https://www.frontiersin.org/articles/10.3389/fimmu.2022.791006 [Accessed November 15, 2023].

Zihni C, Georgiadis A, Ramsden CM, Sanchez-Heras E, Haas AJ, Nommiste B, Semenyuk O, Bainbridge JWB, Coffey PJ, Smith AJ, Ali RR, Balda MS, Matter K (2022) Spatiotemporal control of actomyosin contractility by MRCKβ signaling drives phagocytosis. J Cell Biol 221:e202012042.